Thermodynamic and Morphological Transitions in Crystalline and Soft Material Interfaces

by

Ming Tang

Submitted to the Department of Materials Science and Engineering
in partial fulfillment of the requirements for the degree of

Doctor of Philosophy in Materials Science and Engineering

at the

MASSACHUSETTS INSTITUTE OF TECHNOLOGY

June 2008

© Massachusetts Institute of Technology 2008. All rights reserved.

Author .....
Department of Materials Science and Engineering
May 23, 2008

Certified by.....
W. Craig Carter
Professor of Materials Science and Engineering
Thesis Supervisor

Certified by...
Yet-Ming Chiang
Kyocera Professor of Ceramics
Thesis Supervisor

Accepted by ....
Samuel M. Allen
POSCO Professor of Physical Metallurgy
Chair, Departmental Committee on Graduate Students

MASSACHUSETTS INSTITUTE OF TECHNOLOGY
JUN 16 2008
ARCHIVES

Thermodynamic and Morphological Transitions in Crystalline and Soft Material Interfaces

by

Ming Tang

Submitted to the Department of Materials Science and Engineering
on May 23, 2008, in partial fulfillment of the
requirements for the degree of
Doctor of Philosophy in Materials Science and Engineering

Abstract

Interfaces are defects present in all materials. Interface transitions are characterized by abrupt changes in interface structure, chemistry and/or morphology under suitable conditions. They exist in many material systems and often produce profound changes in material properties. Several interface transitions in crystalline and soft materials that have not been previously well understood were studied in this thesis.

In the first part of this thesis, a diffuse-interface thermodynamic framework was developed for grain boundary structural and chemical transitions. A graphical construction method was developed to predict conditions for grain boundary transitions. A grain boundary premelting transition is predicted for systems of fixed stoichiometry. When extended to binary systems, the diffuse-interface model predicts the existence of a coupled grain boundary premelting/prewetting transition, which produces cooperative grain boundary disordering and segregation at sub-eutectic and sub-solidus temperatures. The analysis rationalizes the thermodynamic origin of intergranular glassy films (IGFs) widely observed in multi-component ceramics and alloys, for which thermodynamic stability has not been well explained in previous research. Predictions on the conditions for IGF's formation are consistent with experiments. As part of this work, a prototype of "grain boundary complexion diagrams" was constructed which delineates the stability domains of different grain boundary "complexions" on bulk phase diagrams.

Morphological transitions of interfaces in soft materials such as surfactant self-assembled structures were investigated in the second part of this thesis. A phase-field model was developed for simulating morphological evolution of surfactant aggregates in solutions. The model captures both the self-assembling behavior of surfactants and the effect of interface-curvature elastic-energy on the morphologies of self-assembled structures. Simulations of single surfactant micelle growth in dilute solutions reveal several previously unknown morphological transitions, including a disk-to-cylinder micellar shape transition and a tip-splitting instability of cylindrical micelles. It is proposed that the observed morphological instabilities provide kinetic pathways to the formation of branch points between individual cylindrical micelles, whose presence has

significant effects on the rheological properties of solutions.

Surface wetting transitions often display simultaneous changes in interface structure and morphology. Despite the extremely broad technical applications of the Si/SiO_2 structure The equilibrium wetting properties of silicon oxide on silicon are poorly understood, This is partly due to the extremely low equilibrium oxygen activity for SiO_2/Si coexistence (e.g. 10^{-37} torr at 700°C), which cannot be reached by current ultra-high vacuum techniques. In the third part of this thesis, a solid-state buffer method was developed to access oxygen partial pressures near the Si/SiO_2 equilibrium with systematic control. It was discovered from experiments that silicon oxide does not perfectly wet Si(001) surfaces near the equilibrium oxygen activity, with the wetting morphology being oxide islands coexisting with a thin oxide layer of $\sim$0.4nm on top of Si.

Thesis Supervisor: W. Craig Carter
Title: Professor of Materials Science and Engineering

Thesis Supervisor: Yet-Ming Chiang
Title: Kyocera Professor of Ceramics

Acknowledgments

I need to thank many people for their help and support through my time at MIT.

My advisor Craig Carter started his long-time support to me by generously offering me financial assistance even before I joined his group. Besides giving me excellent research advice, he taught me so many different things from programming, visualizing abstract concepts, giving good presentations, to appreciating the importance of scientific writing. All of these have helped me become more mature in scientific research over these years. He lends his full support to my career development and provided me with vast opportunities to develop as an independent researcher. I am deeply indebted to him for being my advisor and teacher.

Many thanks to my co-advisor Yet-Ming Chiang for having me involved in experimental research in his lab and giving me very valuable suggestions, which greatly broadened my research horizon. I am truly grateful to him for financially supporting me during some difficult times and giving me the freedom to pursue various research interests.

I would like to express my deep gratitude to the late Rowland Cannon (1943–2006) for being a mentor and a friend. Part of the thesis work was directly initiated by his vision, and his profound insights on many things will keep inspiring me in coming years.

Special thanks to Jian Luo for very helpful discussion on different topics and for sharing his research work and thoughts with me. He also provided micrographs for me to use in the thesis.

I would like to thank Eva Jud and Ana Ramos for fruitful collaboration. Yinlin Xie, Sung-Yoon Chung, Steven Tobias, Dave Isaacson, Nate Quitoriano and Libby Shaw have given me help in experiments at various stages. I owe them many thanks.

Thanks to my thesis committee members Chris Schuh and Greg Rutledge for raising insightful questions and suggestions, and to Chris Schuh for a close reading of my thesis.

Thanks to all past and present members of the Carter and Chiang groups for their

friendship. Catherine Bishop and Edwin Garcia helped me get started at MIT and offered me valuable career advice. Ellen Siem contributed constantly to improve my English. I enjoyed hours of discussion and conversations with Colin Ashe and Hong Zhang. Dan Cogswell used his computer expertise to fix numerous problems for me. Celine Hin listened to my practice talk and I appreciate her insightful suggestions. I also want to thank many other friends for being supportive on many occasions. All of you are an essential part of my great experience at MIT.

I am deeply grateful to my parents. They always encourage me to pursue my ambitions, although having their only child half a world away is never a good choice for them. Without their love and unconditional support, I could not have been where I am today.

I can't thank my wife Hongmei Yan enough for all she has done for me. My life at MIT would have been much more challenging and less satisfying without her companion. I consider myself very fortunate to meet and marry her here, and need to share with her everything I have accomplished at MIT.

Contents

List of Figures

List of Tables

Chapter 1

Introduction

1.1 Interface Transitions

Interfaces, such as grain boundaries, free surfaces and inter-phase boundaries, frequently have a controlling influence on material properties and therefore play a decisive role in a material's utility or its failure [5]. Interfaces are also principal agents of change within materials over time scales varying from nanoseconds to geological time. Motion of interfaces may trigger recrystallization, grain growth and phase changes, all of which may dramatically affect engineering properties.

Interfaces, taken as purely geometrical objects or mathematical representations of these objects, may undergo transformations that need not refer to their internal degrees of freedom (e.g., interface structure and chemistry). For example, the Rayleigh instability [6] and the instability of four interfaces intersecting along a line [7], are both examples of geometric transformations that depend only on the fact that positive work must be transfered to an interface to stretch it. The rate at which this work is done depends on a material property, the surface tension, which is positive for any system in thermodynamic equilibrium. Thus, these geometrical instabilities generically exist for all systems. Another type of transition is introduced below to distinguish these types of transitions from one another. The transitions above will be called *morphological transitions* and are fundamentally connected to the geometric instability of the mathematical representation of the interface.

Interfaces in materials such as grain boundaries and free surfaces are considerably more complex. They depend on the nature and geometric configurations of the bulk materials that abut them. Equilibrium material properties of the bulk phases inevitably influence the properties of the interface. Thus, intensive quantities that affect bulk materials such as chemical potential, temperature, and stress will—in combination—produce extensive changes associated with the interface itself; for example, interface width, chemical content, strain and entropy.

These descendant properties of interfaces were known to van der Waals, who hypothesized that the liquid–vapor interface has a finite thickness across which the molecular density varies rapidly but continuously [8]. However, their first systematic thermodynamic treatment was performed by Gibbs [9]. Gibbs made a choice that differed substantially from that of van der Waals — Gibbs decided that he would declare the interface to be a two-dimensional mathematical object with zero thickness. He then derived thermodynamic properties of interfaces from this supposition. Gibbs clearly understood that interfaces in materials had a finite extent in a direction normal to his mathematical interface; thus, he showed that any quantity derived from his supposition was independent of the supposed position for the mathematical interface.

After Gibbs, the van der Waals approach of treating the the interface as a thin slab of intervening material was re-adopted by Guggenheim [10], and is probably more intuitive than Gibbs' approach. However, the conclusions are all the same.

Much of our intuition of interface behavior derives from soap films [11]. Their morphological instabilities have fascinated and provided diversions for children and mathematicians. Newton was clearly fascinated by their colors and was the first to observe a transition in soap films. He discovered that the colors of soap bubbles disappear continuously as the thickness of soap films decreases, and made the following observation [12]:

> ...And as the bubble grew thinner by the continual subsiding of the water, ... after all the colours were emerged at the top, there grew in the center of the rings a small round black spot, like that in the first observation, which continually dilated itself till it became sometimes more than 1/2 or

> 3/4 of an inch in breadth before the bubble broke... I saw within it several smaller round spots, which appeared much blacker and darker than the rest, whereby I knew that there was some reflection at the other places which were not so dark as those spots...

The "much blacker and darker" spots Newton observed are now often called *Newton-Plateau black films*, as opposed to the "not so dark" spots known as *common black films*. Plateau made a remarkable study of such films 200 years after Newton [13]. Today we understand that the transition from common to Newton-Plateau black films is associated with a discontinuous decrease in soap film thickness and the two types of black films are stabilized by different forces [14]. Thus, there are types of transitions that are associated with the material properties of the interface itself: *these will be called "complexion" transitions.*

In principle, material interfaces could adopt more than one metastable "complexion" (i.e., distinct interfacial structure or composition profile). The term "complexion" [15–17] has been introduced as the two-dimensional analog to a bulk phase: parts of an interface that differ with respect to any equilibrium feature are examples of different complexions of the same interface. Assuming that interfaces can rapidly equilibrate with their abutting phases by local atomic motion, only metastable complexions (i.e., those with local minima in free energy with respect to available degrees of freedom) will be observed. Generally, the metastable complexions, including the one with the lowest free energy (the globally stable complexion) will each have distinct, reproducibly measurable physical properties (densities, structures, compositions, etc.), that differ from those of the abutting bulk materials or crystalline phases. The complexions' stability ranking and physical properties depend on imposed constraints such as temperature, stress, and one or more chemical potentials. As in bulk-phase equilibrium coexistence, interfacial complexions could stably coexist at certain subsets of the possible values of fixed pressure, temperature, chemical potentials, etc. Complexion coexistence, e.g. of grain boundaries, identifies conditions where boundary thermodynamic properties (i.e, structure, composition, etc.) would undergo predictable alteration; derivative physical properties such as transport, creep

behavior, and fracture may undergo profound changes as a consequence.

Even though Gibbs treated an interface as infinitely thin, he was aware of the Newton/Plateau intefacial instability and knew that this instability was associated with an abrupt change in equilbrium thickness [9]. He showed that this transition must also be associated with an abrupt change in surface tension as well.

Analogous transitions are known to occur at the ice–water vapor equilibrium interface. Depending on temperature and humidity, the ice surface can adopt a dense, more amorphous layered configuration [18]. Comparisons to a liquid water coating and pre-melting are natural in this case. However, the layered phase has a longer range order than that of equilibrium bulk-liquid water and is induced by the crystalline nature of the ice phase. These films are *less amorphous* than liquid water; liquid water is unstable except at the triple point. These themes—of degrees of "amorphicity" and of an interface's extra surface tension providing a medium for the appearance of layered "nearly" equilibrium phase —appear repeatedly in this thesis.

In crystalline or anisotropic materials the properties of interfaces have a more complicated theoretical foundation: the relative geometric orientations and translations across the interface and the inclination of the inteface with respect to one of the abutting bulk phases certainly affect the interface. These extra degrees of geometric freedom are distinct from those associated from thermodynamic quantities (such as surface absorption, surface tension and stress, and enthalpy density), but cannot be uncoupled.

This thesis provides thermodynamic derivations of equilibrium interfacial properties in crystalline materials. The treatment indicates how geometric and equilibrium thermodynamic properties collectively produce complexion transitions. There are some simplifications in the treatment. Most importantly for crystalline materials, the equilbrium thermodynamic interface, grain boundary in particular, is treated as flat and dependent on a single misorientation parameter. A theoretical framework to treat all misorientation degrees of freedom was developed recently by other groups [19, 20] (for different applications) which could and should be incorporated into the framework developed here. It is asserted that these extra degrees of misorientation will not

affect the principle conclusions contained in this thesis. They will lead to a richer set of the interface transitions that are predicted here.

In the above discussion, references to equilibrium interfacial properties are necessary. However, equilibrium experiments and their observation at amorphous/crystalline interfaces are considerably more difficult. In particular, controlling the chemical potentials so that the vapor/crystalline interface is in equilibrium is difficult and often ignored. In Si/SiO_2, the equilibrium vapor pressure is many orders of magnitude below that which can be achieved in ultra-high vacuum systems. A method is developed to observe the nature of this important interface at equilibrium in this thesis for the first time.

Studies of morphological transitions of interfaces have been traditionally confined to crystalline materials in the field of materials science. With the continuous evolution of this field, a broader definition of material interfaces is being adopted to include interfaces in soft matters such as biological membranes and surfactant self-assembled structures. However, when such an extension is made, the notion that interface morphologies are determined by the surface tension should also be modified — geometrical instabilities of soft materials are often controlled by material properties other than the surface tension [21], which necessitates a different theoretical framework. Motivated by such a need, a theoretical model is developed in this thesis to investigate kinetic aspects of morphological transitions of a particular type of soft material interface —interfaces of surfactant aggregates in solutions.

In the following sections, a brief introduction of a number of interfacial transitions related to this thesis work and the current research status is presented. The research topics of this thesis will then be introduced and justified. Finally an outline of the organization of the thesis is given.

1.2 Structural and Chemical Transitions of Interfaces

1.2.1 Interfacial Chemical Transitions

Free-surface composition transitions in the context of wetting transitions are among the complexion transitions that were first studied. One of the earliest predictions of interface wetting transitions was given by Cahn's critical point wetting theory (CPWT) [22].

In CPWT, Cahn employs a compositionally-diffuse interface model to treat two-component liquids in contact with a container (which may be vapor). The container provides an interface where stable composition gradients in liquids develop. The bulk liquids have a molar free energy of mixing, $\Delta F(c,T)$, that gives a phase diagram with a miscibility gap [22], as shown in Fig. 1-1. For purposes of discussion, suppose the phase diagram has phase α that is rich in component A (small c) and phase β rich in B (large c). Phase β has a lower surface energy with the container, $\gamma_{c\beta}$, than phase α, $\gamma_{c\alpha}$. For compositions within the miscibility gap, CPWT predicts a complete wetting transition temperature, T_{wet}, above which β is a perfect wetting phase that separates the α-phase and the container (i.e., $\gamma_{c\beta} + \gamma_{\beta\alpha} \leq \gamma_{c\alpha}$). For the A-rich *single*-phase (α) region, a subset of compositions and temperatures, $c(T)$, exists along which two free-surface complexions, χ^{R} and χ^{P}, can coexist: χ^{R} has a larger B-adsorption, Γ_B^{rich}, and a wider characteristic interfacial thickness, L^{thick}; χ^{P} has smaller values of Γ_B^{poor} and L^{thin}. The curve $c(T)$ specifies locations of a first-order complexion transition between χ^{P} and χ^{R} characterized by $\Delta\Gamma_B = \Gamma_B^{\text{rich}} - \Gamma_B^{\text{poor}}$ and $\Delta L = L^{\text{thick}} - L^{\text{thin}}$. $c(T)$ intersects the two-phase region at $(c^{\alpha}, T_{\text{wet}})$. In the single-phase region between $c(T)$ and the miscibility gap, interface complexions are those χ^{R} that reflect the bulk-phase wetting behavior [22]. Such transitions have been directly observed in organic and metallic liquid systems [23, 24].

The complexion transition at $c(T)$ is an example where a microstructural property characteristic (e.g., absorbed layer thickness) can be superimposed onto a bulk equi-

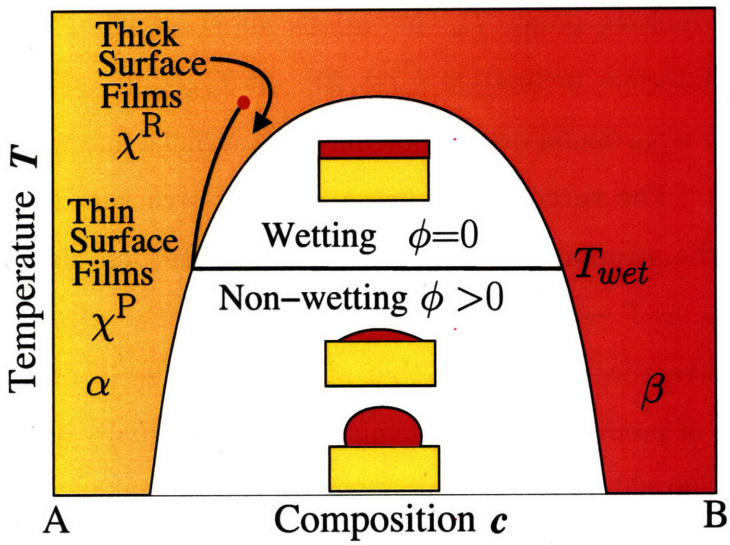

Figure 1-1: Illustration of Cahn's surface wetting diagram. In the two phase region, the B-rich phase completely wets the container surface above T_{wet}, and has a non-zero wetting angle ϕ below T_{wet}. A prewetting line exists in the A-rich single phase region, and intersects the miscibility gap at T_{wet}. The prewetting line delimits two different surface complexions: a complexion χ^R characterized by large B-adsorption, Γ_B^{rich}, and wide interfacial thickness, L^{thick}, and the other complexion χ^P with smaller B-adsorption and thickness. A first-order prewetting transition between χ^P and χ^R occurs when traversing across the prewetting line.

librium phase diagram. Such diagrams could be constructed whenever a microstructural defect produces local variations from equilibrium bulk compositions, structures, or other properties. Each defect (e.g., interface) feature will have characteristic quantities, such as a width and composition, that have equilibrium values and these could be included on a microstructure phase diagram. These microstructural aspects do not produce additional degrees of freedom that would modify the rules governing the topology of bulk phase diagrams. However, conditions for changes in macroscopic physical or mechanical properties that depend on microstructural features can be inferred (e.g., interface diffusivities or migration rates).

1.2.2 Interfacial Structural Transitions

Interfacial melting is another complexion transition and it involves structural changes of interfaces. Free-surface melting has been observed to initiate at temperatures T_{sm}

below the bulk melting point, T_m, in various materials [25–27]. For crystals, T_{sm} can depend on interface inclination $\hat{n}$ [28,29]. At $T_{sm} < T < T_m$, the stable surface configuration for a particular orientation may be a surficial film with finite equilibrium thickness, $w(T)$. The surficial film has a different structure than the equilibrium crystal phase; the structure is usually less ordered and less dense [26,30,31]. For metallic systems, as $T \to T_m$, w diverges as $w \sim w_0 \ln[(T_m - T_{sm})/(T_m - T)]$ and the surficial film's structure approaches that of the liquid [26,32–34]. In addition, well below the onset of premelting, a roughening transition usually initiates for faceted or vicinal surfaces [30,35].

Although grain boundary (GB) melting might also be expected, evidence is scant and contradictory in pure systems. Observations from derivative macroscopic properties (e.g., boundary dihedral angles, GB diffusion, sliding or migration) allude to some type of GB transitions that occur well below T_m even in nominally pure metals [36–39]—however, these could often be plausibly attributed to other causes, including kinetic transitions such as breakaway from solute clouds [40,41]. Direct TEM imaging of boundaries in aluminum specimens indicates preferential melting, but only above $0.999T_m$ [42], and, similarly, that high-angle bismuth GBs are wet by the Bi liquid at T_m [43]. Nonetheless, whether, to what extent, and in what systems GB melting actually can be observed is an open question.

These questions are addressed, but not well resolved, by numerical simulations using interatomic potentials. A lattice gas model for a tilt GB [44,45] exhibits an onset of GB disorder at $T \approx 0.5T_m$, which increases towards a liquid-like state as $T \to T_m$, and the disordered region thickens as $w_0 \ln[T_m/(T_m - T)]$. A number of molecular dynamics (MD) simulations using empirical potentials have also found that various high-angle GBs tend to increase continuously in disorder with rising temperature [46–49], though some others report that GBs do retain significant crystallinity at temperatures close to T_m [50,51]. These simulations suggest that GB melting is continuous. Other simulations indicate that a first-order transition occurs rather than continuous disordering [52] and give wide boundaries well below T_m [53]. Such inconsistencies might originate from numerical artifacts, failure to ascertain the

thermodynamic melting point due to finite simulation size, superheating, use of different boundary conditions, differences in atomic potentials used, and difficulties in achieving the lowest energy equilibrium structures [50, 54–56]. Furthermore, a standard measure or algorithm for departure from crystallinity has not been elucidated. Nonetheless, some MD or Monte Carlo (MC) simulations detect multiple structures that are demonstrably metastable [57–61]. Additional indications for a GB structural transition are associated with discontinuities in activation energies for GB diffusion or migration [62–64].

1.2.3 Cooperative Interfacial Structural and Chemical Transitions

Compared with pure systems, observations of GB structural disordering in alloys are more common and such changes in GB structures are usually accompanied by changes in equilibrium GB segregation. The cooperative structural and chemical transitions are well exemplified by nanometer-thick amorphous films observed at GBs in many multi-component systems, known as intergranular glassy films (IGFs). IGFs were found to exist at general/high angle GBs of both ceramic and metallic systems, including silicon nitride doped with sintering additives such as SiO_2, La_2O_3, Y_2O_3, etc [65–69], ZnO-Bi_2O_3 [2, 70], $SrTiO_3$-TiO_2 [71, 72], Al_2O_3 doped with CaO, SiO_2 and Nd_2O_3 [17, 73, 74], Ni-doped W [75, 76]. Fig. 1-2 shows high resolution TEM images of IGFs in SiO_2-doped Si_3N_4 and Bi_2O_3-doped ZnO. A more comprehensive list of material systems displaying IGFs can be found in a recent review by Luo [77]. The formation of IGFs at GBs has a profound influence on the macroscopic properties of materials, e.g., mechanical strength, fracture toughness, fatigue properties, creep resistance, corrosion susceptibility, electrical and thermal conductivity [77]. Due to their important technological implications on material applications, structural ceramics in particular, IGFs have been extensively studied over the last thirty years.

Several distinct properties of IGFs have been revealed from experimental observations. IGFs display equilibrium thicknesses that depend on the chemical potentials

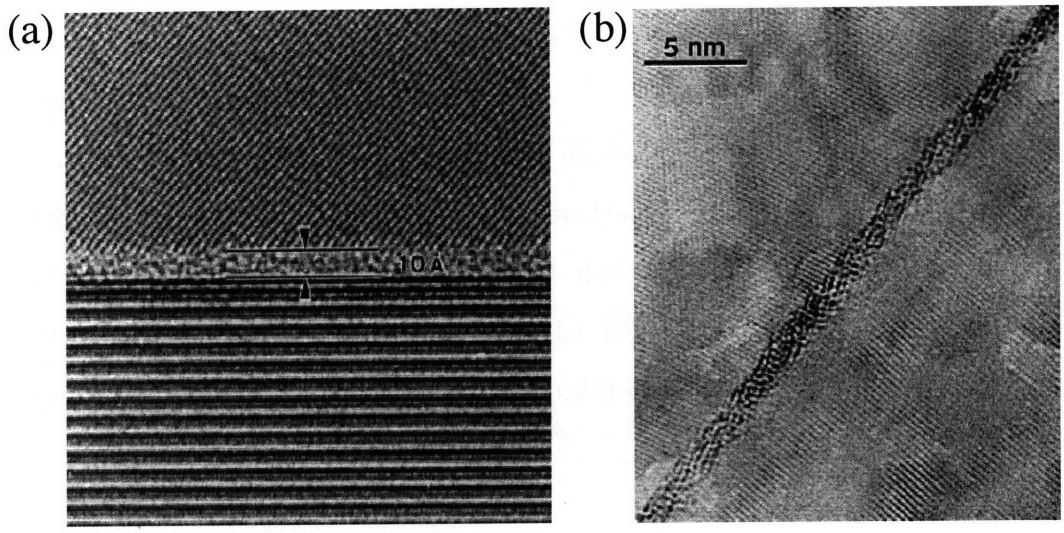

Figure 1-2: (a) High resolution TEM image of an intergranular glassy film in SiO_2-doped Si_3N_4. The film is rich in SiO_2. (b) High resolution TEM image of an intergranular glassy film in Bi_2O_3-doped ZnO. The film is rich in Bi_2O_3. Images are reprinted from Refs. [1] and [2] with permission from the American Ceramic Society.

of minor components [65–67, 69, 78], but are independent of their relative amount when the chemical potentials are fixed, e.g. by the two-phase coexistence. They have compositions that are not stable as a single-phase bulk liquid [2,68,69,78–80]. These films show thermodynamical stability and can exist at sub-solidus and sub-eutectic temperatures [2,65,67,69,78,81,82]. For example, little difference was observed between IGFs in Bi_2O_3-doped ZnO samples which underwent different processing routes but reached the same final condition [2].

A force balance model introduced by Clarke [83,84] has become a standard model to explain the presence and stability of IGFs in the last two decades. The model in its nature is similar to the Derjaguin-Landau-Verwey-Overbeek (DLVO) theory [85] which determines the stability of colloidal systems by considering interaction forces between colloidal particles in solution. Clarke assumed that IGFs consist of quenched liquid phase of secondary additives that are sandwiched between two grains of the primary phase. The equilibrium thicknesses of IGFs result from the balance of various forces acting across the films. Major force terms considered in Clarke's original work [83] include an attractive dispersion force and a repulsive steric force arising from the structural changes across solid-liquid interfaces. Other forces such as the

electrical double-layer repulsion [84] may also be present. The magnitudes of these forces depend on film thickness. For example, the non-retarded dispersion force and the steric force have the following expressions

$$F_{dispersion} = -\frac{A_{121}}{6\pi h^3} \tag{1.1}$$

$$F_{steric} = F_0 e^{-h/\xi} \tag{1.2}$$

where h is the film thickess, A_{121} is the Hamaker constant, and ξ is the structural correlation length of the liquid phase which is comparable to the molecular bond length. Clarke showed that the balance of all the force terms is achieved at a finite film thickness, which thus requires an intergranular film to be present between two grains. Based on estimates of the magnitudes of different force terms, the model predicts that the IGF's thickness should be on the order of ~1 nm and that IGFs are very stable against extrusion by applied pressure [83], which are consistent with experiments.

However, the fundamental assumption of the force balance model that IGFs are quenched liquid phases resulting from mechanical equilibrium has been challenged by recent experiments. In particular, this model has difficulties in rationalizing some of the most distinguished features of IGFs, including:

1) The film compositions are very different from either primary or secondary phase, and do not correspond to any stable bulk phases.

2) IGFs could form at conditions where bulk liquid phases are not present, e.g. at sub-eutectic temperatures and in solid single-phase regions.

3) IGFs are in thermodynamic equilibrium with the adjoining bulk phases.

On the other hand, the behavior displayed by IGFs is strongly reminiscent of the premelting concept as well as the prewetting transitions predicted by various wetting theories. However, the relation between intergranular amorphous films and premelting/prewetting transitions has not been widely recognized.

The free surface counter-parts of IGFs, termed surficial amorphous films (SAFs),

have also been observed in a number of inorganic systems, e.g., ZnO-Bi_2O_3 [86, 87] and TiO_2-V_2O_5 [88]. Two high resolution TEM images of IGFs are shown in Fig. 1-3. SAFs exhibit similar characteristics as IGFs. They can form at sub-eutectic and sub-solidus temperatures, and display different compositions than predicted from bulk phase diagrams, Their thickness, structure and chemistry are thermodynamically controlled by temperature and chemical potentials of minor components. It is suggested that SAFs and IGFs can be explained by similar physical principles [77, 87, 89].

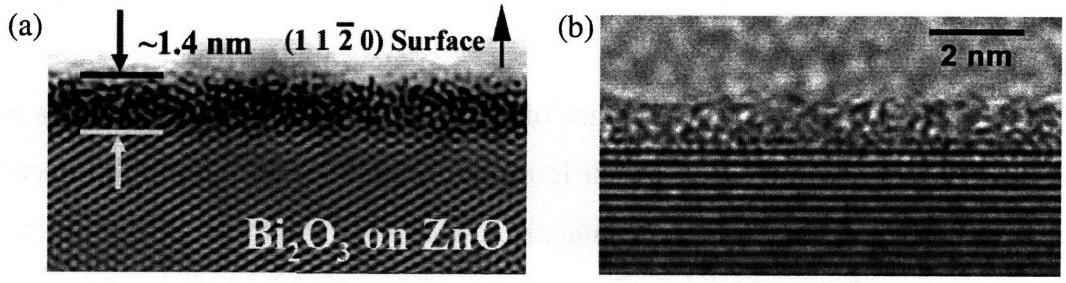

Figure 1-3: (a) High resolution TEM image of a surficial amorphous film in Bi_2O_3-doped ZnO. Courtesy of J. Luo and Y.-M. Chiang. (b) High resolution TEM image of surficial amorphous film in V_2O_5-doped TiO_2. The film is rich in V_2O_5. Courtesy of H. Qian and J. Luo.

1.3 Morphological Transitions of Interfaces

1.3.1 Morphological Transitions of Crystalline Interfaces

Similar to transitions in interface structures and chemistries, the morphologies of material interfaces can undergo transitions with changing external conditions. The nature of morphological transitions could be thermodynamic or dynamic. In the former case, different *equilibrium* interface morphologies exist under different imposed constraints such as temperatures and chemical potentials; transitions between them occur when the constraints change. Examples of such morphological transitions include faceting and roughening transitions of particle surfaces or grain boundaries [90–98], which are often induced by changes in the anisotropy of surface or interface tension. Morphological changes also occur in wetting transitions, where a vanishing

contact angle results in the morphology of a wetting phase on a substrate to switch from droplets to flat films.

In dynamic morphological transitions, morphological evolution of a moving interface is triggered by dynamic instability in non-equilibrium kinetic processes such as crystal growth. One fitting example is the dendritic crystal growth. Crystal dendritic structures with very complex morphologies have been observed in solidified microstructures for hundreds of years and still attract much attention from researchers. During solidification, crystal/liquid interfaces move toward the liquid phase under thermodynamic driving force. Under suitable conditions, moving interfaces with simple (e.g. flat or spherical) geometries become unstable against shape perturbation and evolve into complex shapes such as cellular and dendritic structures [6]. The development of shape perturbations is promoted by the presence of temperature and/or composition gradients in liquid phases — the formation of interfacial protrusions is favored by the volumetric free energy decrease. However, perturbations also increase interface curvature and hence surface energy, which tends to suppress perturbations. Whether a perturbation introduced by thermal fluctuation will grow or decay is determined by the competition of the two opposing forces. The onset of such interface instability was first mathematically analyzed by Mullins and Sekerka in the 1960s [99,100]. In their work they studied the diffusion-limited growth of a spherical B-rich second-phase particle in a A-rich matrix. The particle/matrix interface tension is assumed to be isotropic, and the particle growth is sustained by diffusion of the B component in the matrix to the interface. Mullins and Sekerka considered a small perturbation applied to the particle radius in the form of a spherical harmonic function $Y_{lm}(\theta, \phi)$

$$r(\theta, \phi) = R + \delta Y_{lm}(\theta, \phi) \tag{1.3}$$

where δ is the perturbation amplitude and the subscript l denotes the perturbation wave number. The growth or decay rate of the perturbation is determined by solving the diffusion equation in the matrix under the quasi-steady state assumption and matching the solution to the boundary conditions at the interface. A major finding

of Mullins and Sekerka is that the spherical shape of the particle will become unstable against any perturbations at sufficiently large radii and eventually the dendritic morphology will form. For each perturbation wave number l, there exists a critical radius value, R_c, above which the perturbation will grow with time, i.e., $d\delta/dt > 0$. R_c scales with l as $R_c \propto [(l+1)(l+2)/2+1]$. In real material systems, the perturbation growth and dendrite morphologies are also significantly influenced by other factors such as the anisotropies of interface tension and mobility. To quantitatively predict dendrite growth for real materials remains a very active field in materials modelling and simulations [101].

1.3.2 Morphological Transitions of Soft Material Interfaces

Similar to crystalline materials, interfaces in soft materials such as vesicles and surfactant micelles show a rich variety in morphologies and abundant examples exist for morphological transitions. Vesicles formed by phospholipid bilayer membranes display an amazingly large number of shapes (e.g., spherical, tubular, biconcave, etc), and different types of shape transitions can occur between them, including budding transition [21], discocyte/stomatocyte transition [21], discocyte/starfish transition [21,102–104], and pearling instability [21], etc. Surfactant micellar structures consisting of surfactant monolayers also display various morphologies (e.g., spherical, cylindrical, bilayer and liquid crystalline) and morphological transitions such as sphere-to-cylinder transition [105, 106] and branching of cylindrical micelles [107–109] have been observed. These morphological transitions often result in significant changes in system properties. For example, the discocyte/stomatocyte transition may occur in human red blood cells and is related to liver disease and hereditary stomatocytosis [110]. The development of inter-micellar junctions (branch points) between cylindrical micelles significantly affects the rheological properties of micellar solutions [111,112].

1.4 Thesis Assertions

The overarching goals of this thesis are two-fold:
1) To advance the understanding of interfacial transitions in several material systems where outstanding questions remain and new insights are demanded.
2) To develop theoretical frameworks and experimental methods necessary for addressing the questions, which also have applicability for studying interfacial transitions in a broader spectrum of material systems.

Three particular interfacial transitions were investigated in this thesis: grain boundary transitions, morphological transitions of surfactant self-assembled structures, and wetting transitions at silicon oxide/silicon interfaces.

1.4.1 A Continuum Thermodynamic Framework for Grain Boundary Transitions

As introduced in Section 1.2, the equilibrium structures and chemistries of grain boundaries can undergo transitions under proper conditions. From the modeling perspective, atomistic calculations can provide *detailed and often accurate* information on grain boundary transitions. However, various limitations in its applicability and computation capability make the atomistic approach not always feasible to probe equilibrium grain boundary properties and their transitions in a large parameter space including temperatures, chemical potentials, stresses, misorientations, etc. Classical thermodynamics provides methods for generic stability predictions based on general thermodynamic principles and empirical properties. When supplemented with data from experiments and atomistic calculations, quantitative predictions can be derived from the thermodynamic approach. The successful applications of classical thermodynamics to predicting and calculating bulk phase diagrams has enormously stimulated the development of materials science and engineering. Analogously, thermodynamic frameworks for interface transitions are equally desirable and highly useful. This has been demonstrated by Cahn's critical point wetting theory [22], in which he used

a diffuse-interface thermodynamic model to first predict the general existence of interface wetting transitions. One of the goals of this thesis is to develop a similar thermodynamic framework for grain boundary transitions to quantify stable regions of various grain boundary complexions in the space of environmental parameters, and construct general grain boundary complexion diagrams similar to bulk phase diagrams. In particular, such thermodynamic analysis was aimed at rationalizing some important but puzzling grain boundary phenomena, including grain boundary premelting and the cooperative structural and chemical transitions exemplified by the formation of intergranular glassy films (IGFs). Although these phenomena may be understood by heuristic explanations, the thermodynamic analysis provides rigorous mathematical treatments that are similar to Gibbs and Cahn's works on classical thermodynamics and have general applicability.

1.4.2 Modeling Morphological Transitions of Surfactant Self-Assembled Structures

Different from interfaces in crystalline materials, whose morphologies are governed by the interface tension [6], the morphologies of vesicles and micelles are regulated by the curvature bending energy stored in the membrane bilayers and surfactant monolayers [21]. Curvature elastic energy models, such as Helfrich's model [113] and the area-difference-elasticity model [21, 114], have been successfully developed to explain the dependence of micelle and vesicle morphologies on environmental parameters (spontaneous curvature, temperature, osmotic pressure, etc.), and "phase diagrams" of vesicle morphology can be constructed from these studies [21, 115]. However, most of the curvature models focus on the equilibrium morphological properties. Modelling kinetic aspects of the morphological transitions and dynamic instabilities in soft material interfaces remains a field that has been less explored in spite of its importance.

The phase-field method is a continuum computational approach that has been successfully applied to model morphological evolution of material interfaces e.g., crystal dendrite growth [101] and solid-state phase transformations [116]. In a phase-field

model, a set of field variables are used to distinguish different phases; the interfaces between them are represented by level surfaces of the field variables, which avoids explicit interface tracking and is especially advantageous in modeling complicated interface morphological evolution compared to conventional sharp-interface models. To date the phase-field method finds most of its applications in crystalline systems, but its strength in tracking complex interface evolution also makes it a suitable tool for modeling soft material systems. In fact, phase-field models of polymer segregation [117] and vesicle dynamics [118–120] have begun to emerge in recent years.

In this thesis the phase-field method was extended to modeling morphological evolution of surfactant self-assembled structures. Because of the their difference in interface energetics, a new phase-field formulation different from those for crystalline interfaces was developed to capture the influence of curvature elastic energy on morphologies of soft material interfaces. A second goal of this thesis is to employ the model to reveal kinetics of surfactant self-assembly and the existence of morphological transitions, which could be difficult to directly observe in experiments.

1.4.3 Wetting Transition of Silicon Oxide on Silicon Surface

The surficial amorphous films (SAFs) observed in several inorganic systems can be produced by increasing the chemical potentials of minor components (or adsorbations) toward two-phase coexistence. Their formation represents a particular surface wetting transition known as "pseudo-partial wetting" [121] (or "frustrated-complete wetting" [122]). In pseudo-partial wetting, adsorbates do not completely wet the substrate, but form a microscopic thin film coexisting with droplets on the substrate surface [87, 88, 122, 123]. Complete wetting may be achieved by further increasing the chemical potentials [87, 122]. If treating oxygen as the principal adsorbate, an intriguing question is whether the silicon oxide can display similar wetting behavior on a silicon surface when the oxygen activity is varied near the bulk SiO_2/Si equilibrium. Surprisingly, the equilibrium wetting properties of silicon oxide on silicon have been poorly understood despite the extreme importance of the silicon oxide/silicon interface to microelectronics. This is partly because the equilibrium oxygen partial

pressure for SiO_2/Si equilibrium is extremely low (e.g., $\sim 10^{-40}$ atm at 700°C) and very difficult to access experimentally.

A better understanding of the wetting behavior of silicon oxide on silicon also has technological implications for the on-going development of next-generation gate oxides in metal-oxide semiconductor field-effect transistors (MOSFET) [124,125]. To achieve further down-scaling in semiconductor devices, the SiO_2 gate oxide needs to be replaced by oxides with higher dielectric constants such as HfO_2 and ZrO_2. However, a SiO_x interfacial layer is found to remain present between Si and high-k gate oxides even under conditions where bulk SiO_2 is not stable [126–129], which indicates the thermodynamic stability of the SiO_x/Si interface. A more sound knowledge of wetting properties between silicon oxide and silicon will be very useful to understand such phenomena and further improve device performance.

A third goal of this thesis is to develop an experimental methodology that allows one to access the oxygen activity near SiO_2/Si equilibrium and use the method to study the equilibrium wetting characters of silicon oxide on a silicon surface.

1.5 Overview of the Thesis

This thesis is organized into several chapters and appendices. Chapter 2 and 3 describe the development of diffuse-interface thermodynamic analyses of grain boundary transitions. A diffuse-interface model for systems of fixed stoichiometry, e.g. single-component systems, is introduced in Chapter 2 and applied to predict grain boundary structural transitions. A graphical construction method is described to analyze grain boundary disorder as a function of temperature and misorientation. Different grain boundary premelting behaviors are predicted and compared to experiments and atomistic modeling results.

In Chapter 3, the diffuse-interface analysis is extended to binary systems in which local stoichiometry is variable. A more advanced graphic construction method is presented for analyzing the general behavior of grain boundary disordering and segregation. The results predict the existence of a coupled grain boundary premelt-

ing/prewetting transition which is proposed to be the thermodynamic origin of intergranular glassy films.

Chapter 4 presents a phase-field model for simulating morphological evolution of surfactant self-assembled structures. The phase-field formulation extends Helfrich's curvature elastic model to the kinetic regime. Results of simulations of single micelle growth in dilute solutions are presented. They reveal the existence of morphological transitions of disklike and cylindrical micelles, which provide possible kinetic pathways to the formation of branched micellar structures.

An experimental study of the wetting behavior of silicon oxide on silicon is described in Chapter 5. A solid-state buffer method is first introduced for creating an environment with ultra-low oxygen partial pressures that enables the study of wetting transition of silicon oxide on silicon. Experimental evidence presented in this chapter shows that silicon oxide only partially wets silicon surface at oxygen activities close to the SiO_2/Si bulk equilibrium.

Chapter 2

Grain Boundary Transitions in Systems of Fixed Stoichiometry

2.1 Introduction

A grain boundary (GB) is an interface that separates the two orientations of abutting crystals of the same bulk phase. Many material properties depend on the transmission of forces and fields across a grain boundary and can be sensitive to grain boundary structure, chemistry, and morphology. At equilibrium, a GB's structure (the atomic configuration that produces the misorientation $\mathcal{R}$), morphology (the interface shape characterized by local interface inclination $\hat{n}$), and chemistry (the interfacial excess, Γ_i, of each independent chemical component species) are determined by the minimum of excess energy $\gamma_{\text{GB}}(T, P, \vec{\mu}; \mathcal{R}, \langle\hat{n}\rangle)$ when the abutting crystals are in equilibrium with the same pressure, temperature and chemical potentials $\vec{\mu} = (\mu_1, \mu_2, \ldots, \mu_C)$ [90]. Grain boundary complexion transitions only occur if a different boundary structure, chemistry or morphology has a reduced γ_{GB}.

Grain boundary complexion transitions will produce abrupt changes in boundary-sensitive properties. If a sufficiently large fraction of grain boundaries in a polycrystal transform over a small range of temperatures or $\vec{\mu}$, macroscopic properties can undergo significant alteration. Examples include diffusivity, plasticity, conductivity, corrosion resistance, brittle-ductile transitions and activated sintering [70, 130–133].

Classical (or continuum) thermodynamic considerations omit the complexity that is inherent at length scales of the order of a crystalline lattice parameter. For free surfaces of crystals, which are generally described by two geometrical variables that specify the inclination of the surface with respect to the crystal, such complexity arises from relaxation of atomic positions in the surface region. For grain boundaries, three additional parameters are required to specify the misorientation between the abutting crystals. Explicit calculations of GB structure based on atomic potentials or approximations to electron density functions provide methods for direct, often accurate, calculations of structures and excess energies. However—for behavior over a range of temperature, stress, chemical potentials, misorientations, and inclinations in a variety of stable crystal phases—such calculations are not feasible. Classical thermodynamics provides methods for generic stability predictions based on empirical properties. Atomistic structural and energetic calculations (which are thermodynamic minimizations in the static case) can provide information that supplements empirical data and affirm or refine continuum models.

In this chapter, classical interfacial thermodynamics is extended to a simplified model of grain boundaries in fixed stoichiometric systems. A diffuse-interface model—based on the polycrystalline phase-field model from Kobayashi, Warren, and Carter (KWC) [134–136]—is used to develop a thermodynamic construction to predict GB premelting, often associated with distinct order-disorder transitions. The thermodynamic construction extends previous work of Lobkovsky and Warren that established, and numerically demonstrated, premelting near T_m [137].

2.2 The KWC Diffuse-Interface Model of Grain Boundaries

In the KWC model for a system with fixed stoichiometry, a two-dimensional polycrystalline microstructure is described by two field variables, which are the local crystallinity field $\eta(\vec{x})$ and crystallographic orientation field $\theta(\vec{x})$. The crystallinity

η is a coarse-grained scaled measure of structural disorder. The values $\eta = 1$ and 0 are usually defined as denoting crystalline and liquid states, respectively. The crystallographic orientation field, θ, is a local coarse-grained measure of the "most likely" crystallographic orientation with respect to a fixed axis. Though not specially treated here, the values the orientation field can take are restricted by the symmetry of the crystalline phase. For example, the range of value of θ is [0,π] for a crystal with two-fold symmetry.

The values of crystallinity and crystallographic orientation variables can be calculated from underlying atomistic structures through proper coarse-graining schemes [138–140]. In a possible scheme to derive η and θ, a crystallinity measure can be defined by an atom's (located at $\vec{\zeta}$) radial distribution function $\alpha_{\text{rdf}}(\vec{x}-\vec{\zeta})$ [141], or its bond-angle distribution function $\alpha_{\text{bda}}(\vec{\zeta})$ [138, 139], or the ratio (surface area)/(volume)$^{2/3}$ of its Voronoi tessellation, α_{V} [139]. In each case, a distance metric $\langle , \rangle$ (i.e., $\langle \alpha(\vec{\zeta}), \alpha^{\text{xtal}} \rangle$ that scales with the departure from an ideal crystal, and $\langle \alpha(\vec{\zeta}), \alpha^{\text{amorph}} \rangle$ for an amorphous structure) could be defined and for each atom,

$$\eta(\vec{\zeta}) \equiv \left(\frac{\langle \alpha(\vec{\zeta}), \alpha^{\text{amorph}} \rangle}{\langle \alpha(\vec{\zeta}), \alpha^{\text{xtal}} \rangle} \right)^2 \tag{2.1}$$

which should range from 0 for amorphous to 1 for ideally crystalline structures. Using similar methods, perhaps related to an atom's bond-angle distribution, a bond orientation $\theta(\vec{\zeta})$ could be likewise assigned. Finally, the continuous fields could be defined through the following coarse-graining procedure:

$$\eta(\vec{x}) e^{i\theta(\vec{x})} = \frac{\sum_{\text{atoms}(j)} \int_{\mathcal{V}} \chi(\vec{x} - \vec{\zeta}_j) \eta(\vec{\zeta}_j) e^{i\theta(\vec{\zeta}_j)} \, dV}{\sum_{\text{atoms}(j)} \int_{\mathcal{V}} \chi(\vec{x} - \vec{\zeta}_j) \, dV} \tag{2.2}$$

where $\chi(\vec{x})$ is a convolution function (i.e., with compact support) such as $\exp(-\vec{x} \cdot \vec{x}/\ell^2)$ where ℓ is a coarse-graining length, typically on the order of a few bond lengths.

Fig. 2-1 illustrates a schematic profile of η and θ in a bicrystal. Within each grain, the local crystallinity is equal to one and the orientation field has a constant value. In the GB region, the local crystallinity takes values less than one, implying less ordered

structure, and the local orientation exhibits a change from one value to another.

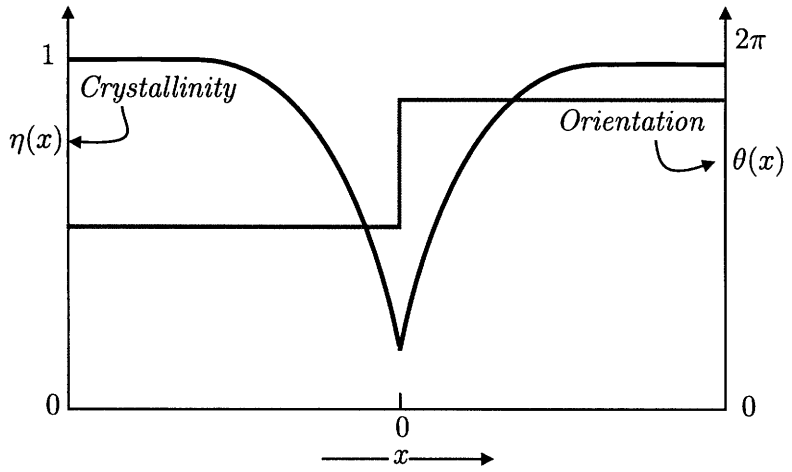

Figure 2-1: Equilibrium profiles for $\eta(x)$ and $\theta(x)$ for a one-dimensional symmetrical GB. The discontinuity in first derivatives of η, which is collocated with the discontinuity of θ at the boundary core, $x = 0$, is a consequence of Eq. 2.12.

The excess free energy of a GB in the KWC model is expressed as a functional of the two field variables, which is

$$F[\eta, \theta; T] = \int_{\mathcal{V}^{\text{sys}}} \left[\Delta f(\eta(\vec{x}), T) + \frac{\nu^2}{2} (\nabla\eta)^2 + s\, g[\eta(\vec{x})]\, |\nabla\theta| \right] dV \tag{2.3}$$

A one-dimensional version of Eq. 2.3 can be employed for a planar GB where all fields are uniform in the GB plane, which is taken to be normal to the x coordinate,

$$F[\eta, \theta; T] = A \int_{\mathcal{L}^{\text{sys}}} \left[\Delta f(\eta(x), T) + \frac{\nu^2}{2} \left(\frac{d\eta}{dx} \right)^2 + s\, g(\eta(x)) \left| \frac{d\theta}{dx} \right| \right) dx \tag{2.4}$$

where A is the GB area and set to unity here.

The integrand of Eqs. 2.3 and 2.4 can be viewed as a low-order approximation to the inhomogeneous free energy density—i.e., the integrand includes the values of η and θ and their spatial derivatives. Different terms of the integrand are discussed briefly below.

$\Delta f(\eta, T)$ is the excess homogeneous free energy density per volume of a uniform material with a crystallinity η measured against a single crystal reference state, i.e., $\Delta f(\eta, T) = f(\eta, T) - f(\eta = 1, T)$. Note that Δf must be independent of θ to meet

the physical requirement that F is rotation invariant. At temperatures close to the melting point, T_m, Δf has the form of a double well with two local energy minima at the crystalline ($\eta = 1$) and liquid ($\eta = 0$) states. At $T < T_m$, $f(\eta = 1) - f(\eta = 0) < 0$ and the crystalline state is more stable.

The rest of the terms in the integrand are energy contributions from the crystallinity and orientation gradient penalties. Several features of the orientation gradient term need some explanation. First, different from most other phase-field models, the leading orientation gradient term is of order one, i.e. $|\nabla\theta|$, instead of the usual quadratic form. A direct consequence of the absence of θ in Δf, this is essential to obtain a locally confined equilibrium GB structure in the model, as Kobayashi et al [134] have previously shown that including only the square gradient term $(\nabla\theta)^2$ results in an unphysical, completely diffuse GB. Although omitted here, higher order terms of the orientation gradient may be added to the energy functional, and Lobkovsky and Warren have shown that the $(\nabla\theta)^2$ quadratic term needs to be included for studying GB motion. Second, the coefficient of the $|\nabla\theta|$ term is dependent on the local crystallinity. The prefactor function, $g(\eta)$, is a monotonically increasing function of η which designates the effect of disorder on reducing the orientation gradient energy, i.e., the misorienation energy penalty: there should be no misorientation penalty in a complete disordered state (liquid); the penalty should increase with the structural order of the material and reach a maximum at $\eta = 1$. A quadratic form, $g(\eta) = \eta^2$, has been used in phase-field simulations [134,136,137,142], but we will keep the form of $g(\eta)$ general here and discuss other choices in the next section. ν and s, the remaining parameters in Eq. 2.4, scale the gradient penalty contributions relative to the homogeneous free energy for the disorder and orientation gradients, respectively.

For the model analysis performed in the following sections, the temperature T is assumed to be uniform within the system. Several other assumptions are implicitly made in Eq. 2.4. It is assumed that point defects in the proximity of a GB always obtain equilibrium concentration profiles, and these equilibrium fields are already implicitly included in Δf. By extending Δf to be a function of defect concentrations, the effects of their spatial variation on the stability of GB structures would be an

extension of the current model framework. It is also assumed that stresses near GBs are fully relaxed by fast atomic transport between the bulk and the interfaces. Therefore, stresses do not represent independent degrees of freedom. Constraints on such transport or upon the number of interfacial sites would require extension of the model to cases where interfacial stresses are included.

2.3 Graphical Analysis of Grain Boundary Order-Disorder Transitions

2.3.1 Parallel Relation Between the KWC Model and Cahn's Critical Point Wetting Theory

In our study, focus is given to analyzing the equilibrium structure of a planar symmetric GB in a bicrystal. Let the GB plane normal to the x axis, the boundary conditions applied to a bicrystal are

$$\begin{aligned} \eta(x = \pm\infty) &= 1 \\ \theta(x = -\infty) &= \theta_- \\ \theta(x = \infty) &= \theta_+ \end{aligned} \tag{2.5}$$

where θ_- and θ_+ are the crystal orientations on both sides of the GB. Because of the symmetry, only half of the bicrystal needs to be modeled, and the boundary conditions accordingly change to

$$\begin{aligned} \eta(x = 0) &= \eta_{\text{GB}} \\ \eta(x = \infty) &= 1 \\ \theta(x = 0) &= \theta_+ - \frac{\Delta\theta}{2} \\ \theta(x = \infty) &= \theta_+ \end{aligned} \tag{2.6}$$

where $\eta(0) = \eta_{GB}$ is the local crystallinity value of the GB core at $x = 0$, and $\Delta\theta \equiv \theta_+ - \theta_-$. $\Delta\theta > 0$ is assumed with no loss of generality.

Equilibrium is obtained when $F(\eta, \theta; T)$ in Eq. 2.4 is minimized with respect to the functions $\eta(x)$ and $\theta(x)$ subject to boundary conditions, Eq. 2.6. Kobayashi and Giga [143] have shown that with the assumption that $\eta(x)$ has only one local minimum at the GB core, i.e. $\eta_{min} = \eta_{GB}$, the equilibrium $\theta(x)$ field must be a step function localizing all of its change at $x = 0$

$$\theta^{eq}(x) = \begin{cases} \theta_- & -\infty < x < 0 \\ \theta_- + \frac{\Delta\theta}{2} & x = 0 \\ \theta_+ & 0 < x < \infty \end{cases} \tag{2.7}$$

With the equilibrium solution of $\theta(x)$ being known, one can reduce the GB excess energy to a functional of $\eta(x)$ only by substituting Eq. 2.7 into Eq. 2.4 and using the equality, $d\theta^{eq}/dx = \Delta\theta\delta(x)$, $\delta(x)$ being the delta function

$$F[\eta; \Delta\theta, T] = s\Delta\theta g(\eta_{GB}) + 2\int_0^\infty \left[\Delta f(\eta, T) + \frac{\nu^2}{2}\left(\frac{d\eta}{dx}\right)^2\right] dx \tag{2.8}$$

in which the effect of the orientation field on the GB excess energy reduces to a scalar misorientation parameter, $\Delta\theta$. F in Eq. 2.8 remains to be minimized with respect to $\eta(x)$ and the unknown η_{GB}. The first term in Eq. 2.8, $s\Delta\theta g(\eta_{GB})$, derives from the boundary condition, and favors the smallest possible η_{GB} value (i.e., $\eta_{GB} = 0$, a disordered GB). The integral in Eq. 2.8 favors a homogeneous crystal (i.e., $\eta(x) = 1$ everywhere). Determined by the competition between these two terms., the equilibrium GB crystallinity, η_{GB}^{eq}, should take a value between 0 and 1. One would expect that the boundary structure becomes less ordered for GBs with larger misorientations $\delta\theta$.

The energy functional, Eq. 2.8, has the exactly same form as the free energy

expression employed in Cahn's critical-point wetting theory (CPWT) [22],

$$F = \Phi(c_s) + \int_0^\infty \left[\Delta f(c,T) + \kappa \left(\frac{dc}{dx} \right)^2 \right] dx \tag{2.9}$$

if the concentration in a two-component fluid, c, is exchanged for crystallinity η. In CPWT, the short-range surface interaction $\Phi(c_s)$-term favors a composition profile with the surface adsorption, c_s, at the minimum of Φ. The integral in CPWT similarly favors a uniform bulk. This analogy suggests, under some conditions, that first-order GB structural transitions may exist below the temperatures at which the boundary is completely wet by the crystal's equilibrium melt as a parallel to the first-order adsorption transitions in CPWT.

2.3.2 Graphical Construction

A graphical construction approach, similar to Cahn's analysis for CPWT, is employed to determine the equilibrium GB solutions and the conditions for GB structural transitions. The $\eta(x)$ that minimizes Eq. 2.8 has a vanishing variational derivative (c.f. Ref. [144]),

$$\frac{\delta F}{\delta \eta} = 0 \tag{2.10}$$

which gives

$$\nu^2 \frac{d^2\eta}{dx^2} = \frac{\partial \Delta f}{\partial \eta} \qquad \text{for } x > 0 \tag{2.11}$$

with the boundary condition at $x = 0$ for a variable end-point problem [144]

$$\left. \frac{d\eta}{dx} \right|_{x=0^+} = \frac{s\Delta\theta}{2\nu^2} \frac{dg}{d\eta}(\eta_{GB}) \tag{2.12}$$

The first integral of Eq. 2.11 (multiplying Eq. 2.11 by $d\eta/dx$ and integrating once) is

$$\frac{\nu^2}{2} \left(\frac{d\eta}{dx} \right)^2 = \Delta f(\eta, T) \qquad \text{for } x > 0 \tag{2.13}$$

where the integration constant is determined to be zero because $\eta(x=\infty)=1$ and $\Delta f(\eta=1)=0$. Because $\eta(x=0)=\eta_{GB}$ is the only minimum of $\eta(x)$, $d\eta/dx>0$ for all $x>0$ and Eq. 2.13 is equivalent to

$$\frac{d\eta}{dx}=\sqrt{\frac{2\Delta f(\eta,T)}{\nu^2}} \qquad \text{for } x>0 \tag{2.14}$$

Rewrite Eq. 2.14 as

$$\frac{dx}{d\eta}=\sqrt{\frac{\nu^2}{2\Delta f(\eta,T)}} \qquad \text{for } x>0 \tag{2.15}$$

Integrating Eq. 2.15 once gives an implicit solution for the equilibrium $\eta(x)$ profile to the right of the GB

$$x(\eta)=\int_{\eta_{GB}}^{\eta}\sqrt{\frac{\nu^2}{2\Delta f(\eta',T)}}d\eta' \tag{2.16}$$

Using Eqs. 2.13 and 2.15 and the following identity

$$g(\eta)=\int_0^{\eta}\frac{dg}{d\eta'}d\eta' \tag{2.17}$$

one rewrites Eq. 2.8 as

$$\frac{F}{2}=\int_0^{\eta_{GB}}\frac{s\Delta\theta}{2}\frac{dg}{d\eta}(\eta)\,d\eta+\int_{\eta_{GB}}^{1}\sqrt{2\nu^2\Delta f(\eta,T)}d\eta \tag{2.18}$$

in which the GB excess energy is expressed as an explicit function of η_{GB}. Therefore, the equilibrium GB solution is uniquely determined by the local crystallinity value at the GB core, η_{GB}, through Eqs. 2.15 and 2.18. The unknown η_{GB} in Eqs. 2.15 and 2.18 is determined by inserting Eq. 2.14 into Eq. 2.12

$$\sqrt{2\nu^2\Delta f(\eta_{GB},T)}=\frac{s\Delta\theta}{2}\frac{dg}{d\eta}(\eta_{GB}) \tag{2.19}$$

its solution is denoted as η_{GB}^{eq}.

In addition to solutions of Eq. 2.19, the bounding values of η, i.e. η=0 and 1, may themselves be the equilibrium values of η_{GB} if F in Eq. 2.18 is an increasing (or decreasing) function of η_{GB} near η_{GB}=0 (or 1). The condition for such "boundary

extrema" to appear will be governed by inequalities which replace Eq. 2.19. To find this inequality for $\eta_{GB}^{eq} = 0$, consider two extremal solutions to Eq. 2.8, $\eta_0(x)$ and $\eta_+(x)$, with *fixed* boundary conditions at $x = 0$: $\eta_0(x = 0) = 0$ and $\eta_+(x = 0) = \delta\eta_{GB}$, where $\delta\eta_{GB}$ is a positive infinitesimal quantity. Because the variational extremum still holds, Eq. 2.11 and Eq. 2.18 hold for $\eta_{GB} = \eta_0$ and η_+. The corresponding values of F are

$$\begin{aligned} F_0 &= 2\int_0^1 \sqrt{2\nu^2\Delta f(\eta,T)}d\eta \\ F_+ &= 2\left[\int_0^{\delta\eta_{GB}} \frac{s\Delta\theta}{2}\frac{dg}{d\eta}d\eta + \int_{\delta\eta_{GB}}^1 \sqrt{2\nu^2\Delta f(\eta,T)}d\eta\right] \\ &= 2\left[\left(\frac{s\Delta\theta}{2}\frac{dg}{d\eta}(\eta=0) - \sqrt{2\nu^2\Delta f(0,T)}\right)\delta\eta_{GB} + \int_0^1 \sqrt{2\nu^2\Delta f(\eta,T)}d\eta\right] \end{aligned} \tag{2.20}$$

$F_+ - F_0$ is the minimum increase of excess energy for a small positive departure $\delta\eta_{GB}$ away from η_{GB}=0. Therefore, the condition that η_{GB} is a boundary minimum is

$$\frac{s\Delta\theta}{2}\frac{dg}{d\eta}(\eta=0) - \sqrt{2\nu^2\Delta f(0,T)} > 0 \tag{2.21}$$

As $g(\eta)$ is a monotonically increasing function, its leading order behavior at $\eta = 0$ is $g(\eta) = \eta^p$ with $p > 0$. The boundary-minimum condition, Eq. 2.21, is never satisfied for any $p > 1$ below T_m. For $p = 1$, the inequality is met within a range of temperatures below T_m where $\Delta f(0)$ is small enough. For $0 < p < 1$, the inequality is met for all $T < T_m$. On the grounds that completely disordered boundaries are minimizers for large undercoolings if $p \leq 1$, this range can be eliminated because it produces unphysical results. Therefore, in the remainder of this chapter, the following scaling behavior for $g(\eta)$ at $\eta = 0$ is assumed

$$g(\eta) = \eta^p \qquad p > 1 \tag{2.22}$$

There is a corresponding inequality for $\eta_{GB} = 1$, but has no consequence in this model and it is determined $\eta_{GB} = 1$ can never be the equilibrium value.

Based on Eqs. 2.18 and 2.19, a graphical approach can be used to determine the

equilibrium values of the crystallinity at the GB core, η_{GB}^{eq}, and the GB excess energy, $F(\eta_{\mathrm{GB}}^{eq}; \Delta\theta, T)$, as demonstrated in Fig. 2-2. η_{GB}^{eq} and $F(\eta_{\mathrm{GB}}^{eq}; \Delta\theta, T)$ can be represented by plotting the two integrands in Eq. 2.18 against the integration variable η (Fig. 2-2). According to Eq. 2.19, η_{GB}^{eq} is determined by the intersection of the curves for $(s\Delta\theta/2)dg/d\eta$ and $\sqrt{2\nu^2\Delta f}$. According to Eq. 2.18, one-half the GB energy, $F/2$, is the area under the first curve between 0 to η_{GB}^{eq} plus the area under the second curve from η_{GB}^{eq} to 1. This representation demonstrates the competition between the boundary condition and the bulk integral terms in Eq. 2.8: The boundary condition term, arising from the region $0 < \eta < \eta_{\mathrm{GB}}^{eq}$, and the bulk term, from $\eta_{\mathrm{GB}}^{eq} < \eta < 1$, are directly coupled through η_{GB}^{eq}.

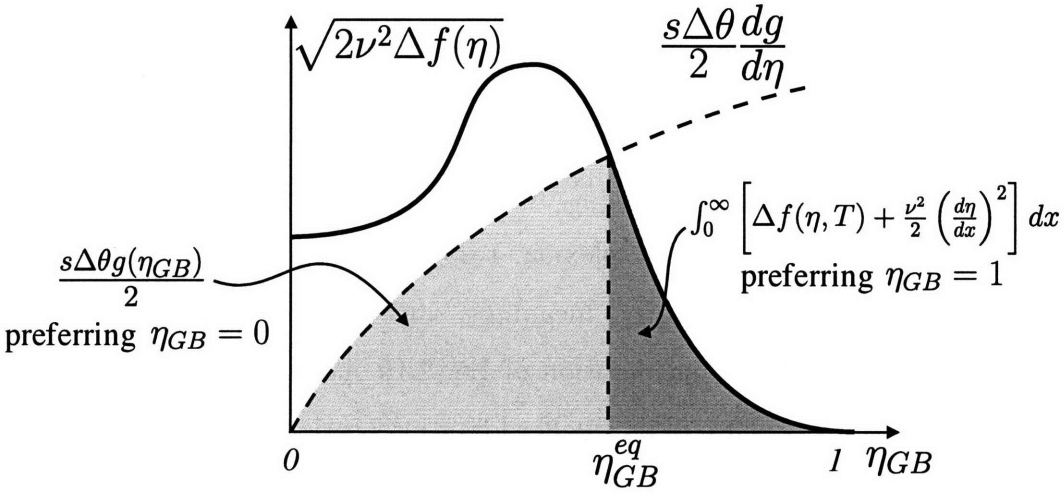

Figure 2-2: Graphical construction for GB complexions (see Eqs. 2.18 and 2.19). The equilibrium GB crystallinity, η_{GB}^{eq}, is the intersection of the curves represented by the integrands in Eq. 2.18 and the sum of the two shaded areas is half of the free energy of an equilibrium GB.

2.3.3 Graphical Analysis of Grain Boundary Order-Disorder Transitions

The graphical construction permits prediction of trends in the temperature dependence of GB complexions based on qualitative aspects of the assumed double-well form of $\Delta f(\eta, T)$ and of the monotonic, temperature-insensitive, behavior of $(s\Delta\theta/2)dg/d\eta$. The latter function follows from Eq. 2.22, or modified versions used elsewhere [134,

145,146]. The energy of the metastable liquid minimum of $\Delta f(\eta, T)$ at $\eta = 0$ increases with the magnitude of undercooling, $\Delta T \equiv T_m - T$, and therefore the intercept of the curve $\sqrt{2\nu^2 \Delta f}$ also increases with ΔT. Fig. 2-3 depicts several situations that differ depending on the relative curvatures of the two integrands. At large undercoolings, ΔT_{large}, a *single intersection* always exists at an η_{GB}^{eq} close to 1, which predicts a relatively ordered GB. As supercooling decreases (increasing T), this intersection moves continuously towards a more disordered η_{GB}^{eq}. At the same time, with the y-intercept of $\sqrt{2\nu^2 \Delta f}$ decreasing, the two curves come close to each other at low η_{GB} values. Fig. 2-3(a) illustrates the situation where two additional equilibrium solutions characterized by smaller (i.e., more disordered) values of η_{GB}^{eq} appear at decreased undercooling, ΔT_{med}.

Of the three intersection appearing in Fig. 2-3(a), the middle intersection $\eta_{\text{GB}}^{eq-\max}$ is an unstable solution of η_{GB}^{eq}—it maximizes the area below the two curves. The remaining intersections, η_{GB}^{Ord} and η_{GB}^{Dis}, are metastable solutions that represent an ordered and a disordered GB complexion, respectively. The terms "ordered" and "disordered" here only have relative meanings, since neither GB structure is purely crystalline nor liquid-like. Consideration of Eq. 2.15 shows that the disordered GB has a larger thickness because of its smaller lower integration limit, η_{GB}^{Dis}. The relative stability rankings of the two solutions depend on their energy values. According to the graphical representation of the GB excess energy, the energy difference of the two solutions, $F(\eta_{\text{GB}}^{Ord})$-$F(\eta_{\text{GB}}^{Dis})$, is equal to the difference of the hatched area A and B shown in Fig. 2-3: the ordered GB is more stable when area A is less than B. When the multiple intersections begin to develop, $\eta_{\text{GB}}^{eq-\max}$ and η_{GB}^{Dis} are close to each other and area A is less than B, so η_{GB}^{Ord} is the globally stable solution. As undercooling decreases, $\eta_{\text{GB}}^{eq-\max}$ gradually moves to η_{GB}^{Ord}, resulting in an increase of A relative to B. The relative stability of the η_{GB}^{Dis} and η_{GB}^{Ord} solutions will switch when area A becomes equal to B at a particular temperature below T_m. If the system parameters support such a switch, this temperature will characterize a first-order GB order-disorder structural transition, where the local crystallinity and thickness of the GB have a discontinuous jump. As the undercooling is reduced further, η_{GB}^{Dis}

decreases continuously and approaches zero at T_m, suggesting that the corresponding GB complexion becomes completely liquid-like at the melting point. An additional aspect is that $\eta_{\mathrm{GB}}^{eq-\max}$ may merge with η_{GB}^{Ord} and then disappear at small enough ΔT, as shown in Fig. 2-3(a). This results in a loss of the η_{GB}^{Ord} solution, and the GB will transform barrierlessly into the disordered GB complexion just below T_m.

However, this sequence and the behavior with undercooling depend on the shapes of the two curves in Fig. 2-3. Two other modalities of GB behavior near T_m can be distinguished by increasing the curvature of $(s\Delta\theta/2)(dg/d\eta)$ relative to that of $\sqrt{2\nu^2\Delta f}$, or, by varying the slope of $(s\Delta\theta/2)(dg/d\eta)$ which is equivalent to changing the GB misorientation $\Delta\theta$. A second situation is illustrated in Fig. 2-3(b), which is realized by a more positive curvature of $(s\Delta\theta/2)(dg/d\eta)$ or a larger $\Delta\theta$ relative to Fig. 2-3(a). In this case, only one intersection, η_{GB}^{eq}, is generated at any undercoolings, and it evolves continuously from $\eta_{\mathrm{GB}}^{eq} \approx 1$ to $\eta_{\mathrm{GB}}^{eq} \approx 0$ as $\Delta T \to 0$. There is no first-order GB transition below T_m, but the solution's asymptotic behavior as $\Delta T \to 0$ is the same as for the disordered GB complexion in the first situation (viz. Fig. 2-3(a)), i.e., the GB possesses a completely liquid-like structure when approaching the melting point. This is the case of continuous GB disordering that leads to preferential GB melting.

Figure 2-3(c) illustrates the third modality that is for small $\Delta\theta$. Again, a single intersection, η_{GB}^{eq}, is generated that decreases with decreasing ΔT, but its value remains finite as $T \to T_m$. In such systems, the ordered GB structure is stable against *complete*, preferential melting upon approach to T_m from below; moreover, they will not be perfectly wet by the liquid at equilibrium at T_m. It will be justified below that $\eta_{\mathrm{GB}}^{eq} \to 0$ corresponds to perfect wetting at T_m, i.e., $2\gamma_{\mathrm{sol-liq}} = \gamma_{\mathrm{GB}}$.

Thus the three transition modalities have differing implications for macroscopic system behavior. The modalities can be cataloged based on two distinguishing phenomena: whether a first-order transition exists below T_m, and whether the GB is perfectly wet (i.e., $\eta_{\mathrm{GB}}^{eq} \to 0$) at $T = T_m$. The particular behavior depends on the modeled system through the forms of $\Delta f(\eta, T)$ and $g(\eta)$ plus the values of gradient coefficients s and ν, and on the misorientation $\Delta\theta$. How $\Delta\theta$ affects GB behaviors is

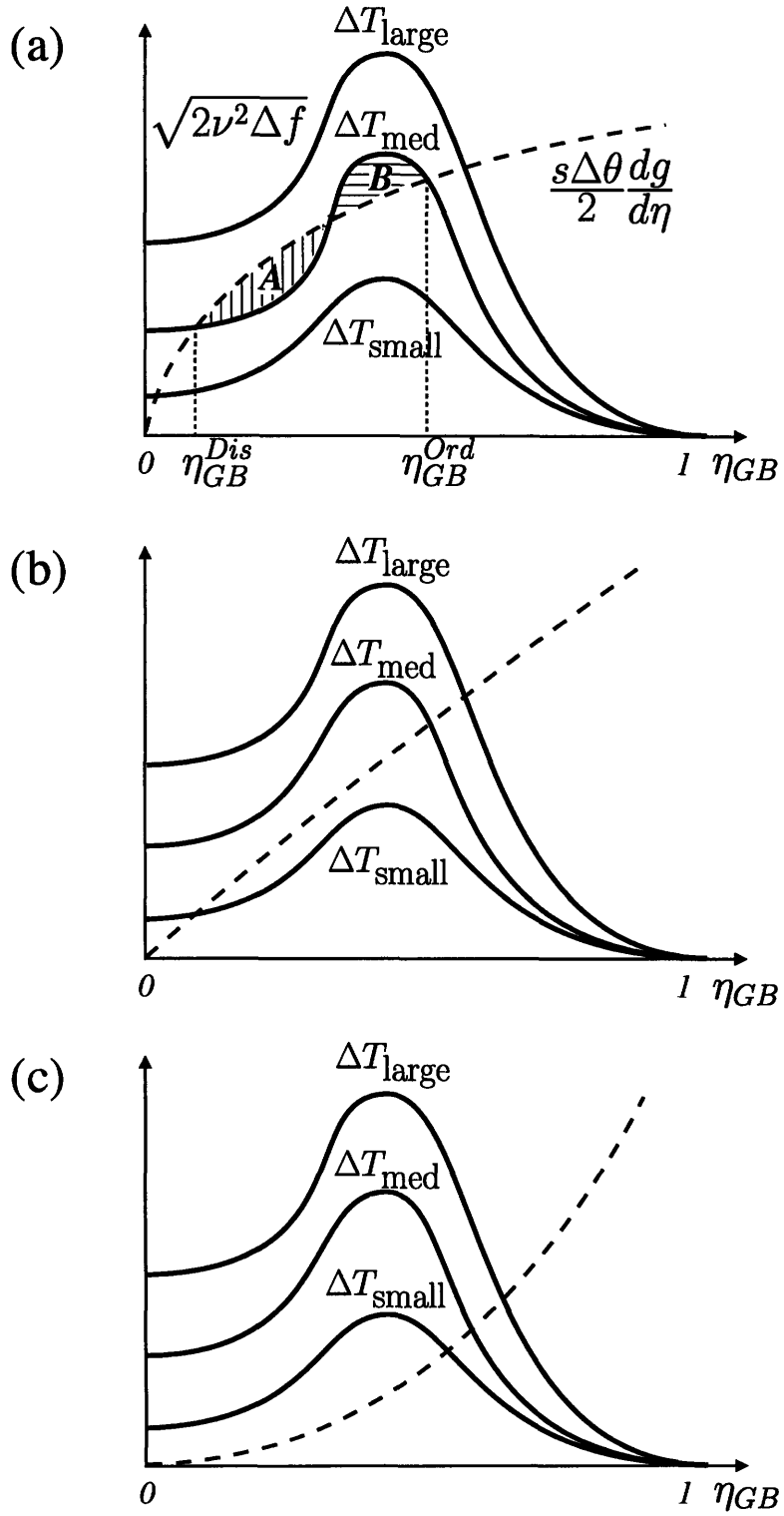

Figure 2-3: Constructions depict differing GB transition behaviors for a range of undercoolings. (a) illustrates the possibility of a first-order GB disorder transition below T_m. (b) and (c) illustrate other types of GB behavior arising from changing curvature for the orientation gradient energy prefactor $g(\eta)$. In (b) only one solution exists that decreases continuously to $\eta_{\mathrm{GB}}^{eq} = 0$ as $T \rightarrow T_m$. In (c) only one solution exists, but has a limiting finite value, $\eta_{\mathrm{GB}}^{eq} > 0$, at $T = T_m$.

of particular interest because it will vary from boundary to boundary in a polycrystal while the others are "system parameters" fixed by the material. An extended graphical analysis of misorientation effects and also of these system parameters follows.

By inserting the leading behavior for $g(\eta)$ from Eq. 2.22, Equation 2.19 becomes

$$[\Delta f(\eta_{\mathrm{GB}}^{eq})]^{\beta} = \alpha \eta_{\mathrm{GB}}^{eq} \tag{2.23}$$

where

$$\begin{aligned} \beta &= \frac{1}{2(p-1)} \\ \alpha &= \left(\frac{sp}{2\sqrt{2}\nu}\Delta\theta\right)^{2\beta} \qquad p > 1 \end{aligned} \tag{2.24}$$

Equations 2.22 and 2.23 permit a general graphical construction for η_{GB}^{eq} by plotting the two sides of Eq. 2.23 against η_{GB}.

In Eq. 2.23, the $\alpha\eta_{\mathrm{GB}}^{eq}$ curve is a straight line that passes through the origin with a slope α proportional to $(\Delta\theta)^{2\beta}$, and the homogeneous free-energy curve is a double-well function raised to a power β.

For a given system, the range of GB misorientations are represented by a fan of lines emanating from the origin. For the case illustrated in Fig. 2-4(a), when there is at least one boundary misorientation that produces three intersections with $[\Delta f(\eta, T)]^{\beta}$ at a temperature T below T_m, two bounding tangent lines, associated with an upper $\Delta\theta_U$ and a lower $\Delta\theta_L$ misorientation, are produced by the fan (It is assumed for this demonstration that both $\Delta\theta_U$ and $\Delta\theta_L$ lie within the range of allowable misorientations which would be $0 < \Delta\theta < 2\pi$ with low-symmetry crystals and reduced by additional crystal symmetry.) Any misorientation $\Delta\theta_L < \Delta\theta < \Delta\theta_U$ will have two (meta)stable GB complexions at the given temperature. A particular $\Delta\theta_{FO}(T)$ that has the equilibrium first-order transition at T separates the GB misorientation into an upper region, $\Delta\theta_{FO} < \Delta\theta < \Delta\theta_U$, wherein the disordered GB η_{GB}^{Dis} is globally stable, and a lower region, $\Delta\theta_L < \Delta\theta < \Delta\theta_{FO}$, where the ordered GB η_{GB}^{Ord} is globally stable.

However, the two tangent lines of $(\Delta f)^\beta$ that define $\Delta\theta_U$ and $\Delta\theta_L$ may not exist at all temperatures. To establish a criterion for their existence, consider the first inflection point of $(\Delta f)^\beta$ (i.e., the inflection with the smallest η value). Of all the tangent lines from $(\Delta f)^\beta$, the one at this point yields the smallest y-intercept value Y_{min}, as drawn in Fig. 2-4(b). This is shown by the expression of the y-intercept of a tangent line at η, $Y(\eta) = [\Delta f(\eta)]^\beta - \eta\partial\Delta f^\beta/\partial\eta$, which is extremized by the condition $\partial^2\Delta f^\beta/\partial\eta^2{=}0$ (i.e. at the inflection point). If $Y_{min} > 0$ at T, no tangent lines can pass through the origin and there is no coexistence of ordered and disordered complexions at this temperature. However, two such lines ($\Delta\theta_U$ and $\Delta\theta_L$) do exist if $Y_{min} < 0$. $Y_{min} < 0$ is thus a sufficient and necessary condition for a first-order GB order-disorder transition to occur at T.

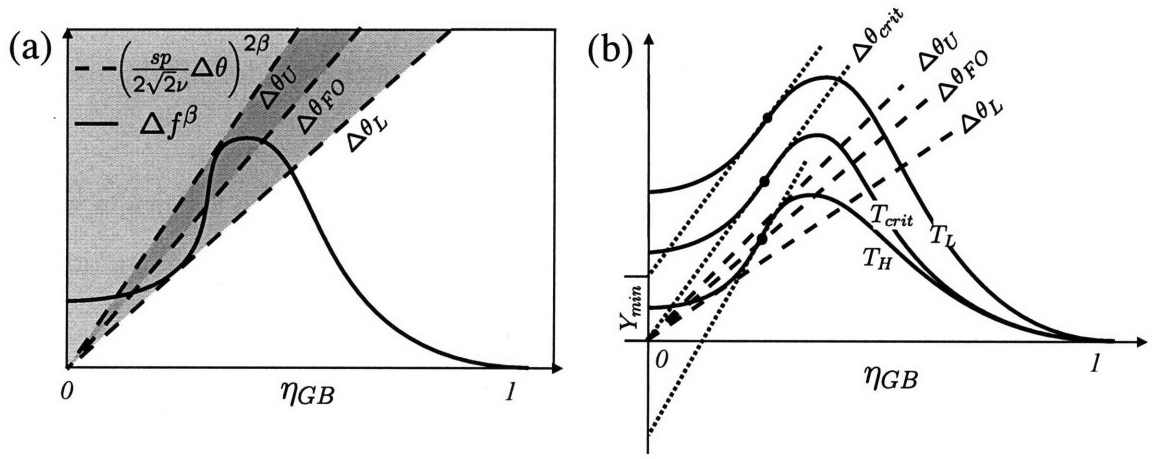

Figure 2-4: Extended construction to reveal behavior as a function of GB misorientation. (a) The $\Delta\theta_U$ and $\Delta\theta_L$ define upper and lower bounds to a fan of lines for those $\Delta\theta$ having three intersections. Frame (b) illustrates how the sign of the y-axis intercept, Y_{min}, of the tangent line of the nearest inflection point of $(\Delta f(\eta))^\beta$ evolves with temperature. No first-order transition at any GB is possible when Y_{min} is positive.

In some systems, Y_{min} may switch sign from positive to negative below T_m. If so, a critical temperature can be defined for an undercooling ΔT_{crit} where $Y_{min} = 0$, as illustrated in Fig. 2-4(b). Then, for $T < T_m - \Delta T_{crit}$, no first-order transition will appear for *any* misorientation angle. $\Delta\theta_U$, $\Delta\theta_L$, and $\Delta\theta_{FO}$ are meaningful only for $\Delta\theta \leq \Delta\theta_{crit}$. At $T = T_m - \Delta T_{crit}$, only that tangent line for the first inflection crosses the origin, which is equivalent to $\Delta\theta_U = \Delta\theta_L = \Delta\theta_{FO}$. The slope of that tangent line

defines a critical misorientation, $\Delta\theta_{crit}$. Misorientations of $\Delta\theta > \Delta\theta_{crit}$ will always have greater values than $\Delta\theta_U(T)$ at temperatures $T > T_m - \Delta T_{crit}$. Therefore, the $\alpha\eta_{\mathrm{GB}}^{eq}$ curve for $\Delta\theta > \Delta\theta_{crit}$ has only one intersection with Δf^{β} which approaches the origin as $\Delta T \rightarrow 0$ (i.e., $\eta_{\mathrm{GB}}^{eq} \rightarrow 0$). Their associated complexions thus exhibit continous melting and have perfect wetting behavior (as elaborated in the next section). For misorientations just less than $\Delta\theta_{crit}$, three intersections will appear above $T_m - \Delta T_{crit}$, and a first-order GB order-disorder transition will happen if $\Delta\theta \geq \Delta\theta_{FO}(T)$ for some T below T_m. Finally, when $\Delta\theta$ is always less than $\Delta\theta_L(T)$ below T_m, there is only one intersection and it remains at a finite η_{GB}^{eq} value as $T \rightarrow T_m$. Such GBs will not be fully disordered nor wet by a liquid at T_m.

Plotting the three characteristic misorientation angles, $\Delta\theta_{FO}$, $\Delta\theta_L$, and $\Delta\theta_U$, against temperature yields three curves on the T–$\Delta\theta$ plane forming an interfacial complexion diagram. These lines represent the first-order GB order-disorder transition line and the two metastable existence limits. The three lines terminate at the critical point $(T_{crit}, \Delta\theta_{crit})$, as shown in Fig. 2-5. The critical conditions, $(T_{crit}, \Delta\theta_{crit})$, are determined by the conditions

$$0 = [\Delta f(\eta_{crit}; T_{crit})]^{\beta} - \eta_{crit} \left.\frac{\partial \Delta f^{\beta}}{\partial \eta}\right|_{\eta_{crit}, T_{crit}} \tag{2.25}$$

$$0 = \left.\frac{\partial^2 \Delta f^{\beta}}{\partial \eta^2}\right|_{\eta_{crit}, T_{crit}} \tag{2.26}$$

$$\Delta\theta_{crit} = \frac{2\sqrt{2}\nu}{sp} \left(\frac{\Delta f^{\beta}(\eta_{crit}, T_{crit})}{\eta_{crit}}\right)^{\frac{1}{2\beta}} \tag{2.27}$$

Within the limits of the metastable existence curves in Fig. 2-5, both the ordered and disordered complexions can exist in metastable equilibrium; whereas outside these limits only one complexion exists. The complexions may coexist stably only at temperatures and misorientations indicated by the first-order transition curve.

Finally, if $Y_{min} \geq 0$ for all $T \leq T_m$, multiple intersections will not be generated, and the three lines will not appear as in Fig. 2-5. In this case, GBs will have continuously increasing but limited disorder up to $T = T_m$.

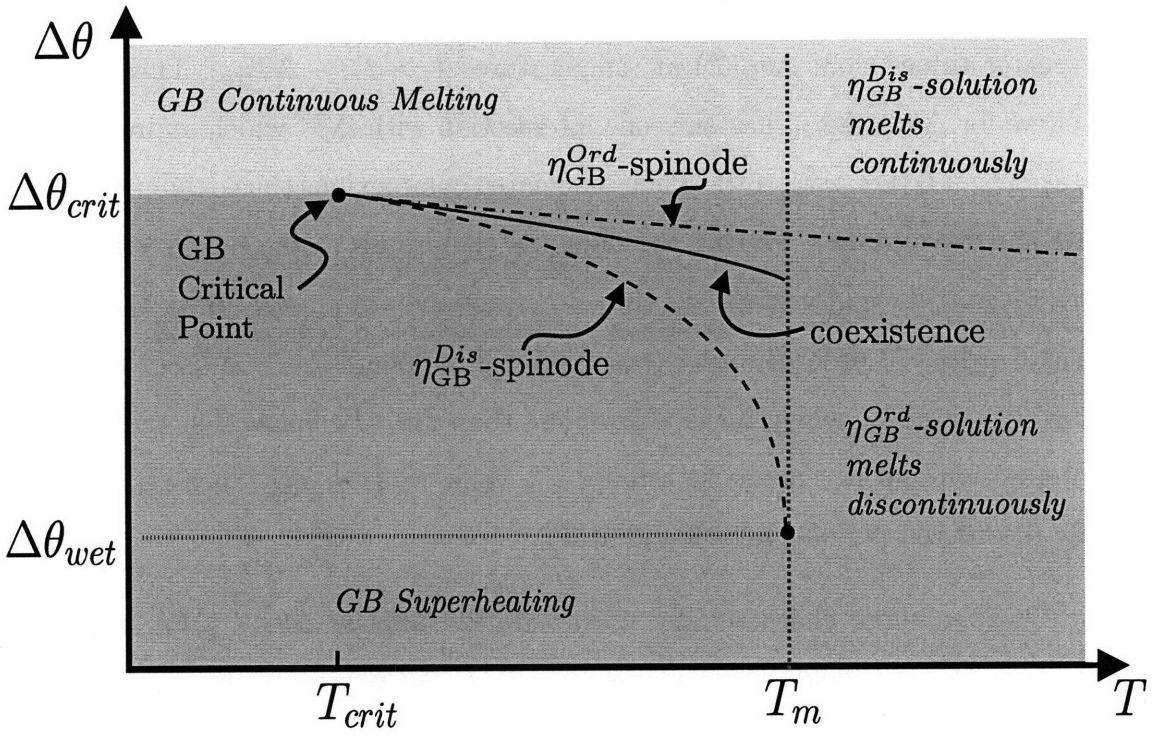

Figure 2-5: An example of a GB-complexion diagram (the interface equivalent of a phase diagram) for a system that admits a first-order interfacial transition. The solid curve delineates first-order grain boundary transitions—on the low T and $\Delta\theta$ side, the more ordered complexion (η_{GB}^{Ord}) is more stable, while the more disordered complexion (η_{GB}^{Dis}) is more stable on the other side. The first-order curve terminates at a critical point ($T_{crit}, \Delta\theta_{crit}$) at which the transition is higher order. The dashed curves indicate existence limits (spinodes) for the metastable extensions of the η_{GB}^{Ord}–solution (upper, dash-dotted curve) and η_{GB}^{Dis}–solution (lower, dashed curve). The extension of the η_{GB}^{Ord} spinode to $T > T_m$ indicates whether an ordered GB could metastably superheat.

2.3.4 Asymptotic Behavior of the Disordered GB complexion

As $T \to T_m$, the asymptotic behavior of GBs can be analyzed by expanding $\Delta f(\eta, T)$ about $\eta = 0$ and $T = T_m$

$$\Delta f(\eta, T) = \frac{\Delta h_m}{T_m}\Delta T + A\eta^q + o(\Delta T, \eta^q) \tag{2.28}$$

where $\Delta T = T_m - T$ is the small undercooling, Δh_m is the melting enthalpy per volume, A is a positive constant, and q is greater than 1. Using Eq. 2.22 for $g(\eta)$ and

inserting Eq. 2.28 into Eq. 2.19 produces

$$\frac{\Delta h_m}{T_m}\Delta T + A\eta^q \approx \left(\frac{sp}{2\sqrt{2}\nu}\Delta\theta\right)^2 \eta^{2(p-1)} \tag{2.29}$$

Equation 2.29 implies that, when $1 < q/(2p-2)$, the crystallinity of a disordered GB (both stable and metastable) goes continuously to zero as

$$\eta_{\mathrm{GB}}^{Dis} \sim \Delta T^{1/(2p-2)} \qquad T \to T_m \tag{2.30}$$

When $1 = q/(2p-2)$, similar scaling relation holds and complete melting occurs, but only for GBs with $\Delta\theta > \Delta\theta_{wet} = \frac{2\nu\sqrt{2A}}{sp}$. When $q/(2p-2) < 1$, there is no solution to Eq. 2.29 at $\eta \approx 0$ (i.e. no disordered GB solution exists because the left-hand side always exceeds the right when η is sufficiently small). For this case, η_{GB}^{eq} remains finite at T_m, which indicates unconditionally that GB premelting at T_m does not occur for any $\Delta\theta$, nor does perfect liquid wetting.

The asymptotic behavior of the GB thickness can be obtained from Eq. 2.15 by assuming a fixed η value (near 1) specifies the edge of the GB core. The thicknesses of disordered GBs always diverge as $T \to T_m$. However, the divergence rate is either logarithmic for $q = 2$ or obeys a power low relationship for $q > 2$,

$$W_{GB} \sim \begin{cases} \ln\left(T_m/(T_m - T)\right) & q = 2 \\ \left((T_m - T)/T_m\right)^{\frac{1}{q}-\frac{1}{2}} & q > 2 \end{cases} \tag{2.31}$$

The logarithmic divergence of film thickness for $q = 2$ is a typical result of mean field theories, and it agrees with the results of other modeling methods [44, 45, 147]. The logarithmic divergence results from a Δf that is quadratic near $\eta = 0$. However, in one MD study it was noted that the widths could fit $(\Delta T)^{-1/4}$ [147], which would agree with the above relation for $q = 4$.

The above analysis establishes that, as $T \to T_m$, a disordered GB with vanishing η_{GB}^{eq} widens due to the gradient penalties. The misorientation penalty disappears as

the boundary thickness increases. In this limit, Eq. 2.18 becomes

$$\frac{\gamma_{\mathrm{GB}}}{2} = \gamma_{\mathrm{sl}} = \int_0^1 \sqrt{2\nu^2 \Delta f(\eta, T_m)} d\eta \tag{2.32}$$

which is the solid/liquid interfacial energy at T_m. The difference between γ_{GB} and $2\gamma_{\mathrm{sl}}$ vanishes as

$$2\gamma_{\mathrm{sl}} - \gamma_{\mathrm{GB}} \sim \Delta T^{p/(2p-2)} \quad T \rightarrow T_m \tag{2.33}$$

Thus, any disordered GB is perfectly wet by the equilibrium liquid at T_m. On the other hand, ordered GBs have a finite η_{GB}^{eq} at T_m and are not perfectly wetted. For this reason, $\Delta\theta_L(T_m)$ corresponds to $\Delta\theta_{wet}$, the wetting transition misorientation, as in Fig. 2-5.

2.3.5 Grain Boundary Superheating

A perfect solid can be superheated in the absence of liquid nucleation. The free surface provides barrierless nucleation if the liquid perfectly wets the solid surface. Not all crystal surfaces are perfectly wet by their equilibrium melt at $T = T_m$; pure Pb(111) is an example [28, 148]. Grain boundaries will also provide nucleation sites, and their wetting behavior will determine whether a solid can be superheated in the absence of free surface nucleation, or suppress superheating and promote melting, especially for confined solids with no free surfaces. To analyze superheated GBs, the complexion diagram can be extended to temperatures above T_m using the graphical analysis. Figure 2-5 shows that, of the three characteristic lines, only the η_{GB}^{Ord} curve extends above T_m. The η_{GB}^{Dis} complexion (liquid in this case) is more stable than the η_{GB}^{Ord} complexion for all $T > T_m$, but the ordered GB is metastable for $\Delta\theta < \Delta\theta_U$ and will melt given a nucleation event. The η_{GB}^{Ord} complexion is unstable for $\Delta\theta > \Delta\theta_U$ above T_m.

2.4 Numerical Calculations

To illustrate different GB behaviors and GB complexion diagram with numerical examples, the following model is considered

$$\Delta f(\eta, T) = \frac{\Delta h_m}{T_m}(T_m - T)(1-\eta)^3(1+3\eta+6\eta^2) + \frac{a^2}{2}\eta^2(1-\eta)^2 + \frac{b^2}{2}\eta^4(1-\eta)^4$$
$$sg(\eta) = s\eta^2 \tag{2.34}$$

The first term of Δf approximates a step function that decreases from $\frac{\Delta h_m}{T_m}(T - T_m)$ to 0 at $\eta = 1/2$. The free energy difference between the liquid and solid states is approximated by $\frac{\Delta h_m}{T_m}(T - T_m)$. The second and third terms simulate an energy barrier between liquid and crystalline states. The parameters a^2 and b^2 have the units J/m^3. The model can be rescaled and the only significant parameter is the b/a ratio. In this first example, b/a=10 is chosen. To develop a GB complexion diagram like Fig. 2-5, the three characteristic lines on the diagram are numerically computed in the following way. First, find the two roots of Eq. 2.25 at a given temperature T, η_U and η_L ($\eta_U > \eta_L$), which correspond to the two limiting misorientations, $\Delta\theta_U(T)$ and $\Delta\theta_L(T)$, through

$$\Delta\theta_{U,L}(T) = \frac{2\sqrt{2}\nu}{sp}\left(\frac{\Delta f^{\beta}(\eta_{U,L}, T)}{\eta_{U,L}}\right)^{1/2\beta} \tag{2.35}$$

The temperature at which the difference between $\Delta\theta_U$ and $\Delta\theta_L$ vanishes is the critical point temperature, T_{crit}. Next, within the range $\Delta\theta_L < \Delta\theta < \Delta\theta_U$, Eq. 2.19 is solved numerically for a given $\Delta\theta$ to find the two metastable roots representing the ordered and disordered GB complexions. Iterate calculating the energies of the two solutions according to Eq. 2.8, and vary $\Delta\theta$ to extract the numerical root of $\Delta\theta_{FO}(T)$ at which the two solutions have equal energies. Repeating the procedure for a set of temperatures generates the $\Delta\theta_U(T)$, $\Delta\theta_L(T)$ and $\Delta\theta_{FO}(T)$ lines. Fig. 2-6(a) is the calculated complexion diagram, in which temperature, length, energy and GB misorientation are rescaled as described in the caption. The first-order GB transition

and the two metastable GB-phase existence limiting lines terminate at a critical point $(\Delta h_m(T_{crit}-T_m)/(a^2T_m),\ s\Delta\theta_{crit}/(a\nu))$=(-0.0148,1.722). The wetting transition misorientation is found to be $s\Delta\theta_{wet}/(a\nu)$=1.

To further illustrate differing GB behaviors, several GB misorientation values are selected for which the temperature dependence of GB crystallinity, energy and thickness are calculated, as shown in Fig. 2-6(b)-(d). The GB thickness is calculated by defining the boundaries of the GB region at η=0.9. The GB energy is compared against the liquid/solid interface energy at T_m, $\gamma_{sl}(T_m)$. The first-order and continuous GB transitions are exhibited by two of the larger misorientations whose normalized values are $s\Delta\theta/(a\nu)$=1.65 and 3. It can be measured from the plots that the local crystallinities, $\eta_{\rm GB}^{eq}$, of both GBs approach 0 as $(T_m - T)^{1/2}$ and their GB thicknesses diverge as -ln$[(T_m - T)/T_m]$, cosistent with predictions of Eqs. 2.30 and 2.31. Fig. 2-6 shows that the energies of the two GBs become twice the liquid/solid interfacial energy at T_m. The GB with a smaller misorientation, $s\Delta\theta/(a\nu)$=0.9, shows no preferential melting. It has finite local crystallinity and thickness at T_m and its energy is less than $2\gamma_{sl}(T_m)$.

In previous simulations of the KWC model, the $\eta^4(1-\eta)^4$ term in Δf was absent from Eq. 2.34, i.e. $b/a = 0$. For comparison, this is used as a second example to show that the complexion diagram is sensitive to the detailed shape of the free energy curve. The absence of the third term in Eq. 2.34 gives a liquid/solid energy barrier that is less steep than the first model. As a result, the three characteristic lines in Fig. 2-5 shrink to a single critical point at $(\Delta h_m(T_{crit}-T)/(a^2T_m), s\Delta\theta_{crit}/(a\nu))$=(0,1), Fig. 2-7(a). In this case, a GB either has no transition below T_m when $\Delta\theta < \Delta\theta_{crit}$, or undergoes a continuous melting for $\Delta\theta > \Delta\theta_{crit}$. This is consistent with the results of previous simulations, in which the first-order GB transitions were not observed for $b/a = 0$ [136, 137]. The temperature dependence of GB crystallinity, thickness and energy for several misorientations are shown in Fig. 2-7(b)-(d). Two of the misorientations, $s\Delta\theta/(a\nu)$=0.5 and 0.8, are below the critical value. The GBs retain finite crystallinity and thickness at T_m, and their energies are less than $2\gamma_{sl}(T_m)$. The largest misorientaion, $s\Delta\theta/(a\nu)$=1.5, shows continuous melting behavior similar to

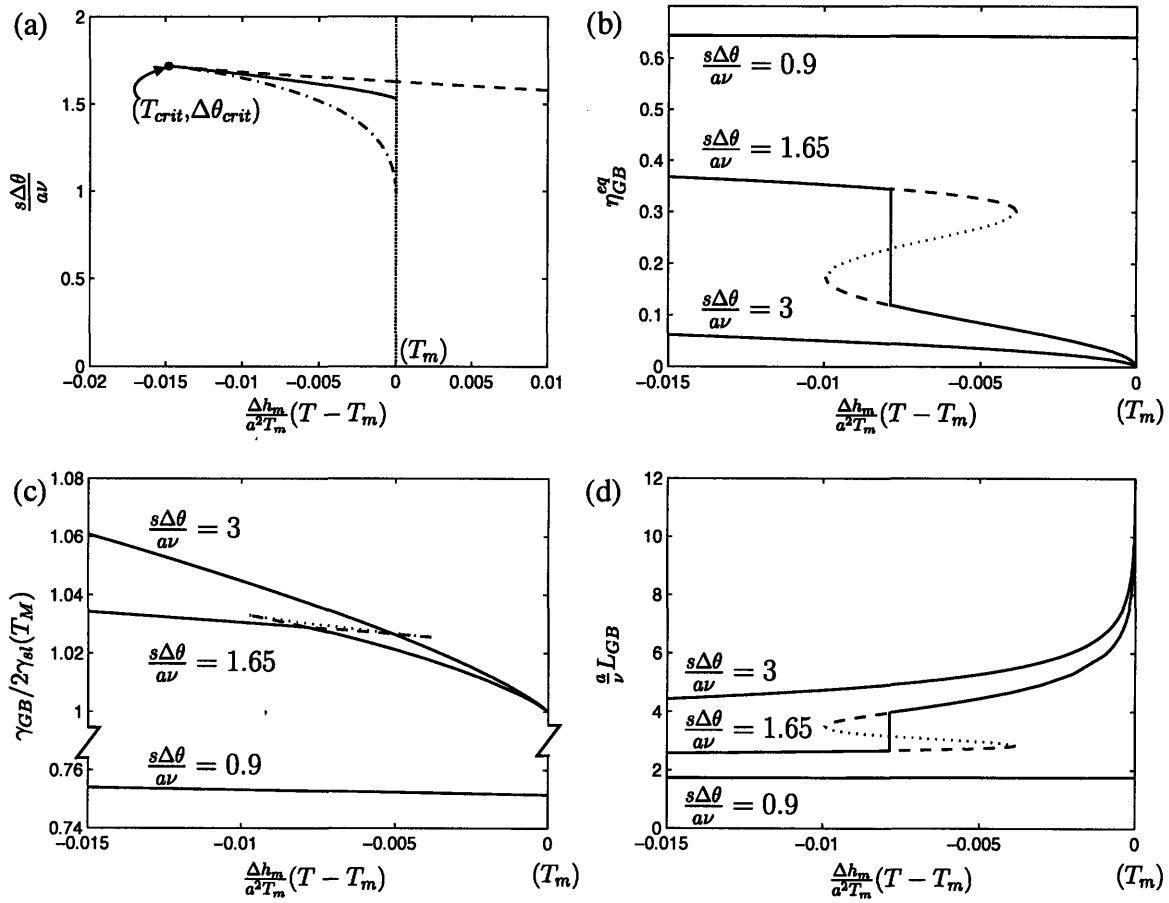

Figure 2-6: (a) Calculated GB complexion diagram for the numerical example with b/a=10 in Δf. (b)–(d) Normalized grain boundary crystallinity, energy and thickness as functions of reduced temperature and misorientation for b/a=10. The temperature is rescaled as $\Delta h_m(T-T_m)/(a^2T_m)$, GB misorientation normalized with $a\nu/s$, GB thickness normalized with $\frac{\nu}{a}$, and GB energy normalized with $2\gamma_{sl}$ (i.e., twice the solid/liquid interface free energy at T_m). γ_{sl} is calculated as $\int_0^1 \sqrt{2\nu^2\Delta f(\eta,T_M)}d\eta$. Small $\Delta\theta$ shows limited disorder up to T_m, intermediate $\Delta\theta$ exhibits a first-order transition, and large $\Delta\theta$ continuously premelts. The dashed lines represent metastable extensions of ordered and disordered GBs. The dotted lines represent the unstable solution.

the first model.

To gain further insight on how the model parameters affect GB wetting characteristics at T_m, the generalized free energy density Δf and prefactor $g(\eta)$ expressions

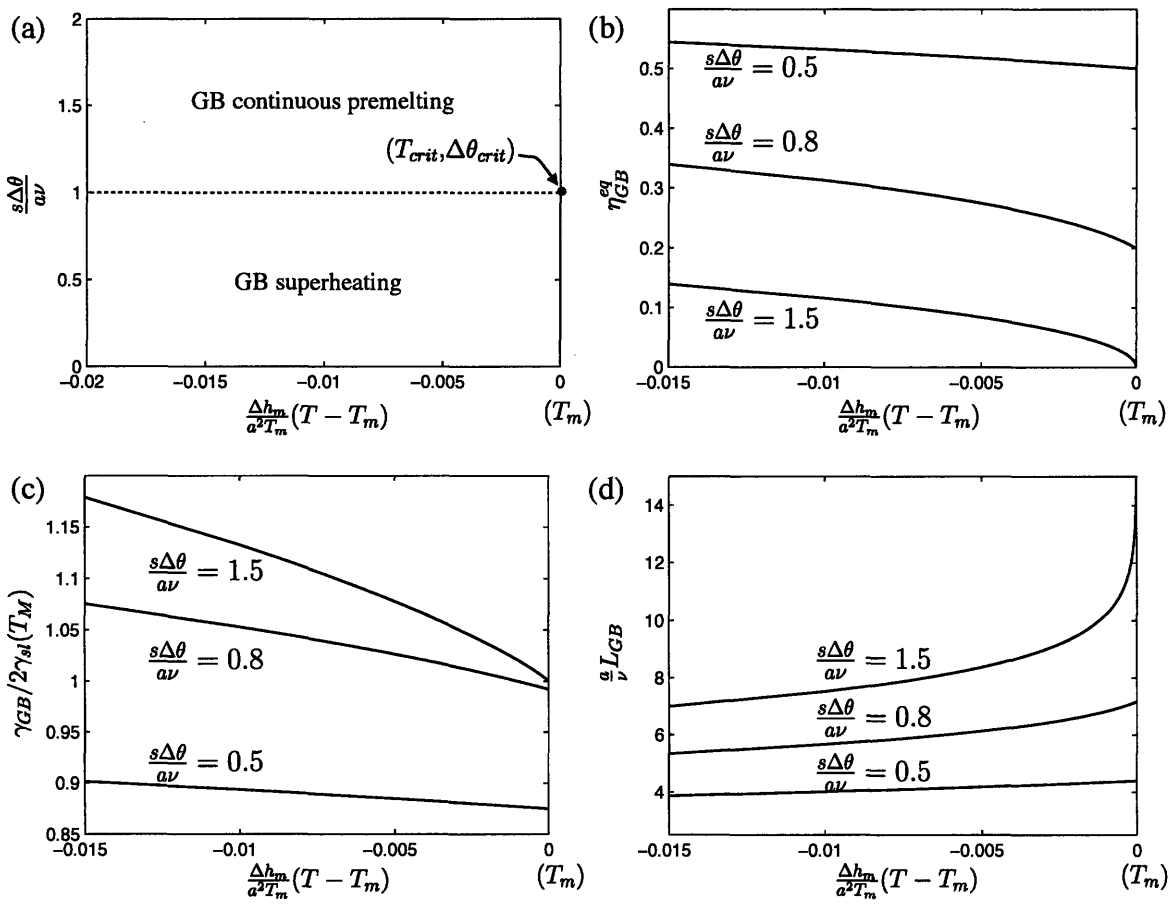

Figure 2-7: A second numerical example illustrates how reduced barrier steepness ($b/a = 0$ in Eq. 2.34) moves the critical point to T_m and thereby eliminates the first-order transition from the complexion diagram.

are considered

$$\Delta f(\eta, T_m) = \frac{a^2}{32}[4\eta(1-\eta)]^q \qquad q \geq 2$$
$$g(\eta) = \eta^p \qquad p > 1 \tag{2.36}$$

produce a model that depends on the choice of parameters p and q. It becomes the second model with b=0 when $p = q = 2$. At the melting point, Eq. 2.23, which determines equilibrium GB states, becomes

$$[4\eta_{\mathrm{GB}}(1-\eta_{\mathrm{GB}})]^{q/(2p-2)} = \left(\frac{4ps\Delta\theta}{a\nu}\right)^{1/(p-1)} \eta_{\mathrm{GB}} \tag{2.37}$$

Fig. 2-8 shows how the solutions of Eq. 2.37 depend on the value of $q/(2p-2)$.

For $q/(2p-2) > 1$, the slope of the left-hand side of Eq. 2.37 is 0 at $\eta_{GB} = 0$. $\eta_{GB} = 0$ is always a solution of Eq. 2.37 and it is metastable as judged by either Eq. 2.21 or from graphical analysis. Therefore, all GBs can be wetted by liquid at the melting point in this case and $\Delta\theta_{wet} \rightarrow 0$ in Fig. 2-5. However, some misorientations may produce three intersections (e.g., $\Delta\theta_1$ in Fig. 2-8) while others produce only one (e.g., $\Delta\theta_2$). Therefore, complete GB wetting can be produced continuously or by a first-order transition.

For $q/(2p-2) < 1$, the slope of the left-hand side of Eq. 2.37 is ∞ at $\eta_{GB} = 0$, and $\eta_{GB} = 0$ is an unstable solution for all $\Delta\theta$. Therefore, no GB is wetted by a liquid at T_m, and furthermore there is no GB transition at any $\Delta\theta$ below T_m — all GBs remain ordered up to T_m.

The intermediate case, $q/(2p-2) = 1$, has a finite slope at η=0 in Fig. 2-8. The $\eta_{GB} = 0$ is a stable solution for $s\Delta\theta/(a\nu) > 1$ (e.g., $\Delta\theta_2$) but not stable at smaller misorientations (e.g., $\Delta\theta_1$). Complete wetting only occurs at GBs with misorientations larger than 1.

Therefore, the phenomenon of complete GB wetting at T_m and GB transitions below T_m is modulated by the ratio of $q/(2p-2)$. This is in agreement with the GB asymptotic behavior analysis in the previous section.

2.5 Discussion

The graphical analysis and numerical results presented in previous sections predict that grain boundaries will have an equilibrium complexion selected from a spectrum of disordered structures. The tendency to disorder increases with misorientation and with temperature up to the melting point where the crystal stably coexists with a completely disordered (e.g., liquid or amorphous) structure. This results can be understood heuristically if the energy increase resulting from a layer of non-equilibrium bulk material is compensated by an energy decrease obtained by converting an ordered grain-boundary interface into two lower energy interfaces. This observation suggests

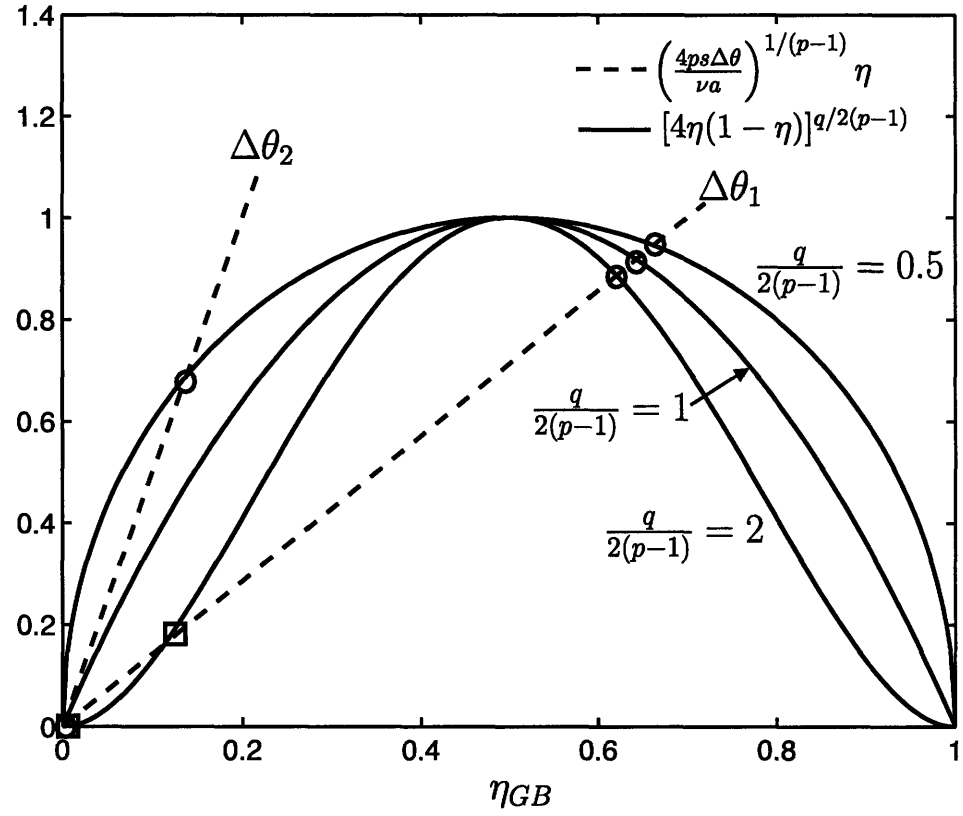

Figure 2-8: Specific examples of three characteristic shapes of $\Delta f(\eta, T_m)^\beta \propto [4\eta(1-\eta)]^{\frac{q}{2(p-1)}}$ that cause different limiting behavior as $T \rightarrow T_m$. Intersections with the straight lines define the behavior of GBs. Three different types of wetting behavior emerge depending upon the types of intersections possible. For $q/(2p-2) > 1$, first-order or continuous disorder transitions lead to complete GB wetting at T_m for all $\Delta\theta$. For $q/(2p-2) = 1$, complete GB wetting can result for $\Delta\theta \geq \Delta\theta_{wet} = (\nu a)/s$, but not for $\Delta\theta < \Delta\theta_{wet}$. For $q/(2p-2) < 1$, every GB will have limited disorder at T_m, and the liquid will not perfectly wet its equilibrium solid phase. The intersections with circle markers represent local energy minima. Those with square markers are local maxima.

that a continuous increase in grain boundary width and disorder as $T \rightarrow T_m$ could be considered a "pre-melting" localized at those grain boundaries with sufficiently large defect energies.

Moreover, the model identifies the conditions that some materials systems will possess first-order transitions between disordered complexions at a specific curve in misorientation-temperature space. Figure 2-5 is a grain-boundary complexion diagram that indicates the temperatures and misorientations where two types of grain-

boundary "phases" exist as a stable or a metastable complexion. The curve at which complexions co-exist at equilibrium is analogous to that in Cahn's CPWT phase diagram [22]: η_{GB}^{eq} is analogous to Γ_B^{eq} which also has two coexistant equilibrium values for which the difference vanishes at a critical point. This similarity is inevitable because KWC and CPWT have isomorphic free energy functionals (Eqs. 2.8 and 2.9). However, in this model, the interface term $s\Delta\theta g(\eta_{\mathrm{GB}})$ is derived from a GB functional in Eq. 2.4.

Of the three transition modalities depicted in Fig. 2-5, the two spinodals pertain for metastable behavior at $T > T_m$. The higher of the two, $\Delta\theta_U(T)$, is the stability limit for ordered complexions. At $T > T_m$, a GB with $\Delta\theta > \Delta\theta_U$ will spontaneously disorder as quickly as interfacial kinetics permit—it cannot be further superheated. However, for GBs that have a metastable η_{GB}^{Ord} structure ($\Delta\theta < \Delta\theta_U$) could be superheated; solids containing only such GBs thus could be superheated metastably until a nucleation event occurs. Simulations of superheated Si and metallic grain boundaries showed that GBs directly disordered, and the liquid band grew as fast as interfacial kinetics allowed [50,51,55]. It is suggested that GBs that melted without incubation above T_m [50,51,55] would completely premelt as $T \to T_m$. This is because the same simulations showed that melting at low-energy free-surface orientations *did* require incubation at $T > T_m$, which implied the GBs' metastability.

In this model, no special misorientations are associated with cusps in $\gamma_{gb}(\Delta\theta)$ (except at $\Delta\theta = 0$) that have been observed elsewhere (e.g., [149–152]). Including multiple cusps in a KWC model would be possible through modification of the $|\nabla\theta|$ term in Eq. 2.3 with a function of $|\nabla\theta|$ that has multiple minima. Furthermore, this model does not provide an upper bound for misorientation—$\Delta\theta$ can be at most 2π in crystals with the lowest possible symmetry, and this upper bound will be smaller in most systems of interest. Therefore in practice, complexion diagrams will be restricted to lower subregions of Fig. 2-5 and the curve of first-order transitions may intersect—and thus terminate without a second-order transition —at the maximum allowed misorientation.

Polycrystalline materials will typically contain grain boundaries with all possi-

ble misorientations; therefore, at a fixed temperature, observable complexions would range over those which appear along a constant temperature (vertical) line in Fig. 2-5. However, microstructural evolution or texture affect the distribution of GB misorientations, and the frequency of observed complexions may not be directly related to their relative line intersection lengths. The behavior of a fixed polycrystalline microstructure may have a complex temperature relationship: some grain boundaries may have continuous or first-order premelting behavior until the grain boundary is replaced with a perfectly wetting liquid at $T = T_m$; others could remain ordered without nucleating a more disordered complexion as $T \rightarrow T_m$. The ranges of misorientations for which these behaviors are possible are separated by the values of $\Delta\theta$ where the curves for the two spinodes and the first-order transitions intersect the line $T = T_m$.

Specific complexion diagrams can be obtained numerically for particular models of free energy, Δf, and misorientation gradient penalty. The manner through which Δf and $g(\eta)$ combine to create a spectrum of diagrams were explored by developing a test model that depends on a ratio $q/(2p-2)$ relating the steepness of the misorientation penalty (via q in Eq. 2.34) to Δf (via p in Eq. 2.22). This generic model could also serve as a foundation upon which material-specific models for p and q could be tuned by comparing model predictions to empirical observation. However, such a tuning scheme would not serve as an independent verification of this model. Preferably, those continuum-model parameters which cannot be obtained through direct observation could be obtained through coarse-graining of atomistic simulation data.

2.5.1 Relation Between Model Predictions and Atomistic Simulations

Some corroborating evidence for the qualitative behavior of the model presented in this chapter can be obtained by comparison to published atomistic grain boundary simulations. Molecular dynamics simulations of metallic grain boundaries have demonstrated that grain boundary cores tend to disorder with increasing temperature

and that this tendency is increased for larger misorientations [150, 153]. Considering that a fixed $\Delta\theta$ requires that a grain boundary system must promote collective bond distortion, this trend could be rationalized through the thermodynamic consideration of entropic and enthalpic differences between ordered grain boundary cores with overlapping elastic fields and disordered cores with reduced elastic energy densities. Such considerations are consistent with the form of Eq. 2.3; in fact, it is possible to modify $g(\eta)$ so that γ_{GB} is the Read-Schockley form derived from interacting dislocations at small misorientations [134].

Molecular dynamic determination of bulk melting temperature is troublesome and incurs errors of at least a few percent [50, 51, 55]. Consequently, molecular dynamic confirmation of grain boundary transitions, such as premelting, is difficult and more uncertain. Structural fluctuations and stochastic grain boundary migration can be misinterpreted as evidence of a complexion transition. There are no estimates of the values for nucleation barriers to complexion transitions which could be used to estimate the duration of an MD simulation which might produce them. Furthermore, characterization is hindered by the absence of a standard measure for local disorder, such as η. Moreover, the complexion diagram's sensitivity to model parameters (such as p and q in Eqs. 2.34 and 2.22) may indicate a similar sensitivity of atomistic simulations to models of interatomic potentials. Systems that are likely candidates for complexion transitions (i.e., those that form glasses, have complex grain boundary structures, or highly-populated unit cells) are probably the most difficult to subject to reliable MD simulations.

Nevertheless, extant simulations do provide evidence that premelting occurs for higher-energy GBs. Simulations on tilt boundaries have demonstrated increasing disorder and characterized divergent grain boundary widths as $T \rightarrow T_m$ [44, 45, 147]. In other simulations, tilt and twist boundaries exhibited wide disordered structures at $0.98T_m$, but the T_m asymptotic behavior was not characterized [60, 154, 155].

In Si simulations [49, 156], low-angle twist boundaries (about [111]) remained narrow and crystalline at $0.95T_m$, but higher-energy density GBs show increasing disorder with T. In several cases high-angle twist boundaries were found to have amorphous

GB structures even at 0K [49, 156]. Recently, von Alfthan, Kaski and Sutton et al. re-examined the structures of Si twist GBs with improved simulation methods [140, 157]. They found that the previously seen disordered GB structures at 0K are indeed simulation artifacts due to insufficient sampling in GB structural configurations. However, their simulations do confirm again the existence of GB premelting in Si as $T \rightarrow T_m$ [158]. Among the three (001) twist GBs they studied, i.e. $\Sigma 25$, $\Sigma 5$ and $\Sigma 29$ that correspond to twist angles of 16°, 37° and 44°, continuous premelting was found for high-angle GBs ($\Sigma 5$ and $\Sigma 29$), which starts at 0.7-0.8T_m, and no melting occurs to the $\Sigma 25$ GB. No evidence of a first-order GB transition was obtained in their simulations. The reason could be that GBs with intermediate energies that exhibit first-order transition behavior were not sampled in their simulations, or that (001) twist GBs in pure Si have a complexion diagram similar to Fig. 2-7 and the first-order complexion transition is thus absent.

Molecular dynamics evidence for first-order grain boundary transitions is often indirect. In one MD study, high-energy GBs clearly disordered below T_m; at T_m, low $\Delta\theta$ remained structurally *stable*, and intermediate cases exhibited ranges of disorder [147]. Several MD and Monte Carlo studies found two or more GB metastable configurations for the same boundary at fixed temperature [52, 57–61].

Other indirect evidence is available from simulations of temperature-dependent grain boundary properties. Simulations of GB migration and diffusion in fcc metals suggest discontinuous reductions in activation energies at (0.6–0.8)T_m and may indicate a first-order GB transition [62–64]. Futhermore, atomic displacements within the GB core become more isotropic above the transition which is consistent with a more disordered GB structure [63, 64].

2.5.2 Relation Between Model Predictions and Experimental Observations

Interpretation of reported experimental results such as TEM evidence is also nontrivial. First, absence of observation does not imply absence of the phenomenon. In

experiments and simulations, there may be a bias towards special boundaries that have higher symmetry and lower energy than random boundaries and towards materials that do not easily form glass. As suggested by Fig. 2-8, transitions tend not to occur at the lower end of the grain boundary energy spectrum. Such a bias would probably under-represent observations of complexion transitions. Second, presumptions that premelting must result in a completely amorphous core may have lead researchers to neglect observations of partially ordered GBs. The structural difference between ordered and disordered GBs could be subtler and harder to discern than expected. To be observed in the best conditions, a disordered region must be several atomic layers thick.

However, an *in situ* TEM study of a Bi tilt boundary near T_m showed the dihedral angle, ψ, where a GB intersects solid/liquid interface, decreased with increasing $\Delta\theta$, and ψ dropped discontinuously to zero at $\Delta\theta = 15°$ [43]. One interpretation is that the GB energy was discontinuous at $\Delta\theta = 15°$, but this is puzzling for complete equilibrium. It may be indicative of a first-order transition allowing coexistence of metastable GB complexions.

Because free-surface premelting is a similar, and a perhaps related, phenomenon, it is instructive to consider the requirements for its observation at the surfaces of pure metals. Premelting of various metallic surfaces has been observed with melted layer widths approximately 5 monolayers at $T_m - T = 1°$ characterized by $\ln[T_m/(T_m - T)]$ [32,33]. That premelting is only observed in TEM observations of Al GBs above $0.999\,T_m$ [42] is qualitatively consistent with surface premelting observations. Metallic free surfaces exhibit about one monolayer of disorder that develops more than 10° below T_m [32,33].

At 0.5–$0.9T_m$, some metallic free surfaces can have roughening transitions [30] where ledges and kinks disorder. For grain boundaries well below T_m, comparable phenomena are that the population of point defects and dislocations in the core's vicinity increases with temperature. TEM observations showed that secondary GB dislocations in pure Al persisted to $0.96\,T_m$ [42,159]. Observations show that particle rotations which are driven by grain boundary anisotropy persist up to 0.96 and 0.99

T_m in Cu and Ag [160, 161]. Both observations indicate that some boundary-core coherency remains even though they may premelt closer to T_m. It is also known that roughening (also known as defaceting) transitions of faceted GBs in pure metals occur at 0.6–0.9T_m [93, 162] suggesting that the resultant stable general GBs are more disordered than the lower-temperature faceted GBs.

Our model suggests that it may be possible to superheat the metastable η_{GB}^{Ord}–solution above T_m in Fig. 2-5 for grain boundaries with $\Delta\theta < \Delta\theta_U$. This can be compared to melting at free surfaces, at which detectable superheating is rare. In rare cases, for example Pb(111), Al(111) and Ge(111), surfaces exhibit some disorder but do not fully premelt [29, 163, 164]. Moreover, not all Pb surfaces are wet by the pure liquid at T_m [28]. Recently it was shown that these highly ordered surfaces could be flash heated to 1.15T_m without fully disordering—suggesting first-order transition behavior [165, 166].

Thus, it is suggested that the general predictions of GB disorder made by the diffuse-interface analyses, including the possibility of a first-order transition in boundary structures, is not inconsistent with published TEM and simulation evidence. Verification of the existence of partially ordered grain boundaries and their transitions, or a demonstration of their absence, constitutes a challenge to the TEM and simulation communities.

If metallic systems are not ideal for the observation of GB structural transitions, which systems would be better? GB disorder is promoted in materials where the molar free energy difference between crystalline and liquid states is small. Systems with short-range order in their liquid phase, as with liquid silicates, will have larger atomic complexes which participate in disorder, so disordered boundary cores will be widened and thus easier to see. The gradient coefficient s should probably increase with the length scale of short-range order. Increased energy barrier height in Δf permits greater undercooling for stablized disorder GBs (as in Fig. 2-6) and premelted GB films should occur over a wider temperature range in good glass formers. Polymeric systems, particularly semi-crystalline polymers, polycrystalline metals that readily form bulk-metallic glasses, and liquid crystals are candidates.

In recent years, colloidal crystal systems have been increasingly used as an alternative "simulation" approach to computer modelling for studying atomistic processes in real materials. Individual particles in colloidal crystals can be imaged by (scanning) confocal microscopes, which allows the structures of crystal defects such as GBs and dislocations and their time-dependent evolutions to be resolved with high resolution. Compared to the current capability of atomistic simulations, A colloidal crystal system can often contain more particles and allow observations at larger time-scales, thus promising significant advances in our understanding of atomistic mechanisms in microstructural evolutions. Indeed, direct imaging of premelted structures near GBs and dislocations in colloidal crystals has been recently reported [167], which serves as first direct evidence of defect-mediated premelting. Other examples include visualization of dislocation dynamics [168] and crystal sublimation dynamics [169].

Compared to pure systems, more abundant evidence of GB structural transitions exists for multicomponent systems. Nanometer thick, equilibrium intergranular glassy films comprise the GBs in various ceramics [2, 65–67, 78]. Such films have thicknesses that depend on the additive chemical potential [65–67, 69, 78], and exhibit thermodynamic stability [2, 65, 67, 69, 78, 81]. In addition, considerable evidence from kinetic behavior points to the existence of GB transitions yielding similar GB structures in metallic alloys [170–173]. However, GB disordering in these cases is usually connected with significant changes in GB compositions [2, 68, 69, 78–80]. A complete thermodynamic analysis of GB transitions in multicomponent systems must be able to treat simultaneous changes of GB structural order and segregation. In the next chapter an extension of the diffuse-interface analysis to binary systems will be presented.

2.6 Conclusions

The KWC diffuse-interface model for grain boundaries in systems of fixed stoichiometry predicts disorder transitions at GBs. The model predictions of disordered GB core material can be associated with the appearance of a liquid phase, and therefore this diffuse interface model can be considered a premelting theory for grain boundaries as

a function of their misorientation. The graphical construction for equilibrium grain boundary properties can be used to construct a "grain boundary complexion diagram" that predicts which of two more and less ordered grain boundary structures would be most stable for values of temperature and misorientation. The model predicts the possibility that first-order transitions between a more ordered and a less ordered grain boundary structure can occur with increasing temperature below the melting temperature. The types of grain boundary structures and the temperature behavior for transitions between the structures will directly affect macroscopic material properties, such as creep and grain boundary migration, for polycrystals. The features on the GB complexion diagram depend on the homogeneous free energy density for the crystalline and non-crystalline fixed stoichiometric material and on models for energy penalties for inhomogenous distributions of disorder and crystallographic orientation. The diagram's possible features are: 1) the critcal point's location $(T_{\text{crit}}/T_m, \Delta\theta_{\text{crit}})$; 2) a spinodal curve for the upper stability limits for the more disordered structure; 3) a spinodal curve for the lower stability limits for the less disordered structure; 4) the upper limit to grain boundary misorientations with equilibrium structures that do not perfectly wet the boundary at T_m. Not all features will appear on a given complexion diagram, as illustrated and predicted from a quantitative measure $q/(2p-2)$ of power law approximations to the free energy density (q) and the disorder dependence of gradient coefficient function for misorientation (p).

Along with premelting behavior, extensions of the model above the melting point show that, when the equilibrium structure perfectly wets its grain boundary, no barrier to melting occurs at $T \geq T_m$. However, low misorientation boundaries in some material systems can have non-perfectly wetting metastable structures that could be superheated in the absence of a nucleation event.

Some experimental observations and atomistic simulations have shown qualitative behaviors that are consistent with the model's predictions. A subset of these simulations models have some quantitative measure that could be used to calibrate model parameters. However, the absence of standard methods to characterize a continuum of disorder from collections of atomic positions from simulation data or from

diffraction data make direct model verification difficult. Characterization of continous spatial distributions of order is a challenge for materials simulators, theorists, and experimentalists.

Chapter 3

Grain Boundary Transitions in Binary Systems

3.1 Introduction

The existence of GB premelting (onset of localized sub-solidus or sub-eutectic structural disorder) was suggested as early as 1952 [174], and has been investigated numerically (lattice models [175], molecular dynamics [147], and Monte-Carlo simulations [176]). While indirect observations support the existence of GB premelting [39, 43], direct experimental observation in pure systems is rare [167]. In comparison, observations of GB structural disordering in alloys are less rare, which has been reported for metals [75, 76, 177], and ceramics, e.g., the intergranular glassy films introduced in Chapter 1 [70, 82]). The disordering is usually accompanied by changes in equilibrium GB segregation, and the two aspects appear to promote each other. Modeling this cooperative phenomenon requires theories beyond those for pure systems.

However, models that treat simultaneous GB premelting and segregation are rare and system specific [175, 177]. Developed along a separate line from models of GB premelting, solute segregation transitions at GBs [178, 179] and surfaces [180] were theoretically studied previously. The effect of structural inhomogeneity on solute segregation behavior was accounted for in these models by considering the excess en-

ergy arising from solute-defect interaction, but the forms of the interaction potentials were invariably assumed to be independent of segregation strength, which neglects any possible coupled changes in defect structures. A unified theoretical framework for understanding cooperative GB disordering and segregation transitions remains to be developed. In this chapter, a generalized diffuse-interface thermodynamic model is presented for cooperative structural and chemical grain boundary transitions in binary alloys. The model is a natural extension of the diffuse-interface analysis for systems of fixed stoichiometry presented in the last chapter. The spatial variation of the stoichiometry of a binary system is permitted besides crystallinity and crystallographic orientation. A similar, but more complicated graphical construction was developed to analyze the temperature and matrix composition dependence of GB behavior and the existence of GB transitions in binary eutectic systems. Based on the analysis, it is proposed that intergranular amorphous films are an high temperature GB complexion resulting from a coupled prewetting/premelting transition.

3.2 The KWC Diffuse-Interface Model for Binary Systems

The KWC model is applied to binary systems where the local concentration is allowed to vary in space. In addition to the crystallographic orientation and crystallinity variables, a third field variable, $c(x)$, is used to describe local concentration variation for a binary system. As in the last chapter, focus is given to planar, symmetric GBs. The total excess free energy of a GB is modeled as as a one-dimensional functional of the three fields:

$$F[c,\eta,\theta;T] = \int_L \left[\Delta f(c,\eta,T) + \frac{\kappa^2}{2}\left(\frac{dc}{dx}\right)^2 + \frac{\nu^2}{2}\left(\frac{d\eta}{dx}\right)^2 + sg(\eta)\left|\frac{d\theta}{dx}\right| \right] dx \tag{3.1}$$

where f is the homogeneous free energy density, and Δf is the excess volumetric free energy density with respect to the perfectly crystalline state ($\eta = 1$) at a fixed bulk composition c_∞:

$$\Delta f = f(c, \eta, T) - f(c_\infty, \eta = 1, T) - \frac{\partial f}{\partial c}(c_\infty, \eta = 1, T)(c - c_\infty) \tag{3.2}$$

The volume fraction of material affected by the GB is assumed to be small enough so that c_∞ is a constant not affected by solute adsorption (i.e., the bulk is a reservoir at fixed chemical potential $\mu(c_\infty)$).

The gradient coefficients for c, η, and θ, i.e. ($\kappa^2/2$, $\nu^2/2$, and s), are treated as constants in this model. As in the single-component model, the prefactor $g(\eta)$ is modeled as a monotonically increasing function of η to reflect the coupling between structural order and orientation gradient, and g is assumed to be independent of concentration. $g(\eta) = \eta^2$ is used for numerical calculations in this chapter. Discussions on the effect of different choices of $g(\eta)$ on GB transition behavior can be found in the last chapter.

The boundary conditions for a solitary GB in a single-phase binary alloy are

$$\begin{aligned} c(x = \pm\infty) &= c_\infty \qquad \eta(x = \pm\infty) = 1 \\ \theta(x = -\infty) &= \theta_- \qquad \theta(x = +\infty) = \theta_+ \end{aligned} \tag{3.3}$$

With consideration similar to the single-component case in the last chapter [143], one finds that under the assumption that $\eta(x)$ has only one local minimum at the GB core located at $x = 0$, the equilibrium solution of $\theta(x)$ concentrates all its change at the GB center at equilibrium,

$$\theta^{\text{eq}}(x) = \theta_- + \Delta\theta\, H(x) = \begin{cases} \theta_- & x < 0 \\ \theta_+ & x > 0 \end{cases} \tag{3.4}$$

where $H(x)$ is a unit step function, $\Delta\theta \equiv \theta_+ - \theta_-$ and $\Delta\theta > 0$ is assumed here.

Substituting $\theta^{eq}(x)$ (i.e., $d\theta^{\mathrm{eq}}/dx = \Delta\theta\delta(x)$) into Eq. 3.1 yields

$$F[c(x),\eta(x);\theta^{\mathrm{eq}},T,\eta_{\mathrm{GB}}] = s\Delta\theta g(\eta_{\mathrm{GB}}) + 2\int_0^{+\infty}[\Delta f(c,\eta,T) + \frac{\kappa^2}{2}\left(\frac{dc}{dx}\right)^2 + \frac{\nu^2}{2}\left(\frac{d\eta}{dx}\right)^2]dx$$

where $\eta_{\mathrm{GB}} \equiv \eta(x=0)$ is the local structural disorder at the GB core. The GB excess energy expression in Eq. 3.5 becomes a functional of only $c(x)$ and $\eta(x)$. The orientation gradient across the boundary is captured by the misorientation parameter $\Delta\theta$. The solutions of $c(x)$ and $\eta(x)$ for a GB at equilibrium are governed by the Euler equations of Eq. 3.5

$$\kappa^2\frac{d^2c}{dx^2} = \frac{\partial\Delta f}{\partial c} \tag{3.5}$$

$$\nu^2\frac{d^2\eta}{dx^2} = \frac{\partial\Delta f}{\partial\eta} \tag{3.6}$$

with the boundary conditions

$$\begin{aligned}\left.\frac{dc}{dx}\right|_{x=0} &= 0\\ \nu^2\left.\frac{d\eta}{dx}\right|_{x=0} &= s\Delta\theta g'(\eta)\\ \left.\frac{dc}{dx}\right|_{x=\infty} &= 0\\ \left.\frac{d\eta}{dx}\right|_{x=\infty} &= 0\end{aligned} \tag{3.7}$$

3.3 Graphical Construction

A graphic approach to identify solutions of the Euler equations, 3.5 and 3.6, will be described in this section.

The first integral of the Euler equations [144] can be obtained by adding Eq. 3.5$\times dc/dx$ and Eq. 3.6$\times d\eta/dx$ and then integrating once, which yields

$$\frac{\kappa^2}{2}\left(\frac{\partial c}{\partial x}\right)^2 + \frac{\nu^2}{2}\left(\frac{\partial\eta}{\partial x}\right)^2 = \Delta f(c,\eta,T) \tag{3.8}$$

The integration constant vanishes in Eq. 3.8 because dc/dx, $d\eta/dx$ and Δf vanish as $x \to \infty$.

Because the only minimum of $\eta(x)$ is at the GB core, $\eta(x=0) = \eta_{GB}$, $d\eta/dx > 0$ holds and thus η increases monotonically with x in $x > 0$ (or $d\eta/dx < 0$ in $x < 0$). This allows one to treat c as a function of η: $c(x) = c(\eta(x))$. Similarly x can be treated as a function of η. The differential of $x = x(\eta)$ can be derived from Eq. 3.8

$$dx = \sqrt{\frac{\nu^2 + \kappa^2 \left(\frac{dc}{d\eta}\right)^2}{2\Delta f(c,\eta,T)}} d\eta \qquad \text{for x>0 and/or d}\eta > 0 \tag{3.9}$$

Substituting Eqs. 3.8 and 3.9 into Eq. 3.5 results in a change of variable from x to η

$$F[c(\eta); \eta_{GB}, \Delta\theta, T] = s\Delta\theta g(\eta_{GB}) + 2\int_{\eta_{GB}}^{1} P(\eta, c(\eta), dc/d\eta) d\eta \tag{3.10}$$

where the integrand P is

$$P(\eta, c(\eta), dc/d\eta) = \sqrt{2\Delta f(c,\eta)\left[\nu^2 + \kappa^2 \left(\frac{dc}{d\eta}\right)^2\right]} \tag{3.11}$$

The GB excess energy expression becomes a functional of $c(\eta)$ only. At equilibrium a GB should have its free energy minimized against $c(\eta)$ and the GB crystallinity η_{GB}, i.e., F should have a vanishing first variation with a fixed end-point ($\eta = 1$, $c(\eta = 1) = c_\infty$) and a free end-point (η_{GB},$c(\eta_{GB}) = c_{GB}$)

$$\begin{aligned} \delta F = 0 = & 2\int_{\eta_{GB}}^{1} \left[\frac{\partial P}{\partial c} - \frac{\partial}{\partial \eta}\left(\frac{\partial P}{\partial \frac{dc}{d\eta}}\right)\right] \delta c d\eta \\ & + \left[s\Delta\theta g'(\eta) - 2P\right]\Big|_{\eta_{GB}, c_{GB}} \delta\eta_{GB} \\ & - 2\kappa^2 \sqrt{\frac{2\Delta f(c,\eta)}{\nu^2 + \kappa^2(\frac{dc}{d\eta})^2}} \frac{dc}{d\eta}\Bigg|_{\eta_{GB}, c_{GB}} \delta c_{GB} \end{aligned} \tag{3.12}$$

which produces the Euler equation

$$2\kappa^2\nu^2\Delta f\frac{d^2c}{d\eta^2}+\left[\nu^2+\kappa^2\left(\frac{dc}{d\eta}\right)^2\right]\left(\kappa^2\frac{\partial\Delta f}{\partial\eta}\frac{dc}{d\eta}-\nu^2\frac{\partial\Delta f}{\partial c}\right)=0 \tag{3.13}$$

and the boundary conditions at the GB core

$$\left.\frac{dc}{d\eta}\right|_{\eta=\eta_{\mathrm{GB}}}=0 \tag{3.14}$$

$$\frac{s\Delta\theta}{2}g'(\eta_{\mathrm{GB}})=\sqrt{2\nu^2\Delta f(c_{\mathrm{GB}},\eta_{\mathrm{GB}})} \tag{3.15}$$

Eqs. 3.14 and 3.15 ensure that F in Eq. 3.12 is minimized against variations in GB concentration, c_{GB}, and GB crystallinity, η_{GB}, respectively. Eq. 3.15 is similar to the boundary condition in the single-component model, Eq. 2.19, and they have analogous physical implication.

A graphical construction for finding GB solutions of Eqs. 3.13–3.15 is presented below. A solution to the Euler equation Eq. 3.13 without the restriction of the boundary conditions Eqs. 3.14 and 3.15 is uniquely determined by its boundary values, (η_{GB}, c_{GB}). Any point on the GB composition–crystallinity plane (viz. Fig. 3-1(a)) represents an energy-extremizing GB state among GBs that have the same boundary-core concentration and crystallinity values, (c_{GB},η_{GB}).

One first seeks solutions to Eq. 3.13 that satisfy only one boundary condition, Eq. 3.14. A family of such solutions will be produced for all $\eta_{\mathrm{GB}}\in(0,1)$, as illustrated by the thin solid curves in Fig. 3-1(a). The end-points (η_{GB},c_{GB}) of all these solutions form a continuous curve in the GB composition–crystallinity plane, which is called $\mathcal{C}_{PDE}$, Fig. 3-1(a). Physically, solutions on $\mathcal{C}_{PDE}$ represent GB states whose energies are extremized with respect to GB concentration, c_{GB}, but not to GB crystallinity, η_{GB}. Locating $\mathcal{C}_{PDE}$ on the c_{GB}–η_{GB} plane requires (numerically) solving the differential equation Eq. 3.13.

Next, solutions that satisfy the boundary condition Eq. 3.15 alone produce another curve, $\mathcal{C}_{LS}$, on the c_{GB}–η_{GB} plane, which represent the zero level set curve of the function $\sqrt{2\nu^2\Delta f(\eta_{\mathrm{GB}},c_{\mathrm{GB}},T)}-(s\Delta\theta/2)g'(\eta_{\mathrm{GB}})$. The excess energy of any GB state

on $\mathcal{C}_{LS}$ is extremized with respect to η_{GB}, but not to c_{GB}. Analogous to the graphic analysis for a single-component system, $\mathcal{C}_{LS}$ can be viewed as the intersection of two surfaces. One surface, $\sqrt{2\nu^2\Delta f(\eta_{\mathrm{GB}}, c_{\mathrm{GB}}, T)}$ is related to the volumetric free energy density of the binary system. The other surface, $(s\Delta\theta/2)g'(\eta_{\mathrm{GB}})$, represents the misorientation–crystallinity coupling. Fig. 3-1(b) illustrates the intersection of the two surfaces and its projection onto the c_{GB}–η_{GB} plane which produces $\mathcal{C}_{LS}$.

Finally, because the equilibrium GB state, characterized by $(\eta_{\mathrm{GB}}^{eq}, c_{\mathrm{GB}}^{eq})$, satisfies both boundary conditions Eqs. 3.14 and 3.15, it is graphically determined by the intersection of $\mathcal{C}_{PDE}$ and $\mathcal{C}_{LS}$, as shown in Fig. 3-1(c).

3.4 Coupled Grain Boundary Premelting/Prewetting Transitions

3.4.1 A Modified Regular Solution Model of Eutectic Systems

Because most intergranular glassy films were found in materials which exhibit eutectic-type phase diagrams, GB transitions in a model eutectic binary system were studied.

For simplicity, the system's two pure components are assumed to have identical thermodynamic properties and thus produce a symmetric eutectic diagram. A *modified* regular solution formulation is used for the volumetric free energy density expression

$$\begin{aligned} f(c,\eta,T) =& \frac{1}{\bar{v}}\{f_A(\eta,T)(1-c) + f_B(\eta,T)c + kT[c\ln c + (1-c)\ln(1-c)] \\ &+ W(\eta)c(1-c)\} \end{aligned} \tag{3.16}$$

where $\bar{v}$ is atomic volume and k is the Boltzmann constant. $W(\eta)$ is the regular solution coefficient and will be described later. $f_A(\eta,T) = f_B(\eta,T) \equiv f(\eta,T)$ are free

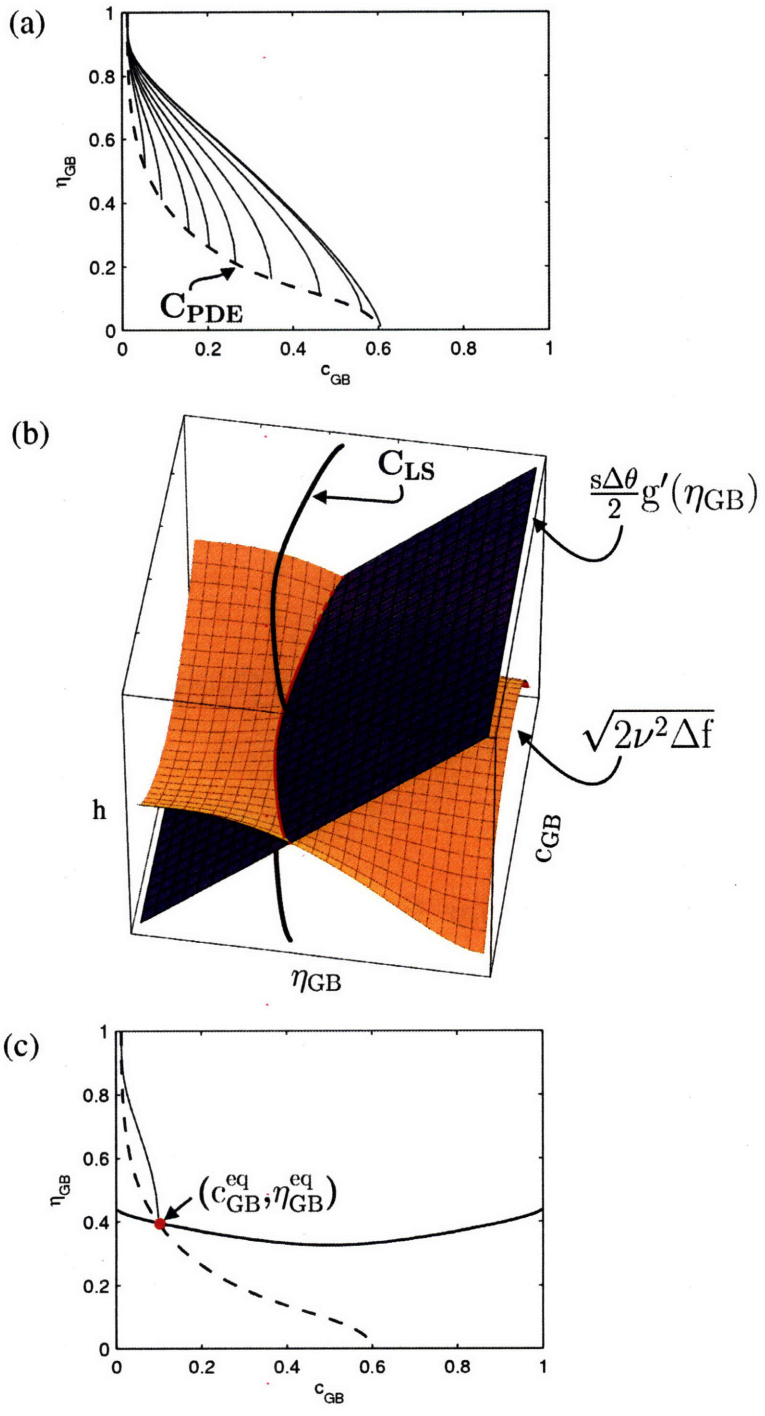

Figure 3-1: Schematic illustration of the graphic construction method for determining equilibrium GB state(s). (a) The end points of solutions to Eqs. 3.13 and 3.14 (thin solid lines) form $\mathcal{C}_{PDE}$ (thick dashed line); (b) $\mathcal{C}_{LS}$ is produced by the intersection between surfaces $h = \sqrt{2\nu^2\Delta f(\eta_{GB}, c_{GB}, T)}$ and $h = (s\Delta\theta/2)g'(\eta_{GB})$. (c) the Intersection between $\mathcal{C}_{PDE}$ (dashed) and $\mathcal{C}_{LS}$ (solid) determines the equilibrium GB crystallinity (η^{eq}_{GB}) and composition (c^{eq}_{GB}). Also shown is the equilibrium solution $c^{eq}(\eta)$ (thin solid).

energies of pure components per atom specified as

$$f(\eta, T) = f^L(T) + \frac{a^2}{2}\eta^2(1-\eta)^2 + \frac{\Delta h_m}{T_m}(T_m - T)p(\eta) \tag{3.17}$$

where f^L is the free energy of liquid state, T_m the melting temperature of pure components, and H_m the melting enthalpy. The other terms on the right hand side of Eq. 3.17 specify the crystallinity dependence of the free energies of pure components. The free energy difference between crystalline and liquid states is assumed to be $\Delta h_m(1-T/T_m)$. The function $p(\eta)$ is a sigmoidal interpolation between $p(0) = 1$ and $p(1) = 0$,

$$p(\eta) = (1-\eta)^3(1+3\eta+6\eta^2) \tag{3.18}$$

The a^2-term in $f(\eta, T)$ represents the energy barrier between bulk solid and liquid phases – it has a maximum at η=1/2. The parameter a^2 scales with the barrier height and is related to the solid/liquid interfacial energy of pure components, γ_{sl}, at T_m

$$\gamma_{sl}(T_m) = \frac{a\nu}{6} \tag{3.19}$$

The regular solution coefficient W in Eq. 3.16 is modelled as a function of η to allow the two components to have varying degrees of miscibility depending on structural order. $W(\eta) = W_0 p(1-\eta)$ with $W_0 > 0$ is used here, which is a decreasing function of η. $W(\eta)$ thus produces a positive regular solution constant W_0 for crystalline states and results in two immiscible, A-rich and B-rich solid phases, α and β. $W(\eta)$ is 0 at $\eta = 0$, i.e. the two components form an ideal liquid solution. Therefore our model depicts a binary system whose two components are more miscible in the liquid phase than in the crystals, a character that often gives rise to eutectic-type phase diagrams. Fig. 3-2 illustrates a schematic volumetric free energy surface based on Eq. 3.16.

In our calculations all variables and parameters are non-dimensionalized in the following fashion: temperatures are scaled by T_m, energies by kT_m, lengths by $\bar{v}^{1/3}$, ν and κ by $kT_m/\bar{v}^{1/6}$, and s by $kT_m/\bar{v}^{2/3}$. $\Delta\theta$ is rescaled by multiplying the dimensionless value of s. $\Delta h_m = a^2 = 1.386$ and $W_0 = 5.883$ are chosen in all calculations

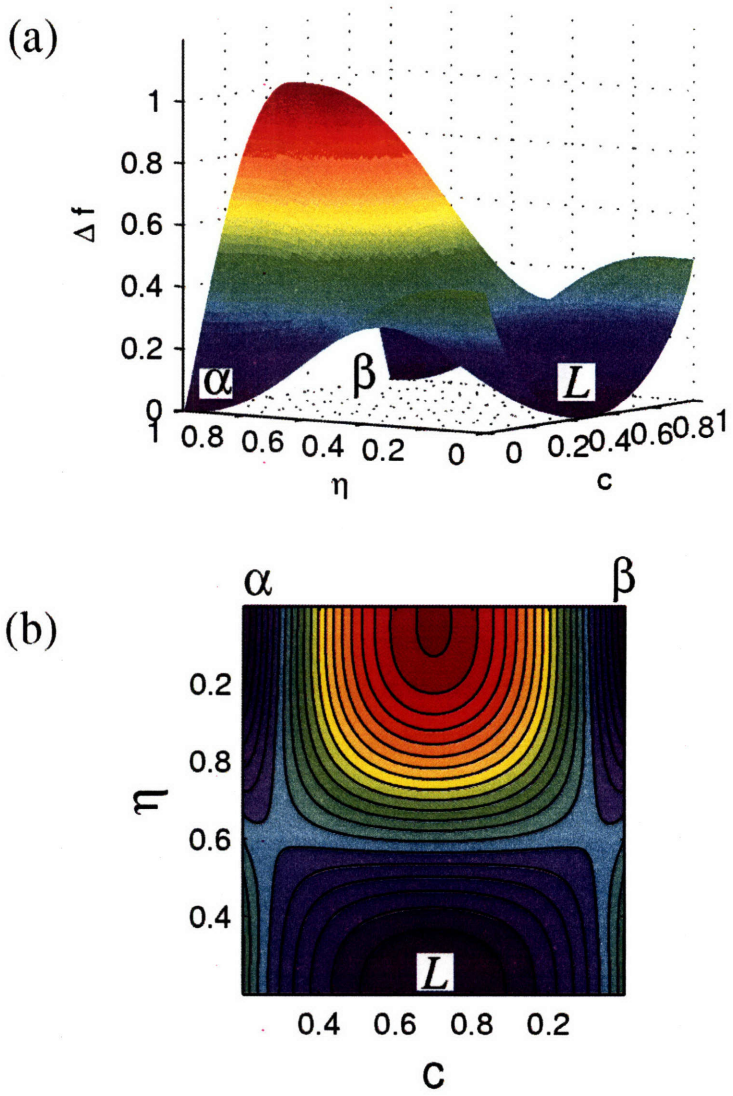

Figure 3-2: Graphic representation of the volumetric free energy density given in Eq. 3.16. (a) 3D surface plot; (b) contour plot. The three local minima on the energy surface correspond to three (meta)stable phases: A-rich α and B-rich β crystalline phases and the liquid phase L.

to produce a eutectic temperature $T_e = 2/3T_m$. Dimensionless ν is fixed at 1 for all calculations, which gives a solid/liquid interface thickness of about 4 atomic layers at T_e. The A-rich part of the bulk phase diagram is shown in Fig. 3-3.

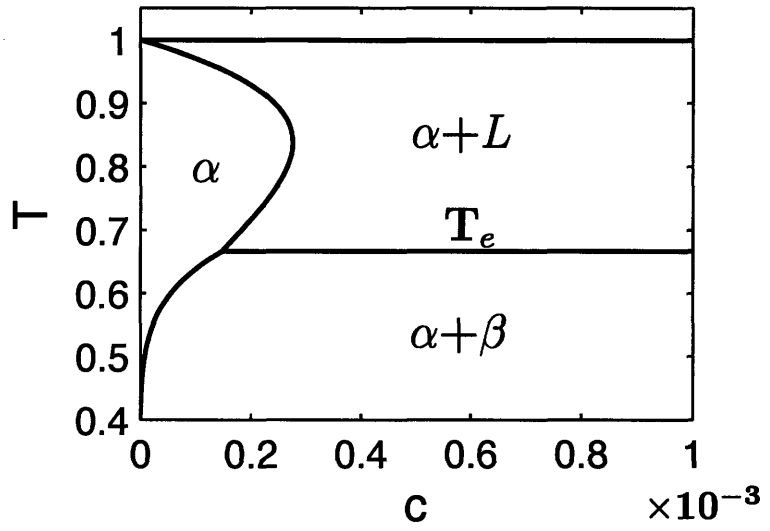

Figure 3-3: The A-rich part of the eutectic phase diagram calculated from the modified regular solution model.

3.4.2 Coupled Grain Boundary Premelting/Prewetting Transitions at Sub-Eutectic Temperatures

The solution behavior was first analyzed for an equilibrium GB in the A-rich crystalline α phase at sub-eutectic temperatures with the matrix composition c_∞ fixed at the solubility limit of component B in α. This situation applies to a system whose average concentration falls into the solid two-phase region below the eutectic point. Fig. 3-4(a) shows C_{PDE} at $T = 0.9T_e$ obtained by numerical solution to Eq. 3.13 subject to the boundary condition Eq. 3.14 for all $\eta_{\text{GB}} \in (0, 1)$. Along C_{PDE}, c_{GB} reaches the matrix concentration c_∞ at η_{GB}=1, which represents a non-equilibrated boundary state with neither structural disorder nor segregation. As η_{GB} decreases, c_{GB} tends towards the eutectic liquid composition, c_e=0.5. This is because Δf is minimized at c_e for small η_{GB} values; hence as c_{GB} nears the eutectic liquid composition, the homogeneous part of the excess energy of a largely disordered boundary is reduced. However, a high GB composition is associated with a larger concentration gradient near the boundary, which results in larger gradient energy penalty and prevents c_{GB} from choosing values that minimize Δf. Fig. 3-4(a) shows that the tendency of $c_{\text{GB}} \rightarrow c_e$ on C_{PDE} is enhanced with decreasing the concentration gradient coefficient,

κ^2. In the limit of $\kappa^2 \to 0$, the concentration gradient energy vanishes, and $\mathcal{C}_{PDE}$ is solely determined by minimizing the volumetric free energy density of the boundary core,

$$\left.\frac{\partial \Delta f}{\partial c_{\mathrm{GB}}}\right|_{c_{\mathrm{GB}},\eta_{\mathrm{GB}}} = 0 \tag{3.20}$$

i.e., $\mathcal{C}_{PDE}$ is formed by the minima of the volumetric free energy curve $\Delta f(c_{\mathrm{GB}}, \eta_{\mathrm{GB}})$ for each $\eta_{\mathrm{GB}} \in (0, 1)$. Fig. 3-4(b) illustrates that $\mathcal{C}_{PDE}$ is also temperature dependent. A larger portion of $\mathcal{C}_{PDE}$ becomes closer to c_e at higher temperatures because the excess volumetric free energy of the eutectic liquid relative to the crystalline state becomes increasingly small as $T \to T_e$. The general shape and topology of $\mathcal{C}_{PDE}$, however, remains unchanged with temperature.

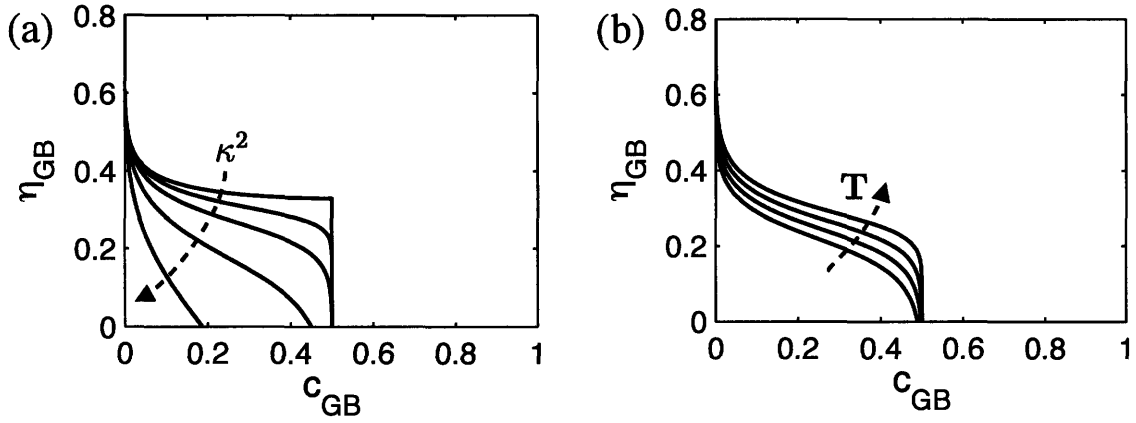

Figure 3-4: $\mathcal{C}_{PDE}$ in the eutectic system. (a) Gradient coefficient κ^2 dependence of $\mathcal{C}_{PDE}$ at $T = 0.9T_e$. The lower to upper curves correspond to κ^2=1, 0.1, 0.01, 0.001 and 0. (b) Temperature dependence of $\mathcal{C}_{PDE}$ for κ^2=0.01. The lower to upper curves correspond to T=$0.7T_e$, $0.8T_e$, $0.9T_e$ and T_e.

For graphical determination of $\mathcal{C}_{LS}$ from Eq. 3.15, function $h = \sqrt{2\nu^2 \Delta f}$ is a two-dimensional surface in the c_{GB}–η_{GB}–h three dimensional space and inherits its features from the volumetric free energy surface Δf (Fig. 3-2). For $T < T_e$, $\sqrt{2\nu^2 \Delta f}$ has two global minima at solid A-rich and B-rich phases and one local minimum at the eutectic liquid state ($\eta = 0$,$c = c_e$), as shown in Fig. 3-5(a). The other function in Eq. 3.15, $h = (s\Delta\theta/2)g'(\eta_{\mathrm{GB}})$, is graphically represented by a plane independent of c_{GB}. The plane intersects $h = 0$ at $\eta_{\mathrm{GB}} = 0$, and its slope is proportional to the

the GB misorientation $\Delta\theta$. As illustrated in Fig. 3-5(a) for a GB misorientation $\Delta\theta$=2.15, $(s\Delta\theta/2)g'(\eta_{GB})$ intersects $\sqrt{2\nu^2\Delta f}$ at relatively large η_{GB} values at large undercoolings $\Delta T \equiv T_e - T$. By projecting the intersecting curve onto the c_{GB}-η_{GB} plane, Fig. 3-5(a) shows that $\mathcal{C}_{PDE}$ and $\mathcal{C}_{LS}$ produce only one intersection which has a relatively large η_{GB}^{eq} and a small c_{GB}^{eq} close to c_∞. This solution physically represents a relatively ordered GB with low solute segregation.

As the temperature raises towards T_e, the metastable liquid minimum of $\sqrt{2\nu^2\Delta f}$ decreases to zero and approaches the $(s\Delta\theta/2)g'(\eta_{GB})$ plane from above at small η_{GB} values. For some values of material parameters and $\Delta\theta$, this results in additional intersection between the two surfaces in the lower η_{GB} region. As illustrated in Fig. 3-5(b), an isolated loop in $\mathcal{C}_{LS}$ develops near the liquid state at a small undercooling $T = 0.99T_e$. Two additional intersections of $\mathcal{C}_{PDE}$ and $\mathcal{C}_{LS}$ may be generated from the topological change of $\mathcal{C}_{LS}$. The middle intersection in Fig. 3-5(b) corresponds to an unstable solution of Eqs. 3.13–3.15, similar to the single-component case (viz. Fig. 2-3(a)). The remaining two intersections are associated with two locally metastable solutions, which are plotted in Fig. 3-6. The solution $c^{Ord}(\eta)$ corresponds to an ordered GB (η_{GB}^{Ord}) with low solute adsorption (c_{GB}^{Ord}) that also exists at lower temperatures (Fig. 3-5(a)). The other solution, $c^{Dis}(\eta)$, only appears at higher temperatures. It has a smaller GB crystallinity η_{GB}^{Dis} and a larger GB composition (c_{GB}^{eq}) close to c_e, and thus represents a more disordered GB with higher solute segregation. The real space profiles of the two solutions are given in Fig. 3-6(a)-(b), which shows that the disordered GB solution also has a larger boundary thickness.

The loop of $\mathcal{C}_{LS}$ expands when temperature rises. Fig. 3-5(c) shows that the two separate segments of $\mathcal{C}_{LS}$ may merge into a single curve at higher temperatures, e.g. $T = 0.995T_e$, while $\mathcal{C}_{LS}$ still maintains three intersections with $\mathcal{C}_{PDE}$ that represents the same types of GB solutions as for $T = 0.99T_e$. However, Fig. 3-6(a)-(b) shows that the $c^{Dis}(\eta)$ solution increases its boundary structural disorder, solute adsorption and thickness as T increases.

The physical reason for the appearance of the $c^{Dis}(\eta)$ solution at higher temperatures is that a disordered GB becomes increasingly energetically favorable as $T \to T_e$.

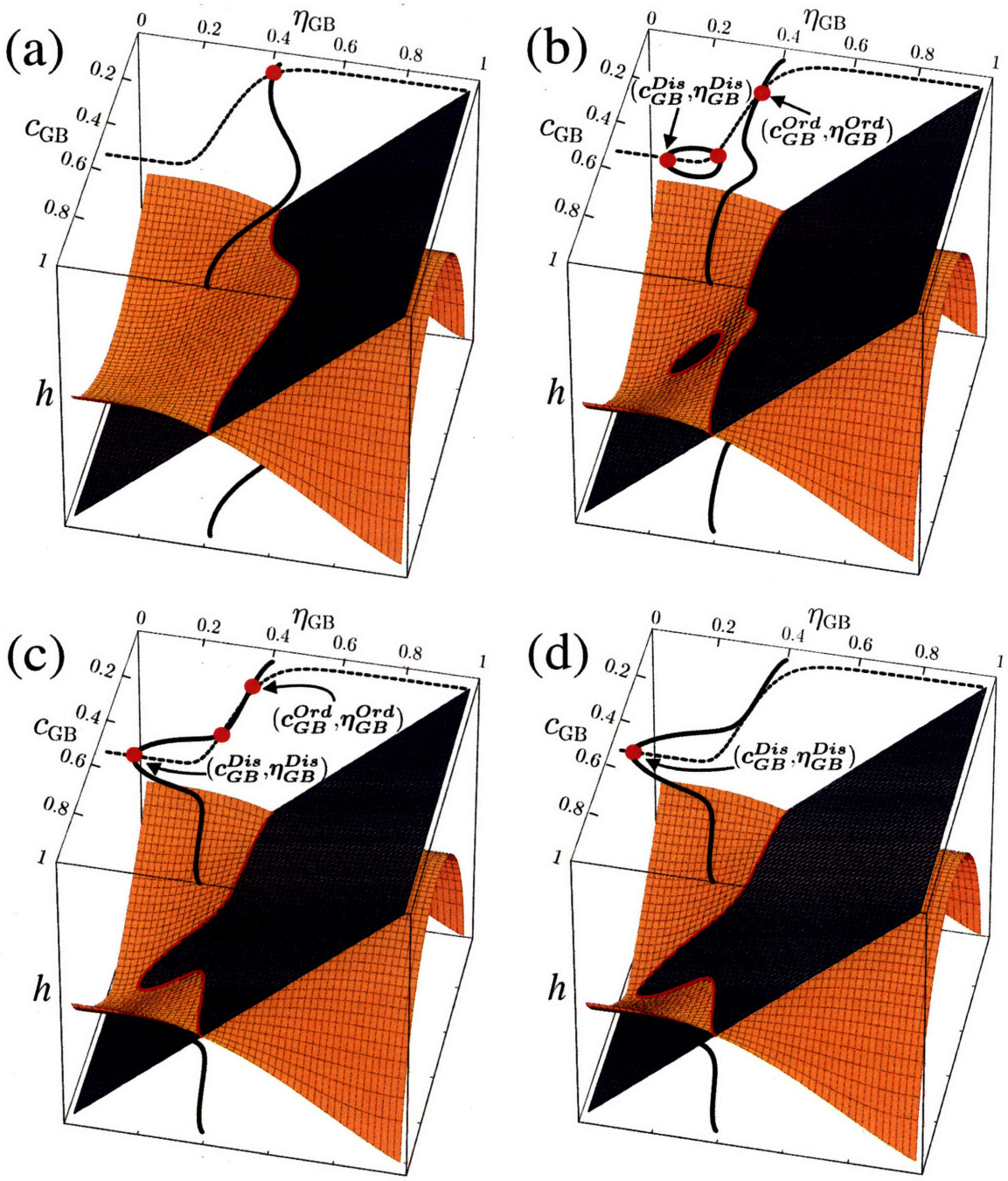

Figure 3-5: C_{LS} (solid line) generated by intersections between the $\sqrt{2\nu^2\Delta f}$ and $(s\Delta\theta/2)g'$ surfaces and its intersection(s) (highlighted by closed circle(s)) with C_{PDE} (dashed line) at (a) T=0.9T_e, (b) 0.99T_e, (c) 0.995T_e, and (d) 0.999T_e. $\Delta\theta$=2.15 and κ^2=0.001.

The GB excess free energy given by Eq. 3.5 has two parts. The non-integral part, $s\Delta\theta g(\eta_{GB})$, is the excess energy for creating a misorientation $\Delta\theta$ across a boundary of a given structural order η_{GB}. This energy term scales with the GB crystallinity

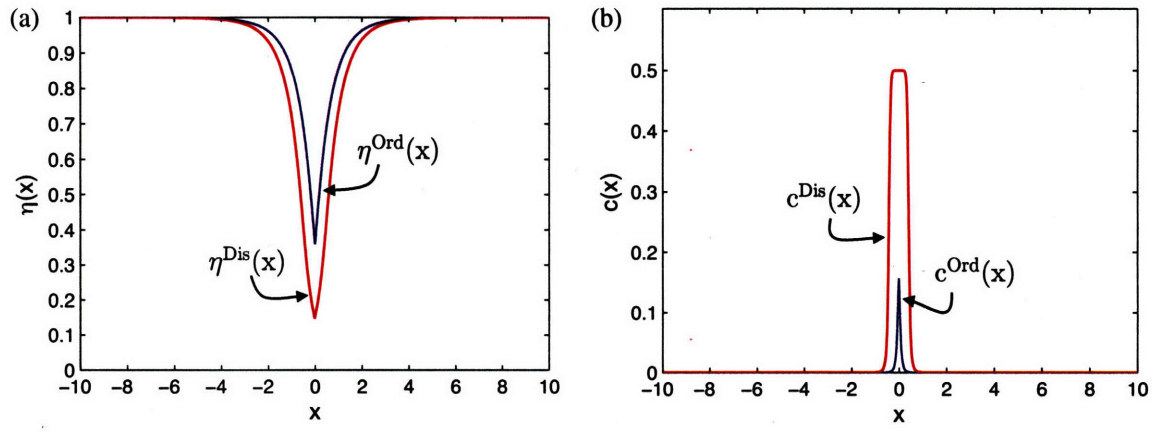

Figure 3-6: Real-space profiles of ordered ($c^{Ord}(\eta)$, blue line) and disordered GB ($c^{Dis}(\eta)$, red line) solutions for $\Delta\theta$=2.15 and T=0.99T_e. κ^2=0.001. (a) Crystallinity $\eta(x)$ profile; (b) Composition $c(x)$ profile.

and thus prefers a completely disordered, liquid-like boundary structure to reduce the misorientation penalty. However, a disordered boundary structure has larger volumetric and gradient free energies than a more ordered structure below T_e, both of which are included in the integral part of Eq. 3.5. The equilibrium boundary structure and composition are thus determined by the competition between the two parts of Eq. 3.5. A disordered GB is energetically forbidden by its very large Δf at temperatures well below T_e, but its excess energy relative to the ordered GB complexion decreases as the eutectic liquid's Δf becomes increasingly close to that of the crystalline state when $T \rightarrow T_e$. For GBs with large misorientations, it is plausible that a more disordered boundary structure becomes more stable at temperatures close enough to T_e. This is the case for $\Delta\theta$=2.15 shown in Fig. 3-7(a), which exhibits an energy cross-over of the two GB solutions at $T = 0.9897T_e$. A GB structural transition occurs at this temperature (defined as T_{PM}) and it is a first-order transition because the boundary properties such as crystallinity, composition and thickness have discontinuous changes at T_{PM}, illustrated in Fig. 3-7. One important feature of the disordered GB complexion is that its boundary core adopts a composition close to the eutectic concentration to effectively reduce the volumetric energy penalty. Therefore boundary structural disordering is coupled with simultaneous increase in solute segregation when the transition happens. In this sense, the GB transition is a coupled GB

premelting/prewetting transition, as it combines features of GB premelting discussed for single-component systems in the last chapter, and interface prewetting that was first predicted by Cahn's critical point wetting theory (CPWT) [22].

As temperature further increases towards T_e, the two intersections for the ordered and the unstable GB solutions may merge and disappear, as shown in Fig. 3-5(d) for $T = 0.999T_e$. This leaves the disordered GB as the only solution at temperatures very close to T_e. The intersection ($\eta_{\rm GB}^{Dis}$,$c_{\rm GB}^{Dis}$) approaches (0,c_e) as $T \rightarrow T_e$. Fig. 3-7(a) shows that its GB energy is equal to twice the solid-liquid interface energy γ_{sl} and the GB thickness diverges at T_e. This suggests that the disordered GB is replaced by two solid/liquid interfaces with a layer of eutectic liquid of arbitrary thickness, i.e., the boundary is perfectly wet by the equilibrium liquid at the bulk eutectic transition temperature.

3.4.3 Multiple Modalities of Grain Boundary Behavior

However, not all GBs may necessarily undergo a first-order coupled premelting/prewetting transition as described in the last section. GB behavior near $T = T_e$ can possess at least two other modalities. For GBs with relatively smaller misorientations (e.g., $\Delta\theta = 1.2$ in Fig. 3-8), the slope of the $(s\Delta\theta/2)g'(\eta_{\rm GB})$ plane in Fig. 3-5 is reduced and does not intersect the $\sqrt{2\nu^2\Delta f}$ surface at small $\eta_{\rm GB}$ to produce an isolated loop in $\mathcal{C}_{LS}$ below T_e. In this case, the relatively ordered GB remains the only solution, as illustrated in Fig. 3-8, and no GB transition happens for $T < T_e$. Different from the disordered GB resulting from the premelting/prewetting transition, the ordered GB retains finite structural order and thickness when reaching the eutectic point (Fig. 3-7), i.e., it is not perfectly wet by the eutectic liquid at T_e. However, the onset of a first-order complete wetting transition may occur at a higher temperature between T_e and T_m, which will be discussed in 3.4.4.

At the other extreme, for GBs with relatively large misorientations, $\mathcal{C}_{LS}$ may be transformed from a high $\eta_{\rm GB}$ to a low $\eta_{\rm GB}$ region without the appearance of a loop and having multiple intersections with $\mathcal{C}_{PDE}$. As shown in Fig. 3-9 for a GB of $\Delta\theta$=2.5, $\mathcal{C}_{LS}$ and $\mathcal{C}_{PDE}$ have only one intersection at all temperatures below T_e, but

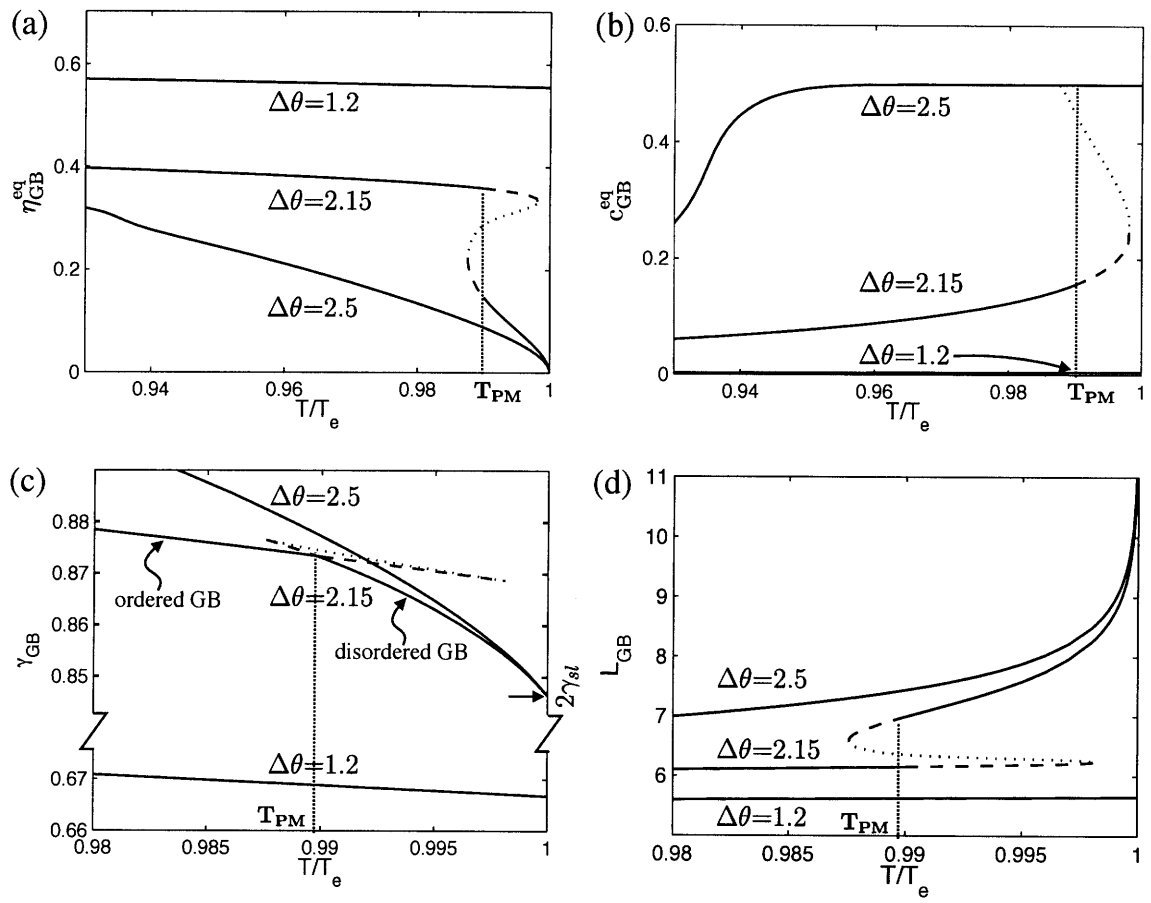

Figure 3-7: Temperature dependence of (a) GB crystallinity (η_{GB}^{eq}), (b) GB composition (c_{GB}^{eq}), (c) GB energy (γ_{GB}), and (d) GB width (L_{GB}) for three GBs of different misorientations: $\Delta\theta$=1.2, 2.15 and 2.5. For $\Delta\theta$=2.15, a first-order GB transition occurs at T_{PM}=0.9897T_e. The dashed lines represent metastable extensions of ordered and disordered GBs, and the dotted lines are for the unstable solution.

it moves continuously from ($\eta \approx 1, c \approx c_\infty$) at low temperatures towards $(0, c_e)$ as $T \rightarrow T_e$. Similarly to the disordered GB solution in 3.4.2, the GB energy reaches twice the solid/liquid interface energy (Fig. 3-7(c)) and the GB thickness diverges at T_e (Fig. 3-7(d)). In this case, the first-order GB premelting/prewetting transition is replaced by a continuous transition: the GB continuously increases it structural disorder and segregation until the boundary becomes perfectly wet by the eutectic liquid at T_e.

The GB misorientation dependence of GB modalities can be summarized a GB complexion diagram (Fig. 3-10(a)) in the $\Delta\theta - T$ space that is analogous to Fig. 2-5 for single-component systems. The solid line in Fig. 3-10(a) denotes conditions for

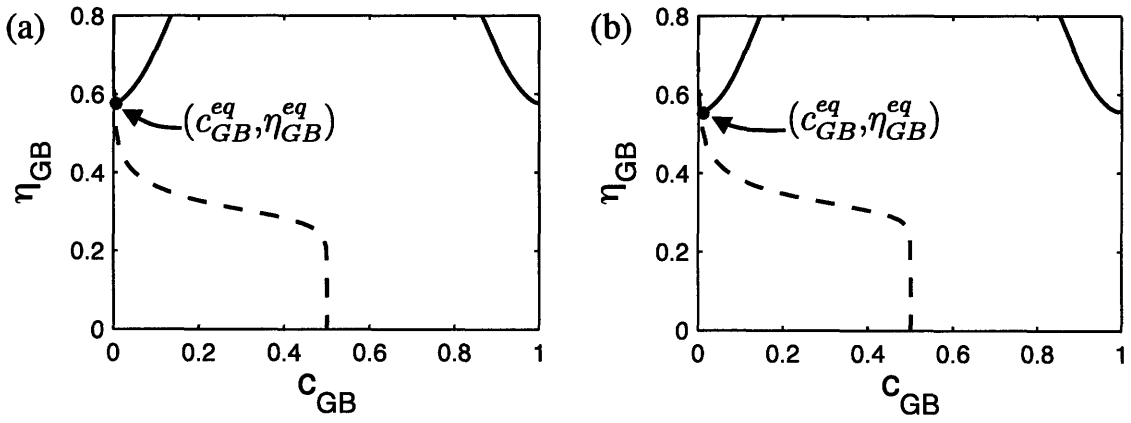

Figure 3-8: GB equilibrium state determined by the intersection between $\mathcal{C}_{PDE}$ (dashed line) and $\mathcal{C}_{LS}$ (solid line) for $\Delta\theta$=1.2 and κ^2=0.001. (a) T=$0.9T_e$ and (b) T=$0.999T_e$.

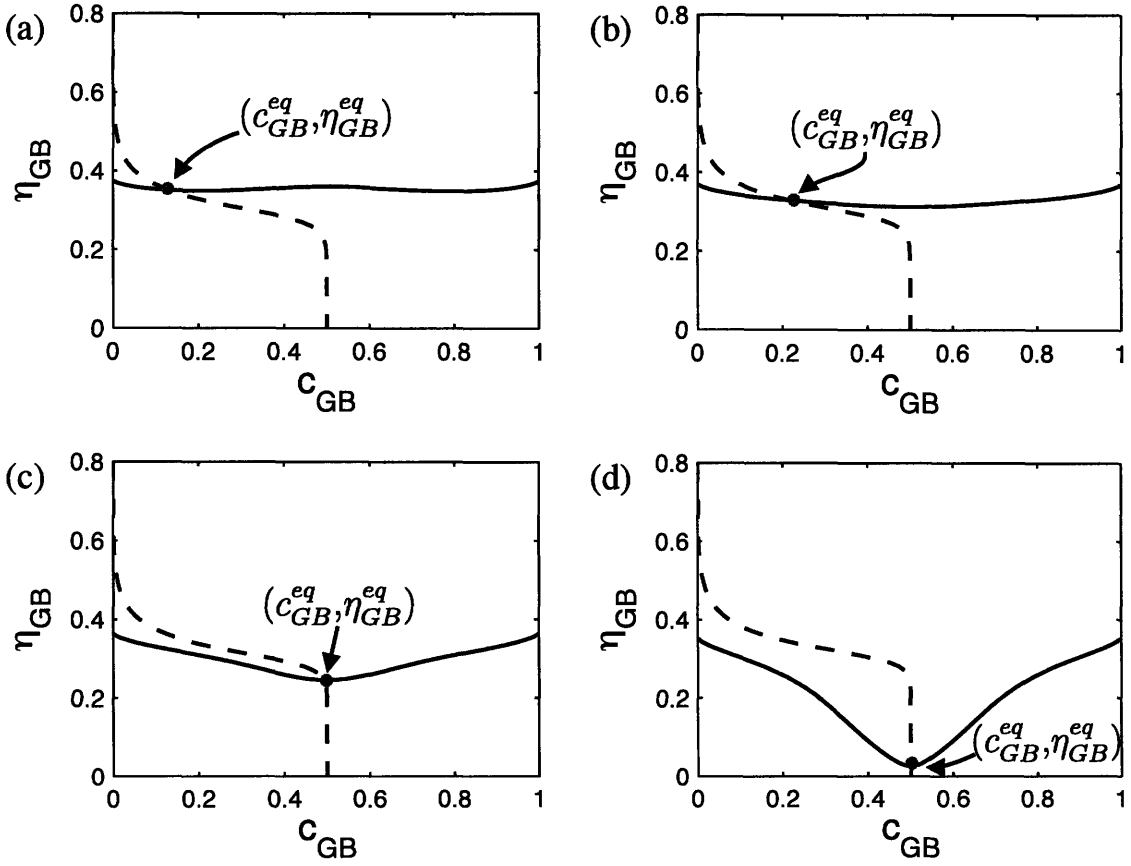

Figure 3-9: GB equilibrium state determined by the intersection between $\mathcal{C}_{PDE}$ (dashed line) and $\mathcal{C}_{LS}$ (solid line) for $\Delta\theta$=2.5 and κ^2=0.001. (a) T=$0.9T_e$, (b) T=$0.925T_e$, (c) T=$0.95T_e$, and (d) T=$0.999T_e$.

ordered/disordered GB complexion coexistence. This coexistence line meets T_e at $\Delta\theta$=1.993. GBs with $\Delta\theta < 1.993$ therefore retains finite structural order when T reaches T_e and premelting/prewetting is absent at these boundaries. Also shown in Fig. 3-10 are the metastable temperature limits (spinodes) of the ordered (dashed line) and disordered GB (dash-dotted line) complexions. The three characteristic lines terminate at a critical point, $(T_{crit},\Delta\theta_{crit})=(0.96T_e, 2.351)$. For $\Delta\theta > \Delta\theta_{crit}$, a continuous GB transition occurs as $T \rightarrow T_e$.

3.4.4 Grain Boundary Complete Wetting Transitions

Fig. 3-10(a) shows that GBs of $\Delta\theta < 1.993$. are stable against perfect wetting by the eutectic liquid at T_e for their boundary energies γ_{GB} are less than $2\gamma_{sl}(T_e)$ (e.g. $\Delta\theta$=1.2 in Fig. 3-7(c)). However, the difference between $2\gamma_{sl}$ and γ_{GB} decreases when T further increases above T_e and c_∞ follows the solidus line. This is because the compositions of equilibrium solid and liquid phases become increasingly close as $T \rightarrow T_m$, which reduces the concentration gradient energy across the solid/liquid interface. For some GBs, a first-order complete wetting transition can happen at a temperature T_{CW} ($T_e < T_{CW} < T_m$) at which $\gamma_{GB} = 2\gamma_{sl}$. The GB is replaced by two solid/liquid interfaces with a layer of equilibrium liquid of arbitrary thickness at $T > T_{CW}$. The ordered GB may retain its metastability above T_{CW} and can be superheated up to reaching its spinode (dashed line above T_e in Fig. 3-10(b)).

Fig. 3-10(b) shows that the complete GB wetting temperature increases with decreasing $\Delta\theta$, and reaches the melting temperature of pure component A as $\Delta\theta \rightarrow$ 1.177. No perfect wetting occurs for $\Delta\theta < 1.177$. This is consistent with results in the last chapter, where it is found that GBs with $\Delta\theta < a\nu/s$ are stable against complete melting at T_m in single-component systems.

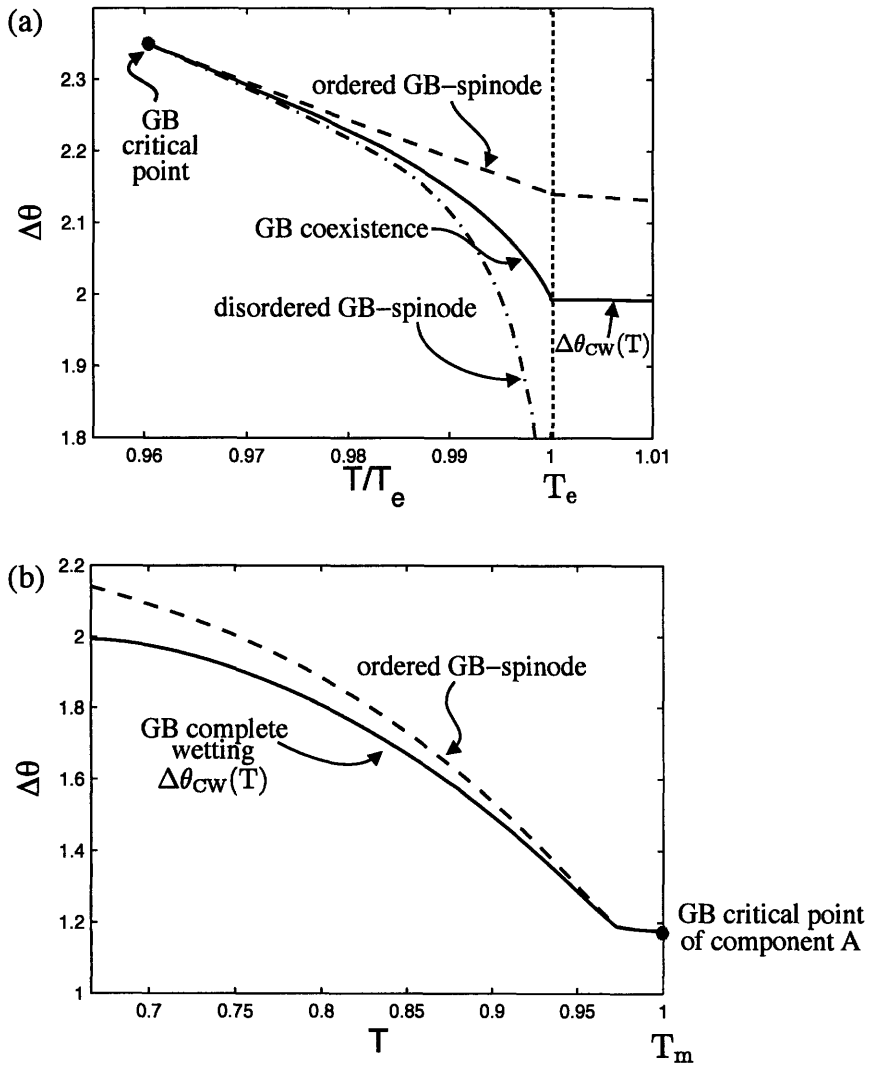

Figure 3-10: GB complexion diagrams in the $\Delta\theta - T$ space for GBs of A-rich α phase under two-phase co-existence. (a) Ordered/disordered GB coexistence line (solid) and the spinodal lines of ordered GB (dashed) and disordered GB (dashed-dotted) at sub-eutectic temperatures. (b) The complete wetting transition line $\Delta\theta_{CW}(T)$ of ordered GB (solid) and its metastable limit (dashed line) at $T_e < T < T_m$.

3.4.5 Coupled Grain Boundary Premelting/Prewetting Transitions in Single-Phase Region

It has been shown in the previous sections that disordered GB complexions can result from a GB transition (either premelting/prewetting or complete wetting) by increasing temperature in a system with its average composition in the two-phase region (either solid/solid or solid/liquid coexistence). The disordered GB complexions may

also exist in the single-phase region, where a GB premelting/prewetting transition can be induced by increasing the matrix composition c_∞ towards the bulk phase boundaries.

To illustrate this, the same graphical analysis can be extended to the single-phase region by choosing a c_∞ that is smaller than the bulk solubility limit, as presented in Fig. 3-11(a)-(c) for various c_∞ with $\Delta\theta$=2.15 and $T = 0.995T_e$. Similar to the case of Fig. 3-5(b), multiple intersections appear between $\mathcal{C}_{PDE}$ and $\mathcal{C}_{LS}$ as c_∞ changes from 1.3×10^{-4} to 1.375×10^{-4}, and the solutions corresponding to the three intersections similarly represent an ordered/low-adsorption (upper intersection), unstable (middle) and disordered/high-adsorption (lower) GB, respectively. The c_∞-dependence of GB energy illustrated in Fig. 3-11(d) shows that a first-order GB premelting/prewetting transition occurs at $c_{PM} = c_\infty = 1.38 \times 10^{-4}$ — the disordered GB is the stable complexion between c_{PM} and the solubility limit.

Fig. 3-12 shows that such GB transition also occurs at $T > T_e$ as c_∞ increases towards the solidus line in the single-phase region. Different from the case of $T < T_e$, the equilibrium GB is perfectly wet by the liquid phase upon c_∞ reaching the solidus line, while the disordered GB still has limited crystallinity and finite thickness at the solubility limit at $T < T_e$.

The graphical and numerical analyses establish that the disordered GB solution has limited persistence within the single-phase region above T_{PM}, and the coexistence between the ordered/low-adsorption and disordered/high-adsorption GBs thus extends into the single-phase region. A GB premelting/prewetting line on the bulk phase diagram can be obtained by determining the bulk compositions at which the two GB solutions coexist at temperatures $T > T_{PM}$, which is shown in Fig. 3-13 for $\Delta\theta$=2.15. This line separates the stability regions of the two GB complexions. It may terminates at a critical point, $(T_{crit},\Delta\theta_{crit})$, together with the characteristic lines for the metastability limits of ordered and disordered GBs. For $\Delta\theta$=2.15, $(T_{crit},\Delta\theta_{crit})$=$(1.06T_e,\ 1.8\times10^{-4})$. At $T > T_{crit}$, the ordered and disordered GBs are no longer distinguishable by a first-order transition. Instead, the GB continuously increases its structural disordering and segregation as c_∞ increases towards the

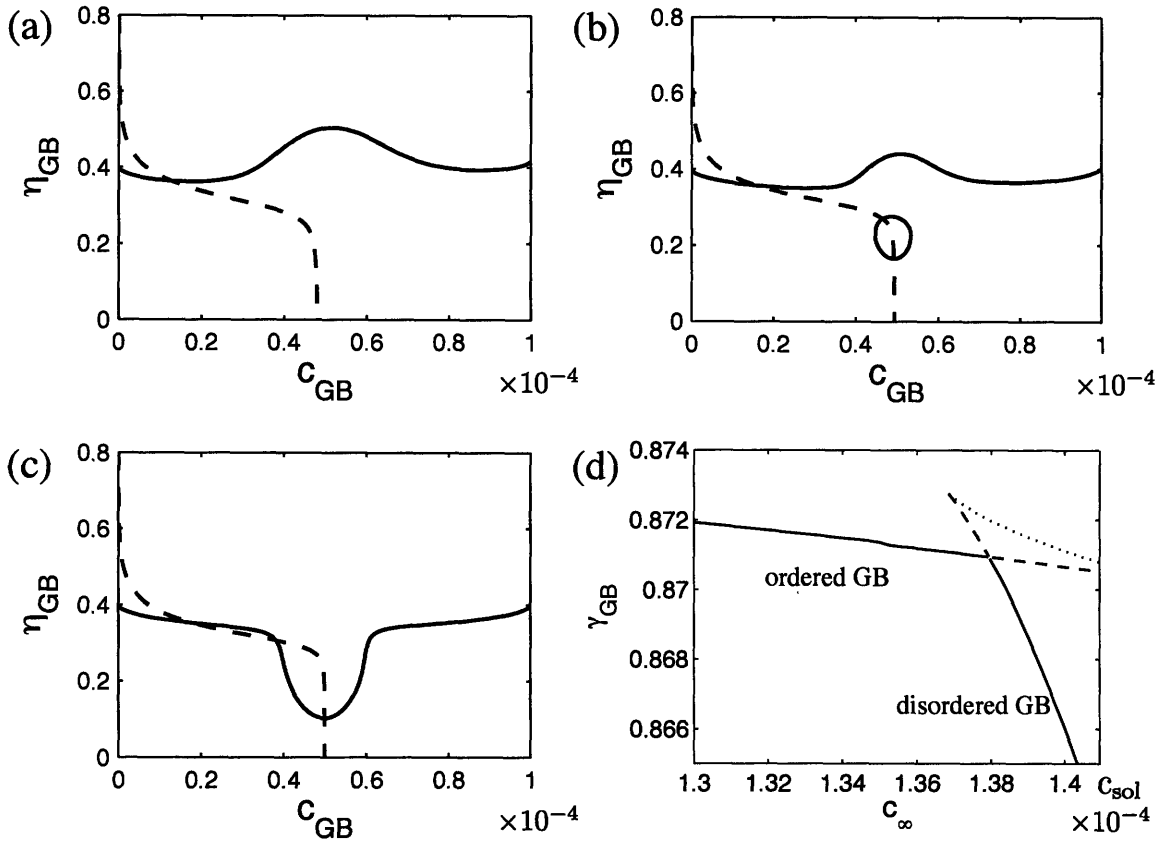

Figure 3-11: (a)-(c) GB equilibrium state determined by intersection(s) between C_{PDE} (dashed line) and C_{LS} (solid line) at different matrix concentrations in the α single-phase region: (a) c_∞=1.3×10^{-4}, (b) c_∞=1.375×10^{-4}, and (c) c_∞=1.375×10^{-4}. $\Delta\theta$=2.15, κ^2=0.001, and T= 0.995T_e. (d) c_∞-dependence of GB energy shows a first-order GB transition occurs at c_∞=1.38×10^{-4}. c_{sol}=1.409×10^{-4} is the solubility limit of B-component in α phase.

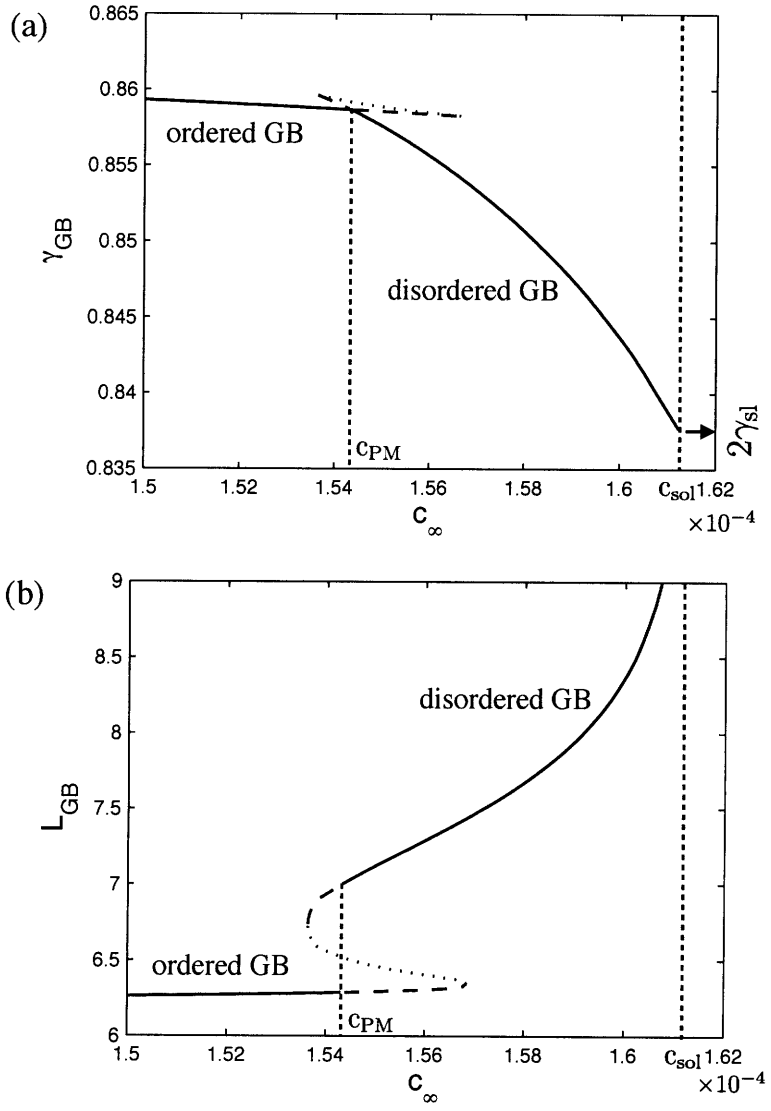

Figure 3-12: c_∞-dependence of (a) GB energy and (b) GB width for $\Delta\theta$=2.15 at T=1.02T_e. A first-order GB transition occurs at $c_{PM} = 1.543 \times 10^{-4}$. The GB width diverges and GB energy become equal to twice of the liquid-solid interfacial energy γ_{sl} when c_∞ approaches the solidus concentration, $c_{sol} = 1.612 \times 10^{-4}$.

solidus line. The GB premelting/prewetting line Fig. 3-13 is analogous to the surface prewetting line predicted by the critical point wetting model [22], except that not only composition but also structure of the boundary undergo discontinuous changes across the line in the GB case.

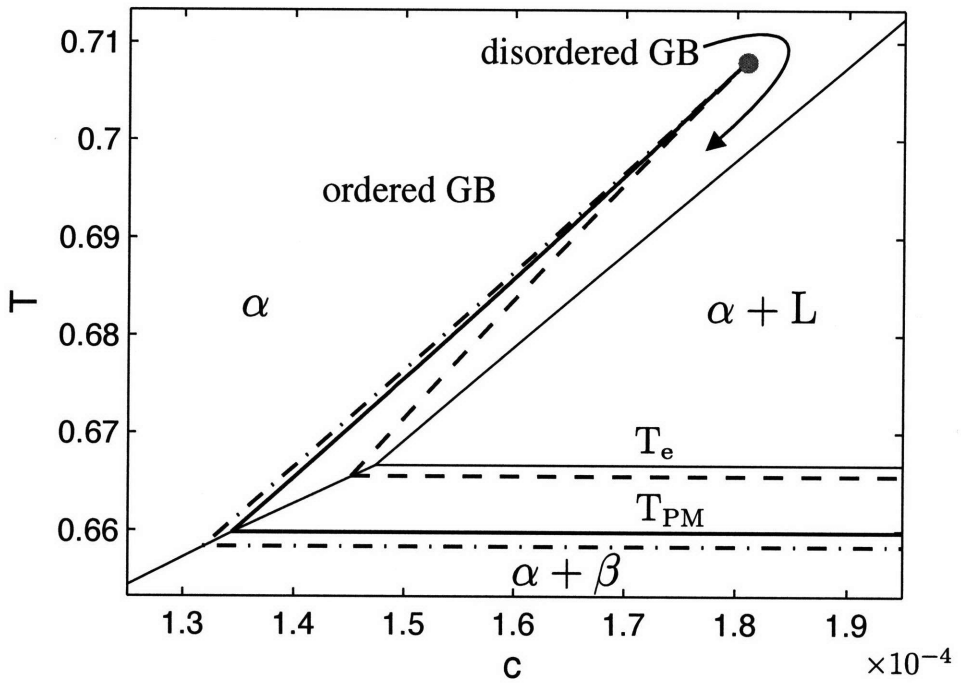

Figure 3-13: Ordered/disordered GB coexistence line (thick solid) shown on the bulk phase diagram for $\Delta\theta$=2.15. The spinodal (metastable limit) lines of ordered GB (dashed) and disordered GB (dashed-dotted) are also shown.

For GBs that undergo a complete wetting transition at $T_{CW} > T_e$ in the solid-liquid two-phase region, the GB coexistence line similarly extends into the single-phase region above T_{CW}, as illustrated in Fig. 3-14 for $\Delta\theta$=1.95,1.9 and 1.85. However, the nature of the GB transition on the coexistence line changes from a complete wetting in the two-phase region, to a premelting/prewetting transition in the single-phase region.

Fig. 3-14 illustrates that a distinct premelting/prewetting line exists for each GB with a different misorientation. The line's location on the bulk phase diagram moves towards higher temperature as $\Delta\theta$ decreases.

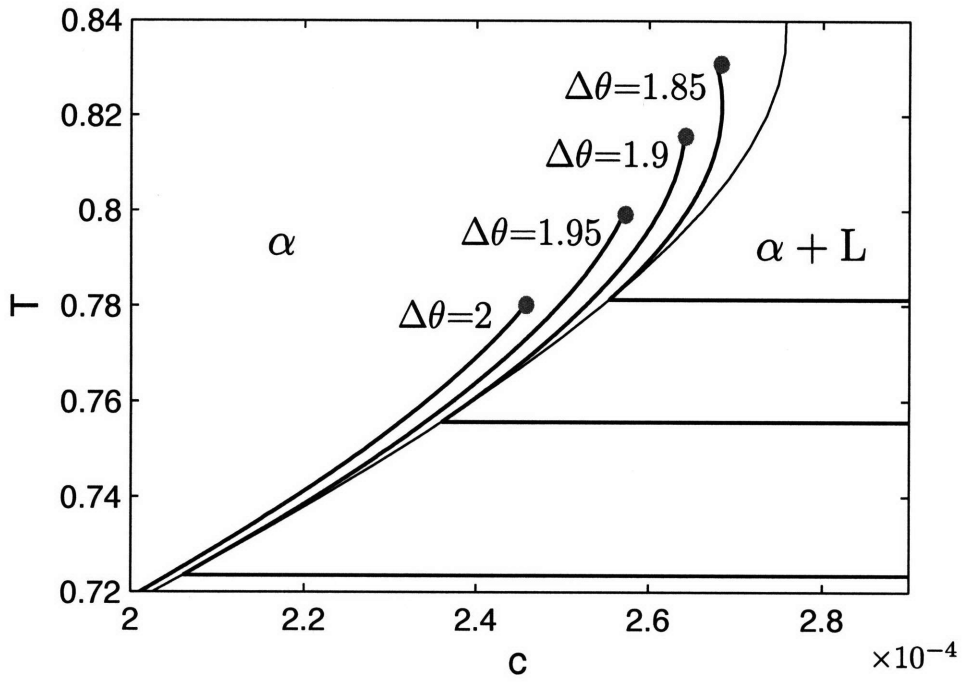

Figure 3-14: Ordered/disordered GB coexistence lines (thick solid) shown on the bulk phase diagram for $\Delta\theta$=2, 1.95, 1.9, and 1.85. GBs with $\Delta\theta$=1.95, 1.9 and 1.85 undergo complete wetting transition in the α-liquid two-phase region at $T > T_e$.

3.5 Discussion

3.5.1 Relations Between Model Predictions and Experimental Observations of Grain Boundary Cooperative Disordering and Segregation

The model analysis presented in previous sections suggests that coupled GB premelting/prewetting transitions can occur in GBs with large misorientations. The transitions produce disordered/solute-rich GB complexions at higher temperatures. The model predictions have been observed in various ceramic and metallic systems, and related experimental results have recently been reviewed by Luo [77].

As mentioned in Chapter 1, cooperative GB disordering and segregation phenomena are exemplified in ceramic systems by nanometer-thick intergranular glassy films (IGFs). The general characteristics of IGFs, e.g. high segregation levels, large

structural disorder and equilibrium thickness, are consistent with the disordered GB complexion in our model. Based on the analysis present in previous sections, it is suggested that IGFs are high-temperature equilibrium GBs from coupled premelting/prewetting transitions, and their unique features and stability could be understood/rationalized from this thermodynamic point of view. Similar to bulk phases, the disordered GB complexion is in thermodynamical equilibrium with its surroundings. The structure, composition and thickness of IGFs are determined by intensive thermodynamic quantities such as temperature and chemical potentials and also quantities specific to GBs such as misorientation and boundary inclination. It is thus not surprising that the segregation and thickness of IGFs show independence of the overall second-phase content in the the two-phase region, in which the chemical potentials are fixed. However, GB complexions are *not* phases and they do not exist in the bulk form. They should possess distinct structures and chemistries from the bulk phases. The theoretical finding that the premelting/prewetting transitions occur at sub-eutectic temperatures and in the single-phase region explains why IGFs were found under conditions where no bulk liquid is present.

Similar coupled premelting/prewetting transitions also occur at material surfaces. The free-surface counterpart of IGFs, called surficial amorphous films (SAFs), have also been observed in ceramic systems, e.g. Bi_2O_3-doped ZnO [86, 87], V_2O_5-doped TiO_2 [88], WO_3-doped TiO_2 [86], etc. In the case of V_2O_5-enriched SAFs on TiO_2 (101) surface, Qian and Luo studied the temperature dependence of film thickness by either heating samples from room temperature to specified temperatures, or firing samples at a higher temperature of 600°C first and then lowering to the desired temperatures [88]. A hysteresis loop in the thickness-temperature plot was observed for these two sets of samples. In V_2O_5+P_2O_5-doped TiO_2 samples, the coexistence of SAFs with almost clean TiO_2 surfaces at a given temperature was observed [181]. These results suggest a first-order character of the surface prewetting/premelting transition.

Experimental evidence for GB transitions are also abundant in metallic systems. Luo and colleagues recently presented direct high resolution TEM (HRTEM) observa-

tion of nanometer-thick disordered intergranular films in Ni-doped W alloys [75,76]. Intergranular films of ~0.6nm thickness were found in a specimen sintered in the Ni-W two phase region at 95°C below the bulk eutectic temperature 1495°C. Auger electron analysis (AES) of fractured GB surfaces confirms that the disordered GBs are also substantially richer in Ni than in the bulk phase. Because the specimens were quenched to room temperature before TEM imaging, it is likely that the GBs at the sintering temperature could possess more disordered structure and larger thickness.

Several other binary/multi-component metallic systems have also been extensively studied for GB premelting/prewetting. In Cu-Bi system, a series of Cu-rich specimens with different bulk Bi compositions and annealing temperatures were prepared by Straumal and colleagues [177, 182]. AES measurements of fractured GBs in these samples reveal that Bi segregation at GBs increases abruptly by about two monolayers when the system conditions (annealing temperature and bulk composition) cross a "GB solidus line" in the Cu single-phase region. In a related study, Dinvinski et al. [183] measured GB diffusivities of Cu and Bi radioisotopes. They found that accompanying the Bi segregation transition is a dramatic increase of GB diffusivities by about two orders of magnitude, which is close to the diffusivity values in solid-liquid bulk two-phase region. GB groove angle measurements by Scholhammer et al. [184] further show that the GB energy has a discontinuity in its first derivative at the locus of these abrupt changes in GB segregation and diffusivity. These studies convincingly establish that a coupled *first-order* GB premelting/prewetting transition occurs in the Cu single-phase region. The "GB solidus line" named in Ref. [177] is the same as the GB premelting/prewetting line predicted by our model analysis.

In a series of studies on (Fe-Si)-Zn quasi-binary systems with fixed Fe-Si atomic ratios, the existence of GB prewetting transitions in the Fe single-phase region is supported by measurements of Zn GB diffusivity [185–187]. Furthermore, the transition line was found to terminate at a critical point in the single-phase region in the two sets of alloys, (Fe-10%Si)-Zn and (Fe-12%Si)-Zn.

In addition to the premelting transition, GB perfect wetting by its equilibrium melt in solid-liquid two-phase region is also documented for a large number of metallic

systems, e.g., Cu-Bi [131], Zn-Sn [188], Al-Sn [189], Al-Zn [190], W-Ni [191]. GB perfect wetting is often experimentally identified by measuring the contact angle θ_d between GBs and bulk liquid phase, which characterizes the energy difference between GB and solid-liquid interfaces in the isotropic case

$$1 - \cos\left(\frac{\theta_d}{2}\right) = \frac{2\gamma_{sl} - \gamma_{GB}}{2\gamma_{sl}} \tag{3.21}$$

When GB perfect wetting occurs at a wetting temperature T_{CW}, γ_{GB} is equal to $2\gamma_{sl}$ and a zero contact angle will be found. Most GB contact angle measurements of different systems have found a scaling relation of $\theta_d \sim (T_{CW} - T)^{1/2}$. Therefore according to Eq. 3.21, $\Delta\gamma \equiv 2\gamma_{sl} - \gamma_{GB}$ scales linearly with $(T_{CW} - T)$ as the wetting temperature is approached, showing that the transition is first-order.

The criterion for GB perfect wetting, $2\gamma_{sl} - \gamma_{GB} = 0$, indicates that the wetting temperature should depend on GB misorientaion or energy – GBs with less energy would not be wet by liquid until they are at higher temperatures. This is seen in our model results, e.g. Fig. 3-10 and Fig. 3-14, and was observed in experiments. In polycrystalline samples of Cu-Bi, Zn-Sn, Al-Zn and Ni-W etc, The onset of GB wetting was found to span a temperature region, $T_{wmin} < T < T_{wmax}$, where T_{wmin} and T_{wmax} correspond to the wetting temperatures of high-angle GBs with minimal and maiximal energy, respectively.

3.5.2 Relations to Grain Boundary Transitions in Systems of Fixed Stoichiometry

By allowing a system to vary its local stoichiometry, the graphical construction developed in this chapter becomes more complicated than the analysis in the last chapter. However, similar results on GB transitions can be found for these two types of systems. In both cases, three types of GB behavior dependent on GB misorientation are predicted: GBs of relatively small $\Delta\theta$ remain ordered up to the melting (or eutectic temperature) and no premelting(/prewetting) happens; GBs with relatively large $\Delta\theta$ values can undergo a first-order premelting(/prewetting) transition below T_m (or T_e),

and the disordered GB complexion is perfectly wet by liquid at T_m (or T_e); for GBs with larger $\Delta\theta$, a continuous premelting(/prewetting) occurs when $T \rightarrow T_m$ (or T_e), and the boundaries are also perfectly wet by the equilibrium liquid phase at T_m (or T_e). Fig. 3-10(a) for binary systems is analogous to Fig. 2-5 for single-component systems. Both show that the GB transition line in the $\Delta\theta - T$ space may terminate at a critical point. For systems with variable stoichiometry, a GB equilibrium in binary systems also depends on the matrix composition as well as $\Delta\theta$ and T. Therefore a comprehensive GB complexion diagram for binary systems should be extended into the $c - \Delta\theta - T$ three dimensional parameter space. Accordingly, it can be envisioned that the loci of GB premelting/prewetting transitions should expand from a line in Fig. 2-5 to a plane in the $c - T - \Delta\theta$ space. The GB premelting/prewetting line shown on the bulk phase diagram, i.e. Fig. 3-13, can be viewed as a cross-section of this plane in the $c - T$ subspace.

There are similar aspects in model behavior, but there are also noteworthy differences between these two systems. The crystal-melt coexistence only occurs at T_m in single-component systems, but by introducing alloying the bulk crystalline and liquid phases co-exist with each other within a temperature range $T_e < T < T_m$ and can also have metastable coexistence at $T < T_e$. The presence of an equilibrium liquid phase below T_m allows GBs to inherit characteristics of the liquid with less volumetric free energy penalty and promotes GB premelting/prewetting. The effect of this difference is manifested by the change in GB behavior between the pure components and their binary alloy of the modified regular solution model present in this chapter. According to the numerical results in Section 2.4 of Chapter 2, A first-order premelting transition is absent in the pure components consisting of the model eutectic system whose free energy is specified by Eq. 3.17. A GB either continuously melts if $\Delta\theta > a\nu/s$ or remains stable against melting at T_m if $\Delta\theta < a\nu/s$. In contrast, such a first-order transition is present in the binary eutectic system. This shows that the tendency to have a first-order GB premelting/prewetting transition is enhanced by allowing GBs to undergo simultaneous disordering and segregation to borrow features from the equilibrium bulk liquid state extrapolated at $T < T_m$.

The difference in bulk solid-liquid coexistence conditions also results in different GB complete wetting behavior in the two systems. For systems of fixed stoichiometry, a complete wetting transition is only possible at T_m at which the bulk crystalline and liquid phases coexist. GBs are either melted or super-heated above T_m. However, GBs in binary systems become perfectly wet by liquid at various temperatures depending on GB misorientation. GB complete wetting is thus initiated and completed within a temperature range in polycrystals of binary systems, resulting in less abrupt changes in the overall material properties than in single-component systems.

3.5.3 Limitations of the Diffuse-Interface Analyses

The diffuse-interface analyses presented in Chapter 2 and this chapter neglect the second order term in the orientation gradient, $\nabla\theta$, in the free energy functional Eq. 3.1, which is shown be necessary for simulating GB kinetics [136, 142]. The inclusion of the $(\nabla\theta)^2$ term also eliminates the jump in $\theta(x)$ across the GB (Eq. 3.4) and smooths the θ profile. However, considering this term is not essential for studying the equilibrium properties of GBs, but causes the graphical construction to be much more complicated, if not impossible. Bishop, Cannon and Carter recently applied the KWC diffuse-interface model to SiO_2-doped Si_3N_4 GBs [192]. Their numerical calculations reached the same qualitative conclusions as our modeling results.

Our model also does not include effects of long-range interaction such as dispersion forces on GB structure and width (most atomistic simulations also disregard these forces). Although weak in comparison to forces that directly affect bonding, repulsive dispersion interactions are known to thicken premelted surface layers in some systems [33]. Because the core of a GB has a different density compared to the bulk, dispersion forces will be attractive across a GB [193]. For an ordered GB in $SrTiO_3$, the dispersion energy accounts for ~5–10% of the total binding energy [194] and is not trivial. It was argued that the presence of an attractive dispersion force makes GB complete wetting never occur [195], i.e., the equilibrium liquid film sandwiched between two crystal grains cannot be arbitrarily thick but has a finite thickness that is controlled by the strength of dispersion forces and usually on the order of a few

to a few tens of nanometers. Whether this hypothesis is true is still uncertain. Considering this effect, the results in Section 3.4.4 need to be modified accordingly: the GB complete wetting transition may be replaced by a transition between a thin, ordered GB and a wider liquid film between two grains. Such a transition is sometimes termed frustrated complete wetting [122] or pseudo-partial wetting [121] in the literature. The GB film resulting from frustrated complete wetting is different in nature from the disordered GB complexion from the premelting/prewetting transition below T_e or in the single-phase region. Thickness of the disordered complexion is limited by the excess volumetric free energy of the disordered structure instead of the dispersion forces. Evidence of the effect of dispersion force on complete wetting was reported for surficial amorphous films (SAFs) in the Bi_2O_3-doped ZnO system. SAFs in such a system remain stable in the solid-liquid two-phase region above the eutectic temperature and they are in coexistence with liquid drops with a finite contact-angle on ZnO substrates [87, 123]. Calculations found an attractive dispersion force across the air/SAF/substrate stack in this system [86], which is believed to prevent the complete wetting of the substrate by the equilibrium liquid at/above the eutectic temperature [87]. However, the liquid phase was found to perfectly wet ZnO surface above 900°C [196], which suggests that complete wetting may still occur at higher temperatures. A possible explanation is that the dispersion force (or the Hamaker constant) changes its sign from attractive to repulsive with increasing temperature. This possibility has been confirmed in systems of alkanes (e.g. hexane, propane etc) films on aqueous solutions, where the magnitude and sign of the Hamaker constant can be tuned by temperature [197] or alkane partial pressure [122]. A sequence of two wetting transitions, a first-order frustrated-complete wetting followed by a critical complete wetting, was observed in alkane films by gradually increasing temperature or alkane pressure. For grain boundaries, however, it is not expected that the two wetting transition sequence would also happen because the dispersion force should also always be attractive due to the grain/GB/grain stack symmetry.

3.6 Conclusions

The KWC diffuse-interface model for grain boundaries in binary systems predicts cooperative disordering and segregation transitions. The predicted disordered GB complexion can be associated with the appearance of a liquid phase which at the same time possesses a distinct composition from the crystalline phase, and hence the transitions can be termed coupled premelting/prewetting transitions. The model predicts that first-order transitions between an ordered/lower-solute-adsorption and a less ordered/higher-solute-adsorption grain boundary structure can occur with increasing temperature below the eutectic temperature, or increasing matrix composition towards the solidus line. Along with premelting behavior, the disordered GBs become perfectly wet by the liquid phase under bulk solid-liquid coexistence conditions. The wetting proceeds with no energy barrier and therefore the disordered GBs cannot be superheated. Premelting/prewetting transitions may not occur in boundaries with relatively low misorientations, which remain stable against melting at the eutectic temperature. However, a first-order complete wetting transition can happen in the solid-liquid two-phase regime above the eutectic temperature when the GB energy becomes larger than twice the solid-liquid interfacial energy.

The graphical construction and numerical calculations for equilibrium grain boundary properties can be used to construct a "grain boundary complexion diagram" that predicts which of two more and less ordered GB complexions as well as the wetted boundary would be most stable for values of temperature, matrix composition and misorientation. The features on the GB complexion diagram depend on the homogeneous free energy density for the crystalline and liquid/amorphous phases and on the detailed forms of the gradient energy penalties for inhomogenous distributions of structural order, composition and crystallographic orientation. The projection of the complexion diagram onto a two-dimensional bulk phase diagram generates misorientation-dependent GB coexistence lines as functions of system's temperature and average composition. The coexistence lines start from the solubility limit or solidus line, extend into the solid single-phase region, and may terminate at critical

points. The locations of the lines move to higher temperatures as misorientation decreases, and may not exist for small misorientations.

Predictions from the diffuse-interface model show qualitative agreement with experimental observations in multi-component ceramic and metallic systems. The features of the disordered GB complexion induced by the coupled premelting/prewetting transitions are consistent with those of intergranular glassy films (IGFs). It is thus proposed that IGFs are a thermodynamically stable complexion. More accurate predictions may be achieved by fitting the free energy functional to thermodynamic databases and interfacial energy measurements of real materials.

Chapter 4

Phase-Field Modeling of Morphological Evolution of Surfactant Self-Assembled Structures

4.1 Introduction

Interfaces in soft materials such as biological membranes and surfactant aggregates display a rich variety of morphologies and morphological transitions. Surfactant molecules represent a large group of amphiphilic molecules that consist of a hydrophilic head group and a hydrophobic tail group. When mixed with solvents, surfactant molecules will form self-organized structures such as micelles at sufficiently large concentrations, as illustrated in Fig. 4-1(a). The topology, shape and size of the self-assembled structures are mediated by many factors, including the surfactant concentrations, the molecular structures of surfactants and the solvent properties. Three typical isolated micellar morphologies have been observed in dilute to semi-dilute surfactant solutions in experiments, which are sphere, cylinder and bilayer (Fig. 4-1(b)). In concentrated solutions these isolated morphologies self-assemble

into ordered structures such as lamellar, hexagonal and cubic phases [198]: there is a hierarchy of self-organization.

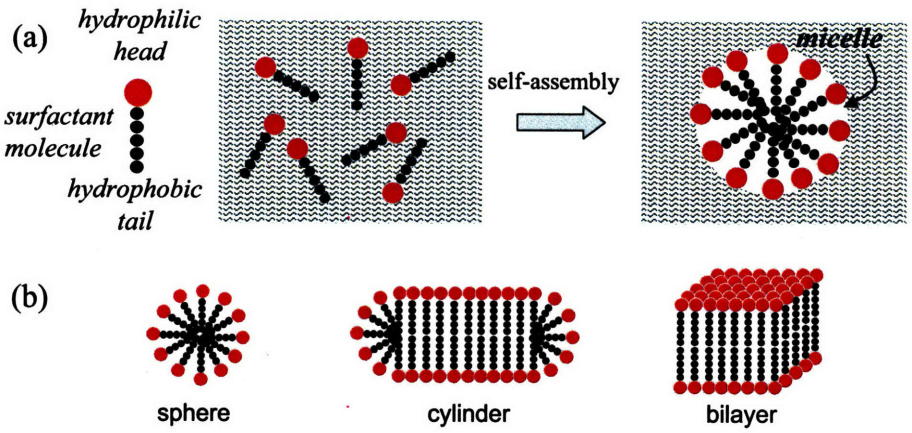

Figure 4-1: (a) Schematic illustrations of surfactant molecules and self-assembling behavior in solvents such as water. (b) Schematics of three typical isolated surfactant micellar structures (i.e., spherical, cylindrical and bilayer structures).

The curvature elastic model introduced by Helfrich [113] provides a simple and successful framework for understanding the morphological stability of surfactant systems. Modeling amphiphilic layers as elastic membranes, Helfrich derives the stored elastic energy as a function of the layer's mean and Gaussian curvatures, H and K:

$$E_{curv} = \iint dA \left[2\kappa(H - H_0)^2 + \bar{\kappa}K\right] \tag{4.1}$$

where κ and $\bar{\kappa}$ are elastic bending moduli for mean and Gaussian curvatures (sometimes called splay and saddle-splay bending constants), and can be evaluated from mean-field thermodynamic calculations [199–207] and atomistic simulations [208]. H_0 is the spontaneous curvature of the surfactant monolayer, an intrinsic property that depends on the particular surfactant and solvent features and on temperature, co-surfactants, pH and salinity, etc. Similarly, H_0 can be estimated theoretically for different surfactant systems [199, 200, 202, 207, 209, 210]. The spontaneous curvature value has a dominant influence on determining the micellar structure that minimizes the curvature elastic energy. A spherical micelle is preferred when $H_0 \sim 1/l_0$, where l_0

is the surfactant molecular length. When H_0 decreases to $\sim 1/(2l_0)$, the energetically favored isolated micellar structure changes to a cylinder, and a surfactant bilayer will be the most stable structure when H_0 further decreases to 0. At large curvatures, it may be necessary to amend Eq. 4.1 with higher-order terms [113, 211–213]. Nevertheless, the Helfrich expression and the spontaneous curvature concept still maintain useful predictive capabilities for experimental observations.

Though the growth and transitions of surfactant structures are closely regulated by the curvature elastic energy, the kinetic aspects of surfactant self-assembly are not treated in Helfrich's model. The phase-field technique provides a tested method to connect thermodynamic information of a material system to a physical kinetic model of its morphological evolution. Because it is a level-set technique, it is particularly well-suited to systems that undergo complicated shape transitions such as tip-splitting, segmentation, or impingement. For reviews on the applications of phase-field models to various fields, see Ref. [101, 116, 117]. In this chapter we propose a phase-field model for studying the kinetics of surfactant micelle growth. The model captures the surfactants' self-assembling tendency in solutions and the effects of the curvature energetics on micellar morphologies. The model is based on a Ginzburg-Landau theory developed by Gompper and co-workers for studying general phase stability and wetting behavior of a water-oil-surfactant ternary system [214–221]. Similar formulations also appear within different contexts, including models for studying phase transitions in block copolymer melts [222, 223] and liquid crystals [224], Rayleigh-Benard convection [225], and a recently developed "phase-field crystal" method for modeling microstructural evolution of crystalline structures on atomic length and diffusive time scales [226, 227]. Phase-field models that apply the Helfrich energy to vesicle membrane statics and dynamics also started to emerge in recent years [118–120, 228–234]. However, several important new features appear in the present model for surfactant self-assembly. Different from Gompper's formulation, our model explicitly incorporates the spontaneous curvature H_0 as a model parameter, and the free energy formulation recovers the curvature elastic energy expression (Eq. 4.1) in the sharp-interface limit, which thus facilitates studying the effects of

spontaneous curvature on micellar growth. The model was extended into the kinetic regime by employing Cahn-Hilliard kinetics [235], which allow one to simulate the growth of surfactant micelles in dilute solution.

4.2 Phase-Field Formulation of Surfactant–Water Binary Systems

A surfactant–polar solvent (e.g. water) binary system is treated within the phase-field model. A scalar order parameter, $\phi(\vec{x})$, is introduced to model the local surfactant concentration. $\phi(\vec{x})$ is assumed to smoothly and monotonically increase along a spatial trajectory that starts from hydrophobic tail-groups of surfactant micelles, traverses through the hydrophilic head-groups, and ends in a polar solvent. $\phi = -1$ represents the maximum possible concentration of surfactants, and $\phi = 1$ represents pure solvent. It is assumed that the head groups of surfactant micelles always abut the polar solvent and their locations define the micelle/solvent interface, which is specified by the level set $(\vec{x}|\phi(\vec{x}) = 0)$. The total free energy of the binary system is expressed as a functional of the order parameter $\phi(\vec{x})$.

4.2.1 One-Dimensional Phase-Field Formulation

To better illustrate the phase-field model, its one-dimensional formulation with zero spontaneous curvature (H_0=0) is first described in this section. A three-dimensional formulation will be developed in the next section. The following free energy functional is proposed for such a 1D system

$$F[\phi(x)] = \int \left[f(\phi) + \frac{\nu(\phi)}{2} \left(\frac{d\phi}{dx} \right)^2 + \frac{\lambda}{2} \left(\frac{\partial^2 \phi}{\partial x^2} - \sigma p(\phi) \right)^2 \right] dx \qquad (4.2)$$

The physical significance of various terms in the functional is described as follows. The $f(\phi)$ term in Eq. 4.2 is the free energy density of a homogenous solution as a function of surfactant concentration. Because water and surfactants are macroscopi-

cally immiscible, $f(\phi)$ has a double-well shape with two minima close to $\phi = \pm 1$ that represent the bulk water and disordered surfactant phase respectively, as illustrated in Fig. 4-2.

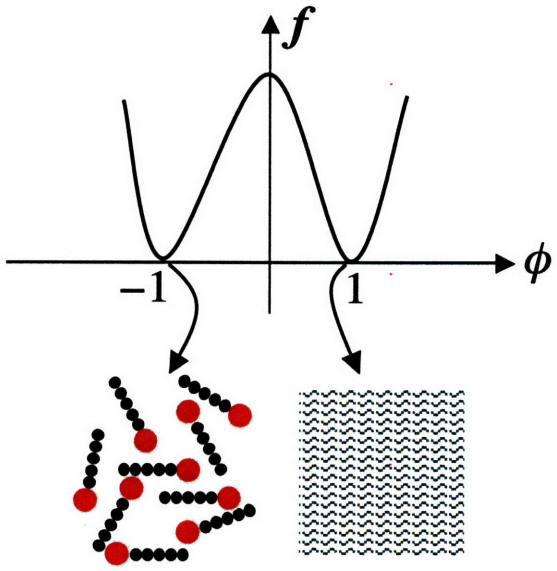

Figure 4-2: A schematic plot of the volumetric free energy curve $f(\phi)$ and its role in promoting macroscopic phase separation of the surfactant–water solution.

However, the macroscopic phase separation promoted by $f(\phi)$ is suppressed by the gradient energy $\nu(\phi)/2(d\phi/dx)^2$. Gradient terms of order parameters contribute to the interfacial energy. Different from most phase-field models, the gradient coefficient $\nu(\phi)$ in Eq. 4.2 is required to be negative in the interfacial region $\phi \sim 0$, which implies a "negative" interfacial energy. Normally, this would give rise to an ill-posed stability criterion but this difficulty is remedied by the λ-dependent term in Eq. 4.2 as described below. The physical origin of such an energy contribution is illustrated in Fig. 4-3. Within the bulk disordered surfactant phase, there are unfavorable interactions between the hydrophilic head and hydrophobic tail groups. With the presence of water-surfactant interface, such interactions can be avoided by removing the head groups from the interior of the surfactant phase to the interface, where they interact more favorably with water molecules. Therefore, the total free energy of the system is reduced by increasing the interface area between water and surfactant aggregates, which results in an apparent negative interfacial energy.

To ensure the stability of the bulk phases, the gradient coefficient ν must be positive for $\phi \sim \pm 1$. Following Gompper et al. [214–221], $\nu(\phi)$ is modeled as

$$\nu(\phi) = \nu_0 + \nu_1 \phi^2 \tag{4.3}$$

with $\nu(0) = \nu_0 < 0$ and $\nu(\pm 1) = \nu_0 + \nu_1 > 0$.

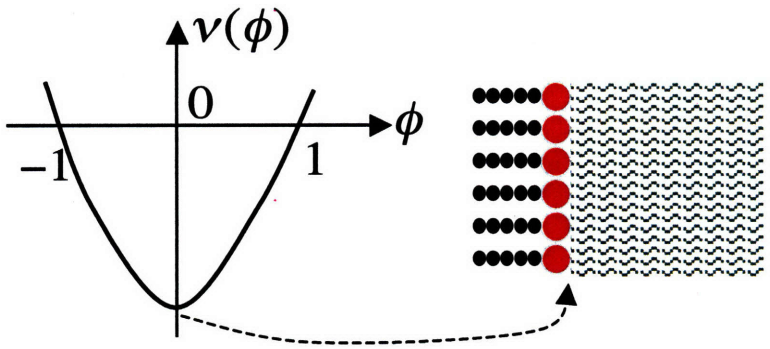

Figure 4-3: A schematic plot of the gradient coefficient $\nu(\phi)$ which favors the formation of interfaces between surfactant aggregates and water.

With only $f(\phi)$ and $\nu(\phi)/2(d\phi/dx)^2$ present in the free energy functional, the system tends to create interfaces everywhere in the solution due to the negative energy contribution from the gradient terms. However, this is physically inadmissable because strong repulsion between tail groups will arise when two interfaces get too close to each other. As illustrated in Fig. 4-4(c), an equilibrium interface separation is established by the finite thickness of a surfactant bilayer structure, and it is approximately equal to twice the surfactant chain length. The $\lambda/2(d^2\phi/dx^2 - \sigma p(\phi))^2$ term in Eq. 4.2 introduces an effective interface-interface interaction that gives rise to such a stable bilayer thickness. Fig. 4-4(a) illustrates that the magnitude of the second derivative $d^2\phi/dx^2$ within a bilayer profile increases when two interfaces approach each other and serves as a measure of interface separation. An equilibrium bilayer thickness d^{eq} depending on the σ parameter is thus introduced by the λ-dependent term – the interface-interface interaction is minimized at d^{eq}. To demonstrate this,

consider a plausible bilayer profile

$$\phi_{bilayer}(x) = \begin{cases} 1 - \frac{32}{d^4}\left(x - \frac{d}{2}\right)^2\left(x + \frac{d}{2}\right)^2 & -\frac{d}{2} < x < \frac{d}{2} \\ 0 & \text{otherwise} \end{cases} \tag{4.4}$$

where d specifies the bilayer thickness. Substituting $\phi_{bilayer}(x)$ into $\lambda/2(d^2\phi/dx^2 - \sigma p(\phi))^2$ and integrate it over (-d/2,d/2), one finds that this energy term is minimized at a finite bilayer thickness d^{eq} that is inversely proportional to $\sigma^{1/2}$ (Fig. 4-4(b)). For $d \approx d^{eq} = 7.24\sigma^{-1/2}$, the interaction energy has a quadratic form: $F_{bilayer} \approx 0.094\lambda\sigma^{5/2}(d - d^{eq})^2 + 1.19\lambda\sigma^{3/2}$. Note that $p(\phi) = 1/16(1-\phi)^3(8 + 9\phi + 3\phi^2)$ is an interpolation function that varies smoothly from $p(-1) = 1$ to $p(1) = 0$. Its presence in Eq. 4.2 ensures that an equilibrium bilayer thickness is only characteristic of the surfactant segregates and does not apply to the solvent.

Therefore it is shown that the free energy functional Eq. 4.2 does capture surfactants' self-assembly behavior in aqueous solution, and surfactant bilayer structures can be stabilized in solution by Eq. 4.2 (Fig. 4-4(c)).

An equivalent free energy formulation to Eq. 4.2 is

$$F[\phi(x)] = \int \left[f(\phi) + \frac{\lambda\sigma^2}{2}p(\phi)^2 + \left(\frac{\nu(\phi)}{2} + \lambda\sigma p'(\phi)\right)\left(\frac{d\phi}{dx}\right)^2 + \frac{\lambda}{2}\left(\nabla^2\phi\right)^2 \right] dx \tag{4.5}$$

Eq. 4.5 can be derived from Eq. 4.2 by integration by parts and it has the same first variation as Eq. 4.2.

4.2.2 Three-Dimensional Phase-Field Formulation

To extend Eq. 4.5 to three dimensions, the first derivative $d\phi/dx$ is replaced with the gradient $\nabla\phi$, $d^2\phi/dx^2$ with the Laplacian $\nabla^2\phi$, and terms related to the spontaneous curvature parameter H_0 are also included

$$\begin{aligned} F[\phi(\vec{x})] = \iiint \Bigg[& f(\phi) + \frac{\lambda\sigma^2}{2}p(\phi)^2 + \left(\frac{\nu(\phi)}{2} + \lambda\sigma p'(\phi) + 2\lambda H_0^2\right)|\nabla\phi|^2 \\ & -4\lambda H_0 |\nabla\phi| \nabla^2\phi + \frac{\lambda}{2}\left(\nabla^2\phi\right)^2 \Bigg] dV \end{aligned} \tag{4.6}$$

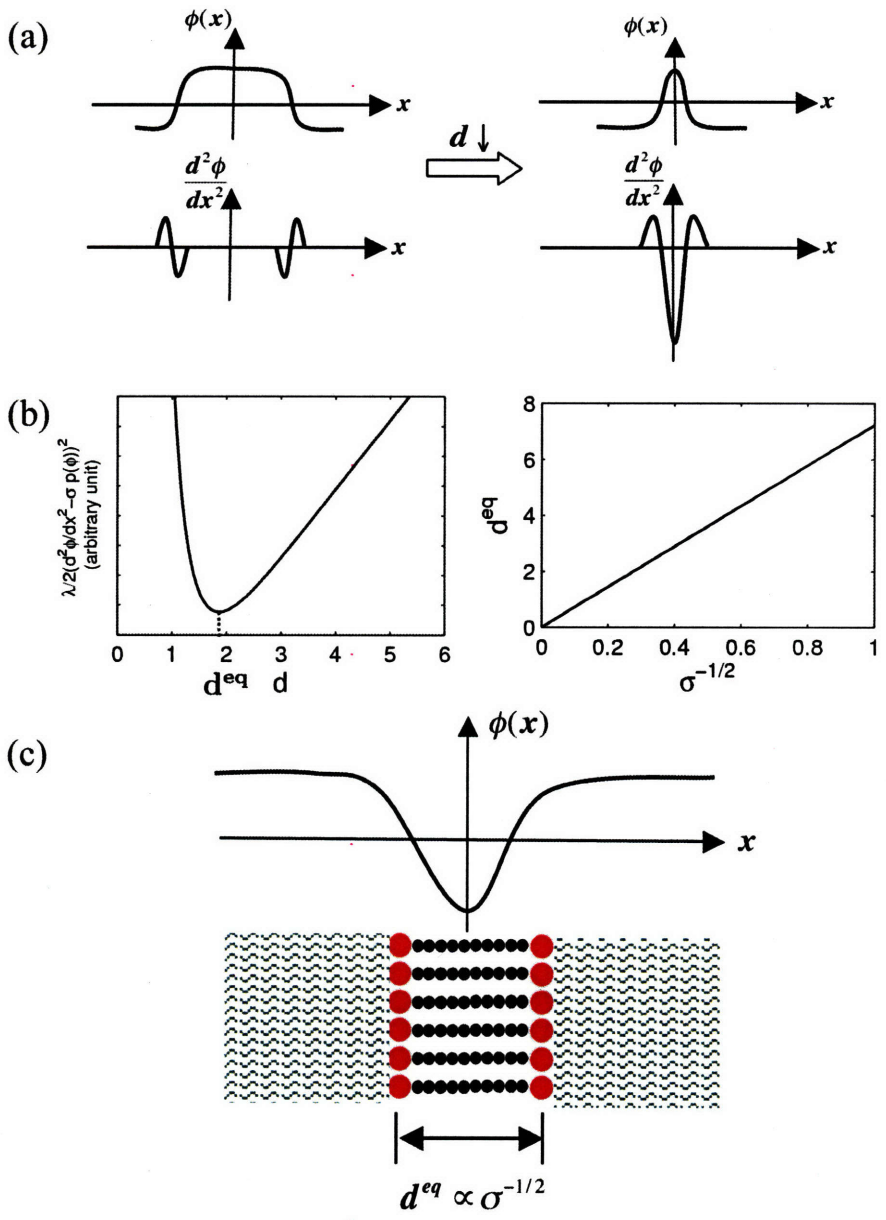

Figure 4-4: (a) A schematic plot demonstrates that the magnitude of $d^2\phi/dx^2$ within a surfactant aggregate increases with decreasing separation between two interfaces. (b) Plots showing that the λ-dependent term of a bilayer profile given by Eq. 4.4 is minimized at an equilibrium bilayer thickness d^{eq}, and d^{eq} scales with $\sigma^{-1/2}$. (c) Illustration of a stabilized surfactant bilayer structure resulting from the free energy functional Eq. 4.2.

It is shown below that the curvature elastic energy is incorporated in the above functional. In particular, the $\nabla\phi - \nabla^2\phi$ coupling term, which is not present in the functional by Gompper et al. [214–221], naturally introduces the spontaneous

curvature H_0.

Assuming that $\phi(\vec{x})$ has continuous gradients, a local orthogonal coordinate system (r,s,t) can be constructed based on the level surfaces of ϕ as illustrated in Fig. 4-5. In such a coordinate system, r is in the direction of $\nabla\phi$ and the constant r coordinate surfaces are the level surfaces of ϕ. s and t are normal to each other and lie in the tangent planes of the ϕ level surfaces. It is assumed that the local r values can be chosen in such a way that $|\partial\vec{x}/\partial r| \equiv |\vec{x}_r| = 1$.

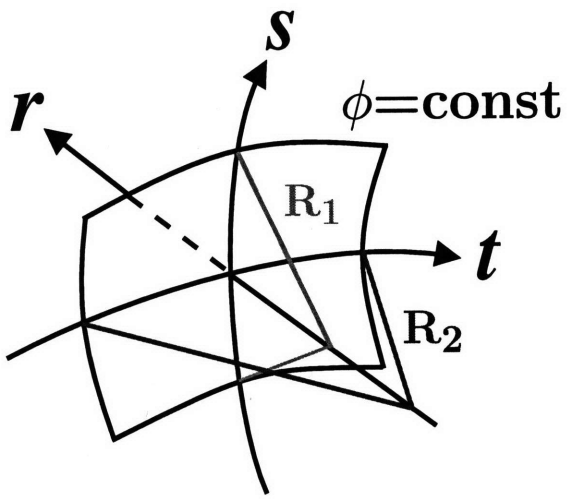

Figure 4-5: Schematic drawing of a local orthogonal coordinate system based on level surfaces of ϕ.

As shown in Appendix A, the gradient and Laplacian of $\phi(\vec{x})$ in such a coordinate system have the following expressions

$$|\nabla\phi| = \frac{\partial\phi}{\partial r} \tag{4.7}$$

$$\nabla^2\phi = \frac{\partial^2\phi}{\partial r^2} + 2H(r,s,t)\frac{\partial\phi}{\partial r} \tag{4.8}$$

In Eq. 4.8, $H(r,s,t)$ is the mean curvature of the ϕ level surface at (r,s,t). The mean (H) and Gaussian (K) curvatures are two characteristic properties of a surface which are related to the principal radii of curvature of the surface (R_1 and R_2 in Fig. 4-5)

through

$$H = \frac{1}{R_1} + \frac{1}{R_2} \tag{4.9}$$

$$K = \frac{1}{R_1 R_2} \tag{4.10}$$

In the local orthogonal coordinates, the mean and Gaussian curvatures of the ϕ level surfaces have the following expressions

$$H(r,s,t) = \frac{1}{2}\left(\frac{|\vec{x}_s|_r}{|\vec{x}_s|} + \frac{|\vec{x}_t|_r}{|\vec{x}_t|}\right) \tag{4.11}$$

$$K(r,s,t) = \frac{|\vec{x}_s|_r\,|\vec{x}_t|_r}{|\vec{x}_s|\,|\vec{x}_t|} \tag{4.12}$$

The derivation of Eqs. 4.11 and 4.12 is given in Appendix A. Eq. 4.8 shows that the curvature information of the surfactant-water interface is incorporated into the Laplacian operator.

Next, rewrite the free energy functional in the (r,s,t) orthogonal coordinate system by substituting Eqs. 4.7 and 4.8 into Eq. 4.6 and changing variables from $dx\,dy\,dz$ to $dr\,ds\,dt$

$$F[\phi(\vec{x})] = \iiint_V dr\,ds\,dt|\vec{x}_s|\,|\vec{x}_t|\left[f(\phi) + \frac{\lambda\sigma^2}{2}p(\phi)^2 + \left(\frac{\nu(\phi)}{2} + \lambda\sigma p'(\phi) + 2\lambda H_0^2\right)\left(\frac{\partial\phi}{\partial r}\right)^2 - 4\lambda H_0\frac{\partial\phi}{\partial r}\left(\frac{\partial^2\phi}{\partial r^2} + 2H(r,s,t)\frac{\partial\phi}{\partial r}\right) + \frac{\lambda}{2}\left(\frac{\partial^2\phi}{\partial r^2} + 2H(r,s,t)\frac{\partial\phi}{\partial r}\right)^2\right] \tag{4.13}$$

where the Jacobian for the change of variables is $|\vec{x}_s|\,|\vec{x}_t|$. Separating the free energy

F into the curvature-independent and curvature-dependent parts yields

$$F[\phi(\vec{x})] = \underbrace{\iiint_V dr\,ds\,dt|\vec{x}_s|\,|\vec{x}_t|\left[f(\phi)+\frac{\lambda\sigma^2}{2}p(\phi)^2+\left(\frac{\nu(\phi)}{2}+\lambda\sigma p'(\phi)\right)\left(\frac{\partial\phi}{\partial r}\right)^2\right]}_{F_{1D}}$$
$$\underbrace{+2\lambda\iint_A ds\,dt\int_{r_-}^{r_+} dr|\vec{x}_s|\,|\vec{x}_t|(H^2-4HH_0+H_0^2)\left(\frac{\partial\phi}{\partial r}\right)^2}_{\mathcal{I}_1}$$
$$\underbrace{+2\lambda\iint_A ds\,dt\int_{r_-}^{r_+} dr|\vec{x}_s|\,|\vec{x}_t|(H-2H_0)\frac{\partial\phi}{\partial r}\frac{\partial^2\phi}{\partial r^2}}_{\mathcal{I}_2} \tag{4.14}$$

It is seen that the curvature-independent integral F_{1D} in Eq. 4.14 has the same expression as the one-dimensional formulation (Eq. 4.5) along the r-axis. For the curvature-dependent integrals $\mathcal{I}_1$ and $\mathcal{I}_2$, the integration is limited to the interfacial region, $r_- < r < r_+$, as $|\partial\phi/\partial r|$ vanishes outside the interfacial region.

By applying integration by parts to $\mathcal{I}_2$, one obtains

$$\begin{aligned}\mathcal{I}_2 &= \lambda\iint_A ds\,dt\left\{-\int_{r_-}^{r_+} dr\frac{\partial}{\partial r}\left[|\vec{x}_s|\,|\vec{x}_t|(H-2H_0)\right]\left(\frac{\partial\phi}{\partial r}\right)^2+(H-2H_0)\left(\frac{\partial\phi}{\partial r}\right)^2\Big|_{r_-}^{r_+}\right\}\\ &= \lambda\iint_A ds\,dt\int_{r_-}^{r_+} dr|\vec{x}_s|\,|\vec{x}_t|\,(4H_0H-K)\end{aligned} \tag{4.15}$$

Eq. 4.15 follows from the reasonable assumption $\partial\phi/\partial r|_{r_\pm}$=0, Eqs. 4.11 and 4.12, and the following equality

$$\frac{\partial H}{\partial r} = -\frac{1}{2}\left(\frac{|\vec{x}_s|_r^2}{|\vec{x}_s|^2}+\frac{|\vec{x}_t|_r^2}{|\vec{x}_t|^2}\right) \tag{4.16}$$

The proof of Eq. 4.16 is given in Appendix A.

Combining Eq. 4.15 with $\mathcal{I}_1$ produces the curvature-dependent part of the free

energy functional

$$F_{curv} \equiv \mathcal{I}_1 + \mathcal{I}_2 = \lambda \iint_A ds\, dt \int_{r_-}^{r_+} dr |\vec{x}_s| \, |\vec{x}_t| \left(\frac{\partial \phi}{\partial r}\right)^2 \left[2(H(r,s,t) - H_0)^2 - K(r,s,t)\right] \tag{4.17}$$

Because $|\partial\phi/\partial r|$ is negligible away from the interface, Eq. 4.17 can be further approximated by a two-dimensional integral over the ϕ=0 level surface

$$F_{curv} = \iint dA \left[2\kappa(H(r,s,t) - H_0)^2 + \overline{\kappa} K(r,s,t)\right] + O(\xi H) \tag{4.18}$$

where ξ is the interface thickness, and κ and $\overline{\kappa}$ are the bending rigidities for the mean and Gaussian curvatures

$$\kappa = -\overline{\kappa} = \lambda \int_{r_-}^{r_+} \left(\frac{\partial \phi}{\partial r}\right)^2 dr \tag{4.19}$$

Eq. 4.18 shows that F_{curv} reproduces the curvature elastic energy Eq. 4.1 in the thin/flat interface limit when ξ and H approach zero.

Thus it is shown that the free energy functional given by Eq. 4.6, F=$F_{1D} + F_{curv}$, captures both the self-assembling tendency of surfactants in aqueous solution (through F_{1D}) and the dependence of surfactant aggregation energy on its interfacial curvature (through F_{curv}).

4.2.3 Kinetic Equation

Because the surfactant concentration field is a conserved variable, the kinetic evolution of the system is modeled with the Cahn-Hilliard equation [235], which simulates both the growth of surfactant micelles and the diffusion of surfactants in solutions

$$\frac{\partial \phi}{\partial t} = \nabla \cdot \left(M \nabla \frac{\delta F}{\delta \phi}\right) \tag{4.20}$$

In Eq. 4.20, M is the mobility of surfactant molecules and assumed to be a constant here. $\delta F/\delta\phi$ is the first variational derivative of $F(\phi)$

$$\begin{aligned}\frac{\delta F}{\delta\phi} &= f'(\phi) + \lambda\sigma^2 p(\phi)p'(\phi) - \left(\frac{\nu'(\phi)}{2} + \lambda\sigma p''(\phi)\right)(\nabla\phi)^2 \\ &\quad - (\nu(\phi) + 2\lambda\sigma p'(\phi) + 4\lambda H_0^2)\nabla^2\phi \\ &\quad + 4\lambda H_0 \nabla\cdot\left(\frac{\nabla^2\phi\nabla\phi - \nabla\nabla\phi\cdot\nabla\phi}{|\nabla\phi|}\right) + \lambda\nabla^4\phi\end{aligned} \tag{4.21}$$

In Eq. 4.21, $\nabla\nabla\phi$ is a second-rank covariant tensor: $(\nabla\nabla\phi)_{ij} = \partial^2\phi/\partial x_i\partial x_j$.

4.3 Numerical Implementation

4.3.1 Choosing Parameters and Non-Dimensionalization of the Kinetic Equation

For short-chained surfactant molecules, the effect of the connectivity of surfactant on the configurational entropy of the water-surfactant solution may be neglected. Thus one can model $f(\phi)$ in Eq. 4.6, the homogeneous free energy per unit volume of the solution, with the simple regular solution model

$$f(\phi) = \frac{RT}{V_m}(\chi c_w c_s + c_w \ln c_w + c_s \ln c_s) \tag{4.22}$$

where c_w and c_s are the volume fractions of water and surfactant molecules, respectively, which are related to the order parameter ϕ by $c_s = 1 - c_w = (1-\phi)/2$. V_m is the volume per base-mole of the solution (1 base-mole is defined as one mole of water molecules and surfactant monomers), and $V_m = 18\text{cm}^3/\text{mole}$ is used (the molar volume of water). The χ parameter characterizes the non-ideal interaction between solvent and solute; $\chi \approx 5$ has been estimated for water-hydrocarbon systems [198].

To avoid the time-consuming evaluation of the logarithmic function and the diverging derivatives of $f(\phi)$ at $c_s = 0, 1$, a double-well piece-wise polynomial approximation

is used to model $f(\phi)$ in numerical simulations for computational efficiency

$$f(\phi) = \begin{cases} \frac{a}{4\phi_m^4}(\phi^2 - \phi_m^2)^2 & |\phi| \leq \phi_m \\ b(\phi^2 - \phi_m^2)^2 & \phi_m < |\phi| < 1 \end{cases} \tag{4.23}$$

We choose $a = 311\text{J/cm}^3$, $b = 100a$ and $\phi_m = 0.999$ to "mimic" the regular solution free energy curve given by Eq. 4.22, as shown in Fig. 4-6. The polynomial approximation has no effect on the physical behavior below.

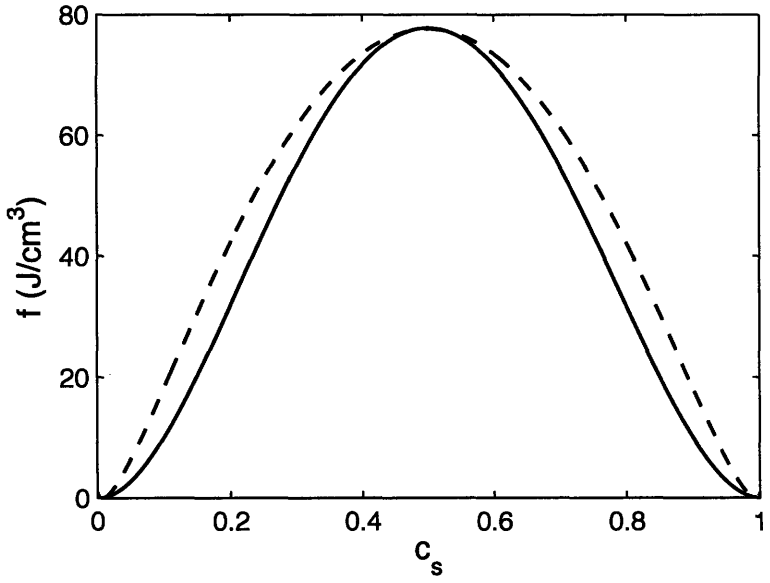

Figure 4-6: The regular solution free energy curve (dashed line) is fitted by a piecewise polynomial curve (solid line) given by Eq. 4.23 in numerical calculations.

The mobility value M for surfactant molecules in a dilute solution can be estimated from its relation to the diffusion coefficient, $D \approx Mf''(\phi) \approx 2Ma$. The self-diffusion coefficient D of surfactant monomers in aqueous solution is on the order of $10^{-10}\text{m}^2/\text{s}$ (e.g., D=$3.1\times10^{-10}\text{m}^2/\text{s}$ for $C_{12}E_5$ [236]), which gives $M \approx 10^{-9}\text{cm}^5/(\text{J}\cdot\text{s})$.

In numerical calculations, the kinetic equation Eq. 4.20 is solved in its dimensionless form by rescaling length, energy and time against the units $\bar{l} = 2\text{nm}$, $\bar{\epsilon} = a\bar{l}^3 \approx 600kT$ and $\bar{t} = \bar{l}^3/(Ma) \approx 0.1\mu\text{s}$, respectively. This scaling sets the dimensionless values of a and M both to be unity. All model parameters will be given dimensionless values in the following. The λ parameter determines the bending rigidities of surfactant layers (Eq. 4.19) — λ=0.005–0.01 are used in simulations to produce $\kappa \sim 10kT$,

which are the typical values of the bending stiffness of unary surfactant systems. The σ parameter, which controls surfactant micelle dimensions, is set to be 15 to give a bilayer thickness of $d^{eq} \sim 2\bar{l} = 4$nm. The remaining parameters in Eq. 4.6, ν_0 and ν_1 (Eq. 4.3), are related to the water-head group interaction strength. ν_0=-0.075 and ν_1=0.076 are chosen to give a critical micelle concentration (CMC) (the lowest surfactant concentration at which surfactant micelles become thermodynamically stable in solution) less than 0.1%. Such parameter choices produce properties that simulate short-chained ionic surfactants such as hexadecyltrimethylammonium bromide (CTAB). The calculated profile of a stable bilayer micelle in solution with the chosen parameters is shown in Fig. 4-7.

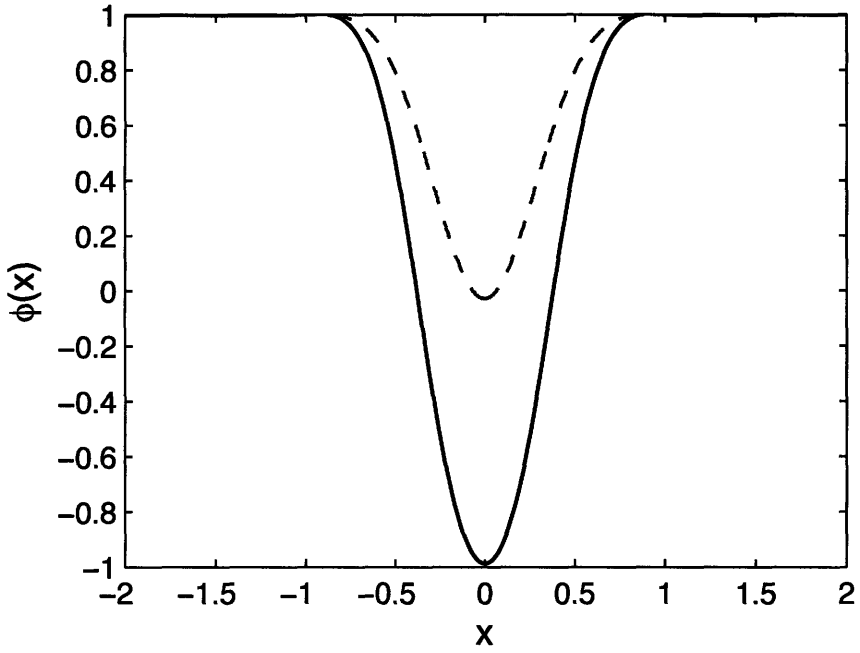

Figure 4-7: A calculated one-dimensional surfactant bilayer structure (solid line) in a solution of ϕ=0.999 with λ=0.005, H_0=0 and other parameters as specified in the text. Also shown is a saddle-point solution (dashed line) representing the critical micellar nucleus.

4.3.2 Numerical Algorithms for Solving the Kinetic Equation

A semi-implicit spectral method developed by Chen and Shen [237,238] is used to solve the equation of motion Eqs. 4.20 and 4.21 with periodic boundary conditions. The

semi-implicit scheme enables relatively large time steps while maintaining numerical stability. Details of the algorithm are given in Appendix B.

A singularity appears in Eq. 4.21 at $\nabla\phi = 0$ due to the $1/|\nabla\phi|$ term. A numerical approximation described in Ref. [136] is employed to remove this singularity by applying a cut-off to the inverse function

$$I_\gamma(\xi) = \begin{cases} \gamma, & 0 \le \xi \le \gamma \\ \frac{1}{\xi}, & \xi > 1/\gamma \end{cases} \tag{4.24}$$

where γ=1000 is chosen. This numerical treatment is equivalent to smoothing the discontinuity of $|\nabla\phi|$ at $\nabla\phi = 0$ in Eq. 4.6 by replacing it with the function

$$A_\gamma(|\nabla\phi|) = \begin{cases} \frac{\gamma}{2}|\nabla\phi|^2, & 0 \le |\nabla\phi| \le \gamma \\ \frac{1}{|\nabla\phi|} - \frac{1}{2\gamma}, & |\nabla\phi| > 1/\gamma \end{cases} \tag{4.25}$$

In all simulations except those noted in the following sections, a cubic cell of size 10×10×10 discretized by a 64×64×64 mesh was used. A refined mesh of 128×128×128 grid points was used in a few cases to confirm mesh size convergence, which are not shown here. Parallel codes were developed to run simulations on parallel computers using 16-64 CPUs, and the FFTW [239] numerical package is used to perform the fast Fourier transforms (FFT) required by the spectral method.

4.4 Simulations of Single Micelle Growth in Dilute Solutions

The phase-field model was applied to simulate the growth of a single micelle in a dilute but over-saturated (i.e. above the critical micelle concentration) surfactant solution. At the start of simulations, a small spherical micellar nucleus was "seeded" at the center of the simulation cell by using the following initial concentration configuration

$$\phi_0(x, y, z, t = 0) = \phi_s - (1 + \phi_s) \exp\left(-\frac{x^2 + y^2 + z^2}{r_0^2}\right) \tag{4.26}$$

where r_0 suggests the nucleus size and was set to 0.5. The solution surrounding the nucleus has a uniform surfactant concentration, ϕ_s (or a volume fraction of $c_s = (1 - \phi_s)/2$). A small Gaussian noise with an amplitude of $\Delta\phi = 0.005$ was added to the starting concentration profile to break the symmetry in the solution. Because c_s is above CMC, the micelle nucleus will grow at $t = 0$. The micellar growth was monitored by tracking the zero level set of $\phi(\vec{x}, t)$.

4.4.1 Effects of Spontaneous Curvature and Bending Moduli on Micellar Growth

A series of simulations were performed to examine how different spontaneous curvature (H_0) and bending rigidity (κ,$\bar{\kappa}$) values affect the micelle growth behavior in the phase-field model. The results were then compared to predictions from Helfrich's curvature elastic model. First, c_s=0.02, λ=0.0075 and H_0=1 were chosen. H_0=1 is a curvature value comparable to the reciprocal of the surfactant chain length (or one half of the bilayer thickness), $l_0 \approx 1$. Fig. 4-8 shows the snapshots of the micelle shape at different times. It is seen that the nucleus rapidly expands at the beginning of the simulation and becomes a stable spherical micelle by $t = 4$. Afterwards the micelle retains its spherical shape and size throughout the rest of the simulation although the surfactant concentration in the solution is still above CMC.

Next H_0 was decreased to 0.5, or $\sim 1/(2l_0)$, while keeping other parameters unchanged. As shown in Fig. 4-9, the nucleus first follows a similar expansion to form a spherical micelle as in the case of H_0=1. However, its shape begins to elongate in one direction after $t \approx 30$ and eventually becomes a rod-like micelle.

When H_0 remains at 0.5 and λ is reduced to 0.005, which corresponds to a decrease in the bending stiffness of the surfactant layer, a similar growth behavior is seen (i.e. a nucleus expansion followed by one-dimensional elongation, and a cylindrical micelle forms, viz. Fig. 4-10). However, the micellar growth demonstrates more flexibility than in the case of λ=0.0075 as the surfactant layer becomes "softer". A micellar morphology that is called "wormlike" or "threadlike" [240–242] is produced at the end

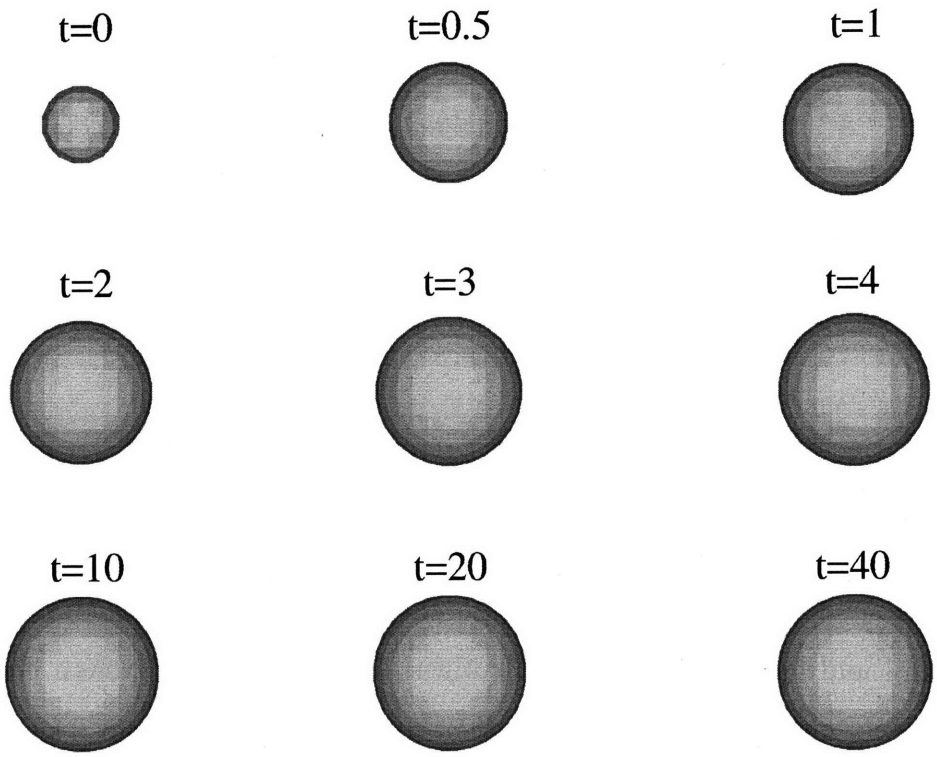

Figure 4-8: Snapshots of the $\phi = 0$ level surface during micellar growth at c_s=0.02, λ=0.0075 and H_0=1. The purpose of this figure is to test the model for the simplest known case and for comparison to subsequent simulations.

of simulation. The rodlike-to-wormlike morphological change induced by decreasing λ is associated with a decreased persistence length, l_p, of the cylindrical micelle [243]. l_p is related to the coherence of molecular angular-correlations along the micellar axis and scales with the interfacial bending rigidity [243]. In experiments, the bending stiffnesses of cylindrical micelles can be tuned by counter-ions, temperature, and co-surfactants. For example, adding co-surfactants with a shorter chain length to a micellar solution can significantly reduce the bending rigidity and l_p, and produce wormlike micelles which otherwise do not form in the absence of co-surfactants [244].

For both rodlike (Fig. 4-9) and wormlike (Fig. 4-10) micelles, it is noticeable that the end caps of the micelles are "swollen" and have larger radii than the cylindrical body. This feature can be explained by considering the variation of the curvature elastic energy density along the micelle: compared to the cylinder segment, the end

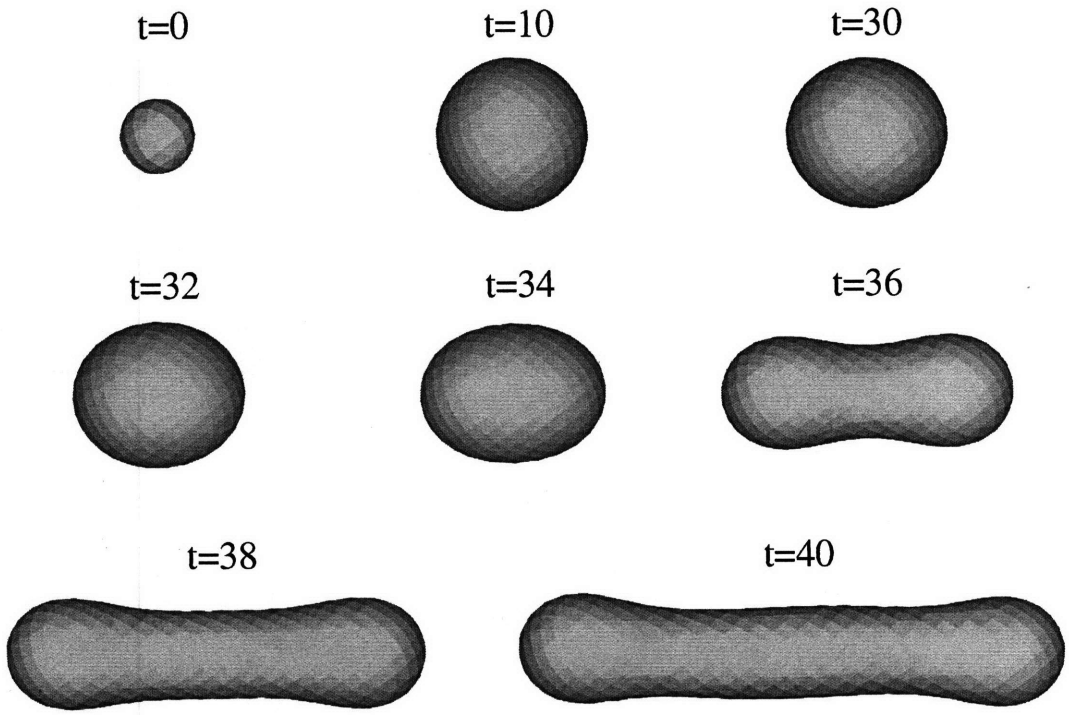

Figure 4-9: Snapshots of micellar growth show that a nucleus grows into a rodlike micelle at c_s=0.02, λ=0.0075 and H_0=0.5.

caps are associated with high curvature energies because their mean curvatures are significantly larger than the spontaneous curvature value, H_0=0.5. Increasing the cap radii reduces the magnitude of $H - H_0$ and thus diminishes the curvature energy difference between the end caps and cylindrical body. Similar predictions have been previously made for the equilibrium shape of rodlike micelles by curvature elastic energy calculations [213] and by molecular thermodynamic theories [245, 246], and was confirmed by cryo-TEM observations [106, 247].

In a surfactant solution with multiple micelles in thermodynamic equilibrium, a cylindrical micelle has an equilibrium length. Increasing the average micelle length decreases the density of end caps in solution and thus lower the excessive curvature energy associated with them. On the other hand, decreasing the average length can increase the total translational entropy of micellar solution. The competition between the two trends produces an equilibrium micelle length. It is shown [248] that this equilibrium length increases exponentially with the end cap energy. The

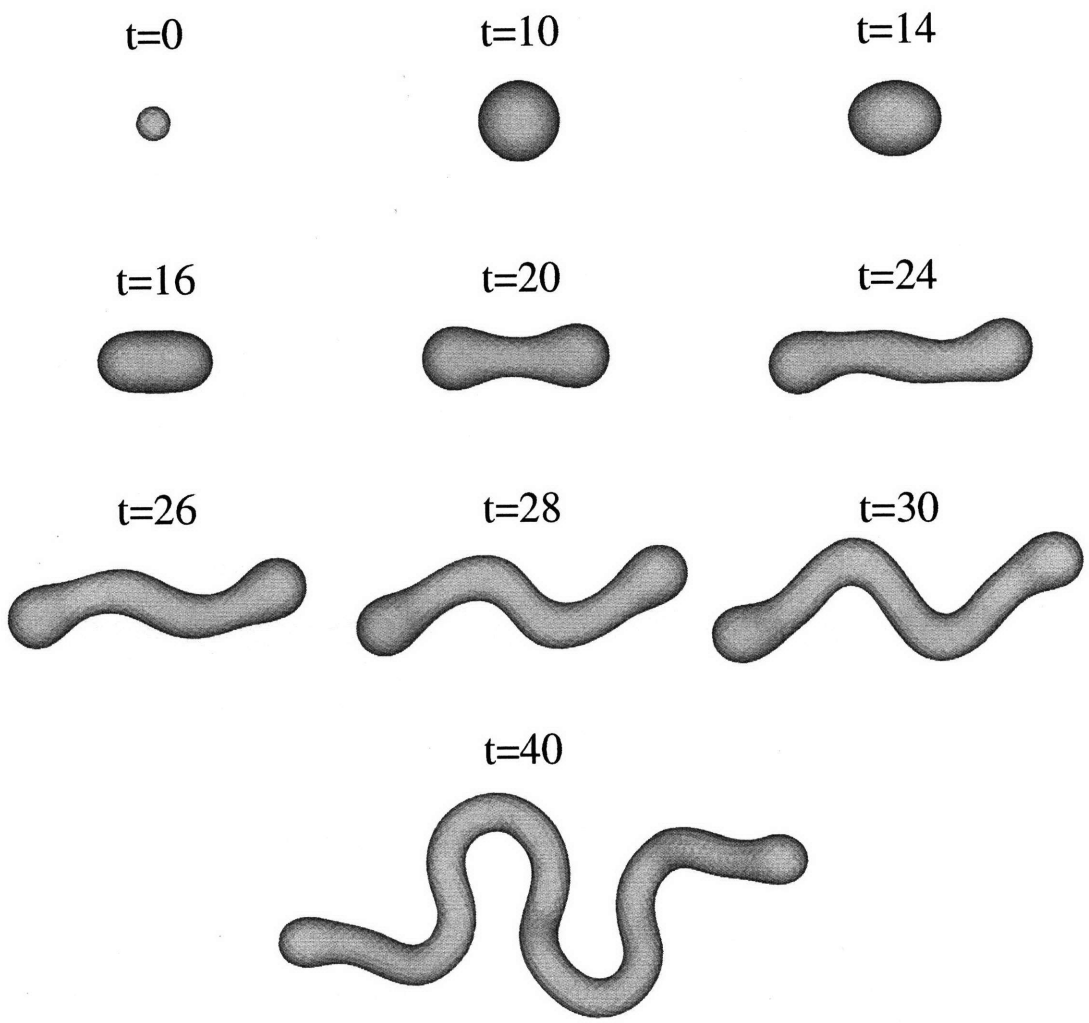

Figure 4-10: Snapshots of micellar growth show that a wormlike micelle forms at a lower bending rigidity, λ=0.005, with c_s=0.02 and H_0=0.5.

equilibration however is absent in our simulations of *single* micellar growth, where the cylinder length is only limited by the availability of surfactants (i.e., $\int \phi dV$) in the system and not by the equilibrium between micelles.

As H_0 was further decreased to 0, the micelle growth switches from one-dimensional to two-dimensional growth mode, producing a disklike micelle as shown in Fig. 4-11. The inner part of the disklike micelle has a zero mean curvature (i.e., is equal to the spontaneous curvature), but the rim region of the micelle is associated with a larger curvature energy penalty. With same reasoning as above, the disk rim with a swollen shape in Fig. 4-11 reduces its curvature energy. The disk micelle continues to expand with time to increase the area of its bilayer region favored by the zero spontaneous

curvature.

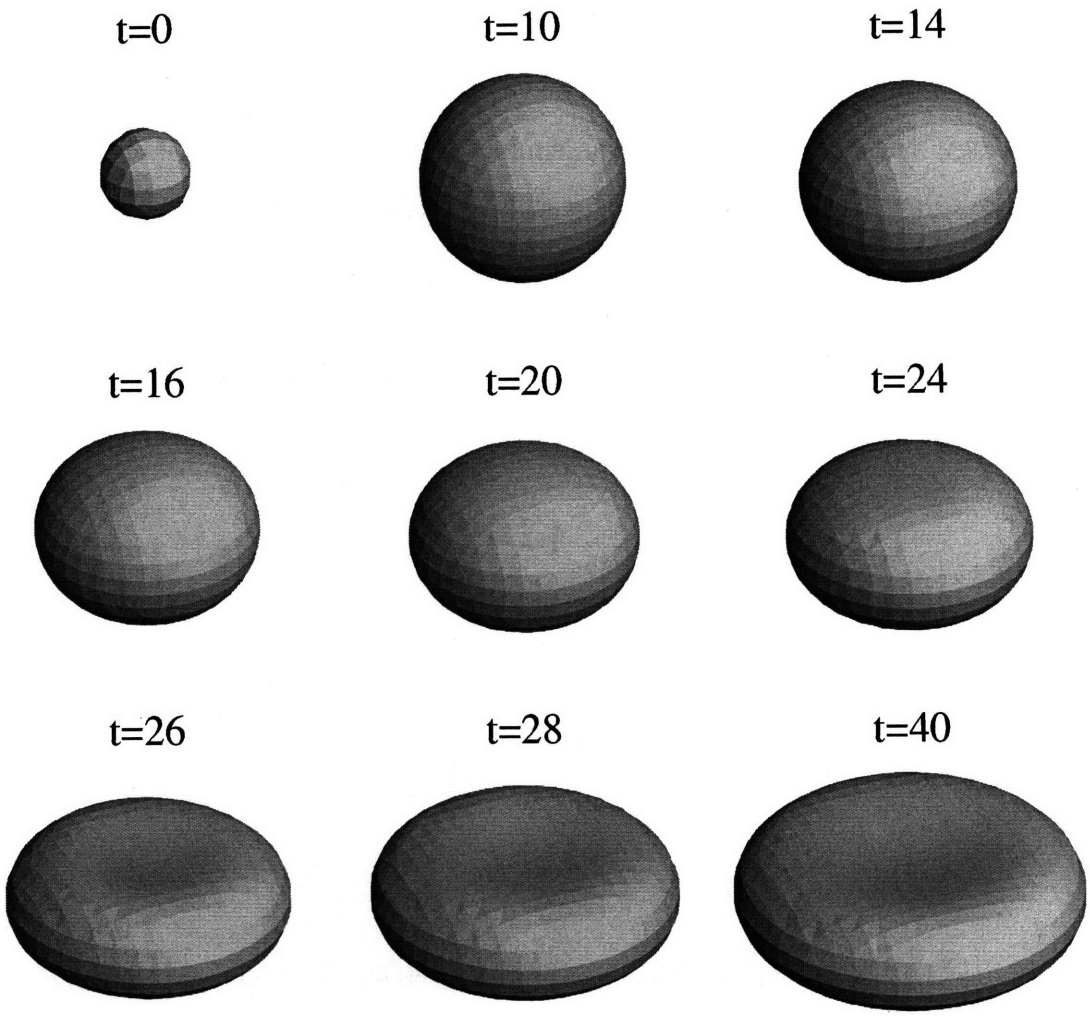

Figure 4-11: Formation of a disklike micelle at c_s=0.02, λ=0.005 and H_0=0.

The micelle morphologies presented in Figs. 4-8–4-11 and their dependence on the spontaneous curvature and bending rigidity conform to predictions made from the Helfrich model as described in 4.1. The simulations thus establishes that the phase-field model captures the curvature elastic energetics and its effect on micellar growth.

4.4.2 Morphological Instability of Micellar Growth: Disklike-to-Cylindrical Shape Transition

In the previous section, typical spontaneous curvature values ($H_0 \sim 1/l_0$, $1/(2l_0)$ and 0) that favor spherical, cylindrical and bilayer micelles were chosen in simulations for model validation. To further examine the spontaneous curvature effect on micelle morphology, the micellar growth was simulated with an intermediate spontaneous curvature value, H_0=0.25, which is between the H_0 preferred by cylinders and bilayers. Fig. 4-12 shows that a wormlike micelle forms at c_s=0.02 and λ=0.005 despite the unfavored spontaneous curvature. However, the micelle has a slightly larger radius (or lower mean curvature) than the wormlike micelle for H_0=0.5, which help reduce the curvature energy penalty.

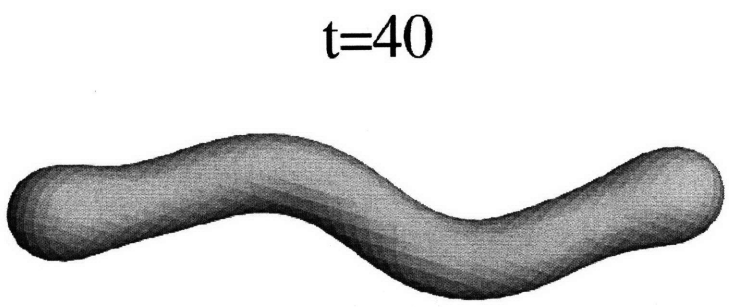

Figure 4-12: A wormlike micelle forms at c_s=0.02, λ=0.005 and H_0=0.25.

However, a different micellar growth behavior occurs at a higher surfactant concentration, c_s=0.03. As shown by the snapshots in Fig. 4-13, the nucleus initially grows into a disklike micelle that expands with time. However, the micelle develops a morphological instability at large disk radii, where the circular shape of the disk rim becomes unstable against radial perturbations. The amplitude of the perturbations grows with time, and four protuberances emerge at the growth front at $t \approx 28$. They continue to grow as finger-like cylindrical arms at the expense of the disk's bilayer region. At the end of the simulation, the disklike micelle is transformed into four cylindrical micelles connected by two"Y-shaped" three-way junctions. Similar branched

micellar structures have been observed in experiments [106–109, 242, 247, 249, 250] and they are termed branched wormlike micelles.

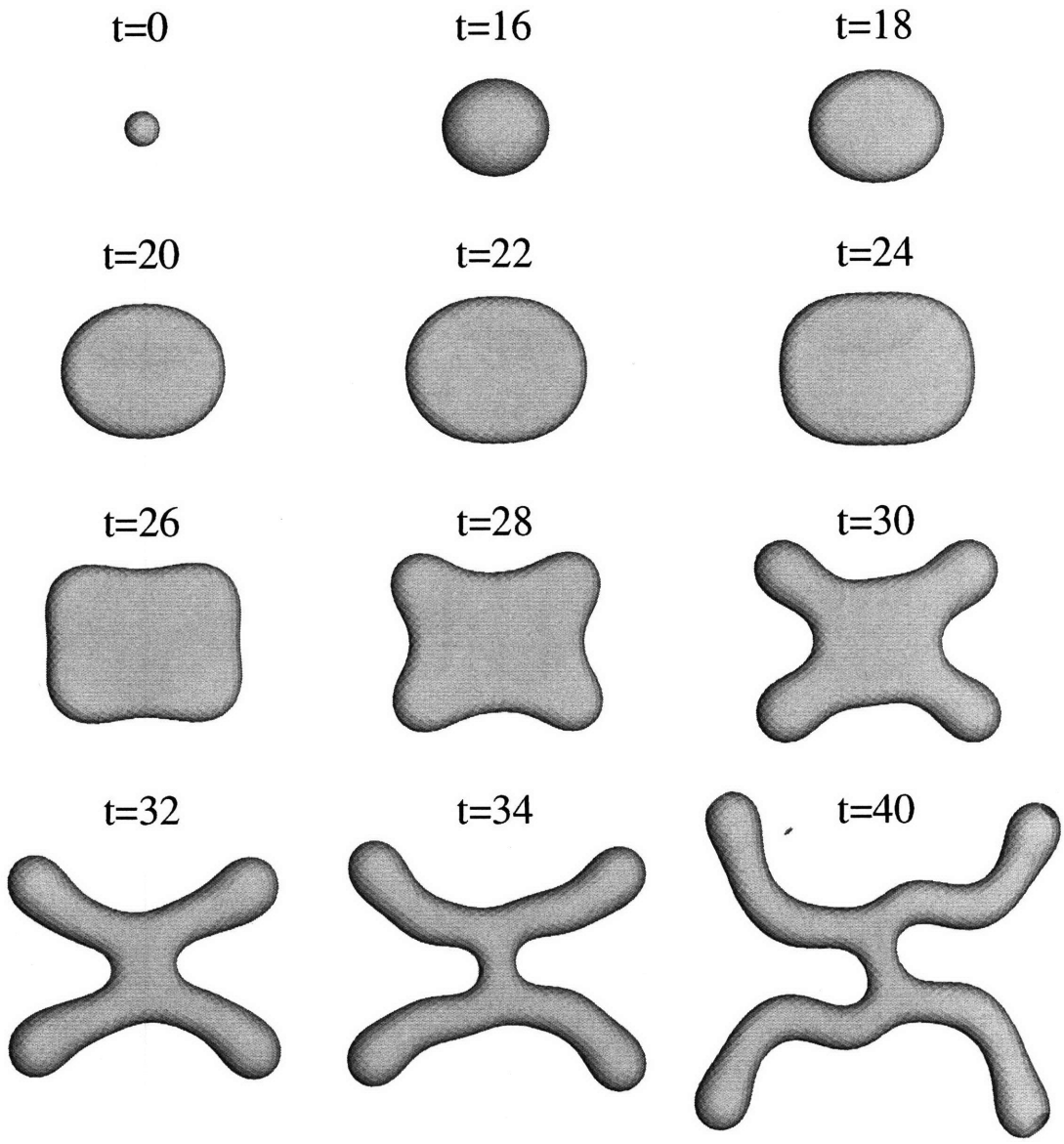

Figure 4-13: Snapshots of micellar growth at c_s=0.03, λ=0.005 and H_0=0.25.

A similar disk-to-cylinder morphological transition is also observed for micellar growth at c_s=0.04 (viz. Fig. 4-14), but six branches form from the disk shape perturbation, leading eventually to a branched micelle with more individual arms connected by four three-way junctions.

In Fig. 4-15, the scaled micelle volume is plotted against time for micellar growth

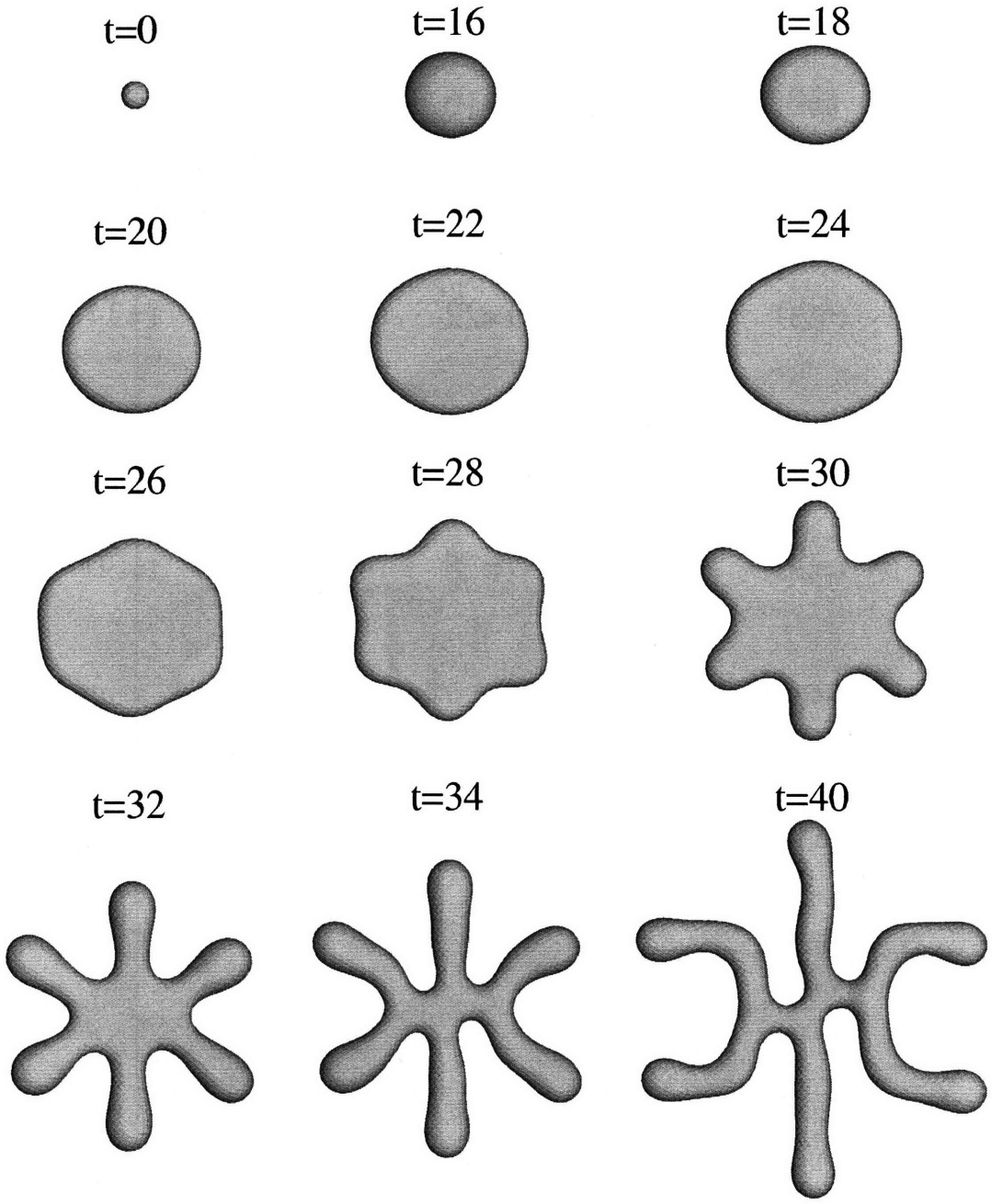

Figure 4-14: Snapshots of micellar growth at c_s=0.04, λ=0.005 and H_0=0.25.

with H_0=0.25 at the three concentrations c_s=0.02, 0.03 and 0.04. The micelle volume is calculated by multiplying the number of mesh points at which $\phi < 0$ by $(10/64)^3$ (the average space occupied by each mesh point). Micellar evolution at c_s=0.02 can

be divided into two stages. In the first stage, the nucleus quickly grows into a spherical micelle and then enters into an "incubation" period where the volume-growth rate becomes very low while the micelle transforms from spherical to ellipsoidal and then to cylindrical morphologies. Rapid growth recommences in the second stage during which the end caps of the cylindrical micelle extend at steady rate. The evolution changes qualitatively when c_s is increased to 0.03. Following the less pronounced "incubation"" period, the growth recommences by a fast two-dimensional disk expansion and then a slower cylinder-elongation regime. The growth-rate changes as the disk-rim perturbation develops and micelle morphological stability occurs between the two regimes. The relatively constant slope in the disklike growth regime suggests that the disk area increases at a steady rate and the radius growth rate decreases as $dr/dt \propto 1/r$. The growth curve of c_s=0.04 displays similar features to that of c_s=0.03, but the micellar growth rate is higher and the disk-to-cylinder transition occurs at larger radii.

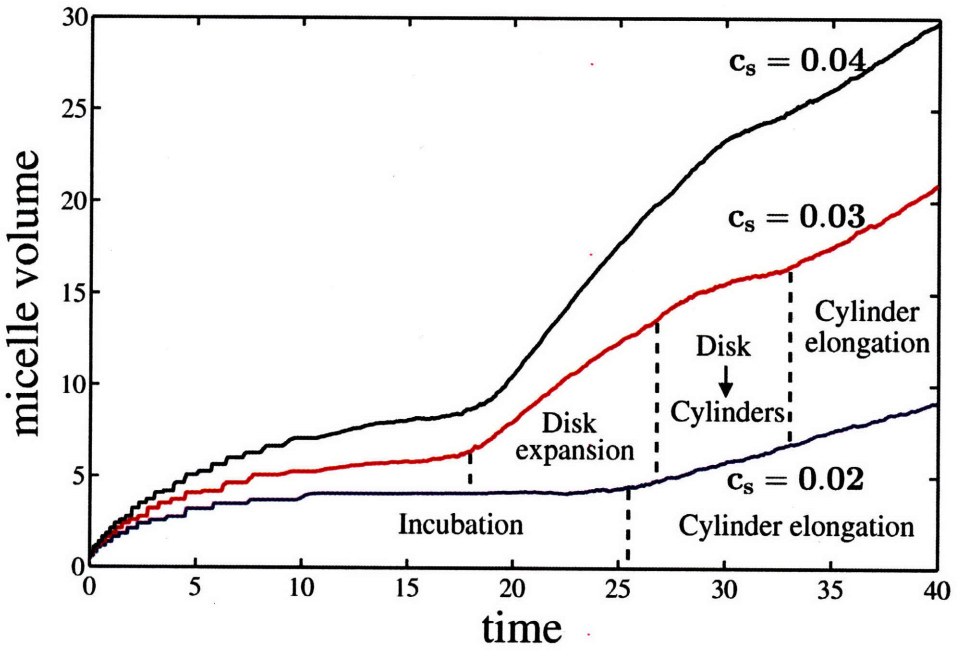

Figure 4-15: Micelle volume vs time curves for c_s=0.02, 0.03 and 0.04 with λ=0.005 and H_0=0.25.

An increase in the chemical driving force at higher surfactant concentrations (c_s=0.03 and 0.04) should be responsible for the change of the initial micellar growth

mode from one-dimensional cylindrical elongation to two-dimensional disk expansion. The total driving force for micellar growth consists of a curvature energy term, E_{curv}, and a chemical term, E_{chem}, which is the chemical potential difference between surfactants in solution and in a surfactant monolayer. Compared to a cylindrical micelle, the growth of a disklike micelle is associated with a smaller driving force due to its higher curvature energy density. However, such a difference in E_{curv} becomes relatively small compared to the magnitude of E_{chem} at high surfactant concentrations because E_{chem} increases with c_s but E_{curv} remains relatively constant. Despite the lower driving force, a disklike micelle may achieve a higher growth rate at large enough c_s through its two-dimensional growth and thus be kinetically favored. An analogous phenomenon, where surfactants preferring a spherical micelle shape grow into cylindrical micelles at relative high surfactant concentrations, has been observed in experiments [106].

The morphological instability of the disklike micelle and the formation of the branched micelle configuration also depends on the spontaneous curvature H_0. When H_0 is reduced to 0, the micelle retains the disklike shape throughout the simulations for c_s=0.03 and 0.04 (see Fig. 4-17). A shape transition does not occur when the simulations are stopped at $t = 40$, but the development of small perturbations is already visible around the disk rim. To further understand the origin of the disk-to-cylinder morphological transition, a perturbation analysis on the shape stability of a disklike micelle will be presented in the next section.

The geometry of a "Y-shaped" junction in a branched micelle can be modeled as consisting of a bilayer region and a saddle-like semi-toroidal region with two principle curvatures of opposite signs [201,251]; the mean curvatures in both regions are significantly lower than that of the cylindrical body. Thus it is expected that the existence of micellar branch points will become more energetically unfavorable as the spontaneous curvature increases. This was confirmed by simulations performed for H_0=0.5 at c_s=0.03 and 0.04 (Fig. 4-17). It is seen from Fig. 4-16 that a similar morphological instability occurs during the micellar growth at H_0=0.5 and c_s=0.03 which produces a transient branched micellar configuration. However, the inter-connections between

individual micelles are broken at a later stage due to the large curvature elastic energy stored in them. The micellar structure at the end of the simulation consists of two non-branched cylindrical micelles. Similar transition pathways are seen in the simulation of c_s=0.4— only one branch point survives from the evolution when the simulation was stopped (Fig. 4-17).

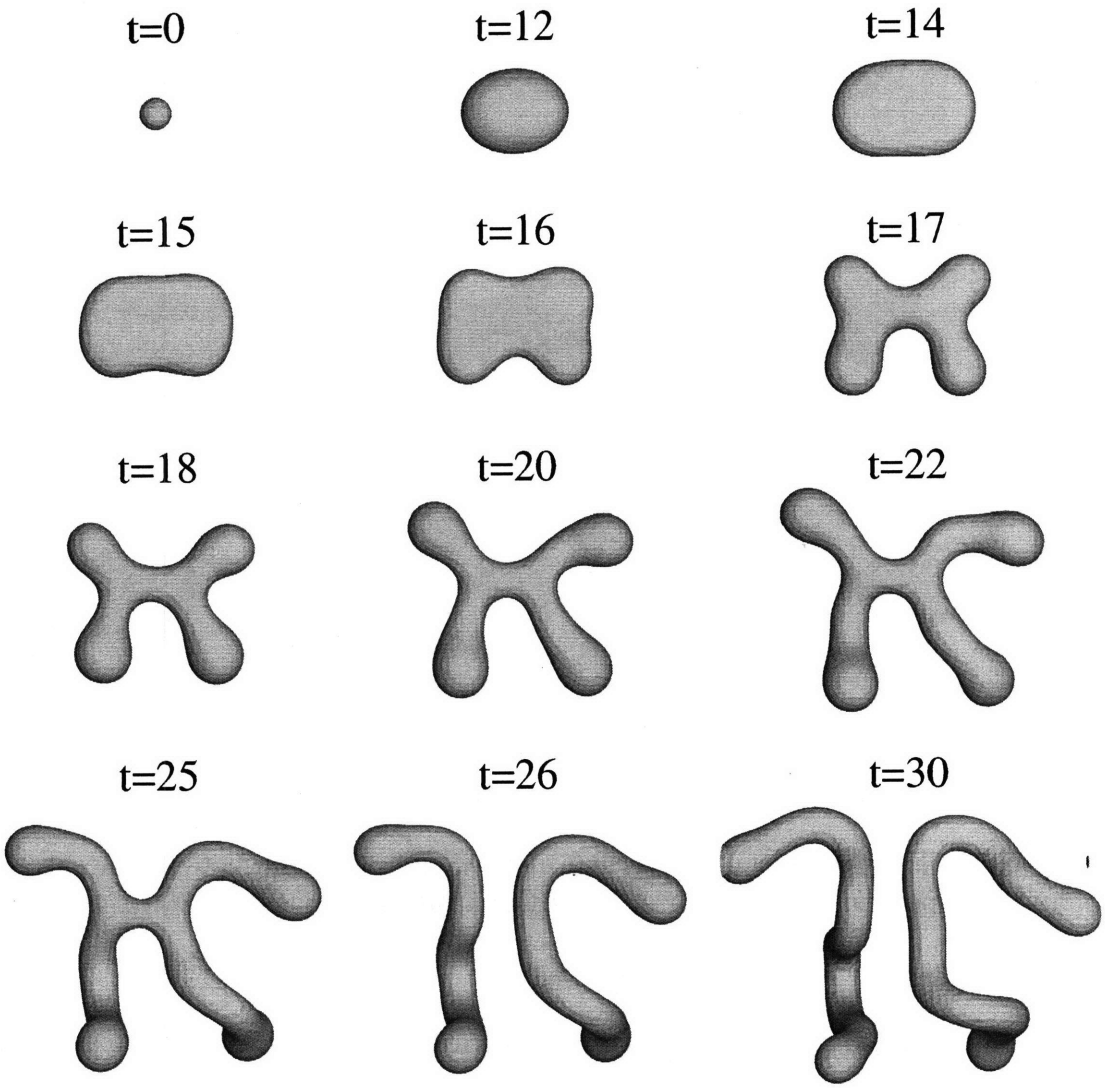

Figure 4-16: Snapshots of micellar growth at c_s=0.03, λ=0.005 and H_0=0.5. The transient branching points obtained from the disk-to-cylinder transition disappear by t=30 due to the high curvature energy of the junctions.

The above simulation results are summarized in Fig. 4-17, which displays the micelle morphology as a function of surfactant volume fraction (c_s=0.02–0.04) and

spontaneous curvature (H_0=0–0.5). Fig. 4-17 shows that the formation of branched micellar structure is promoted by increasing surfactant concentration and decreasing the spontaneous curvature.

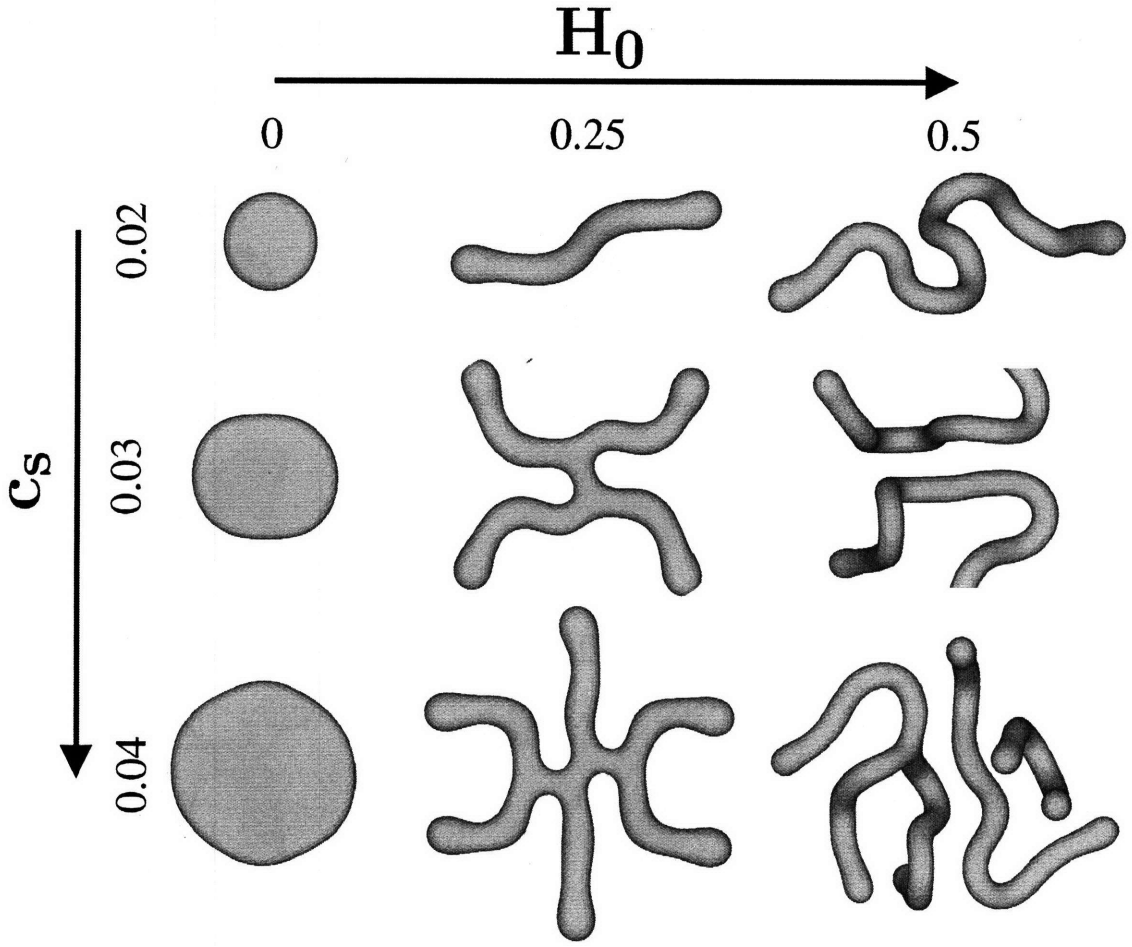

Figure 4-17: The dependence of micellar morphology on the surfactant concentration, c_s, and the spontaneous curvature, H_0. All snapshots are taken at t=40.

4.4.3 Perturbation Analysis of the Shape Stability of Disklike Micelles

The disk morphological instability observed in our simulations can be explained by a perturbation analysis of a sharp-interface model. Both the volumetric free energy change upon micellar growth and the curvature elastic energy of the micellar interface are considered in the model.

Consider a simplified disk micelle geometry as illustrated in Fig. 4-18. The disk's bilayer region has a radius R and thickness $2l_0$, with l_0 being the surfactant chain length. The disk rim has the shape of a half-torus with radii R and l_0. A perturbation in the form of sinusoidal wave is applied to the rim with an amplitude $\epsilon(t = 0)$ and n-fold symmetry:

$$r(\theta, t = 0) = R + l_0 + \epsilon(t = 0)\cos(n\theta) \quad n = 1, 2, ... \tag{4.27}$$

where n is the perturbation wavenumber.

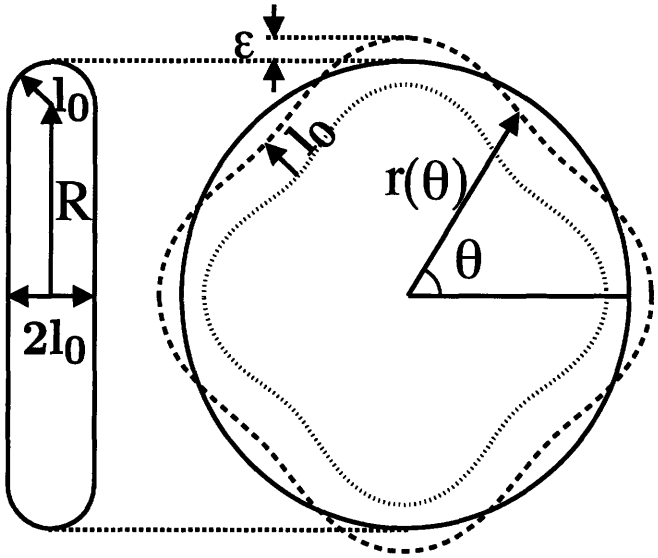

Figure 4-18: Schematic drawing of a disk micelle. The dashed and dotted lines illustrate the disk edge and the boundary of the bilayer region after a perturbation with n=4 in Eq. 4.27.

The total micellar free energy is partitioned into a curvature energy part and a curvature-independent chemical free energy part,

$$E_{tot} = E_{curv} + E_{chem} \tag{4.28}$$

Each part has contributions from the bilayer and the rim regions. With the assumptions that $R >> l_0$ and the thickness of the rim region remains l_0 after perturbation,

the curvature-energy part is given by

$$\begin{aligned} E_{curv} &= E_{curv}^{rim} + E_{curv}^{bilayer} \\ E_{curv}^{rim} &= \frac{\pi\kappa l_0}{2}\int_0^{2\pi}\left(c_r + \frac{1}{l_0} - 2H_0\right)^2 \sqrt{r(\theta)^2 + r'(\theta)^2}\,d\theta \\ E_{curv}^{bilayer} &= 2\kappa H_0^2 \int_0^{2\pi}(r(\theta) - l_0)^2 d\theta \end{aligned} \tag{4.29}$$

where the rim's radial curvature component, c_r, is

$$c_r = \frac{r(\theta)^2 - r(\theta)r''(\theta) + 2r'(\theta)^2}{r(\theta)^2 + r'(\theta)^2}^{3/2} \tag{4.30}$$

Because the total Gaussian curvature energy remains invariant when the micellar topology does not change, it is omitted in Eq. 4.29. The curvature-independent part is given by

$$\begin{aligned} E_{chem} &= E_{chem}^{rim} + E_{chem}^{bilayer} \\ E_{chem}^{rim} &= \frac{\pi\Delta\mu l_0^2}{2}\int_0^{2\pi}\sqrt{r(\theta)^2 + r'(\theta)^2}\,d\theta \\ E_{chem}^{bilayer} &= \Delta\mu l_0 \int_0^{2\pi}(r(\theta) - l_0)^2 d\theta \end{aligned} \tag{4.31}$$

where $\Delta\mu \equiv \mu^{\text{soln}} - \mu^{\text{mic},0} > 0$ is the chemical potential change per unit volume of surfactant molecules when they are transferred from over-saturated solution to micelles in a reference state (e.g. bilayer). Applying Eq. 4.27 to Eqs. 4.29 and 4.31 and Eq. 4.28, one finds the change of the micelle free energy upon a small perturbation to be

$$\begin{aligned} \Delta E_{tot}(\epsilon) &\equiv \Delta E_{tot}^{(2)}(\epsilon) + O(\epsilon^3) \\ &= \left\{ \frac{(n^2-1)^2}{2} - \left[\frac{\pi\Delta\mu l_0}{4\kappa} - \left(\frac{1}{2l_0} - H_0\right)^2\right] n^2 R^2 \right. \\ &\quad \left. - \left(\frac{\Delta\mu}{\kappa} - \frac{2H_0^2}{l_0}\right) R^3 \right\} \frac{\pi\kappa l_0}{R^3}\epsilon^2 + O(\epsilon^3) \end{aligned} \tag{4.32}$$

The leading term in the *perturbation* energy, $\Delta E_{tot}^{(2)}$, is proportional to $\epsilon(t=0)^2$.

Provided that $\Delta\mu$ is sufficiently large, a perturbation of any periodicity n can lower the micelle energy when the radius R is large enough to make Eq. 4.32 negative. At the early growth stage, the fast uniform expansion of the disk radius may eclipse any perturbation growth. Because dr/dt decreases, the perturbations at the disk rim will develop eventually if Eq. 4.32 is negative. As a first approximation, the perturbation growth rate $d\epsilon/dt$ is proportional to $-\partial\Delta E^{(2)}/\partial\epsilon \approx -2\Delta E^{(2)}/\epsilon$ (e.g., in a interface-limited growth), i.e.

$$\frac{d\epsilon}{dt} \propto -\frac{(n^2-1)^2}{2} + \left[\frac{\pi\Delta\mu l_0}{4\kappa} + \left(\frac{1}{2l_0} - H_0\right)^2\right] n^2R^2 + \left(\frac{\Delta\mu}{\kappa} - \frac{2H_0^2}{l_0}\right) R^3 \qquad (4.33)$$

Minimizing $d\epsilon/dt$ against n, the fastest growing wavenumber is

$$n_{\max} = 1 + \left[\frac{\pi\Delta\mu l_0}{4\kappa} - \left(\frac{1}{2l_0} - H_0\right)^2\right] R^2 \qquad (4.34)$$

which increases with R and $\Delta\mu$ (we use d/dn, but any physical n must be an integer). This is consistent with the simulations that show an increased n as c_s changes from 0.03 to 0.04. Moreover, $d\epsilon/dt$ is minimized by $H_0 = [2l_0(1+2R/(n^2l_0))]^{-1}$ with other parameters being fixed, which shows that the instability is mostly likely to occur at H_0 values that are in between the spontaneous curvatures preferred by bilayers or cylinders (i.e., $0 < H_0 < 1/(2l_0)$).

4.4.4 Morphological Instability of Cylindrical Micellar Growth

The simulations and the linear stability analysis presented in 4.4.2 and 4.4.3 show that a large driving force for micellar growth promotes the morphological instability of disk micelles. Through simulations it was found that a different morphological instability can similarly be induced at the growth fronts of cylindrical micelles when facing large driving forces (i.e. high surfactant concentrations).

To illustrate the cylindrical micellar instability, a two-stage simulation was run in a simulation box of size 10×10×20 on a 64×64×128 mesh grid. In the first stage of the simulation, a cylindrical micelle is induced to grow along the cell's long axis

in a solution of c_s=0.02 with H_0=0.25. The second stage commences at t=10, at which the surfactant concentration in the solution is suddenly increased to c_s=0.03 (this is done by locating the mesh points at which $\phi > 0.94$ and and setting their ϕ values to 0.94), and hence a large driving force is applied to the cylindrical growth. This simulates the local chemical environment variation a micelle may experience in solution during its growth. As shown by the snapshots in Fig. 4-19, the end cap of the micelle undergoes a morphological transition at the same time while the cylinder keeps elongating after t=10. The end cap first "swells" and flattens to form a bilayer-like local structure, and then splits into two individual arms which further grow into two cylindrical micelles and leaves a "Y-shaped" junction behind. Therefore, inter-micellar junctions may be produced from the disk-to-cylindrical micellar transition, and also from the tip-splitting event that occurs at the growth front of cylindrical micelles. The instability may similarly be studied by a perturbation analysis as in 4.4.3.

The morphological instability of cylindrical micelles is not seen in the simulation shown in Fig. 4-13 which was also run at an initial c_s of 0.03. This, however, is a finite-size effect of the simulation cell. Because the total amount of surfactants is conserved in simulations, the surfactant concentration in the remaining solution keeps decreasing with micellar growth. When cylindrical micelles emerge from the disk-to-cylinder transition, the surfactant concentration may drop well below its initial value and there is not a large enough driving force to trigger their morphological instabilities. This decrease of driving force with micellar growth can be reduced by increasing the simulation cell size. A different simulation was thus performed with the same parameter settings as in Fig. 4-13, except with a larger simulation box of size 40×40×40 discretized by a 256×256×256 mesh. In the simulation (Fig. 4-20), the micelle first undergoes the same disk-to-cylinder transition which produces four inter-connected protrusions, and more cylinder segments are further generated afterwards by the tip-splitting at the end caps of several cylindrical arms.

Fig. 4-20 illustrates a kinetic pathway through which branched points can be repeatedly produced at the micelle growth front through the morpholgoical instabilities

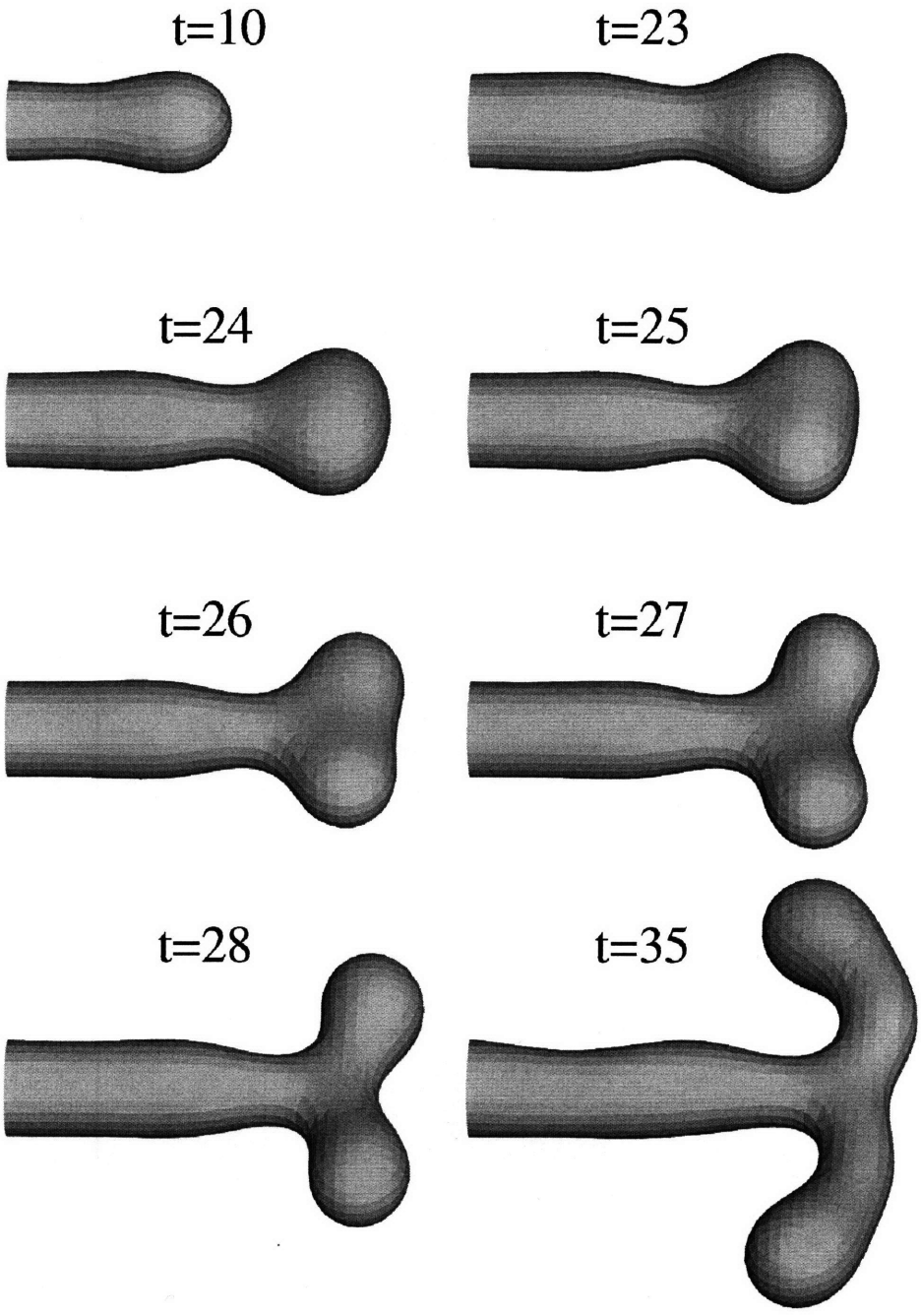

Figure 4-19: Snapshots of the growth of a cylindrical micelle at c_s=0.03, λ=0.005 and H_0=0.25.

of disklike and cylindrical micelles. Thus it is possible to generate an inter-connected cylindrical micellar network from a single micellar nucleus.

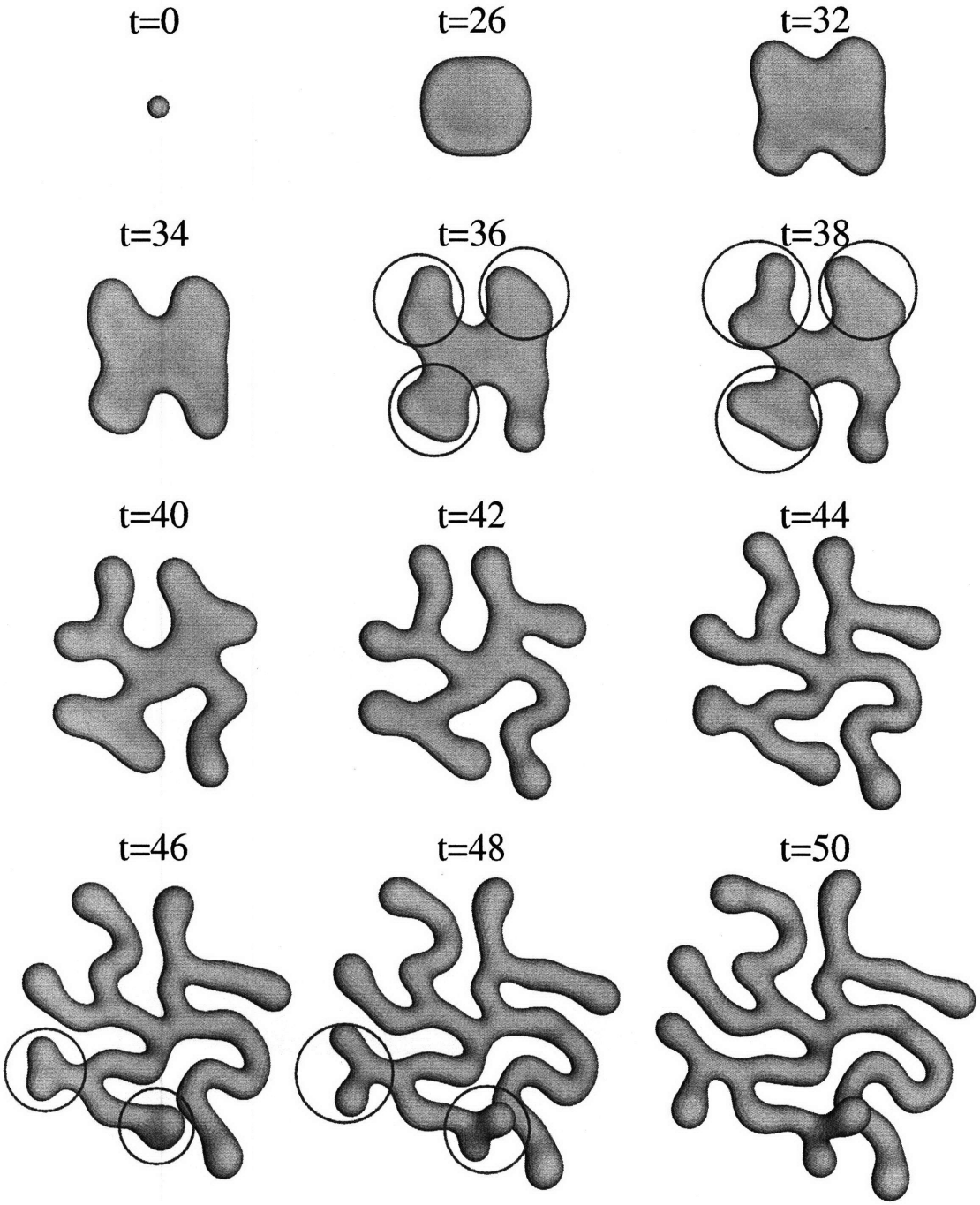

Figure 4-20: Snapshots of micellar growth at c_s=0.03, λ=0.005 and H_0=0.25 in a large simulation cell of size 40×40×40 discretized by a 256×256×256 mesh. The tip-splitting events that occur at the end-caps of cylindrical micelles are highlighted by circles.

4.5 Discussion

The morphological instabilities of disklike and cylindrical micelles observed in simulations provide possible kinetic pathways to the formation of branched wormlike micelle structures. Branched micelles have been experimentally observed and extensively studied in various surfactant systems [106–109, 111, 112, 242, 247, 249, 250, 252–256]. Micellar branching can result in significant changes in structural and rheological properties of surfactant solutions [107,109,111,112,252–256] and has technical importance. For example, the formation of branching points was found to change the repetition mechanism of the entangled wormlike micelles during stress relaxation and causes a decrease in viscosity.

Theoretical studies on micellar branching have been mainly focused on the energetics of micellar junctions [201, 213, 251] and on the thermodynamic stability of the inter-connected micellar network [257–261]. Molecular-level model calculations show that forming a Y-shaped junction always results in a positive energy change to the micellar structure [201], similar to forming other micellar defects such as end caps of cylindrical micelles. However, defects will exist in solutions at equilibrium because of their entropic contribution, whose population is proportional to $\exp(-\Delta E_d/kT)$, where ΔE_d is the formation energy of a specific type of defect. Statistical mechanical models [257–261] predict that branched networks will become the equilibrium micellar structure over non-branched micelles when the formation energy of branching points is smaller than that of end-caps. Some predictions of these models (e.g. the existence of a phase separation of semi-dilute solutions of branched micelles into a micelle-rich and micelle-depleted phase) have been confirmed by experiments [108].

Combining molecular-level calculations of junction energetics and the statistical theories, the conditions under which a branched network becomes thermodynamically stable can be understood. However, how micellar junctions evolve or develop has not been satisfactorily explained. One hypothesis is that a Y-shaped junction forms when a cylindrical micelle's end-cap merges with another micelle [201, 213]. In a coarse-grained atomistic simulation, it was found that Y-shaped junctions can be

produced from the impingement of wormlike micelles under tension [262]. Our simulations suggest a plausible and different scenario, in which the formation of branching points does not necessarily involve multiple micelles. Multiple junctions and inter-micellar network structures can be produced from the morphological transitions of a single disklike or cylindrical micelle through disk-to-cylinder transition and splitting of cylindrical end caps, as illustrated in Fig. 4-20. The transitions depicted here are not two-body processes and do not depend on low-probability collisions, and hence might be the dominant mechanisms for generating branch points, especially in dilute surfactant solutions which have low micelle densities. However, these modes of Y-shaped junction formation certainly do not exclude one another — they may happen simultaneously during micellar growth.

Our simulations show that the tendency towards stabilized branch points during micellar growth increases with surfactant concentration (compare c_s=0.02, 0.03 and 0.04 in Fig. 4-17) and with a decreased spontaneous curvature (compare H_0=0.5 and 0.25 in Fig. 4-17). This tendency can be rationalized by the effects of c_s and H_0 on the kinetic pathways. Similar trends have been confirmed in experiments. The development of junctions between cylindrical micelles has been found to occur with increasing surfactant concentrations [106, 108, 254], increasing electrolyte concentrations for ionic surfactant systems [107, 109, 111, 112, 254], and increasing temperature for non-ionic surfactant systems [108]. Adding salts (electrolytes) to ionic surfactant solutions can effectively screen the eletrostatic repulsion between head groups and reduce H_0. Similarly, increasing temperature can reduce the H_0 of a non-ionic surfactant layer due to a decreased hydration number (the concentration of water molecules between head groups) at higher temperatures [263]. The observed dependence of micellar branching on surfactant and salt concentrations and temperature has mainly been explained from the thermodynamic stability of inter-micellar junctions [107, 109, 254]. Simulations suggest that kinetics can also contribute to such phenomena.

Transitions that are analogous to the micellar morphological instabilities observed in the phase-field simulations have been reported for vesicle systems. Different from a

micellar structure, a vesicle consists of a bilayer interface which separates the solution into the outer and inner parts. However, morphologies of both structures are regulated by the curvature elastic energy. Light microscopy observations revealed a vesicle shape transition that transforms an initially disklike vesicle to a structure termed "starfish" vesicle upon increasing the vesicle's surface-area-to-volume ratio [21, 102–104]. Experimentally such a transition can be induced by gradually increasing the osmotic pressure of the solution (e.g., adding salts) outside a vesicle to decrease its volume and keep its surface area constant. The "starfish" vesicles display a very similar morphology to the branched cylindrical structure, and its transition sequence is analogous to the disk-to-cylinder transition observed in the simulations [102].

Compared to vesicle shape transitions, direct observation of morphological transitions of micellar structures could be more difficult. Because of their nanoscale sizes, surfactant micelles need to be imaged by TEM. Current TEM techniques (e.g. cryogenic TEM) usually require samples of micellar solutions to be frozen and imaged at the liquid nitrogen temperature to avoid artifacts such as solvent evaporation and staining [264]. This essentially excludes the possibility of in-situ observation of micellar morphological transitions. Recent development in neutron, X-ray and light scattering techniques with high time resolution provides an alternative approach for studying the dynamics of morphological instabilities of micellar structures [265, 266]. For example, the kinetic pathways of the micelle-to-vesicle transitions in lecithin-bile salt mixtures have been revealed in details by time-resolved light and neutron scattering experiments [267, 268]. It is expected that such techniques can be applied to verify the disk-to-cylinder shape transition predicted here.

4.6 Conclusions

The morphological evolution of surfactant aggregates in solutions is studied in this chapter. A new phase-field model for simulating surfactant micellar growth was proposed. A detailed analysis of the free energy functional shows that the phase-field formulation both captures the self-assembling behavior of surfactants in solutions

and incorporates the curvature elastic energy of surfactant layers. This was further validated by numerical simulations. The phase-field model recovers the Helfrich model [113] in the limit of sharp/flat interfaces. Moreover, it extends the curvature elastic energy model to the kinetic regime and thus increases its predicative power.

Simulations of single micelle growth in dilute solutions were performed based on the phase-field model. The simulations produce a rich set of micellar structures that depend on physically measurable quantities such as the spontaneous curvature and bending rigidity of surfactant layers. In each case, the theory and simulations agree with experimental observations. Dynamic morphological instabilities are revealed to develop at micellar growth fronts at relatively high surfactant concentrations. For micelles that form a disklike shape during the initial growth, a disk-to-cylinder shape transition can occur at a later stage and transforms the micelle into multiple cylindrical micelles connected by Y-shaped junctions. The branch points tend to break off at relatively large spontaneous curvatures, but remain stable with decreasing the spontaneous curvature. A perturbation analysis of the shape stability of disklike micelles shows that the disk shape is unstable against the growth-front perturbation at sufficiently large disk radii. The shape instability is promoted by increasing surfactant concentration and spontaneous curvature.

A second type of morphological instability was observed to occur at the end caps of cylindrical micelles, where a micelle splits into individual cylinders connected by a branch point. It was found that the two shape transitions can occur subsequently during micellar growth: the end caps of cylindrical micelles can undergo tip splitting repeatedly following the disk-to-cylinder transition to produce an increasing number of cylindrical segments and Y-shaped junctions.

Based on the numerical simulation results, it is proposed that micellar morphological instabilities provide kinetic pathways to the formation of branched wormlike micelles observed in experiments. Unlike previously proposed mechanisms that depend on two-body collision events [201, 213, 262], multiple inter-micellar junctions can be produced from a single micelle through morphological transitions.

Chapter 5

Equilibrium Wetting of Silicon Oxide on Silicon Surfaces

5.1 Introduction

The oxidized silicon surface arguably forms the most important interfacial structure in the history of technology, having underpinned the development of microelectronics. Moore's law, being dependent on gate feature length scales, now relies on nanometer scale siliceous or modified composition gate oxides. The silicon free-surface spontaneously forms a silicon oxide when the ambient P_{O_2} exceeds its equilibrium value determined by reduction in molar free energy, ΔG, for the reaction $Si+O_2 \Leftrightarrow SiO_2$: $P_{O_2} = P_{O_2}^{ref} \exp(-\Delta G/RT)$. Perhaps because top-down device fabrication has typically been conducted at oxygen partial pressures many orders of magnitude above that for Si/SiO_2 coexistence, the wetting behavior of the silicon oxide on silicon near thermodynamic equilibrium has not been well-understood. At equilibrium in a closed system of an adsorbate on a substrate, there are three different wetting characters [269–271]: complete wetting where adsorbate forms a flat thick layer on the substrate surface, partial wetting where adsorbate forms islands upon a bare substrate or a microscopic adsorbate layer, and pseudopartial wetting where adsorbate islands coexist with a flat, thin adsorbate film due to the competition between short-range and van der Waals forces. In an open system where the adsorbate phase can grow, the

adsorbate's kinetic morphology is also affected by its wetting behavior that relates to different growth modes such as Frank-van der Merwe, Volmer-Weber and Stranski-Krastanov growth [272]. Thermal or native silicon oxides usually form a perfectly flat layer on silicon, but they are grown under conditions so far from equilibrium that they do not represent the equilibrium wetting behavior. It has been discovered in several two-phase inorganic material systems [86, 87] that near chemical equilibrium conditions, wetting equilibrium consists of impurity-rich surficial films having a self-selecting nanometer scale thickness. The thickness, structure and composition of such films are thermodynamically controlled by the impurity activities. In this chapter, we developed a solid-state buffer method to systematically access oxygen activity near Si/SiO_2 coexistence. Treating oxygen as the impurity we found that a similar sub-nanometer surficial oxide layer is present on the Si(001) surface at oxygen partial pressures close to and above the Si/SiO_2 equilibrium. This discovery may provide a new methodology for the control of gate oxide interfacial structures in planar silicon devices as well as new topologies for use in nanoelectronics.

5.2 Experimental Methods

To ascertain the equilibrium wetting properties of the silicon–oxygen system, experiments accessing extremely low values of P_{O_2} must be designed. Current UHV systems, with upper limits of vacuum degree around 10^{-14}atm, cannot produce low enough oxygen partial pressure to reach the Si/SiO_2 equilibrium level, e.g., $P_{O_2}^{SiO_2/Si} = 10^{-40}$atm at 700°C . In addition, the under-saturated SiO vapor phase in UHV systems causes SiO_2 to decompose at high temperatures [273, 274], a phenomenon accommodated in device processing but which poses serious problems for the understanding of the stable silicon oxide-silicon interface structure at low oxygen activities.

To overcome these limitations, a simple experimental methodology was developed, in which the sample of interest (here, a section of Si(001) wafer) is annealed together with a solid-state two-phase buffer to thermochemically establish the oxygen activity in an encapsulated quartz tube. The experimental setup is illustrated in Fig. 5-1.

Zr/ZrO_2 buffers were used in experiments. The Zr/ZrO_2 buffer lies below Si/SiO_2 on the Ellingham diagram (Fig. 5-1(a)), has high melting points, and has no intermediate oxides. The buffer consists of Zr (average particle size (APS) 23μm, 95+% purity, Hf nominal 2%) and ZrO_2 (APS 1μm, 99.5% purity, Hf<100ppm) powders which were obtained from Alfa Aesar, USA and loosely pressed into a tablet. Undoped Si(001) wafers were cut into pieces of less than 1cm×1cm each, and native oxide on the surface was removed by dipping in 10%HF for 1-2 minutes before the wafers were encapsulated into quartz tubes together with the buffer. Fused quartz tubes (made from General Electric grade 214 quartz) were obtained from G. Finkenbeiner Inc. and cleaned by water and isopropanol before use. An initial vacuum of $\leq 10^{-6}$ torr within the tubes was obtained using a diffusion pump before sealing the tubes.

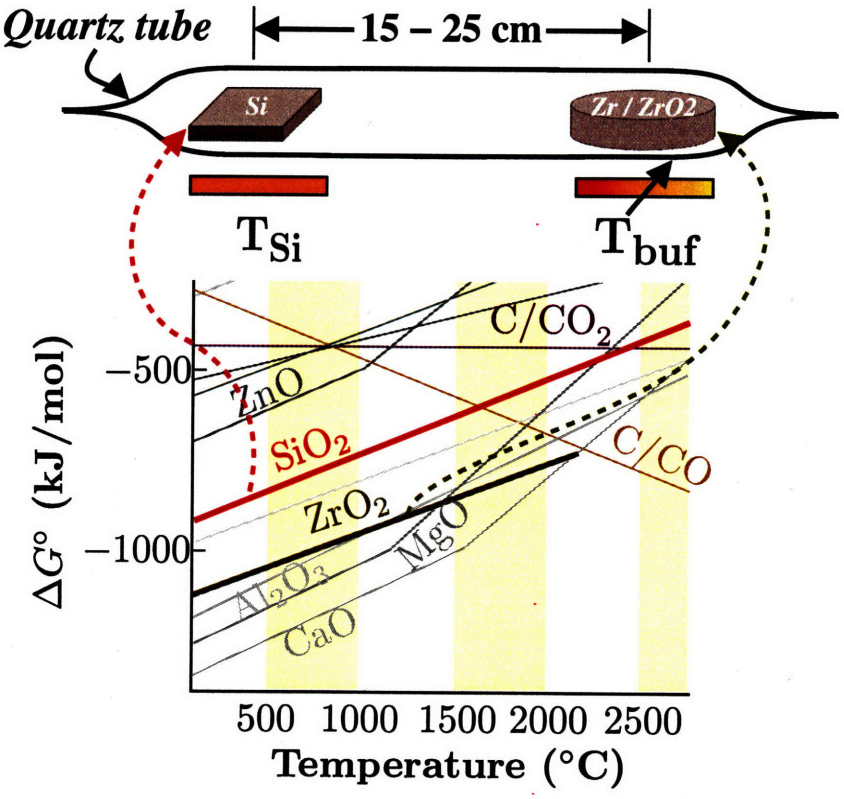

Figure 5-1: Schematic illustration of the solid-state buffer method for equilibrating the Si(001) surface at ultralow P_{O_2} : a Si(001) wafer and a Zr/ZrO_2 two-phase buffer are placed at the two ends of a sealed quartz tube. The silicon wafer temperature is fixed at 700°C , and the buffer is at an adjustable second temperature that specifies the ambient P_{O_2} as illustrated by the Ellingham diagram.

Following encapsulation, the samples were placed in a Lindberg/Blue tube furnace with controllable heating zones. The silicon wafer was held at a fixed temperature (700°C) and the buffer is at an adjustable second temperature. The total surface area of the buffer powders is orders of magnitude greater than that of the silicon wafer or the inner surface of the quartz tube. The P_{O_2} within the tube is thus fixed by the equilibrium at the buffer, which is furthermore controlled by the buffer temperature, T_{buf}, according to:

$$P_{O_2}[\text{atm}] = \exp\left[-\frac{\Delta G^{\circ}_{Zr/ZrO_2}(T_{\text{buf}})}{RT_{\text{buf}}}\right] \tag{5.1}$$

where $\Delta G^{\circ}_{Zr/ZrO_2}(T)$ is the standard free energy of oxidation for Zr as a function of temperature as illustrated by the Ellingham diagram. During annealing, P_{O_2} in excess of the equilibrium value is eventually fixed by oxidation of the buffer metal, while oxygen is readily supplied to the silicon wafer at fixed P_{O_2} upon reduction of the buffer oxide.

The surface structure and morphology of the post-annealed samples were characterized by X-ray photoelectron spectroscopy (XPS), atomic force microscopy (AFM) and transmission electron microscopy (TEM). XPS measurements were carried out on a Kratos AXIS Ultra Imaging Spectrometer with a monochromatic Al Kα beam at 1487eV. AFM measurements were performed on a Digital Instruments NanoScope IIIa, and images were analyzed with the accompanied software (version 5.12r5). TEM images of cross-sectioning samples were recorded on a JEOL-2010 microscope. It is noted that the samples were exposed to air for a short time (less than 5 minutes) during their transfer from quartz tubes to the XPS chamber, which may introduce undesired surface oxidation and override the original surface state. However, this possibility was excluded by a series of control experiments (see next section).

Analysis of the acquired XPS spectra was conducted using CasaXPS [275] and based on the deconvolution procedure recommended by Seah et al. [276], which is outlined below.

After removal of a Shirley background and X-ray satellites in CasaXPS, the metallic Si 2p peak was separated into the $2p_{3/2,1/2}$ spin-orbit splitting with 50% of the

intensity and a 0.6 eV difference in binding energy (BE). The oxidized Si 2p structure was fitted with 4 peaks (70% Gaussian, 30% Lorentian), where the Si^{1+}, Si^{2+} and Si^{3+} peaks are respectively at 0.95eV, 1.75eV and 2.48eV higher BE with respect to the metallic Si $2p_{3/2}$ peak [4, 277, 278]. The Si^{4+} peak was allowed to float freely between 3.3 and 4.2 eV higher BE. All peaks' full widths at half-maxima (FWHM) were constrained between 0.5 and 1.8 eV. In the next step, the intensity ratios of oxidized to metallic silicon signal were determined at 0°, 35° and 70° take-off angles (measured against the surface normal), where the intensity of oxidized silicon was calculated as the sum of the individual intensities for all oxidized states. An average oxide composition of SiO_x was determined from the intensity-weighted average of Si^{x+} (x=1,2,3,4) peaks. Using this information, the attenuation length λ_{SiO_x} was calculated as a linear interpolation between the attenuation lengths of Si in Si (2.72nm) and in SiO_2 (3.62nm) [279, 280]. Because bulk non-stoichiometric SiO_x is not available, the intensity per unit surface area from a bulk SiO_x sample, $I^{\infty}_{SiO_x}$, is approximated by $I^{\infty}_{SiO_2}$, which was acquired with I^{∞}_{Si} at take-off angles θ=0° , 35° and 70° .

5.3 Results and Discussion

5.3.1 Control Experiments

When the silicon wafer is at T_{Si} =700°C, Fig. 5-2 shows that a Zr/ZrO_2 buffer at T_{buf} =700°C produces a P_{O_2} of $<10^{-49}$ atm that should strongly reduce any surface silicon oxide to silicon. This was demonstrated in a series of control experiments shown in Fig. 5-3. First, a null experiment (a 24-hour anneal of a Si(001) surface at 700°C with no Zr/ZrO_2 buffer to fix P_{O_2}) was conducted. The XPS Si 2p spectrum shows a large Si^{4+} peak at <103 eV, indicating the presence of a greater than 1 nm SiO_2 film at the Si surface that is formed by reaction with residual oxygen in the tube. The Si(001) wafer was then annealed at 700°C for 24h with a Zr/ZrO_2 buffer at T_{buf} =700°C using two different initial surface conditions: either the oxidized wafer from

the null experiment, or an HF cleaned wafer was used. The disappearance of the large Si^{4+}-peak in the XPS spectra of both samples confirms that the buffer fixes the P_{O_2} below the Si/SiO_2 equilibrium level and reduces the surficial SiO_2 to Si. The XPS Si 2p spectrum of an HF-cleaned surface was also measured after about 30 minutes of exposure to air prior to XPS analysis. It shows a barely detectable oxide similar to the second and third control samples, most likely arising from the brief air exposure of the samples during transfer to the XPS chamber. The four control experiments together establish that the buffers are thermodynamically and kinetically effective in controlling the amount of surface oxide.

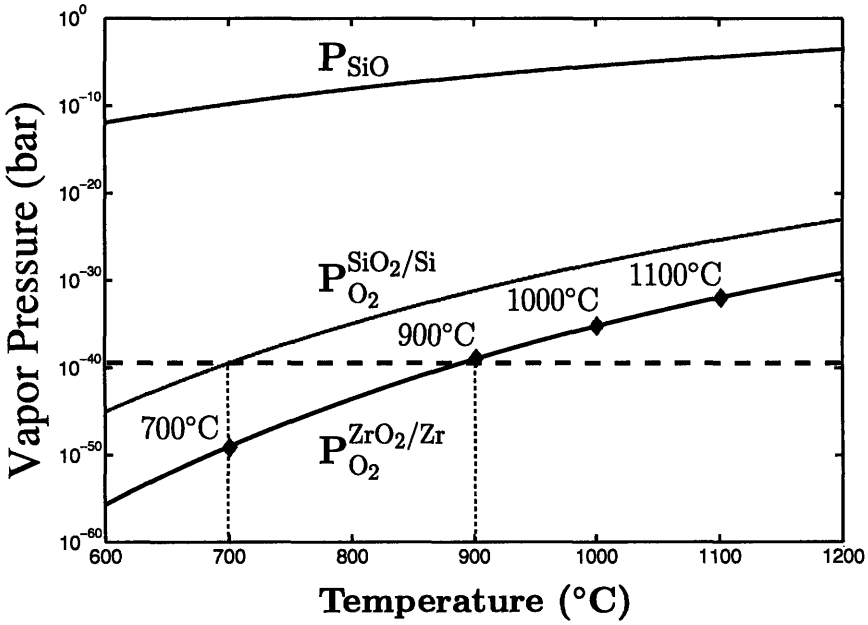

Figure 5-2: Equilibrium partial pressure of oxygen for the Si/SiO_2 and Zr/ZrO_2 systems illustrating the equilibrium P_{O_2} for the annealing experiment. The high partial pressure of SiO vapor, which is fixed by equilibration of silica surfaces at the buffer end of the experiment, is also illustrated; it provides a potential source of oxygen and silicon for rapid equilibration at the Si surface. Thermodynamic data are taken from Ref. [3].

5.3.2 Si Surface Oxidation and the Formation of SiO_x Islands

When the silicon wafer temperature is fixed at T_{Si} =700°C and T_{buf} is increased to 900°C , 1000°C and 1100°C , the ambient P_{O_2} changes systematically from strongly

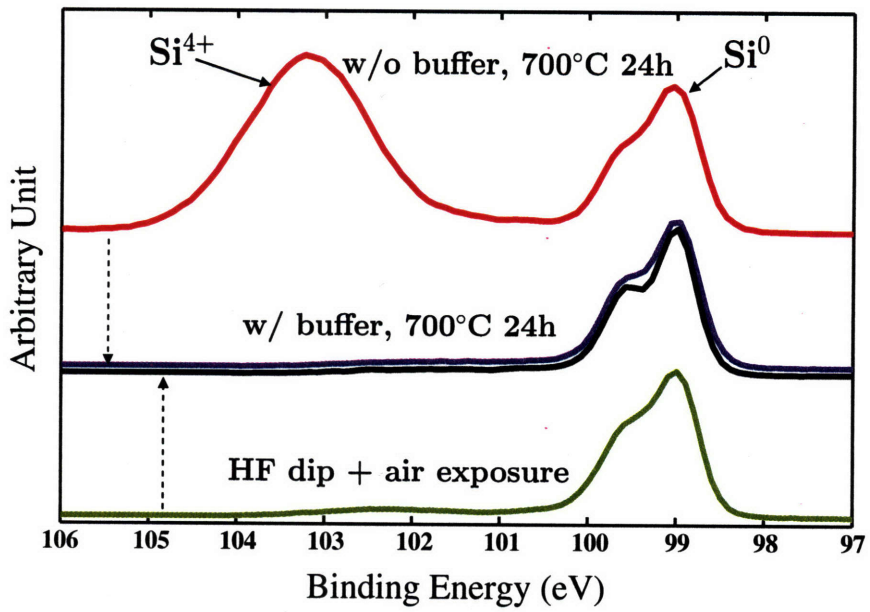

Figure 5-3: XPS Si 2p spectra of Si(001) wafer surfaces in control experiments, measured at takeoff angle θ=70° off-normal. The top curve illustrates the null experiment, that is, Si(001) annealed at 700°C for 24 h without the Zr/ZrO_2 buffer. The two middle curves are the results of the Si(001) surface after 24h of annealing with Zr/ZrO_2 buffer at T_{buf} =700°C ; the oxidized wafer from the null experiment was used for annealing in the blue curve, and an HF-cleaned wafer was used in the black curve. The lower curve is obtained from an HF-cleaned surface with about 30 min of air exposure and without annealing.

reducing to near-equilibrium to oxidizing, as shown in Fig. 5-2. Comparing the XPS Si 2p spectra in Fig. 5-4 to that in Fig. 5-3 shows that a stable surficial silicon oxide appears on the Si(001) surface as the P_{O_2} increases to and beyond the Si/SiO_2 equilibrium level (48h annealed samples). Note that upon varying the buffer temperature from T_{buf} =900°C to T_{buf} =1000°C , the P_{O_2} increases by a factor of 10^4, yet very similar Si 2p spectra are observed, indicating a broad activity regime of stable adsorbate coverage. XPS analysis of the Si chemical shift shows that the surficial oxide is sub-stoichiometric with an average composition $SiO_{1.61}$. When T_{buf} is increased to 1100°C , P_{O_2} is now 8 orders of magnitude above its equilibrium value, yet the Si(001) surface still shows a limited degree of oxidation. As a consequence, the surficial oxide does become more stoichiometric, as shown in Fig. 5-4, and its average composition is determined to be $SiO_{1.73}$.

To characterize the morphology of the surficial silicon oxide observed in XPS,

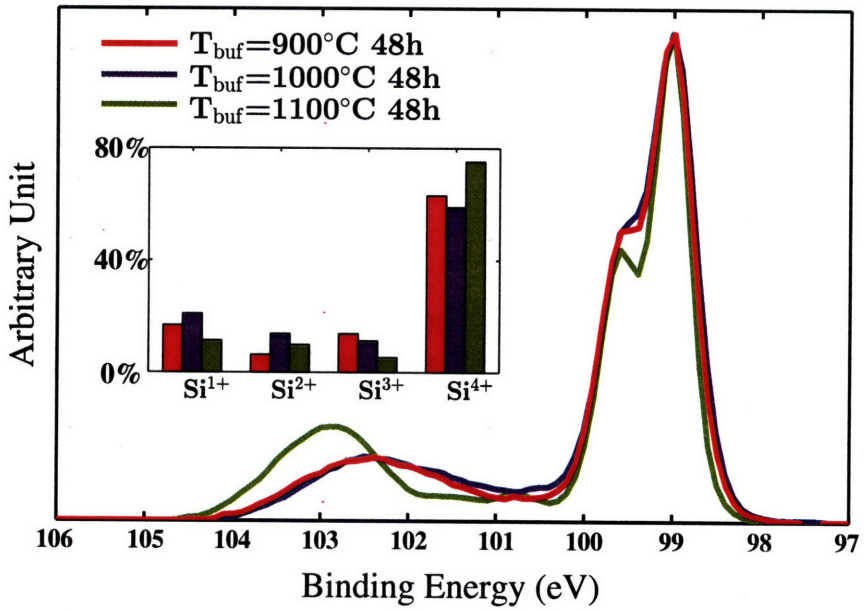

Figure 5-4: Comparisons of XPS Si 2p spectra (θ=70°) of Si(001) with 48h anneals at 700°C with T_{buf} =900°C, 1000°C and 1100°C (corresponding to ambient P_{O_2} of 10^{-40},10^{-36}, and 10^{32} atm), showing that the SiO_x stoichiometry increases with increasing P_{O_2}. The inset bar chart (same color scheme as that for the curves) gives the percentages of different oxidized silicon components, obtained by decomposing the Si 2p photoelectron line as in Ref. [4].

tapping-mode AFM measurements were conducted on Si(001) surfaces after annealing. AFM height images of the Si surface that was in equilibrium with the strongly reducing Zr/ZrO_2 buffer at 700°C are essentially featureless (viz. Fig. 5-5(a)). However, AFM height images of the surface equilibrated at T_{buf} =900°C show numerous islands having a spherical cap shape. Fig. 5-5(b) shows the islands on a sample annealed for 48h. As measured from the image, these island features have average heights of 21±6nm and average diameters of 220±50nm. A narrow distribution of wetting angle ϕ=15.3° ±2.4° was determined by measuring 35 islands. The spherical cap morphology of the islands is also clearly seen in cross-sectional TEM images (Fig. 5-6(a)-(b)). XPS composition analysis of the sample surface confirms that the surface is predominantly Si and O, with trace amounts of C, F (presumably from HF cleaning), and Zr (from the buffer) being detected. The oxide comprising the spherical caps also exhibits no diffraction contrast in the TEM; it is concluded that the islands are amorphous silicon oxide.

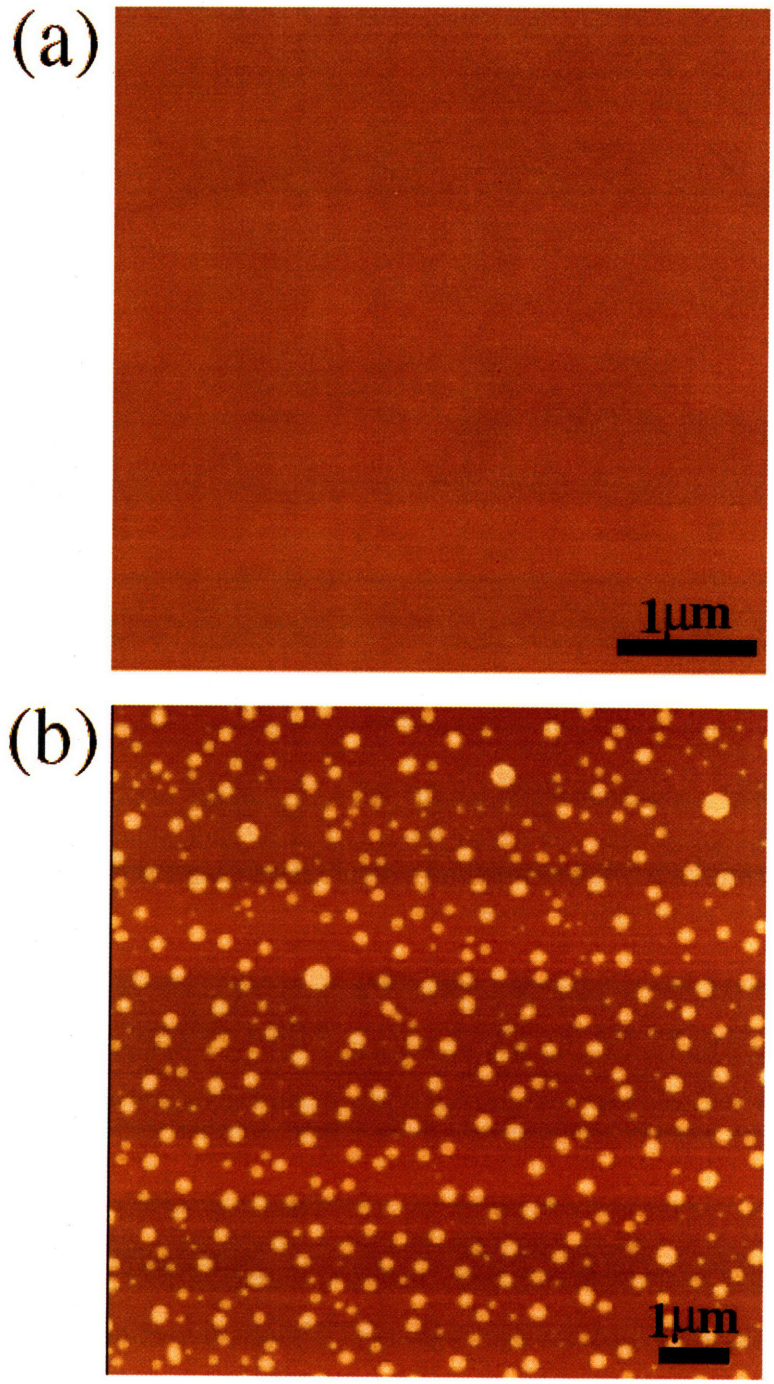

Figure 5-5: Tapping-mode AFM height images of Si(001) surface morphology with different buffer annealing temperatures, T_{buf} . (a) a $5\mu m \times 5\mu m$ area of the Si(001) surface annealed for 48 h with T_{buf}=700°C demonstrating no noticeable features. (b) a $10\mu m \times 10\mu m$ area of the Si(001) surface after equilibrating at T_{Si}=700°C with a Zr/ZrO_2 buffer at T_{buf}= 900°C for 48h, showing the presence of islands on an otherwise flat surface near thermodynamic equilibrium.

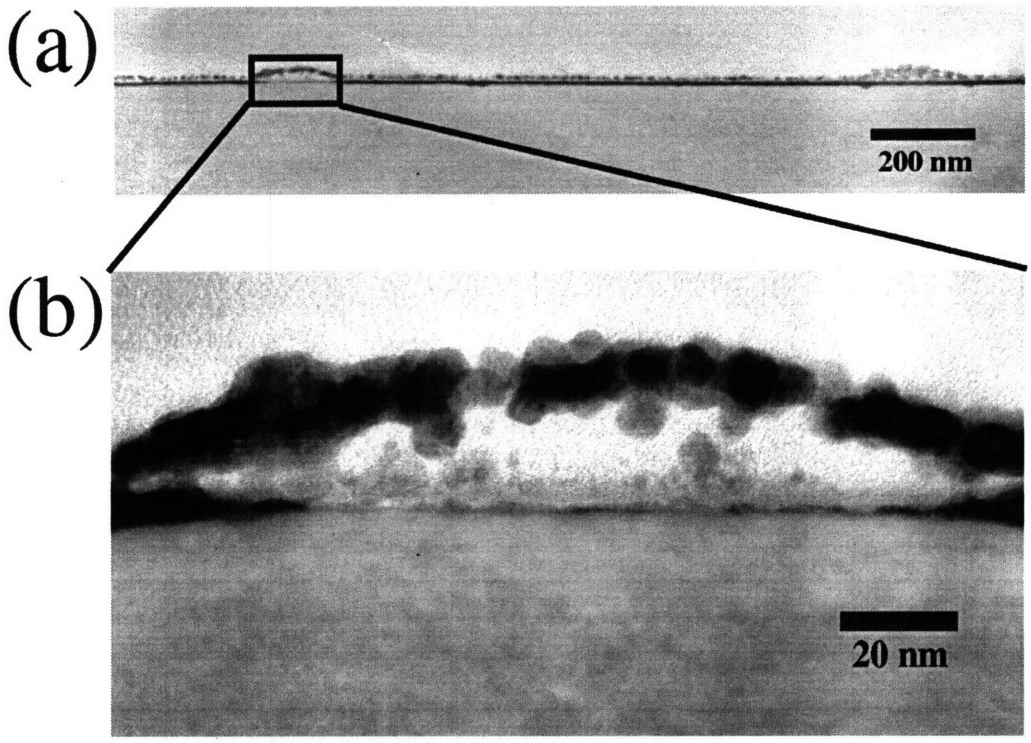

Figure 5-6: TEM cross-sectional images showing island and interface morphology. The sample was coated with a <10 nm Au-Pd layer by thermal evaporation to preserve the surface morphology. Two islands are visible in (a), and the close-up image of one island at a higher resolution is shown in (b).

As shown in Fig. 5-7(a)-(c), the characteristic SiO_x island size increases with annealing time. A ten-fold increase in island height and diameter is seen when annealing time increases from 4h to 48h. The total aggregate volume of islands as measured from Fig. 5-7(a)-(c) increases with annealing time. However, AFM scanning reveals that the island density varies considerably throughout the Si(001) surface of all samples, where Fig. 5-7(a)-(c) represent the regions of highest densities. XPS Si 2p spectra, which cover a surface analysis area of $700\mu m \times 300\mu m$, show that the average oxide coverage on a much larger length scale is relatively constant, even decreasing slightly at long annealing times, as shown in Fig. 5-8. This suggests that the islands grow by coarsening. Thermodynamic calculation shows that the SiO vapor pressure created at the buffer end, which is determined by the reaction between the buffer and quartz tube

$$Zr + 2SiO_2 \Leftrightarrow ZrO_2 + 2SiO \tag{5.2}$$

exceeds the equilibrium level at the sample wafer (held at 700°C) by a factor of 10^7. Remarkably, continued growth of the SiO_x layer on the wafer does not occur. Noting that vapor phase SiO must decompose and nucleate Si in order to grow the SiO_x layer, e.g., $2SiO \Leftrightarrow Si + SiO_2$, the stability of the surface oxide and islands is attributed to the existence of a large nucleation barrier for SiO decomposition. On the other hand, equilibration of gaseous oxygen with the surface is evidently fast, as illustrated by the facile film formation and removal in the control experiments (Fig. 5-3). Given the experimental results, the following scenario is suggested: the equilibrium oxygen activity in the tube is not fully established by the buffer at the initial stage of the annealing, and residual oxygen in the tube creates a much larger oxygen partial pressure which may oxidize the silicon wafer surface and form a non-equilibrium oxide film, as supported by the null control experiment. After the oxygen activity is reduced by equilibration with the buffer, over-saturated surfacial oxide is removed by the vapor phase and by surface transport to nucleate islands at preferential sites that are possibly related to underlying defects in the wafer. The islands subsequently coarsen to reduce their total surface energy.

5.3.3 Angle-Resolved XPS Analysis of Silicon Surficial Oxide Wetting Morphology

After finding the formation of silicon oxide islands on Si(001), a next goal is to establish whether the non-wetting islands coexist with a bare Si surface or a continuous SiO_x film. Cross-sectional TEM is often used for characterization of such films, but the uncertainties introduced by added long-time exposure to high oxygen activity environment during TEM sample preparation, which took several hours to a day, are unacceptable. However, angle-resolved XPS analysis allows non-destructive characterization of very thin films [4, 276]. For a Si(001) surface covered by a flat nanometer-scale SiO_x film, the intensity ratio of Si^{x+} to Si^0 is expected to have the

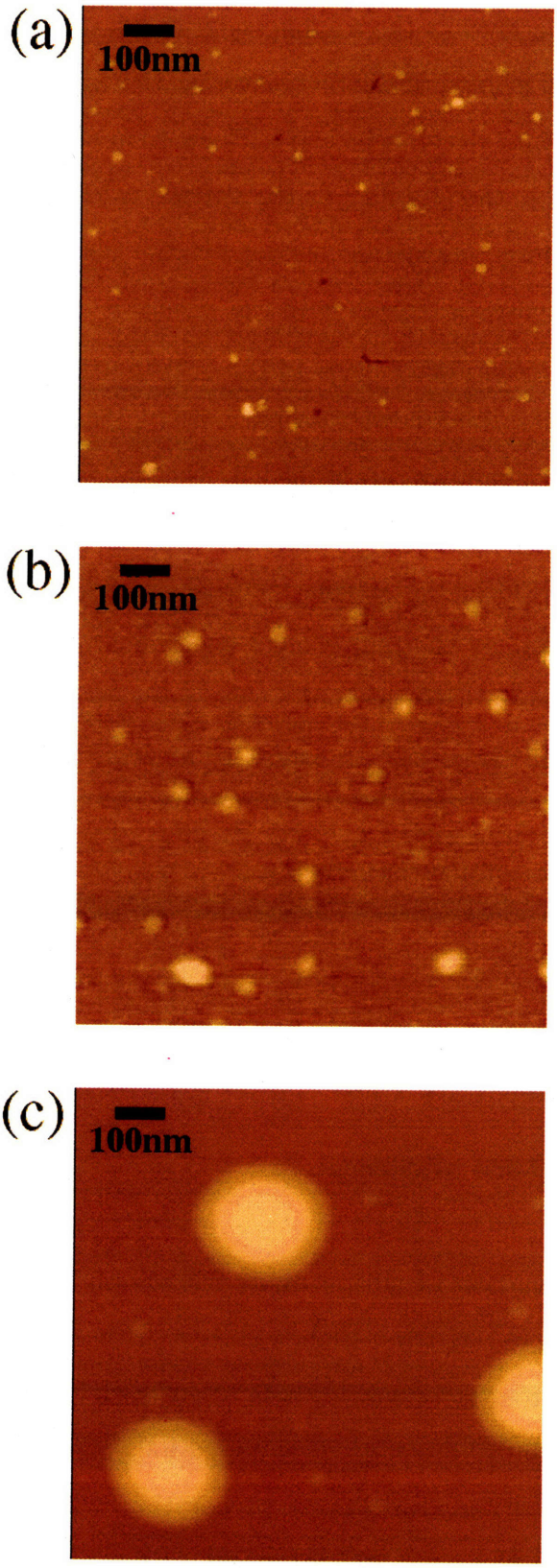

Figure 5-7: Chronological sequence of AFM images of Si(001) surfaces equilibrated with T_{buf} =900°C for 4, 8, and 48h, showing that the islands coarsen by decreasing their number density while increasing their length scale.

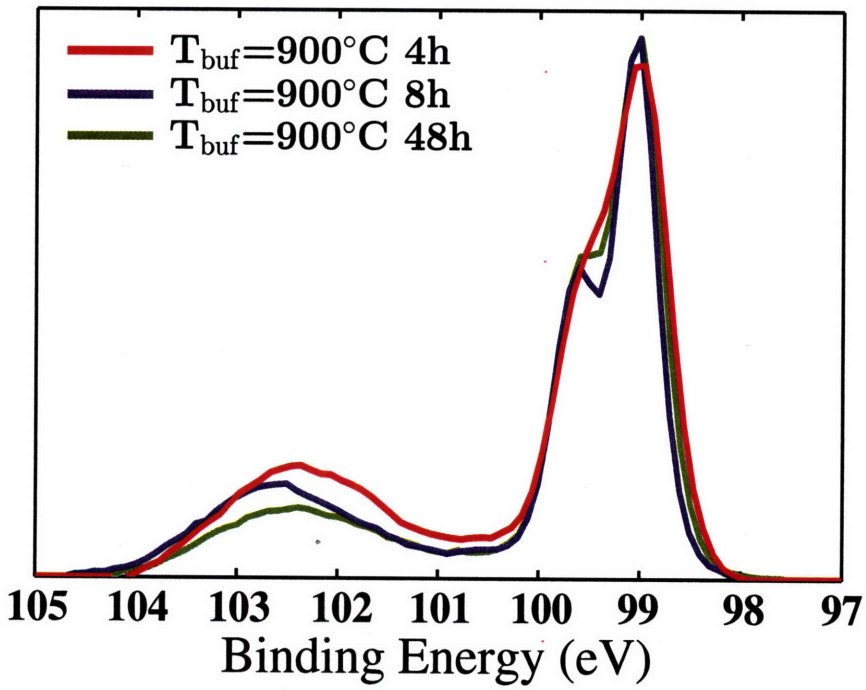

Figure 5-8: XPS Si 2p spectra (θ=70°) showing that the average oxide coverage, measured from an area 10^3 times larger than the AFM scanning area, does not vary significantly with annealing time.

following angular dependence [276,277]

$$\frac{I_{SiO_x}}{I_{Si}} = \frac{I^{\infty}_{SiO_x}\left[1-\exp\left(-\frac{d}{\lambda_{SiO_x,SiO_x}\cos\theta}\right)\right]}{I^{\infty}_{Si}\exp\left(-\frac{d}{\lambda_{Si,SiO_x}\cos\theta}\right)} \tag{5.3}$$

where d is the film thickness, and λ_{SiO_x,SiO_x} and λ_{Si,SiO_x} are the attenuation lengths in SiO_x for Si 2p photoelectrons generated from SiO_x and Si, which are usually assumed to have the same value λ_{SiO_x}. $I^{\infty}_{SiO_x}$ and I^{∞}_{Si} are the intensities per unit surface area from bulk SiO_x and Si samples, respectively. For a Si surface covered only by nanoscale islands, such angle dependence is expected to be much weaker because their thicknesses are comparable to the photo-electron escape-depth. Therefore, the silicon surface is expect to display different angle-dependence behaviors depending whether a thin oxide layer exists between islands or not.

We collected Si 2p spectra at three take-off angles: θ=0°, 35° and 70°, and observed a clear angle dependence of the Si^{x+}/Si^0 intensity ratio, which is the signature of a thin silicon oxide layer. Fig. 5-9 plots a function of I_{SiO_x}/I_{Si}, i.e., $\ln[(I_{SiO_x}/I_{Si})(I^{\infty}_{SiO_x}/I^{\infty}_{Si}+1]$, against $1/\cos\theta$ for various annealed samples, which shows that the intensity ration quantity increases significantly with $1/\cos\theta$ in all samples. In the case of an island-free Si surface covered by a continuous flat oxide film, the I_{SiO_x}/I_{Si} ratio changes with the take-off angle θ as dictated by Eq. 5.3 and a linear dependence should be seen in the plot with the slope being d/λ_{SiO_x} (i.e., dashed curves in Fig. 5-9).

It is necessary to account for the contribution of the islands to the total XPS signal because the area of analysis is large compared to the island spacing. A geometrical model was developed to treat the additive contributions from a continuous film and islands. The model was adapted from Mack et al. [279] to estimate from the XPS data the thickness of the oxide film. The islands are assumed to have a spherical cap shape and a single-size, and are uniformly distributed on the substrate. The islands' area fraction f and their average height and diameter were determined by AFM, with the assumption that the film and islands have the same composition. Let h and R be the height and base radius of the islands. The intensity per unit surface area of Si 2p

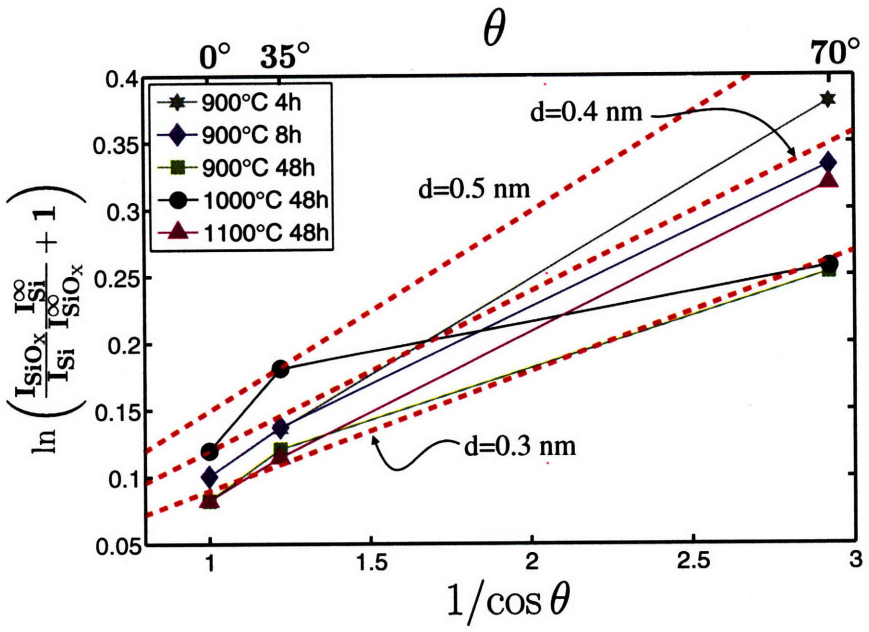

Figure 5-9: Take-off angle dependence of the XPS Si 2p intensity ratio I_{SiO_x}/I_{Si} for Si(001) samples with different buffer temperatures and annealing times. The dashed curves represent the intensity ratios for a Si surface covered by a uniform oxide layer with thickness d=0.3nm, 0.4nm and 0.5nm.

electrons emitted from the island region is given by

$$I^{\text{island}}_{SiO_x} = I^{\infty}_{SiO_x} \int_0^{2\pi} d\beta \int_0^R r dr \left[1 - \exp\left(-\frac{L(r,\beta)}{\lambda_{SiO_x}\cos\theta}\right)\right] \tag{5.4}$$

where θ is the take-off angle. Here (r, β) are the polar coordinates of a point in the base circle of the spherical cap, with the origin, (r=0, β=0), located at the circle center. The direction of $\beta = 0$ is taken to be parallel to the projection of the take-off direction onto the base plane. $L(r, \beta)$ is the distance that electrons emitted at the point (r, β) travels in the take-off direction to escape the island. Geometric calculation gives

$$\begin{aligned} L(r,\beta) = &- r\cos(\beta)\sin(\theta) - (R-h)\cos(\theta) \\ &+ \left[2Rh - R^2 - h^2 + (r\cos(\beta)\sin(\theta) + (R-h)\cos\theta)^2\right]^{1/2} \end{aligned} \tag{5.5}$$

Note that Eq. 5.4 is exact when 90°-θ is larger than the contact angle α of the islands, which is true in our case because the largest θ is 70° and α is less than 20°. If a thin,

homogeneous oxide film of thickness d exists between the islands, it also contributes Si^{x+} signal. The Si 2p intensity per unit area of the film is

$$I_{SiO_x}^{film} = I_{SiO_x}^{\infty}\left[1 - \exp\left(-\frac{d}{\lambda_{SiO_x}\cos\theta}\right)\right] \tag{5.6}$$

Similarly, the metallic Si^0 signal from the substrate can be divided into two parts. One part passes through the islands and the other part through the film. Their intensities per unit surface area are given respectively by

$$I_{Si}^{island} = I_{Si}^{\infty}\int_0^{2\pi} d\beta \int_0^R r dr \exp\left(-\frac{L(r,\beta)}{\lambda_{SiO_x}\cos\theta}\right) \tag{5.7}$$

$$I_{Si}^{film} = I_{Si}^{\infty}\exp\left(-\frac{d}{\lambda_{SiO_x}\cos\theta}\right) \tag{5.8}$$

The shadowing effects [281] by the islands, which may affect Eqs. 5.6 and 5.8, is negligible because $90° - \theta > \alpha$.

Given that the islands cover a fraction f of the total surface area, the intensity ratio of Si^{x+} to Si^0 is calculated as

$$\frac{I_{SiO_x}}{I_{Si}} = \frac{f I_{SiO_x}^{island} + (1-f) I_{SiO_x}^{film}}{f I_{Si}^{island} + (1-f) I_{Si}^{film}} \tag{5.9}$$

All parameters in Eq. 5.9 except the film thickness d were determined by experiments or taken from literature. Thus d can be estimated by fitting the calculated intensity ratio with the XPS data. Table 5.3.3 shows the film thicknesses fitted from angle-resolved XPS data using this method. In the case of the samples annealed for 4h and 8h, the island fraction f is small (1-4%) and their contribution to the total oxidized silicon component signal is minor. Nonetheless, their effects are included in the columns for film thickness labeled lower bound, in which we assumed that the entire XPS-analysed area had an island area fraction f equal to the largest value observed in any single AFM image. The columns labeled "upper bound" in Table 5.3.3 give thicknesses calculated assuming no islands (f=0). Consistently, the results indicate a continuous film of ~0.4nm thickness to be present. In the sample annealed for 48h,

much of the surface was free of islands, while a few areas had a high density as shown in Fig. 5-5(b). Here, also, the calculated upper bound value for film thickness is 0.3-0.4 nm. It is emphasized that the angle-resolved XPS spectra yielding these numerical values are clearly and substantially enriched in Si^{x+} compared to the control samples (Figs. 5-3 and 5-4 and Fig. 5-8). Thus the results indicate presence of a continuous SiO_x layer that remains relatively constant in thickness throughout annealing while the islands nucleate and coarsen.

Table 5.1: Calculated Film Thickness with (Lower Bound) or without (Upper Bound) Island Contribution

anneal time	thickness (nm)					
	0°		35°		70°	
	lower bound	upper bound	lower bound	upper bound	lower bound	upper bound
4h	N/A	N/A	0.37 (f=1.6%)	0.38	0.44 (f=1.6%)	0.45
8h	0.32 (f=3.1%)	0.35	0.36 (f=3.1%)	0.39	0.38 (f=3.1%)	0.39

5.3.4 Incomplete Wetting Behavior of Silicon Oxide on Si

Analyzing the angle-resolved XPS data of the T_{buf} =1000°C and 1100°C samples resulted in the same conclusion that a surficial oxide layer is present on the Si(001) surface. Fig. 5-10(b) summarizes the film thicknesses for a number of samples. It is seen that the silicon oxide film retains a thickness of ~0.4nm despite an 8 orders of magnitude change in P_{O_2} as T_{buf} is increased from 900°C to 1100°C . The films are stable in the presence of high SiO vapor over-saturation. The results show that the observed surficial oxide film is a (meta)stable Si(001) surface configuration over a wide range of P_{O_2} and P_{SiO} beyond that for Si/SiO_2 bulk equilibrium.

Several possible interfacial adsorption behaviors are demonstrated in Fig. 5-10(a). As illustrated in the plot, if the second phase perfectly wets the first (contact angle ϕ=0, curve 1), then the interfacial adsorbate excess $\Gamma \rightarrow \infty$ as the adsorbate's chemical potential approaches the two-phase coexistence, i.e., $\mu \rightarrow \mu^{2-\text{phase}-\text{eq}}$. In cases of partial wetting (ϕ >0), Γ goes to a finite value at $\mu^{2-\text{phase}-\text{eq}}$ and may form a multilayer film (curve 2) or remain as a sub-monolayer in the case where Langmuir-

Maclean (L-M) adsorption behavior holds up to the limit of solubility (curve 3). The wetting transition accompanied by a diverging Γ (curve 2) may occur in the super-saturation region ($\mu > \mu^{2-\text{phase}-\text{eq}}$). In the case of multilayer adsorption, Γ may have first-order transitions as predicted by critical wetting theory [22] and may coincide with interface structural transitions as described in Chapters 2 and 3. The system of Si/SiO_2 exemplifies the incomplete wetting behavior illustrated in Fig. 5-10(a), where adsorbate coverage in excess of the Langmuir-McLean partial monolayer is stable over a wide range of adsorbate activity (in this case, oxygen). At still higher oxygen activity, the equilibrium configuration may approach that of a wetting film which can thicken without energy penalty. The origin of the partial wetting character or the Stranski-Krastonov behavior of silicon oxide on Si(001) surface probably derives from the strain energy present at the Si-SiO_x interface due to bond-density mismatch [277, 282] analogous to the case of Ge island growth on Si [283, 284], Ag on Si [285] and InAs on GaAs [286]. It has been found by various experimental characterization methods [277, 287, 288] that the SiO_2 /Si(001) interface consists of 2-3 atomic layers which are subject to lattice distortion and thus store strain energy [277, 282]. When oxygen activity is beyond the Si/SiO_2 equilibrium, a chemi-adsorbed SiO_x monolayer is expected to readily form on Si surface which eliminates dangling bonds of surface silicon atoms. However, the thermodynamic driving force for the growth of subsequent oxide layers is much smaller due to the need to break Si-Si bonds. Furthermore, the associated strain energy may make them energetically unfavorable to form at small oxygen over-saturation, which accounts for the observed stability of a relative constant surface oxide coverage over a broad range of oxygen partial pressures above the equilibrium level.

Similar phenomena have also been observed in other isotropic systems. Ice is an exemple for materials that exhibit surface premelting [18]. Elbaum et al. [289] have found that the basal plane of ice premelts to form a continuous quasiliquid layer beginning at about two degrees undercooling. With further heating closer to but still below the bulk melting point, liquid droplets of small contact angle form, showing that the bulk liquid does not wet the premelted film. In other examples, above the

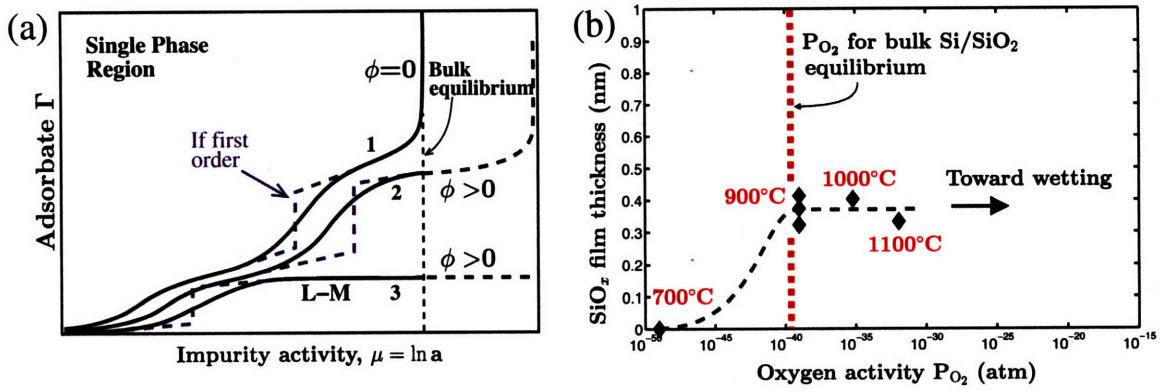

Figure 5-10: Oxygen activity dependence of the equilibrium silicon oxide film thickness about the Si/SiO_2 equilibrium P_{O_2}. (a) Schematic view of several possible interfacial adsorption behaviors, in which the interfacial excess, Γ, varies with adsorbate chemical potentials. (b) Results from this study for the surficial oxide (upper bound) thickness (averaged over values at three take-off angles) on Si(001) at 700°C as a function of oxygen activity shows the oxide thickness increasing to a relatively constant value at coexistence and well into the supersaturation regime. The dashed line is a guide to the eye. Samples included in the plot: 700°C buffer 24h, 900°C buffer 4, 8, and 48h, and 1000°C and 1100°C 48h.

dew-point for hydrophobic surfaces, water will form spherical-droplets surrounded by a thin hydrated layer with thicknesses of 0.2-0.4nm [290,291]. Liquid droplets of pure Pb and Pb-Bi alloy were found to be in equilibrium with a monolayer film on Cu(111) substrate [292]. Alkanes on aqueous solution surfaces form droplets with a thin alkane film covering the surfaces [122,293,294]. Silicon surfaces in equilibrium with its oxide may be a high-temperature version of these similar phenomena.

5.4 Conclusions

Despite the extremely broad technical applications of the Si/SiO_2 structure, the equilibrium wetting properties of silicon oxide on silicon were previously not well understood. To study the equilibrium wetting behavior a solid-state buffer method is used to systematically titrate oxygen activity about the Si/SiO_2 coexistence value. The equilibrium morphology at the Si(001) surface over 8 orders of magnitude of P_{O_2} about coexistence is revealed to be a uniform SiO_x layer coexisting with secondary island structures which coarsen with annealing time. These results establish

the utility of the solid-state buffer approach for controlling P_{O_2} in ranges not accessible by vacuum technology. In the on-going development of next-generation gate oxides [124,125,295,296] the oxide-silicon interfacial structure has been proven to be critical to device performance. Although many criteria must be met for any thin film to perform effectively as a gate oxide [124,295], the methodology presented here opens up the possibility of tailoring the gate oxide-silicon interfacial structure by thermodynamic equilibration. Further demonstration appears in work where this approach has been used in experiments on controlling the surficial film structure, thickness and stoichiometry on Hf-doped Si(001) surfaces [129]. The obtained experimental data on the surficial oxide layer and islands can be compared with theoretical calculations to gain insight into the Si/SiO_2 interface energetics. The solid-state buffer method developed here can also be used to study the wetting properties of other metal/oxide systems.

Appendix A

Expressions of Mean and Gaussian Curvatures and the Laplace Operator in Triply Orthogonal Coordinate Systems

A.1 Some basic definitions of differential geometry of surfaces

Some basic notations and definitions from differential geometry of surfaces will be briefly described in this section. They are necessary for deriving the curvature expressions in triply orthogonal coordinate systems in the next section. For a complete exposition of differential geometry of surfaces, see Ref. [297].

A.1.1 Tangent space of a surface

Let $\mathcal{S}$ be a two-dimensional surface bounding a three-dimensional body. Let (s,t) be a coordinate system defined on $\mathcal{S}$, and $\vec{x}(s,t) \in \mathbf{R}^3$ be the three-dimensional position vector pointing from the origin to a point on $\mathcal{S}$. Define $\vec{x}_s \equiv \partial\vec{x}/\partial s$ and $\vec{x}_t \equiv \partial\vec{x}/\partial t$ as the derivatives of the vector with respect to s and t at a surface point $\mathbf{p} = (s,t)$.

The tangent space to $\mathcal{S}$ at $\mathbf{p}$ is defined as

$$T_p\mathcal{S} = \{v_1\vec{x}_s + v_2\vec{x}_t | \forall \mathbf{v} = (v_1, v_2) \in \mathbf{R}^2\} \tag{A.1}$$

Any vector in $T_p\mathcal{S}$ is a *tangent vector* to $\mathcal{S}$ at $\mathbf{p}$. Geometrically, the tangent space consists of all vectors in the tangent plane of $\mathcal{S}$ at point $\mathbf{p}$ – it is a two-dimensional space spanned by two independent tangent vectors, $\vec{x}_s$ and $\vec{x}_t$.

A.1.2 Surface normal vector

The surface normal vector N to $\mathcal{S}$ at $\mathbf{p} = (s,t) \in \mathcal{S}$ is defined as a unit vector normal to any tangent vectors to $\mathcal{S}$ at $\mathbf{p}$. By definition

$$\vec{N} \cdot \vec{x}_s = \vec{N} \cdot \vec{x}_t = 0 \tag{A.2}$$

It can be shown that [297]

$$\vec{N} = \frac{\vec{x}_s \times \vec{x}_t}{|\vec{x}_s \times \vec{x}_t|} \tag{A.3}$$

where $|\cdot|$ denotes the norm of a vector: $|\vec{x}| = \sqrt{\vec{x} \cdot \vec{x}}$.

A.1.3 The first fundamental form

The first fundamental form (or Riemannian metric) of a surface defines how the distance along a curve on the surface is measured.

The first fundamental form of $\mathcal{S}$ at $\mathbf{p}$ is defined as the inner product of any two vectors belonging to the tangent space $T_p\mathcal{S}$, $\vec{v} = ds\vec{x}_s + dt\vec{x}_t$ and $\vec{w} = ds'\vec{x}_s + dt'\vec{x}_t$

$$I_p(\vec{v}, \vec{w}) = \vec{v} \cdot \vec{w} \tag{A.4}$$

$I_p(\vec{v}, \vec{v})$ gives the expression of the arc length dl between two points $\mathbf{p} = (s,t)$ and $\mathbf{p}' = (s + ds, t + dt)$ on a curve on $\mathcal{S}$ when $ds, dt \to 0$

$$dl^2 = I_p(\vec{v}, \vec{v}) = Eds^2 + 2Fds\,dt + Gdt^2 \tag{A.5}$$

where E, F and G are called the *the coefficients of the first fundamental form* and have the following expressions

$$\begin{aligned} E &= |\vec{x}_s|^2 \\ F &= \vec{x}_s \cdot \vec{x}_t \\ G &= |\vec{x}_t|^2 \end{aligned} \tag{A.6}$$

The first fundamental form written in the matrix form is

$$I_p(\vec{v}, \vec{w}) = \begin{bmatrix} ds & dt \end{bmatrix} \begin{bmatrix} E & F \\ F & G \end{bmatrix} \begin{bmatrix} ds' \\ dt' \end{bmatrix} \tag{A.7}$$

A.1.4 Shape operator and the second fundamental form

Shape operator $\vec{S}_p$ is a linear operator defined on the tangent space $T_p\mathcal{S}$. It provides a metric of the bending of surface $\mathcal{S}$ at $\mathbf{p}$.

Let $\vec{N}$ be a surface normal vector to $\mathcal{S}$ defined in the neighborhood of a point $\mathbf{p} = (s,t) \in \mathcal{S}$, and $\vec{v} = ds\,\vec{x}_s + dt\,\vec{x}_t$ be any tangent vector to $\mathcal{S}$ at $\mathbf{p}$. The shape operator at $\mathbf{p}$ is given by (see Ref. [297] for a more rigorous definition of the shape operator)

$$\vec{S}_p(\vec{v}) = -ds\vec{N}_s - dt\vec{N}_t \tag{A.8}$$

where $\vec{N}_s$ and $\vec{N}_t$ are derivatives of $\vec{N}$ with respect to s and t.

The second fundamental form is defined as the first fundamental form (i.e., inner product) between $\vec{S}_p(\vec{v})$ and a tangent vector to $\mathcal{S}$ at $\mathbf{p}$, $\vec{w} = ds'\,\vec{x}_s + dt'\,\vec{x}_t$

$$\begin{aligned} II_p(\vec{v}, \vec{w}) &= I_p(\vec{S}_p(\vec{v}), \vec{w}) \\ &= \vec{S}_p(\vec{v}) \cdot \vec{w} \\ &= \vec{S}_p(\vec{w}) \cdot \vec{v} \end{aligned} \tag{A.9}$$

It can be shown that [297]

$$\begin{aligned} II_p(\vec{v},\vec{v}) &= \vec{S}_p(\vec{v})\cdot\vec{v} \\ &= eds^2 + 2fdsdt + gdt^2 \end{aligned} \tag{A.10}$$

where e, f and g are called the *coefficients of the second fundamental form*, and have the following expressions

$$\begin{aligned} e &= -\vec{N}_s\cdot\vec{x}_s \\ f &= \vec{N}_s\cdot\vec{x}_t = \vec{N}_t\cdot\vec{x}_s \\ g &= -\vec{N}_t\cdot\vec{x}_t \end{aligned} \tag{A.11}$$

The matrix form of the second fundamental form is

$$II_p(\vec{v},\vec{w}) = \begin{bmatrix} ds & dt \end{bmatrix} \begin{bmatrix} e & f \\ f & g \end{bmatrix} \begin{bmatrix} ds' \\ dt' \end{bmatrix} \tag{A.12}$$

Let the matrix form of the shape operator $\vec{S}_p$ be M_S, i.e.

$$\begin{aligned} \vec{S}_p(\vec{x}_s) &= M_S(1,1)\vec{x}_s + M_S(1,2)\vec{x}_t \\ \vec{S}_p(\vec{x}_t) &= M_S(2,1)\vec{x}_s + M_S(1,2)\vec{x}_t \end{aligned} \tag{A.13}$$

where $M_S(i,j)$ (i,j=1,2) is the matrix element on the i-th row and j-th column. Using the matrix form of the first fundamental form, Eq. A.7, one derives

$$\begin{aligned} II_p(\vec{v},\vec{w}) &= \begin{bmatrix} ds & dt \end{bmatrix} M_S \begin{bmatrix} E & F \\ F & G \end{bmatrix} \begin{bmatrix} ds' \\ dt' \end{bmatrix} \\ &\equiv \begin{bmatrix} ds & dt \end{bmatrix} \begin{bmatrix} e & f \\ f & g \end{bmatrix} \begin{bmatrix} ds' \\ dt' \end{bmatrix} \end{aligned} \tag{A.14}$$

which leads to an expression for M_S

$$\begin{aligned} M_S &= \begin{bmatrix} e & f \\ f & g \end{bmatrix} \begin{bmatrix} E & F \\ F & G \end{bmatrix}^{-1} \\ &= \frac{1}{EG - F^2} \begin{bmatrix} eG - fF & fE - eF \\ fG - gF & gE - fF \end{bmatrix} \end{aligned} \tag{A.15}$$

A.1.5 Mean and Gaussian curvatures

The shape operator provides information on the curvatures of a surface. The two principal curvatures, κ_1 and κ_2, at a surface point $\mathbf{p}$ are determined by the eigenvalues of the shape operator matrix M_S, and the corresponding eigenvetors represent the principal directions. The mean and Gaussian curvatures are often defined as the mean and product of the principal curvatures

$$H = \frac{1}{2}(\kappa_1 + \kappa_2) \tag{A.16}$$

$$K = \kappa_1 \kappa_2 \tag{A.17}$$

Formally, the mean and Gaussian curvatures at a point $\mathbf{p}$ are defined as the trace and determinant of the shape operator at p

$$H = \frac{1}{2}\text{tr}(M_S) = \frac{eG - 2fF + gE}{2(EG - F^2)} \tag{A.18}$$

$$K = \det(M_S) = \frac{eg - f^2}{EG - F^2} \tag{A.19}$$

A.2 Curvature expressions of mean and Gaussian curvatures in triply orthogonal coordinate systems

In this section the expressions of the mean and Gaussian curvatures are derived for triply orthogonal coordinate systems, where the three coordinate axes are orthogonal

to each other at any point in the three dimensional space.

Let (r,s,t) be the coordinates of a triply orthogonal coordinate system. $\vec{x}_s$ and $\vec{x}_t$ are tangent vectors to the level surfaces of r and they are orthogonal to each other. By definition of triply orthogonal coordinates, $\vec{x}_r \cdot \vec{x}_s = \vec{x}_r \cdot \vec{x}_t = 0$, where $\vec{x}_r \equiv \partial\vec{x}/\partial r$. This shows that $\vec{x}_r$ is normal to tangent vectors. Thus the surface normal vector to the level surfaces of r can be written as

$$\vec{N} = \frac{\vec{x}_s(s,t) \times \vec{x}_t(s,t)}{|\vec{x}_s(s,t) \times \vec{x}_t(s,t)|} = \frac{\vec{x}_r}{|\vec{x}_r|} \tag{A.20}$$

In a triply orthogonal coordinate system, the coefficients of the first fundamental form of the level surfaces of r have the following expressions

$$E = |\vec{x}_s|^2 \tag{A.21}$$

$$F = \vec{x}_s \cdot \vec{x}_t = 0 \tag{A.22}$$

$$G = |\vec{x}_t|^2 \tag{A.23}$$

For the coefficients of the second fundamental form of the level surfaces of r, one finds

$$\begin{aligned} e &\equiv \vec{N}_s \cdot \vec{x}_s \\ &= \left(\frac{\vec{x}_r}{|\vec{x}_r|}\right)_s \cdot \vec{x}_s \\ &= \frac{\vec{x}_{rs} \cdot \vec{x}_s}{|\vec{x}_r|} - \frac{(\vec{x}_r \cdot \vec{x}_s)|\vec{x}_r|_s}{|\vec{x}_r|^2} \\ &= \frac{|\vec{x}_s|\,|\vec{x}_s|_r}{|\vec{x}_r|} \end{aligned} \tag{A.24}$$

in which the following equality is used

$$|\vec{x}_s|_r = \frac{\partial}{\partial r}\left(\sqrt{\vec{x}_s \cdot \vec{x}_s}\right) = \frac{\vec{x}_{sr} \cdot \vec{x}_s}{|\vec{x}_s|} \tag{A.25}$$

Similarly one derives

$$\begin{aligned} g &\equiv \vec{N}_t \cdot \vec{x}_t \\ &= \frac{|\vec{x}_t|\,|\vec{x}_t|_r}{|\vec{x}_r|} \end{aligned} \tag{A.26}$$

The other coefficient f is

$$\begin{aligned} f &\equiv \vec{N}_s \cdot \vec{x}_t \\ &= \left(\frac{\vec{x}_r}{|\vec{x}_r|}\right)_s \cdot \vec{x}_t \\ &= \frac{\vec{x}_{rs} \cdot \vec{x}_t}{|\vec{x}_r|} - \frac{(\vec{x}_r \cdot \vec{x}_t)|\vec{x}_r|_s}{|\vec{x}_r|^2} \\ &= \frac{(\vec{x}_s \cdot \vec{x}_t)_r - \vec{x}_{rt} \cdot \vec{x}_s}{|\vec{x}_r|} \\ &= -\frac{\vec{x}_{rt} \cdot \vec{x}_s}{|\vec{x}_r|} \\ &= -\vec{N}_t \cdot \vec{x}_s \equiv -f \end{aligned} \tag{A.27}$$

which suggests that $f = 0$ in a triply orthogonal system.

The expressions of the mean and Gaussian curvatures of level surfaces of r are given by substituting Eqs. A.21–A.27 into Eqs. A.18 and A.19

$$H = \frac{1}{2|\vec{x}_r|}\left(\frac{|\vec{x}_s|_r}{|\vec{x}_s|} + \frac{|\vec{x}_t|_r}{|\vec{x}_t|}\right) \tag{A.28}$$

$$K = \frac{1}{|\vec{x}_r|^2}\frac{|\vec{x}_s|_r\,|\vec{x}_t|_r}{|\vec{x}_s|\,|\vec{x}_t|} \tag{A.29}$$

By assuming that $|\vec{x}_r| \equiv 1$, Eqs. A.28 and A.29 become

$$H = \frac{1}{2}\left(\frac{|\vec{x}_s|_r}{|\vec{x}_s|} + \frac{|\vec{x}_t|_r}{|\vec{x}_t|}\right) \tag{A.30}$$

$$K = \frac{|\vec{x}_s|_r\,|\vec{x}_t|_r}{|\vec{x}_s|\,|\vec{x}_t|} \tag{A.31}$$

Furthermore, Differentiating $|\vec{x}_r| \equiv 1$ with respect to r, s and t produces

$$\vec{x}_{rr} \cdot \vec{x}_r = 0 \tag{A.32}$$

$$\vec{x}_{rs} \cdot \vec{x}_r = -\vec{x}_{rr} \cdot \vec{x}_s = 0 \tag{A.33}$$

$$\vec{x}_{rt} \cdot \vec{x}_r = -\vec{x}_{rr} \cdot \vec{x}_t = 0 \tag{A.34}$$

Eqs. A.32–A.34 show that the inner products between $\vec{x}_{rr}$ and three independent vectors, $\vec{x}_r$, $\vec{x}_s$ and $\vec{x}_t$, are all zero. Thus in a triply orthogonal system

$$\vec{x}_{rr} = 0 \tag{A.35}$$

According to Eqs. A.27 and A.33, $\vec{x}_{sr} \cdot \vec{x}_t = \vec{x}_{sr} \cdot \vec{x}_r = 0$. Therefore $\vec{x}_{sr}$ is a vector parallel to $\vec{x}_s$ and can be written as

$$\vec{x}_{sr} = \pm \frac{|\vec{x}_{sr}|}{|\vec{x}_s|} \vec{x}_s \tag{A.36}$$

Using Eq. A.36 one finds

$$|\vec{x}_s|_r = \frac{\vec{x}_{sr} \cdot \vec{x}_s}{|\vec{x}_s|} = \pm |\vec{x}_{sr}| \tag{A.37}$$

and similarly

$$|\vec{x}_t|_r = \frac{\vec{x}_{tr} \cdot \vec{x}_t}{|\vec{x}_t|} = \pm |\vec{x}_{tr}| \tag{A.38}$$

By using Eqs. A.35, A.37 and A.38, the derivative of the mean curvature with

respect to r, $\partial H/\partial r$, in a triply orthogonal system is found to be

$$\begin{aligned}
\frac{\partial H}{\partial r} &= \frac{1}{2}\frac{\partial}{\partial r}\left[\frac{|\vec{x}_s|_r}{|\vec{x}_s|} + \frac{|\vec{x}_t|_r}{|\vec{x}_t|}\right] \\
&= \frac{1}{2}\left[\frac{|\vec{x}_s|_{rr}}{|\vec{x}_s|} - \frac{|\vec{x}_s|_r^2}{|\vec{x}_s|^2} + \frac{|\vec{x}_t|_{rr}}{|\vec{x}_t|} - \frac{|\vec{x}_t|_r^2}{|\vec{x}_t|^2}\right] \\
&= \frac{1}{2}\left[\pm\frac{|\vec{x}_{sr}|_r}{|\vec{x}_s|} - \frac{|\vec{x}_s|_r^2}{|\vec{x}_s|^2} \pm \frac{|\vec{x}_{tr}|_r}{|\vec{x}_t|} - \frac{|\vec{x}_t|_r^2}{|\vec{x}_t|^2}\right] \\
&= \frac{1}{2}\left[\pm\frac{(\vec{x}_{rr})_s \cdot \vec{x}_{sr}}{|\vec{x}_{sr}|\,|\vec{x}_s|} - \frac{|\vec{x}_s|_r^2}{|\vec{x}_s|^2} \pm \frac{(\vec{x}_{rr})_t \cdot \vec{x}_{tr}}{|\vec{x}_{tr}|\,|\vec{x}_t|} - \frac{|\vec{x}_t|_r^2}{|\vec{x}_t|^2}\right] \\
&= -\frac{1}{2}\left[\frac{|\vec{x}_s|_r^2}{|\vec{x}_s|^2} + \frac{|\vec{x}_t|_r^2}{|\vec{x}_t|^2}\right]
\end{aligned} \tag{A.39}$$

A.3 Expression of the Laplace operator in triply orthogonal coordinate systems

The expression of the Laplacian of a scalar field $\phi(r,s,t)$ in a triply orthogonal coordinate system is [298, 299]

$$\nabla^2\phi = \frac{1}{|\vec{x}_r|\,|\vec{x}_s|\,|\vec{x}_t|}\left[\frac{\partial}{\partial r}\left(\frac{|\vec{x}_s|\,|\vec{x}_t|}{|\vec{x}_r|}\frac{\partial\phi}{\partial r}\right) + \frac{\partial}{\partial s}\left(\frac{|\vec{x}_t|\,|\vec{x}_r|}{|\vec{x}_s|}\frac{\partial\phi}{\partial s}\right) + \frac{\partial}{\partial t}\left(\frac{|\vec{x}_r|\,|\vec{x}_s|}{|\vec{x}_t|}\frac{\partial\phi}{\partial t}\right)\right] \tag{A.40}$$

In the special case that the level surfaces of $\phi(r,s,t)$ coincide with the surfaces of constant r, i.e. $\partial\phi/\partial s = \partial\phi/\partial t = 0$, Eq. A.40 reduces to

$$\nabla^2\phi = \frac{1}{|\vec{x}_r|\,|\vec{x}_s|\,|\vec{x}_t|}\frac{\partial}{\partial r}\left(\frac{|\vec{x}_s|\,|\vec{x}_t|}{|\vec{x}_r|}\frac{\partial\phi}{\partial r}\right) \tag{A.41}$$

By choosing $|x_r| \equiv 1$, the Laplacian of ϕ further becomes

$$\begin{aligned}
\nabla^2\phi &= \frac{\partial^2\phi}{\partial r^2} + \left(\frac{|\vec{x}_s|_r}{|\vec{x}_s|} + \frac{|\vec{x}_t|_r}{|\vec{x}_t|}\right)\frac{\partial\phi}{\partial r} \\
&\equiv \frac{\partial^2\phi}{\partial r^2} + 2H(r,s,t)\frac{\partial\phi}{\partial r}
\end{aligned} \tag{A.42}$$

Appendix B

Semi-Implicit Fourier Spectral Scheme

The equation of motion for the order parameter $\phi(\vec{x})$, Eq. 4.20, in Chapter 4 is solved by the Fourier spectral method with a semi-implicit scheme [237, 238].

The normalized equation of motion is

$$\frac{\partial \phi}{\partial t} = \nabla^2 \frac{\delta F}{\delta \phi} \tag{B.1}$$

where

$$\begin{aligned} \frac{\delta F}{\delta \phi} &= f'(\phi) + \lambda \sigma^2 p(\phi) p'(\phi) - \left(\frac{\nu'(\phi)}{2} + \lambda \sigma p''(\phi) \right) (\nabla \phi)^2 \\ &\quad - (\nu(\phi) + 2\lambda \sigma p'(\phi) + 4\lambda H_0^2) \nabla^2 \phi \\ &\quad + 4\lambda H_0 \nabla \cdot \left(\frac{(\nabla^2 \phi \nabla \phi - \nabla \nabla \phi \cdot \nabla \phi}{|\nabla \phi|} \right) + \lambda \nabla^4 \phi \end{aligned} \tag{B.2}$$

Let's divide $\delta F / \delta \phi$ into two parts

$$\frac{\delta F}{\delta \phi} \equiv G(\phi(\vec{x})) + \lambda \nabla^4 \phi(\vec{x}) \tag{B.3}$$

in which $G(\phi(\vec{x}))$ contains all the terms of $\delta F / \delta \phi$ except the fourth-derivative of ϕ.

The spectral method solves the equation of motion in the Fourier space. The

Fourier transform of Eq. B.1 is written as

$$\frac{\partial\hat{\phi}(\vec{k},t)}{\partial t} = -k^2\mathcal{F}[G(\phi(\vec{x},t))](\vec{k}) - \lambda k^6\hat{\phi}(\vec{k},t) \tag{B.4}$$

where $\mathcal{F}$ denotes the Fourier transform and $\hat{\phi}(\vec{k}) \equiv \mathcal{F}[\phi(\vec{x})](\vec{k})$. In the semi-implicit scheme, Eq. B.4 is discretized as

$$\frac{\hat{\phi}^{n+1}(\vec{k}) - \hat{\phi}^n(\vec{k})}{\Delta t} = -k^2\mathcal{F}[G(\phi^n(\vec{x}))](\vec{k}) - \lambda k^6\hat{\phi}^{n+1}(\vec{k}) \tag{B.5}$$

where the superscipt n denotes the function value at the n-th time step and Δt is the time step size. Eq. B.5 treats the linear fourth-derivative term in $\delta F/\delta\phi$ implicitly and the nonlinear part $G(\phi(\vec{x}))$ explicitly. The resulting first-order time-stepping scheme is

$$\hat{\phi}^{n+1}(\vec{k}) = \frac{\hat{\phi}^n(\vec{k}) - k^2\mathcal{F}[G(\phi^n(\vec{x}))](\vec{k})}{1 + \Delta t\lambda k^6} \tag{B.6}$$

Eq. B.6 requires $G(\phi(\vec{x}))$ to be evaluated in the real space at each time step. $G(\phi^n(\vec{x}))$ depends on ϕ^n, $\nabla\phi^n$ and $\nabla^2\phi^n$, for which real-space values are obtained by applying the inverse Fourier transforms to $\hat{\phi}^n$

$$\begin{aligned}
\phi^n(\vec{x}) &= \mathcal{F}^{-1}[\hat{\phi}^n(\vec{k})](\vec{x}) \\
\nabla\phi^n(\vec{x}) &= \mathcal{F}^{-1}[i\vec{k}\hat{\phi}^n(\vec{k})](\vec{x}) \\
\nabla^2\phi^n(\vec{x}) &= \mathcal{F}^{-1}[-k^2\hat{\phi}^n(\vec{k})](\vec{x})
\end{aligned} \tag{B.7}$$

The forward and inverse Fourier transforms are performed by the Fast Fourier transform (FFT), which evaluates ϕ and $\hat{\phi}$ on a regular mesh grid.

Appendix C

List of Symbols

Chapter 2 and 3:

$\vec{x}$	position vector
$\theta(\vec{x})$	crystallographic orientation field
$\eta(\vec{x})$	crystallinity field
$c(\vec{x})$	concentration field
$\Delta\theta$	grain boundary (GB) misorientation
η_{GB}	crystallinity at the GB core
η_{GB}^{eq}	equilibrium GB crystallinity
η_{GB}^{Ord}	GB crystallinity of the ordered GB complexion
η_{GB}^{Dis}	GB crystallinity of the disordered GB complexion
c_{GB}	composition at the GB core
c_{GB}^{eq}	equilibrium grain boundary composition
c_{GB}^{Ord}	GB composition of the ordered GB complexion
c_{GB}^{Dis}	GB composition of the disordered GB complexion
c_{∞}	bulk composition of the binary systems
c_{sol}	solubility limit of B-component in A-rich α phase
T	temperature
T_m	melting temperature
T_e	eutectic temperature

T_{PM}	GB transition temperature
T_{CW}	GB complete wetting transition temperature
ΔT	undercooling
s	crystallographic orientation gradient coefficient
$g(\eta)$	prefactor function of the orientation gradient energy term
ν^2	crystallinity gradient coefficient
κ^2	concentration gradient coefficient
F	total free energy
Δf	volumetric free energy density
a^2	energy barrier height of Δf
Δh_m	melting enthalpy
$W(\eta)$	regular solution coefficient as a function of η
$p(\eta)$	a smooth interpolation function between $p(\eta = 0)$=1 and $p(\eta = 1)$=0
k	Boltzmann constant
$\bar{v}$	atomic volume
γ_{GB}	GB energy
γ_{sl}	solid-liquid interface energy
L_{GB}	GB width
p	exponent of the function $g(\eta) = \eta^p$
q	exponent of the function $\Delta f = a^2[4\eta(1-\eta)]^q/32$

Chapter 4:

H	mean curvature
K	Guassian curvature
H_0	spontaneous curvature
κ	bending modulus for the mean curvature
$\bar{\kappa}$	bending modulus for the Guassian curvature
l_0	surfactant chain length
$\phi(\vec{x})$	phase-field variable representing local concentration of surfactant solution

$f(\phi)$	volumetric free energy density of the binary solution
a	energy barrier height of $f(\phi)$
$\nu(\phi)$	gradient coefficient function of ϕ
λ	parameter that determines the bending moduli of surfactant monolayers
σ	parameter that controls the equilibrium surfactant bilayer thickness
$p(\phi)$	a smooth interpolation function between $p(\phi = -1)$=1 and $p(\phi = 1)$=0
r, s, t	coordinates of a local coordinate system built on the level surfaces of ϕ
$\vec{x}_r, \vec{x}_s, \vec{x}_t$	derivatives of the position vector $\vec{x}$ with respect to r, s and t
M	surfactant mobility
t	time
c_s	initial surfactant concentration of the solution
θ	polar angle
$r(\theta)$	local radius of a perturbed disk micelle
R	uniform disk radius without perturbation
$\Delta\mu$	surfactant chemical potential difference between solution and micelles
ϵ	perturbation amplitude
n	perturbation wave number

Chapter 5:

P_{O_2}	oxygen partial pressure
R	gas constant
T	temperature
T_{Si}	silicon wafer temperature
T_{buf}	solid-state buffer temperature
ΔG	free energy of oxidation
θ	XPS take-off angle
d	silicon oxide layer thickness
λ_{SiO_x}	attenuation length of Si 2p electrons in SiO_x
f	area fraction of silicon surface covered by islands

I_{SiO_x}	peak intensity of Si 2p electrons from silicon surficial oxide
I_{Si}	peak intensity of Si 2p electrons from silicon substrates
$I^{\infty}_{SiO_x}$	peak intensity of Si 2p electrons from *bulk* silicon oxide
I^{∞}_{Si}	peak intensity of Si 2p electrons from *bulk* silicon

Bibliography

[1] M. Yoshiya, H. Adachi, and I. Tanaka. Interpretation of Si-$L_{2,3}$ edge electron energy loss near edge structures (ELNES) from intergranular glassy film of Si_3N_4 ceramics. *J. Am. Ceram. Soc.*, 82(11):3231–3236, 1999.

[2] H. Wang and Y.-M. Chiang. Thermodynamic stability of intergranular amorphous films in bismuth-doped zinc oxide. *J. Am. Ceram. Soc.*, 81:89–95, 1998.

[3] M. W. Chase. *NIST-JANAF Thermochemical Tables*, volume 9 of *Journal of Physical and Chemical Reference Data Monographs*. American Institute of Physics, 4th edition, 1998.

[4] M. P. Seah, S. J. Spencer, F. Bensebaa, I. Vickridge, H. Danzebrink, M. Krumrey, T. Gross, W. Oesterle, E. Wendler, B. Rheinlander, Y. Azuma, I. Kojima, N. Suzuki, M. Suzuki, S. Tanuma, D. W. Moon, H. J. Lee, H. M. Cho, H. Y. Chen, A. T. S. Wee, T. Osipowicz, J. S. Pan, W. A. Jordaan, R. Hauert, U. Klotz, C. van der Marel, M. Verheijen, Y. Tarnminga, C. Jeynes, P. Bailey, S. Biswas, U. Falke, N. V. Nguyen, D. Chandler-Horowitz, J. R. Ehrstein, D. Muller, and J. A. Dura. Critical review of the current status of thickness measurements for ultrathin SiO_2 on Si part V. results of a CCQM pilot study. *Surf. Interf. Anal.*, 36(9):1269–1303, 2004.

[5] A. P. Sutton and R. W. Balluffi. *Interfaces in Crystalline Materials*. Oxford University Press, Oxford, 1996.

[6] R. W. Balluffi, S. M. Allen, and W. C. Carter. *Kinetics of Materials*. John Wiley and Sons, New York, 2005.

[7] F. J. Almgren and J. E. Taylor. The geometry of soap films and soap bubbles. *Scientific American*, 235(1):82–93, 1976.

[8] J. D. van der Waals. Thermodynamische theorie der capillariteit in de onderstelling van continue dichtheidsverandering. *Verh. K. Akad. Wet. Amsterdam (Sect. 1)*, 1:8, 1893. English translation, "The thermodynamic theory of capillarity under the hypothesis of a continuous variation of density", *J. Stat. Phys.*, 20:197, 1979.

[9] J. W. Gibbs. On the equilibrium of heterogeneous substances (1876). In *Collected Works*, volume 1. Longmans, Green, and Co., 1928.

[10] E.A. Guggenheim. *Thermodynamics.* North-Holland, Amsterdam, 5th edition, 1967.

[11] C. V. Boys. *Soap-Bubbles: Their Colours and the Forces Which Mold Them.* Dover Publications, New York, 1959.

[12] I. Newton. *Opticks.* Dover, New York, 1952.

[13] J. Plateau. *Experimental and Theoretical Statics of Liquids Subject to Molecular Forces Only (in French).* Ganthier-Villar, Paris, 1873. See English translation by K. Brakke: http://www.susqu.edu/brakke/PlateauBook/PlateauBook.html.

[14] E. Ruckenstein and M. Manciu. On the stability of the common and newton black films. *Langmuir*, 18(7):2727–2736, 2002.

[15] M. Tang, W. C. Carter, and R. M. Cannon. A diffuse interface model for structural transitions of grain boundaries. *Phys. Rev. B*, 73:024102, 2006.

[16] M. Tang, W. C. Carter, and R. M. Cannon. Grain boundary transitions in binary systems. *Phys. Rev. Lett.*, 97:075502, 2006.

[17] S. J. Dillon, M. Tang, W. C. Carter, and M. P. Harmer. Complexion: A new concept for kinetic engineering in materials science. *Acta Mater.*, 55:6208–6218, 2007.

[18] J. G. Dash, A. W. Rempel, and J. S. Wettlaufer. The physics of premelted ice and its geophysical consequences. *Rev. Mod. Phys.*, 78(3):695–741, 2006.

[19] T. Pusztai, G. Bortel, and L. Granasy. Phase field theory of polycrystalline solidification in three dimensions. *Europhys. Lett.*, 71(1):131–137, 2005.

[20] R. Kobayashi and J. A. Warren. Modeling the formation and dynamics of polycrystals in 3D. *Physica A*, 356:127–132, 2005.

[21] U. Seifert. Configurations of fluid membranes and vesicles. *Adv. Phys.*, 46(1):13–137, 1997.

[22] J. W. Cahn. Critical point wetting. *J. Chem. Phys.*, 66:3667–3672, 1977.

[23] M. R. Moldover and J. W. Cahn. An interface phase transition: Complete to partial wetting. *Science*, 207:1073–1075, 1980.

[24] D. Chatain and P. Wynblatt. Experimental evidence for a wetting transition in liquid Ga-Pb alloys. *Surf. Sci.*, 345:85–90, 1996.

[25] J. W. M. Frenken and J. F. van der Veen. Observation of surface melting. *Phys. Rev. Lett.*, 54:134–141, 1985.

[26] J. W. M. Frenken, P. M. J. Maree, and J. F. van der Veen. Observation of surface initiated melting. *Phys. Rev. B*, 34:7506–7516, 1986.

[27] J. G. Dash. Surface melting. *Cont. Phys.*, 30:89–100, 1989.

[28] D. Chatain and P. Wynblatt. Anisotropy of wetting of Pb crystals by their own melt and by liquid Ga-Pb alloys. In P. M. Duxbury and T. J. Pence, editors, *Dynamics of Crystal Surfaces and Interfaces*, pages 53–58, New York, 1997. Plenum Press.

[29] B. Pluis, A. W. Denier van der Gon, J. F. van der Veen, and A. J. Riemersma. Surface-induced melting and freezing. I. Medium-energy ion scattering investigation of the melting of Pb(hkl) crystal faces. *Surf. Sci.*, 239:268–281, 1990.

[30] J. Lapujoulade, B. Salanon, F. Fabre, and B. Loisel. The roughening transition of vicinal surfaces. In M. G. Lagally, editor, *Kinetics of Ordering and Growth at Surfaces*, pages 355–368, New York, 1990. Plenum Press.

[31] R. Lipowsky, U. Breuer, K. C. Prince, and H. P. Bonzel. Multicomponent order parameter for surface melting. *Phys. Rev. Lett.*, 62(8):913–916, 1989.

[32] J. F. van der Veen, B. Pluis, and A. W. Denier van der Gon. Ion scattering studies of surface melting. In M. G. Lagally, editor, *Kinetics of Ordering and Growth at Surfaces*, pages 343–354, New York, 1990. Plenum Press.

[33] J. F. van der Veen. Surface-induced melting of solids. In H. Taub *et al*, editor, *Phase Transitions in Surface Films*, volume 2, pages 289–305, New York, 1991. Plenum Press.

[34] B. Pluis, D. Frenkel, and A. J. Riemersma. Surface-induced melting and freezing. II. A semi-empirical Landau-type model. *Surf. Sci.*, 239:282–300, 1990.

[35] R. Vanselow and R. F. Howe. *Chemistry and Physics of Solid Surfaces*, volume 7. Springer-Verlag, Berlin, 1988.

[36] H. Gleiter. Observations suggesting a transformation in the structure of high-angle grain boundaries in lead. *Z. Metall.*, 61:282–297, 1970.

[37] D. W. Demianczuk and K. T. Aust. Effect of solute and orientation on the mobility of near-coincidence tilt boundaries in high purity aluminum. *Acta Metall.*, 23:1149–1162, 1975.

[38] T. Watanabe, S. I. Kimura, and S. Karashima. The effect of a grain boundary structural transformation on sliding in (1010)-tilt zinc bicrystals. *Phil. Mag A*, 49:845–864, 1984.

[39] E. L. Maksimova, L. S. Shvindlerman, and B. B. Straumal. Transformation of $\Sigma 17$ special tilt boundaries to general grain boundaries in tin. *Acta Metall.*, 36:1573–1583, 1988.

[40] K. Lücke and H.-P. Stüwe. On the theory of impurity controlled grain boundary migration. *Acta Metall.*, 19:1687–1699, 1971.

[41] D. A. Molodov, U. Czubayko, G. Gottstein, and L. S. Shvindlerman. On the effect of purity and orientation on grain boundary motion. *Acta Mater.*, 46:1573–1583, 1998.

[42] T.E. Hsieh and R.W. Balluffi. Experimental study of grain-boundary melting in aluminum. *Acta Metall.*, 37(6):1637–1644, 1989.

[43] M. E. Glicksman and C. L. Vold. Heterophase dislocations - an approach towards interpreting high temperature grain boundary behavior. *Surf. Sci.*, 31:50–67, 1972.

[44] R. Kikuchi and J. W. Cahn. Grain boundary melting transition in a two-dimensional lattice-gas model. *Phys. Rev. B*, 21:1893–1897, 1980.

[45] G. Besold and O. G. Mouritsen. Grain boundary melting: A Monte Carlo study. *Phys. Rev. B*, 50:6573–6576, 1994.

[46] G. Ciccotti, M. Guillope, and V. Pontikis. High-angle grain-boundary premelting transition: A molecular dynamics study. *Phys. Rev. B*, 27:5576–5585, 1983.

[47] G. A. Evangelakis, M. Hou, C. Maunier, and V. Pontikis. A molecular dynamics study of the thermal displacive properties of the Σ=13(θ=22.6°)[001] twist boundary in noble metals. *J. Physique Colloq.*, 51(C1):127–132, 1990.

[48] M. Meyer and C. Waldburger. Grain boundary structure in NiO, temperature evolution: A molecular dynamics study. *Mater. Sci. Forum*, 126–128:229–232, 1993.

[49] P. Keblinski, S. R. Phillpot, D. Wolf, and H. Gleiter. Continuous thermodynamic-equilibrium glass transition in high-energy grain boundaries? *Philos. Mag. Lett*, 76:143–151, 1997.

[50] S. R. Phillpot, J. F. Lutsko, D. Wolf, and S. Yip. Molecular-dynamics study of lattice-defect-nucleated melting in silicon. *Phys. Rev. B*, 40:2831–2840, 1989.

[51] T. Nguyen, P. S. Ho, T. Kwok, C. Nitta, and S. Yip. Thermal structural disorder and melting at a crystalline interface. *Phys. Rev. B*, 46:6050–6060, 1992.

[52] P. Deymier, A. Taiwo, and G. M. Kalonji. A grain boundary phase transition studied by molecular dynamics. *Acta Metall.*, 35:2719–30, 1987.

[53] T. Nguyen, P. S. Ho, T. Kwok, C. Nitta, and S. Yip. Grain-boundary melting transition in an atomistic simulation model. *Phys. Rev. Lett.*, 57:1919–1922, 1986.

[54] V. Pontikis. Grain boundary structure and phase transformations: A critical review of computer simulation studies and comparison with experiment. *J. Physique Colloq.*, 49(C5):327–336, 1988.

[55] J. F. Lutsko, D. Wolf, S. R. Phillpot, and S. Yip. Molecular-dynamics study of lattice-defect-nucleated melting in metals using an embedded-atom-method potential. *Phys. Rev. B.*, 40:2841–2855, 1989.

[56] S. J. Plimpton and E. D. Wolf. Effect of interatomic potential on simulated grain-boundary diffusion and bulk diffusion: A molecular dynamics study. *Phys. Rev. B*, 41:2712–2721, 1990.

[57] M. Guillope. Allotropic transition in Σ=5(210) grain boundary at intermediate temperatures. *J. Physique.*, 47:1347–1356, 1986.

[58] S. M. Foiles, M. I. Baskes, and M. S. Daw. Atomistic studies of interfacial structure and properties. *Mater. Res. Soc. Symp. Proc.*, 122:343–354, 1988.

[59] R. Najafabadi, D. J. Srolovitz, and R. Lesar. Thermodynamic and structural properties of (001) twist boundaries in gold. *J. Mater. Res.*, 6:999–1011, 1991.

[60] L.-Q. Chen and G. Kalonji. Finite temperature structure and properties of Σ=5(310) tilt grain boundaries in NaCl: A molecular dynamics study. *Philos. Mag. A*, 66:11–26, 1992.

[61] D. N. Seidman. Subnanoscale studies of segregation at grain boundaries: Simulation and experiments. *Ann. Rev. Mater. Res.*, 32:235–269, 2002.

[62] B. Schönfelder, P. Keblinski, D. Wolf, and S. R. Phillpot. On the relationship between grain-boundary migration and grain boundary diffusion by molecular-dynamics simulation. *Mater. Sci. Forum*, 294-296:9–16, 1999.

[63] P. Keblinski, D. Wolf, S. R. Phillpot, and H. Gleiter. Self diffusion in high-angle FCC metal grain boundaries by molecular dynamics simulation. *Philos. Mag. A*, 79:2735–2761, 1999.

[64] B. Schönfelder, G. Gottstein, and L. S. Shvindlerman. Comparative study of grain-boundary migration and grain-boundary self-diffusion of [001] twist-grain boundaries. *Acta Mater.*, 53:1597–1609, 2005.

[65] H.-J. Kleebe, M. K. Cinibulk, R. M. Cannon, and M. Rühle. Statistical analysis of the intergranular film thickness in silicon nitride ceramics. *J. Amer. Ceram. Soc.*, 76:1969–77, 1993.

[66] I. Tanaka, H.-J. Kleebe, M. K. Cinibulk, J. Bruley, D. R. Clarke, and M. Rühle. Calcium concentration dependence of the intergranular film thickness in silicon nitride. *J. Am. Ceram. Soc.*, 77:911–914, 1994.

[67] C.-M. Wang, X. Pan, M. J. Hoffmann, R. M. Cannon, and M. Rühle. Grain boundary films in rare-earth-based silicon nitride. *J. Am. Ceram. Soc.*, 79:788–792, 1996.

[68] H. Gu, R. M. Cannon, and M. Rühle. Composition and chemical width of ultrathin amorphous films at grain boundaries in silicon nitride. *J. Mater. Res.*, 13:376–387, 1998.

[69] H. Gu, X. Pan, R. M. Cannon, and M. Rühle. Dopant distribution in grain-boundary films in calcia-doped silicon nitride ceramics. *J. Am. Ceram. Soc.*, 81:3125–3125, 1998.

[70] J. Luo, H. Wang, and Y.-M. Chiang. Origin of solid-state activated sintering in Bi_2O_3-doped ZnO. *J. Am. Ceram. Soc.*, 82:916–920, 1999.

[71] F. Ernst, O. Kienzle, and M. Rühle. Structure and composition of grain boundaries in ceramics. *J. Eur. Ceram. Soc.*, 19(6–7):665–673, 1999.

[72] S. Y. Chung and S. J. L. Kang. Intergranular amorphous films and dislocations-promoted grain growth in $SrTiO_3$. *Acta Mater.*, 51:2345–2354, 2003.

[73] P. Svancarek, D. Galusek, C. Calvert, F. Loughran, A. Brown, R. Brydson, and F. Riley. A comparison of the microstructure and mechanical properties of two liquid phase sintered aluminas containing different molar ratios of calcia-silica sintering additives. *J. Eur. Ceram. Soc.*, 24(12):3453–3463, 2004.

[74] P. Svancarek, D. Galusek, F. Loughran, A. Brown, R. Brydson, A. Atkinson, and F. Riley. Microstructure-stress relationships in liquid-phase sintered alumina modified by the addition of 5wt.% of calcia-silica additives. *Acta Mater.*, 54(18):4853–4863, 2006.

[75] J. Luo, V. K. Gupta, D. H. Yoon, and H. M. Meyer. Segregation-induced grain boundary premelting in nickel-doped tungsten. *Appl. Phys. Lett.*, 87:231902, 2005.

[76] V. K. Gupta, D. H. Yoon, H. M. Meyer III, and J. Luo. Thin intergranular films and solid-state activated sintering in nickel-doped tungsten. *Acta Mater.*, 55:3131–3142, 2007.

[77] J. Luo. Stabilization of nanoscale quasi-liquid interfacial films in inorganic materials: A review and critical assessment. *Crit. Rev. Solid State Mater. Sci.*, 32:67–109, 2007.

[78] Y.-M. Chiang, L. A. Silverman, R. H. French, and R. M. Cannon. Thin glass film between ultrafine conductor particles in thick-film resistors. *J. Am. Ceram. Soc.*, 77:1143–1152, 1994.

[79] H. Gu, R.M. Cannon, H.J. Seifert, M.J. Hoffmann, and I. Tanaka. Solubility of Si_3N_4 in liquid SiO_2. *J. Am. Ceram. Soc.*, 85:25–32, 2002.

[80] H. Gu, R.M. Cannon, I. Tanaka, and M. Rühle. Calcia partition in phase-separated intergranular glass and interfaces in doped silicon nitride produced by hot isostatic pressing. *Mater. Sci. Eng. A*, 422:51–65, 2006.

[81] R. M. Cannon and L. Esposito. High temperature colloidal behavior: Particles in liquid silicates. *Z. Metall.*, 90:1002–1015, 1999.

[82] I. MacLaren, R. M. Cannon, M. A. Gülgün, R. Voytovych, N. P. Pogrion, C. Scheu, U. Täffner, and M. Rühle. Abnormal grain growth in alumina: synergistic effects of yttria and silica. *J. Am. Ceram. Soc.*, 86:650–659, 2003.

[83] D. R. Clarke. On the equilibrium thickness of intergranular glass phases in ceramic materials. *J. Am. Ceram. Soc.*, 70:15–22, 1987.

[84] D. R. Clarke, T. M. Shaw, A. P. Philipse, and R. G. Horn. Possible electrical double-layer contribution to the equilibrium thickness of intergranular glass films in polycrystalline ceramics. *J. Am. Ceram. Soc.*, 76:1201–1204, 1993.

[85] J. Israelachvili. *Intermolecular and Surface Forces.* Academic Press, London, 1992.

[86] J. Luo and Y.-M. Chiang. Existence and stability of nanometer-thick disordered films on oxide surfaces. *Acta Mater.*, 48(18-19):4501–4515, 2000.

[87] J. Luo, Y.-M. Chiang, and R. M. Cannon. Nanometer-thick surficial films in oxides as a case of prewetting. *Langmuir*, 21(16):7358–7365, 2005.

[88] H. J. Qian and J. Luo. Vanadia-based equilibrium-thickness amorphous films on anatase (101) surfaces. *Appl. Phys. Lett.*, 91:061909, 2007.

[89] J. Luo, M. Tang, R. M. Cannon, W.C. Carter, and Chiang Y.-M. Pressure-balance and diffuse-interface models for surficial amorphous films. *Mater. Sci. Eng. A*, 422(1-2):19–28, 2006.

[90] J. W. Cahn. Transitions and phase equilibria among grain boundary structures. *J. de Physique*, 43(C6):199–213, 1982. Proceedings of Conference on the Structure of Grain Boundaries, Caen, France.

[91] C. Rottman and M. Wortis. Statistical-mechanics of equilibrium crystal shapes - interfacial phase-diagrams and phase-transitions. *Phys. Rep.*, 103(1-4):59–79, 1984.

[92] T.G. Ference and R.W. Balluffi. Observation of a reversible grain-boundary faceting transition induced by changes of composition. *Scripta Metall.*, 22(12):1929–1934, 1988.

[93] T. E. Hsieh and R. W. Balluffi. Observations of roughening/defaceting phase-transitions in grain-boundaries. *Acta Metall.*, 37(8):2133–2139, 1989.

[94] J. E. Blendell, W. C. Carter, and C. A. Handwerker. Faceting and wetting transitions of anisotropic interfaces and grain boundaries. *J. Am. Ceram. Soc.*, 82:1889–1900, 1999.

[95] B. K. Lee, S. Y. Chung, and S.-J. L. Kang. Grain boundary faceting and abnormal grain growth in $BaTiO_3$. *Acta Mater.*, 48:1575–1580, 2000.

[96] C. W. Park and D. Y. Yoon. Effects of SiO_2, CaO_2, and MgO additions on the grain growth of alumina. *J. Am. Ceram. Soc.*, 83(10):2605–2609, 2000.

[97] H. Gabrisch, L. Kjeldgaard, E. Johnson, and U. Dahmen. Equilibrium shape and interface roughening of small liquid Pb inclusions in solid Al. *Acta Mater.*, 49(20):4259–4269, 2001.

[98] D. Chatain, P. Wynblatt, and G. S. Rohrer. Equilibrium crystal shape of Bi-saturated Cu crystals at 1223K. *Acta Mater.*, 53(15):4057–4064, 2005.

[99] W. W. Mullins and R. F. Sekerka. Morphological stability of a particle growing by diffusion or heat flow. *J. Appl. Phys.*, 34(2):323–329, 1963.

[100] W. W. Mullins and R. F. Sekerka. Stability of a planar interface during solidification of a dilute binary alloy. *J. Appl. Phys.*, 35(2):444–451, 1964.

[101] W. J. Boettinger, J. A. Warren, C. Beckermann, and A. Karma. Phase-field simulation of solidification. *Annu. Rev. Mater. Res.*, 32:163–194, 2002.

[102] H. Hotani. Transformation pathways of liposomes. *J. Mol. Biol.*, 178(1):113–120, 1984.

[103] W. Wintz, H. G. Dobereiner, and U. Seifert. Starfish vesicles. *Europhysics Letters*, 33(5):403–408, 1996.

[104] M. Yanagisawa, M. Imai, and T. Taniguchi. Shape deformation of ternary vesicles coupled with phase separation. *Phys. Rev. Lett.*, 100(14):148102, 2008.

[105] Z. Lin, J. J. Cai, L. E. Scriven, and H. T. Davis. Spherical-to-wormlike micelle transition in CTAB solutions. *J. Phys. Chem.*, 98(23):5984–5993, 1994.

[106] A. Bernheim-Groswasser, R. Zana, and Y. Talmon. Sphere-to-cylinder transition in aqueous micellar solution of a dimeric (gemini) surfactant. *J. Phys. Chem. B*, 104(17):4005–4009, 2000.

[107] Z. Lin. Branched worm-like micelles and their networks. *Langmuir*, 12(7):1729–1737, 1996.

[108] A. Bernheim-Groswasser, E. Wachtel, and Y. Talmon. Micellar growth, network formation, and criticality in aqueous solutions of the nonionic surfactant C_12E_5. *Langmuir*, 16(9):4131–4140, 2000.

[109] V. Croce, T. Cosgrove, G. Maitland, T. Hughes, and G. Karlsson. Rheology, cryogenic transmission electron spectroscopy, and small-angle neutron scattering of highly viscoelastic wormlike micellar solutions. *Langmuir*, 19(20):8536–8541, 2003.

[110] R. Lipowsky and E. Sackmann. *Structure and Dynamics of Membranes.* Elsevier, Amsterdam, 1995.

[111] A. Khatory, F. Kern, F. Lequeux, J. Appell, G. Porte, N. Morie, A. Ott, and W. Urbach. Entangled versus multiconnected network of wormlike micelles. *Langmuir*, 9(4):933–939, 1993.

[112] A. Khatory, F. Lequeux, F. Kern, and S. J. Candau. Linear and nonlinear viscoelasticity of semidilute solutions of wormlike micelles at high-salt content. *Langmuir*, 9(6):1456–1464, 1993.

[113] W. Helfrich. Elastic properties of lipid bilayers - theory and possible experiments. *Z. Naturf. C*, 28(11):693–703, 1973.

[114] L. Miao, U. Seifert, M. Wortis, and H. G. Dobereiner. Budding transitions of fluid-bilayer vesicles — the effect of area-difference elasticity. *Phys. Rev. E*, 49(6):5389–5407, 1994.

[115] H. G. Dobereiner, E. Evans, M. Kraus, U. Seifert, and M. Wortis. Mapping vesicle shapes into the phase diagram: A comparison of experiment and theory. *Phys. Rev. E*, 55(4):4458–4474, 1997.

[116] L. Q. Chen. Phase-field models for microstructure evolution. *Annu. Rev. Mater. Res.*, 32:113–140, 2002.

[117] L. Granasy, T. Pusztai, and J. A. Warren. Modelling polycrystalline solidification using phase field theory. *J. Phys.-Condens. Mat.*, 16(41):R1205–R1235, 2004.

[118] Q. Du, C. Liu, and X. Q. Wang. A phase field approach in the numerical study of the elastic bending energy for vesicle membranes. *J. Comput. Phys.*, 198(2):450–468, 2004.

[119] T. Biben, K. Kassner, and C. Misbah. Phase-field approach to three-dimensional vesicle dynamics. *Phys. Rev. E*, 72(4):041921, 2005.

[120] F. Campelo and A. Hernandez-Machado. Dynamic model and stationary shapes of fluid vesicles. *Eur. Phys. J. E*, 20(1):37–45, 2006.

[121] F. Brochardwyart, J. M. Dimeglio, D. Quere, and P. G. Degennes. Spreading of nonvolatile liquids in a continuum picture. *Langmuir*, 7(2):335–338, 1991.

[122] E. Bertrand, H. Dobbs, D. Broseta, J. Indekeu, D. Bonn, and J. Meunier. First-order and critical wetting of alkanes on water. *Phys. Rev. Lett.*, 85(6):1282–1285, 2000.

[123] H. J. Qian, J. Luo, and Y.-M. Chiang. Anisotropic wetting of ZnO by Bi_2O_3 with and without nanometer-thick surficial amorphous films. *Acta Mater.*, 56:862–873, 2008.

[124] G. D. Wilk, R. M. Wallace, and J. M. Anthony. High-κ gate dielectrics: Current status and materials properties considerations. *J. Appl. Phys.*, 89(10):5243–5275, 2001.

[125] J. Robertson. High dielectric constant oxides. *Eur. Phys. J. Appl. Phys.*, 28(3):265–291, 2004.

[126] K. I. Seo, D. I. Lee, P. Pianetta, H. Kim, K. C. Saraswat, and P. C. McIntyre. Chemical states and electrical properties of a high-κ metal oxide/silicon interface with oxygen-gettering titanium-metal-overlayer. *Appl. Phys. Lett.*, 89(14):142912, 2006.

[127] L. V. Goncharova, M. Dalponte, T. Gustafsson, O. Celik, E. Garfunkel, P. S. Lysaght, and G. Bersuker. Metal-gate-induced reduction of the interfacial layer in Hf oxide gate stacks. *J. Vac. Sci. Technol. A*, 25(2):261–268, 2007.

[128] K. Nakajima, A. Fujiyoshi, Z. Ming, M. Suzuki, and K. Kimura. In situ observation of oxygen gettering by titanium overlayer on $HfO_2/SiO_2/Si$ using high-resolution rutherford backscattering spectroscopy. *J. Appl. Phys.*, 102(6):064507, 2007.

[129] E. Jud, M. Tang, and Y.-M. Chiang. Stability of HfO_2/SiO_x/si surficial films at ultralow oxygen activity. *J. Appl. Phys.*, 2008 (in press).

[130] W. Lojkowski and H.-J. Fecht. The structure of intercrystalline interfaces. *Prog. Mater. Sci.*, 45:339–568, 2000.

[131] B. Straumal and B. Baretzky. Grain boundary phase transitions and their influence on properties of polycrystals. *Interface Sci.*, 12:147–155, 2004.

[132] L. Liu and J. K. Shang. Interfacial embrittlement by bismuth segregation in copper/tin-bismuth Pb-free solder interconnect. *J. Mater. Res.*, 16:1651–1659, 2001.

[133] W. J. Huppmann and H. Riegger. Modeling of rearrangement processes in liquid-phase sintering. *Acta. Metall.*, 23:965–971, 1975.

[134] R. Kobayashi, J. A. Warren, and W. C. Carter. A continuum model of grain boundaries. *Physica D*, 140:141–150, 2000.

[135] R. Kobayashi, J. A. Warren, and W. C. Carter. Vector-valued phase field model for crystallization and grain boundary formation. *Physica D*, 119:415–423, 1998.

[136] J.A. Warren, R. Kobayashi, A.E. Lobkovsky, and W.C. Carter. Extending phase field models of solidification to polycrystalline materials. *Acta Mater.*, 51(20):6035–6058, 2003.

[137] A.E. Lobkovsky and J.A. Warren. Phase field model of premelting of grain boundaries. *Physica D*, 164:202–12, 2002.

[138] A. P. Sutton. Modelling of the atomic and electronic structures of interfaces. In *Materials Research Society Proceedings*, volume 122, pages 81–96, Warrendale, PA, 1988. Materials Research Society.

[139] C. M. Bishop and W. C. Carter. Relating atomistic grain boundary simulation results to the phase-field model. *Comp. Mater. Sci.*, 25:378–386, 2002.

[140] S. von Alfthan, P. D. Haynes, K. Kaski, and A. P. Sutton. Are the structures of twist grain boundaries in silicon ordered at 0K? *Phys. Rev. Lett.*, 96:055505, 2006.

[141] R. Zallen. *The Physics of Amorphous Solids.* Wiley-Interscience, New York, 1998.

[142] A.E. Lobkovsky and J.A. Warren. Sharp interface limit of a phase-field model of crystal grains. *Phys. Rev. E*, 63:051605, 2001.

[143] R. Kobayashi and Y. Giga. Equations with singular diffusivity. *J. Stat. Phys.*, 95:1187–1220, 1999.

[144] I. M. Gelfand and S. V. Fomin. *Calculus of Variations.* Dover Publications, Mineola, NY, 1963.

[145] L. Granasy, T. Borzsonyi, and T. Pusztai. Nucleation and bulk crystallization in binary phase field theory. *Phys. Rev. Lett.*, 88:206105, 2002.

[146] L. Granasy, T. Pusztai, T. Borzsonyi, J. A.Warren, and J. F. Douglas. A general mechanism of polycrystalline growth. *Nature Mater.*, 3:645–650, 2004.

[147] J. Q. Broughton and G. H. Gilmer. Thermodynamic criteria for grain-boundary melting: A molecular-dynamics study. *Phys. Rev. Lett.*, 56:2692–2696, 1986.

[148] B. Pluis, A. W. Denier van der Gon, J. W. M. Frenken, and J. F. van der Veen. Crystal-face dependence of surface melting. *Phys. Rev. Lett.*, 59:2678–2681, 1987.

[149] R. W. Balluffi. Grain boundary diffusion mechanisms in metals. *Metall. Trans. A*, 13:2069–2095, 1982.

[150] D. Wolf and K. L. Merkle. Correlation between the structure and energy in grain boundaries in metals. In D. Wolf and S. Yip, editors, *Materials Interfaces*, pages 87–150, London, 1992. Chapman and Hall.

[151] N. A. Gjostein and F. N. Rhines. Absolute interfacial energies of [001] tilt and twist grain boundaries in copper. *Acta Metall.*, 7:319–330, 1959.

[152] H. B. Aaron and G. F. Bolling. Free volume as a criterion for grain boundary models. *Surf. Sci.*, 31:27–49, 1972.

[153] D. Wolf. A Read-Shockley model for high-angle grain boundaries. *Scripta Metall.*, 23:1713–1718, 1989.

[154] C. Counterman, L.-Q. Chen, and G. Kalonji. Molecular dynamics study of the structure and properties of twist boundaries. *J. Physique Colloq.*, 49(C5):139–150, 1989.

[155] L.-Q. Chen and G. Kalonji. Structure and dynamic properties of twist boundaries in NaCl through a molecular dynamics study. *Philos. Mag. A*, 60:525–544, 1989.

[156] P. Keblinski, S. R. Phillpot, D. Wolf, and H. Gleiter. On the thermodynamic stability of amorphous intergranular films in covalent materials. *J. Am. Ceram. Soc.*, 80:717–732, 1997.

[157] S. von Alfthan, K. Kaski, and A. P. Sutton. Order and structural units in simulations of twist grain boundaries in silicon at absolute zero. *Phys. Rev. B*, 74:134101, 2006.

[158] S. von Alfthan, K. Kaski, and A. P. Sutton. Molecular dynamics simulations of temperature-induced structural transitions at twist boundaries in silicon. *Phys. Rev. B*, 76:245317, 2007.

[159] S. W. Chan, J. S. Liu, and R. W. Balluffi. Test for a possible 'melting' transition in grain boundaries in aluminum near the melting point. *Scripta Metall.*, 19:1251–1255, 1985.

[160] R.W. Balluffi and R. Maurer. On rotating sphere-on-a-plate experiments and the question of whether high angle grain-boundaries melt below bulk melting temperatures. *Scripta Metall.*, 22(5):709–713, 1988.

[161] U. Erb and H. Gleiter. The effect of temperature on the energy and structure of grain boundaries. *Scripta Metall.*, 13:61–64, 1979.

[162] U. Dahmen and K. H. Westmacott. Studies of faceting by high voltage/high resolution microscopy. In C. S. Pande, B. B. Rath, and D. A. Smith, editors, *Interface: Structure and Properties*, pages 133–167, Switzerland, 1993. Trans Tech Publications.

[163] A. W. Denier van der Gon, R. J. Smith, J. M. Gay, D. J. O'connor, and J. F. van der Veen. Melting of Al surfaces. *Surf. Sci.*, 227:143–149, 1990.

[164] A. W. Denier van der Gon, J. M. Gay, J. W. M. Frenken, and J. F. van der Veen. Order-disorder transitions at the Ge(111) surface. *Surf. Sci.*, 241:335–345, 1991.

[165] J. W. Herman and H. E. Elsayed-Ali. Time-resolved structural studies of the low-index faces of lead. *Phys. Rev. B*, 49:4886–4897, 1994.

[166] X. Zeng and H. E. Elsayed-Ali. Time-resolved structural study of low-index surfaces of germanium near its bulk melting temperature. *Phys. Rev. B*, 64:085410, 2001.

[167] A.M. Alsayed, M. F. Islam, J. Zhang, P. J. Collings, and A. G. Yodh. Premelting at defects within bulk colloidal crystals. *Science*, 309:1207–1210, 2005.

[168] P. Schall, I. Cohen, D. A. Weitz, and F. Spaepen. Visualization of dislocation dynamics in colloidal crystals. *Science*, 305:1944–1948, 2004.

[169] J. R. Savage, D. W. Blair, A. J. Levine, R. A. Guyer, and A. D. Dinsmore. Imaging the sublimation dynamics of colloidal crystallites. *Science*, 314:795–798, 2006.

[170] E. I. Rabkin, L. S. Shvindlerman, W. Gust, and B. B. Straumal. Grain boundaries: Phase transitions and critical phenomena. *Mater. Sci. Forum*, 126–128:305–313, 1993.

[171] B. B. Straumal and W. Gust. Lines of grain boundary phase transitions in bulk phases diagrams. *Mater. Sci. Forum*, 207–209:59–68, 1996.

[172] B. B. Straumal, P. Zieba, and W. Gust. Grain boundary phase transitions and phase diagrams. *Int. J. Inorg. Mater.*, 3:1113–1115, 2001.

[173] C. M. Bishop, M. Tang, R. M. Cannon, and W. C. Carter. Continuum modelling and representations of interfaces and their transitions in materials. *Mater. Sci. Eng. A*, 422:102–114, 2006.

[174] C. S. Smith. Grain shapes and other metallurgical applications of topology. In *Structure and Properties of Solid Surfaces*, page 65. American Society for Metals, 1952. Also, see discussion by von Neumann following article, page 108.

[175] R. Kikuchi and J. W. Cahn. Grain-boundary melting transition in a two-dimensional lattice-gas model. *Phys. Rev. B*, 21:1893–1897, 1980.

[176] O. G. Mouritsen and M. J. Zuckermann. Model of interfacial melting. *Phys. Rev. Lett*, 58:389–392, 1987.

[177] L.-S. Chang, E. Rabkin, B. B. Straumal, B. Baretzky, and W. Gust. Thermodynamic aspects of the grain boundary segregation in cu(bi) alloys. *Acta Mater.*, 47:4041–4046, 1999.

[178] J. W. Cahn. The impurity-drag effect in grain boundary motion. *Acta Metall.*, 10:789–798, 1962.

[179] N. Ma, S. A. Dregia, and Y. Wang. Solute segregation transition and drag force on grain boundaries. *Acta Mater.*, 51:3687–3700, 2003.

[180] P. Wynblatt, A. Saul, and D. Chatain. The effects of prewetting and wetting transitions on the surface energy of liquid binary alloys. *Acta Mater.*, 46:2337–2347, 1998.

[181] H. J. Qian and J. Luo. Nanoscale surficial films and a surface transition in V_2O_5-TiO_2-based ternary oxide systems. *Acta Mater.*, 2008 (in press).

[182] B. B. Straumal, N.E. Sluchanko, and W. Gust. Influence of grain boundary phase transitions on the properties of Cu-Bi polycrystals. *Def. Diff. Forum*, 188-190:185–194, 2001.

[183] S. Divinski, M. Lohmann, C. Herzig, B. Straumal, B. Baretzky, and W. Gust. Grain-boundary melting phase transition in the cu-bi system. *Phys. Rev. B*, 71:104104, 2005.

[184] J. Scholhammer, B. Baretzky, W. Gust, E. Mittemeijer, and B. Straumal. Grain boundary grooving as an indicator of grain boundary phase transformations. *Interface Sci.*, 9:43–53, 2001.

[185] O. I. Noskovich, E. I. Rabkin, V. N. Semenov, B. B. Straumal, and L. S. Shvindlerman. Wetting and premelting phase-transitions in 38-degree [100] tilt grain-boundary in (Fe-12%Si)-Zn alloy in the vicinity of the A2-B2 bulk ordering in Fe-12%Si alloy. *Acta Metall. Mater.*, 39:3091–3098, 1991.

[186] E. I. Rabkin, V. N. Semenov, L. S. Shvindlerman, and B. B. Straumal. Penetration of tin and zinc along tilt grain-boundaries 43° [100] in Fe-5%Si — premelting phase-transition. *Acta Metall. Mater.*, 39:627–639, 1991.

[187] B. B. Straumal, O. I. Noskovich, V. N. Semenov, L. S. Shvindlerman, W. Gust, and B. Predel. Premelting transition on 38<100> tilt grain boundaries in (Fe-10at.%Si)-Zn alloys. *Acta Metall. Mater.*, 40:795–801, 1992.

[188] B. B. Straumal, W. Gust, and T. Watanabe. Tie lines of the grain boundary wetting phase transition in the Zn-rich part of the Zn-Sn phase diagram. *Mater. Sci. Forum*, 294-296:411–414, 1999.

[189] B. B. Straumal, W. Gust, and D. Molodov. Wetting transition on grain-boundaries in Al contacting with a Sn-rich melt. *Interface Sci.*, 3:127–132, 1995.

[190] B. B. Stramaul, A. A. Mazilkin, O. A. Kogtenkova, S. G. Protasova, and B. Baretzky. Grain boundary phase observed in Al-5at.%Zn alloy by using HREM. *Phil. Mag. Lett.*, 87:423–430, 2007.

[191] V.G. Glebovsky, B. B. Straumal, V. N. Semenov, V. G. Sursaeva, and W. Gust. Grain boundary penetration of a Ni-rich melt in tungsten polycrystals. *High Temp. Mater. Proc.*, 13:67, 1994.

[192] C. M. Bishop, R. M. Cannon, and W. C. Carter. A diffuse interface model of interfaces: Grain boundaries in silicon nitride. *Acta Mater.*, 53:4755–4764, 2005.

[193] R. H. French. Origins and applications of London dispersion forces and Hamaker constants in ceramics. *J. Am. Ceram. Soc.*, 83:2117–2146, 2000.

[194] K. Van Benthem, G. Tan, L.K. DeNoyer, R.H. French, and M. Rühle. Local optical properties, electron densities, and London dispersion energies of atomically structured grain boundaries. *Phys. Rev. Lett.*, 93:227201, 2004.

[195] R. Lipowsky. Melting at grain boundaries and surfaces. *Phys. Rev. Lett.*, 57:2876–2876, 1986.

[196] J.-G. Li. Some observations on wetting in the Bi_2O_3-ZnO system. *J. Mater. Sci. Lett.*, 13:400–403, 1994.

[197] N. Shahidzadeh, D. Bonn, K. Ragil, D. Broseta, and J. Meunier. Sequence of two wetting transitions induced by tuning the hamaker constant. *Phys. Rev. Lett.*, 80(18):3992–3995, 1998.

[198] K. Holmberg, B. Jonsson, B. Kronberg, and B. Lindman. *Surfactants and Polymers in Aqueous Solution.* Wiley, Chichester, 2nd edition, 2003.

[199] P. A. Barneveld, J. M. H. M. Scheutjens, and J. Lyklema. Bending moduli and spontaneous curvature. 1. bilayers and monolayers of pure and mixed nonionic surfactants. *Langmuir*, 8(12):3122–3130, 1992.

[200] P. A. Barneveld, D. E. Hesselink, F. A. M. Leermakers, J. Lyklema, and J. M. H. M. Scheutjens. Bending moduli and spontaneous curvature. 2. bilayers and monolayers of pure and mixed ionic surfactants. *Langmuir*, 10(4):1084–1092, 1994.

[201] S. May, Y. Bohbot, and A. BenShaul. Molecular theory of bending elasticity and branching of cylindrical micelles. *J. Phys. Chem. B*, 101(43):8648–8657, 1997.

[202] V. N. Paunov, S. I. Sandler, and E. W. Kaler. A simple molecular model for the spontaneous curvature and the bending constants of nonionic surfactant monolayers at the oil/water interface. *Langmuir*, 16(23):8917–8925, 2000.

[203] M. Bergstrom. Thermodynamics of anisotropic surfactant micelles. ii. a molecular interpretation of the micellar curvature free energy. *J. Chem. Phys.*, 113(13):5569–5579, 2000.

[204] M. Bergstrom. Derivation of expressions for the spontaneous curvature, mean and Gaussian bending constants of thermodynamically open surfactant monolayers and bilayers. *J. Chem. Phys.*, 118(3):1440–1452, 2003.

[205] L. M. Bergstrom. Bending elasticity of charged surfactant layers: The effect of layer thickness. *Langmuir*, 22(8):3678–3691, 2006.

[206] L. M. Bergstrom. Bending elasticity of charged surfactant layers: The effect of mixing. *Langmuir*, 22(16):6796–6813, 2006.

[207] S. D. Stoyanov, V. N. Paunov, H. Kuhn, and H. Rehage. A general method for calculating bending moduli and spontaneous curvature of polymer brushes in terms of local density functional theory. *Macromolecules*, 36(13):5032–5038, 2003.

[208] R. Goetz, G. Gompper, and R. Lipowsky. Mobility and elasticity of self-assembled membranes. *Phys. Rev. Lett.*, 82(1):221–224, 1999.

[209] J. Daicic, A. Fogden, I. Carlsson, H. Wennerstrom, and B. Jonsson. Bending of ionic surfactant monolayers. *Phys. Rev. E*, 54(4):3984–3998, 1996.

[210] S. May and A. Benshaul. Spontaneous curvature and thermodynamic stability of mixed amphiphilic layers. *J. Chem. Phys.*, 103(9):3839–3848, 1995.

[211] A. Fogden, I. Carlsson, and J. Daicic. Beyond the harmonic bending theory of ionic surfactant interfaces. *Phys. Rev. E*, 57(5):5694–5706, 1998.

[212] A. Fogden, S. T. Hyde, and G. Lundberg. Bending energy of surfactant films. *J. Chem. Soc. Faraday Trans.*, 87(7):949–955, 1991.

[213] T. Tlusty and S. A. Safran. Microemulsion networks: the onset of bicontinuity. *J. Phys.-Condens. Mat.*, 12(8):A253–A262, 2000.

[214] G. Gompper and M. Schick. Correlation between structural and interfacial properties of amphiphilic systems. *Phys. Rev. Lett.*, 65(9):1116–1119, 1990.

[215] G. Gompper and S. Zschocke. Elastic properties of interfaces in a Ginzburg-Landau theory of swollen micelles, droplet crystals and lamellar phases. *Europhys. Lett.*, 16(8):731–736, 1991.

[216] G. Gompper and S. Zschocke. Ginzburg-Landau theory of oil-water-surfactant mixtures. *Phys. Rev. A*, 46(8):4836–4851, 1992.

[217] G. Gompper and M. Kraus. Ginzburg-Landau theory of ternary amphiphilic systems. 1. Gaussian interface fluctuations. *Phys. Rev. E*, 47(6):4289–4300, 1993.

[218] G. Gompper and M. Kraus. Ginzburg-Landau theory of ternary amphiphilic systems. 2. Monte-Carlo simulations. *Phys. Rev. E*, 47(6):4301–4312, 1993.

[219] G. Gompper and M. Schick. Scattering from internal interfaces in microemulsion and sponge phases. *Phys. Rev. E*, 49(2):1478–1482, 1994.

[220] G. Gompper and J. Goos. Fluctuating interfaces in microemulsion and sponge phases. *Phys. Rev. E*, 50(2):1325–1335, 1994.

[221] G. Gompper and M. Schick. *Self-Assembling Amphiphilic Systems*, volume 16 of *Phase Transitions and Critical Phenomena*. Academic, London, 1994.

[222] A. C. Shi. Nature of anisotropic fluctuation modes in ordered systems. *J. Phys.-Condens. Mat.*, 11(50):10183–10197, 1999.

[223] R. A. Wickham, A. C. Shi, and Z. G. Wang. Nucleation of stable cylinders from a metastable lamellar phase in a diblock copolymer melt. *J. Chem. Phys.*, 118(22):10293–10305, 2003.

[224] E. I. Kats, V. V. Lebedev, and A. R. Muratov. Weak crystallization theory. *Phys. Rep.*, 228(1-2):1–91, 1993.

[225] J. Swift and P. C. Hohenberg. Hydrodynamic fluctuations at convective instability. *Phys. Rev. A*, 15(1):319–328, 1977.

[226] K. R. Elder, M. Katakowski, M. Haataja, and M. Grant. Modeling elasticity in crystal growth. *Phys. Rev. Lett.*, 88(24):245701, 2002.

[227] K. R. Elder and M. Grant. Modeling elastic and plastic deformations in nonequilibrium processing using phase field crystals. *Phys. Rev. E*, 70(5):051605, 2004.

[228] Q. Du, C. Liu, and X. Q. Wang. Simulating the deformation of vesicle membranes under elastic bending energy in three dimensions. *J. Comput. Phys.*, 212(2):757–777, 2005.

[229] T. Biben and C. Misbah. Tumbling of vesicles under shear flow within an advected-field approach. *Phys. Rev. E*, 67(3):031908, 2003.

[230] T. Biben, C. Misbah, A. Leyrat, and C. Verdier. An advected-field approach to the dynamics of fluid interfaces. *Europhys. Lett.*, 63(4):623–629, 2003.

[231] D. Jamet and C. Misbah. Towards a thermodynamically consistent picture of the phase-field model of vesicles: Local membrane incompressibility. *Phys. Rev. E*, 76(5):051907, 2007.

[232] F. Campelo and A. Hernandez-Machado. Shape instabilities in vesicles: A phase-field model. *Eur. Phys. J. Special Topics*, 143:101–108, 2007.

[233] F. Campelo and A. Hernandez-Machado. Model for curvature-driven pearling instability in membranes. *Phys. Rev. Lett.*, 99(8):088101, 2007.

[234] F. Campelo and A. Hernandez-Machado. Polymer-induced tubulation in lipid vesicles. *Phys. Rev. Lett.*, 100:158103, 2008.

[235] J.W. Cahn and J.E. Hilliard. Free energy of a nonuniform system I: Interfacial free energy. *J. Chem. Phys.*, 28:258–267, 1958.

[236] M. Schonhoff and O. Soderman. PFG-NMR diffusion as a method to investigate the equilibrium adsorption dynamics of surfactants at the solid/liquid interface. *J. Phys. Chem. B*, 101(41):8237–8242, 1997.

[237] L.-Q. Chen and J. Shen. Applications of semi-implicit Fourier-spectral method to phase field equations. *Comput. Phys. Comm.*, 108:147–158, 1998.

[238] J. Zhu, L.-Q. Chen, J. Shen, and V. Tikare. Coarsening kinetics from a variable-mobility cahn-hilliard equation: Application of a semi-implicit Fourier spectral method. *Physical Review E*, 60:3564–3572, 1999.

[239] M. Frigo and S. G. Johnson. The design and implementation of FFTW3. *Proceedings of the IEEE*, 93(2):216–231, 2005.

[240] P. K. Vinson and Y. Talmon. Electron-diffraction observed in the gigantic micelle-producing system of CTAB aromatic additives - comment. *J. Colloid Interf. Sci.*, 133(1):288–289, 1989.

[241] M. E. Cates and S. J. Candau. Statics and dynamics of worm-like surfactant micelles. *J. Phys.-Condens. Mat.*, 2(33):6869–6892, 1990.

[242] Y. I. Gonzalez and E. W. Kaler. Cryo-TEM studies of worm-like micellar solutions. *Curr. Opin. Colloid Interface Sci.*, 10(5-6):256–260, 2005.

[243] W.M. Gelbart, A. Ben-Shaul, and D. Roux, editors. *Micelles, Membranes, Microemulsions and Monolayers.* Springer, Berlin, 1994.

[244] S. Ezrahi, E. Tuval, and A. Aserin. Properties, main applications and perspectives of worm micelles. *Adv. Colloid Interface Sci.*, 128:77–102, 2006.

[245] J. C. Eriksson and S. Ljunggren. The mechanics and thermodynamics of rod-shaped micelles. *J. Chem. Soc. Faraday Trans. II*, 81(8):1209–1242, 1985.

[246] J. C. Eriksson and S. Ljunggren. Model-calculations on the transitions between surfactant aggregates of different shapes. *Langmuir*, 6(5):895–904, 1990.

[247] D. Danino, A. Bernheim-Groswasser, and Y. Talmon. Digital cryogenic transmission electron microscopy: an advanced tool for direct imaging of complex fluids. *Colloids Surf. A*, 183:113–122, 2001.

[248] J. N. Israelachvili. *Intermolecular and Surface Forces.* Academic, New York, 1992.

[249] D. Danino, Y. Talmon, H. Levy, G. Beinert, and R. Zana. Branched thread-like micelles in an aqueous-solution of a trimeric surfactant. *Science*, 269(5229):1420–1421, 1995.

[250] A. Bernheim-Groswasser, R. Zana, and Y. Talmon. Microstructures in aqueous solutions of mixed dimeric surfactants: Vesicle transformation into networks of thread-like micelles. *J. Phys. Chem. B*, 104(51):12192–12201, 2000.

[251] V. A. Andreev and A. I. Victorov. Molecular thermodynamics for micellar branching in solutions of ionic surfactants. *Langmuir*, 22(20):8298–8310, 2006.

[252] M. In, G. G. Warr, and R. Zana. Dynamics of branched threadlike micelles. *Phys. Rev. Lett.*, 83(11):2278–2281, 1999.

[253] R. D. Koehler, S. R. Raghavan, and E. W. Kaler. Microstructure and dynamics of wormlike micellar solutions formed by mixing cationic and anionic surfactants. *J. Phys. Chem. B*, 104(47):11035–11044, 2000.

[254] S. Y. Kwon and M. W. Kim. Topological transition in aqueous nonionic micellar solutions. *Phys. Rev. Lett.*, 89(25):258302, 2002.

[255] S. R. Raghavan, H. Edlund, and E. W. Kaler. Cloud-point phenomena in wormlike micellar systems containing cationic surfactant and salt. *Langmuir*, 18(4):1056–1064, 2002.

[256] C. Flood, C. A. Dreiss, V. Croce, T. Cosgrove, and G. Karlsson. Wormlike micelles mediated by polyelectrolyte. *Langmuir*, 21(17):7646–7652, 2005.

[257] T. J. Drye and M. E. Cates. Living networks — the role of cross-links in entangled surfactant solutions. *J. Chem. Phys.*, 96(2):1367–1375, 1992.

[258] T. Tlusty, S. A. Safran, and R. Strey. Topology, phase instabilities, and wetting of microemulsion networks. *Phys. Rev. Lett.*, 84(6):1244–1247, 2000.

[259] A. G. Zilman and S. A. Safran. Thermodynamics and structure of self-assembled networks. *Phys. Rev. E*, 66(5):051107, 2002.

[260] A. Zilman, T. Tlusty, and S. A. Safran. Entropic networks in colloidal, polymeric and amphiphilic systems. *J. Phys.-Condens. Mat.*, 15(1):S57–S64, 2003.

[261] J. T. Kindt. Simulation and theory of self-assembled networks: Ends, junctions, and loops. *J. Phys. Chem. B*, 106(33):8223–8232, 2002.

[262] W. J. Briels, P. Mulder, and W. K. den Otter. Simulations of elementary processes in entangled wormlike micelles under tension: A kinetic pathway to y-junctions and shear induced structures. *J. Phys.-Condens. Mat.*, 16(38):S3965–S3974, 2004.

[263] R. Strey. Microemulsion microstructure and interfacial curvature. *Colloid Polymer Sci.*, 272(8):1005–1019, 1994.

[264] P. K. Kilpatrick, W. G. Miller, and Y. Talmon. Staining and drying-induced artifacts in electron-microscopy of surfactant dispersions. 2. change in phase-behavior produced by variation in ph modifiers, stain, and concentration. *J. Colloid Interface Sci.*, 107(1):146–158, 1985.

[265] M. Gradzielski. Kinetics of morphological changes in surfactant systems. *Curr. Opin. Colloid Interface Sci.*, 8(4-5):337–345, 2003.

[266] M. Gradzielski. Investigations of the dynamics of morphological transitions in amphiphilic systems. *Curr. Opin. Colloid Interface Sci.*, 9(3-4):256–263, 2004.

[267] S. U. Egelhaaf and P. Schurtenberger. Micelle-to-vesicle transition: A time-resolved structural study. *Phys. Rev. Lett.*, 82(13):2804–2807, 1999.

[268] J. Leng, S. U. Egelhaaf, and M. E. Cates. Kinetics of the micelle-to-vesicle transition: Aqueous lecithin-bile salt mixtures. *Biophysical Journal*, 85(3):1624–1646, 2003.

[269] S. Dietrich. *Wetting Phenomena*, volume 12 of *Phase Transitions and Critical Phenomena*. Academic, London, 1988.

[270] P. G. de Gennes. Wetting — statics and dynamics. *Rev. Mod. Phys.*, 57(3):827–863, 1985.

[271] F. Brochardwyart, J. M. Dimeglio, D. Quere, and P. G. de Gennes. Spreading of nonvolatile liquids in a continuum picture. *Langmuir*, 7(2):335–338, 1991.

[272] J. A. Venables, G. D. T. Spiller, and M. Hanbucken. Nucleation and growth of thin-films. *Rep. Prog. Phys.*, 47(4):399–459, 1984.

[273] J. J. Lander and J. Morrison. Low voltage electron diffraction study of the oxidation and reduction of silicon. *J. Appl. Phys.*, 33(6):2089–2092, 1962.

[274] R. Tromp, G. W. Rubloff, P. Balk, F. K. Legoues, and E. J. Vanloenen. High-temperature SiO_2 decomposition at the SiO_2/Si interface. *Phys. Rev. Lett.*, 55(21):2332–2335, 1985.

[275] N. Fairly. See http://www.casaxps.com.

[276] M. P. Seah and D. Briggs, editors. *Practical Surface Analysis — Auger and X-ray Photoelectron Spectroscopy*. Wiley, Chichester, 2nd edition, 1990.

[277] F. J. Himpsel, F. R. Mcfeely, A. Talebibrahimi, J. A. Yarmoff, and G. Hollinger. Microscopic structure of the SiO_2/Si interface. *Phys. Rev. B*, 38(9):6084–6096, 1988.

[278] J. W. Keister, J. E. Rowe, J. J. Kolodziej, H. Niimi, H. S. Tao, T. E. Madey, and G. Lucovsky. Structure of ultrathin SiO_2/Si(111) interfaces studied by photoelectron spectroscopy. *J. Vac. Sci. Technol. A*, 17(4):1250–1257, 1999.

[279] P. Mack, R. G. White, J. Wolstenholme, and T. Conard. The use of angle resolved XPS to measure the fractional coverage of high-κ dielectric materials on silicon and silicon dioxide surfaces. *Appl. Surf. Sci.*, 252(23):8270–8276, 2006.

[280] J. Wolstenholme. Private communication.

[281] A. I. Martin-Concepcion, F. Yubero, J. P. Espinos, and S. Tougaard. Surface roughness and island formation effects in ARXPS quantification. *Surf. Interf. Anal.*, 36(8):788–792, 2004.

[282] Y. Tu and J. Tersoff. Structure and energetics of the Si-SiO_2 interface. *Phys. Rev. Lett.*, 84(19):4393–4396, 2000.

[283] Y. W. Mo, D. E. Savage, B. S. Swartzentruber, and M. G. Lagally. Kinetic pathway in stranski-krastanov growth of Ge on Si(001). *Phys. Rev. Lett.*, 65(8):1020–1023, 1990.

[284] G. Wedler, J. Walz, T. Hesjedal, E. Chilla, and R. Koch. Stress and relief of misfit strain of Ge/Si(001). *Phys. Rev. Lett.*, 80(11):2382–2385, 1998.

[285] J. A. Venables, J. Derrien, and A. P. Janssen. Direct observation of the nucleation and growth modes of Ag-Si(111). *Surf. Sci.*, 95(2-3):411–430, 1980.

[286] B. Elman, E. S. Koteles, P. Melman, C. Jagannath, J. Lee, and D. Dugger. Insitu measurements of critical layer thickness and optical studies of ingaas quantum wells grown on GaAs substrates. *Appl. Phys. Lett.*, 55(16):1659–1661, 1989.

[287] D. E. Aspnes and J. B. Theeten. Spectroscopic analysis of the interface between Si and its thermally grown oxide. *J. Electrochem. Soc.*, 127(6):1359–1365, 1980.

[288] A. Cerezo, C. R. M. Grovenor, and G. D. W. Smith. Pulsed laser atom probe analysis of semiconductor-materials. *J. Microscopy*, 141:155–170, 1986.

[289] M. Elbaum, S. G. Lipson, and J. G. Dash. Optical study of surface melting on ice. *J. Crystal Growth*, 129(3-4):491–505, 1993.

[290] A. Poynor, L. Hong, I. K. Robinson, S. Granick, Z. Zhang, and P. A. Fenter. How water meets a hydrophobic surface. *Phys. Rev. Lett.*, 97(26):266101, 2006.

[291] M. Mezger, H. Reichert, S. Schoder, J. Okasinski, H. Schroder, H. Dosch, D. Palms, J. Ralston, and V. Honkimaki. High-resolution in situ X-ray study of the hydrophobic gap at the water-octadecyl-trichlorosilane interface. *Proc. Natl. Acad. Sci. USA*, 103(49):18401–18404, 2006.

[292] J. Moon, S. Garoff, P. Wynblatt, and R. Suter. Pseudopartial wetting and precursor film growth in immiscible metal systems. *Langmuir*, 20(2):402–408, 2004.

[293] T. Pfohl, H. Mohwald, and H. Riegler. Ellipsometric study of the wetting of air/water interfaces with hexane, heptane, and octane from saturated alkane vapors. *Langmuir*, 14(18):5285–5291, 1998.

[294] H. Matsubara, N. Ikeda, T. Takiue, M. Aratono, and C. D. Bain. Interfacial films and wetting behavior of hexadecane on aqueous solutions of dodecyltrimethylammonium bromide. *Langmuir*, 19(6):2249–2253, 2003.

[295] A. I. Kingon, J. P. Maria, and S. K. Streiffer. Alternative dielectrics to silicon dioxide for memory and logic devices. *Nature*, 406(6799):1032–1038, 2000.

[296] K. J. Hubbard and D. G. Schlom. Thermodynamic stability of binary oxides in contact with silicon. *J. Mater. Res.*, 11(11):2757–2776, 1996.

[297] A. Gray. *Modern Differential Geometry of Curves and Surfaces with Mathematica.* CRC Press, Boca Raton, 2nd edition, 1998.

[298] L.P. Eisenhart. *A treatise on the differential geometry of curves and surfaces.* Dover, New York, 1960.

[299] G. B. Arfken and H. J. Weber. *Mathematical Methods for Physicists.* Academic Press, London, 5th edition, 2000.